Multijunction Solar Cells from Monolithic Integration of Dilute Nitrides on Gallium Arsenide (GaAs) and Silicon (Si) Wafers : defect studies

Artem Baranov

NNT : 2018SACLS137

Cellules solaires à multijonctions par intégration monolithique de nitrures dilués sur substrats d'arséniure de gallium (GaAs) et de silicium (Si): études des défauts

Thèse de doctorat de St Petersburg Academic University et de l'Université Paris-Saclay, préparée à l'Université Paris-Sud

École doctorale n°575 : electrical, optical, bio : physics and engineering (EOBE)
Spécialité de doctorat: Electronique et Optoélectronique, Nano- et Microtechnologies

Thèse présentée et soutenue à Gif-sur-Yvette, le 26 juin 2018, par

M. Artem Baranov

Composition du Jury :

Mme. Chantal Fontaine Directeur de Recherche, CNRS-LAAS	Rapporteur
M. Jean-Pierre Vilcot Directeur de Recherche, CNRS-IEMN	Rapporteur
M. Georges Brémond Professeur des Universités, INSA-Lyon	Examinateur
M. Père Roca i Cabarrocas Directeur de Recherche, Ecole polytechnique-LPICM	Président
M. Jean-Paul Kleider Directeur de Recherche, l'Université Paris-Saclay-GeePs	Directeur de thèse
M. Alexander Gudovskikh Directeur de Recherche, St Petersburg Academic University	Co-Directeur de thèse
M. Arouna Darga Maître de Conférences, UPCM-GeePs	Invité

Thèse de doctorat

Titre : Cellules solaires à multijonctions par intégration monolithique de nitrures dilués sur substrats d'arséniure de gallium (GaAs) et de silicium (Si): études des défauts.

Mots clés : cellules, hétérostructures, composés III-V

Résumé : Les cellules solaires à multi-jonctions de type III-V possèdent des rendements de conversion de l'énergie très élevés (46%). Cependant, les méthodes de fabrication généralement utilisées sont complexes et coûteuses, notamment pour les cellules solaires non monolithiques associées par des techniques de collage et à structure inversée. Cette thèse vise à augmenter les rendements de conversion des cellules solaires monolithiques à l'aide de méthodes prospectives. Le travail est focalisé sur l'étude des défauts électroniquement actifs dans les matériaux constituant les cellules solaires au moyen de techniques photoélectriques et capacitives, et il peut être scindé en trois parties.
La première partie traite des cellules solaires à simple jonction avec des couches absorbantes non dopées d'alliages InGaAsN de 1 eV de bande interdite de différentes épaisseurs obtenues sous forme de super-réseaux (InAs / GaAsN) par épitaxie à jets moléculaires (MBE) sur des substrats de GaAs. Pour des épaisseurs inférieures à 1200 nm, la concentration de défauts est négligeable et n'affecte pas fortement les propriétés photoélectriques, tandis que que pour une épaisseur de 1600 nm, la forte concentration de défauts détectés réduit la durée de vie des porteurs photogénérés, et conduit à une baisse significative du rendement quantique externe et des performances de la cellule.
La deuxième partie du travail est consacrée à l'étude de cellules solaires à une et plusieurs jonctions avec des couches actives de (In)GaP(As)N obtenues par MBE sur des substrats respectifs de GaP et de Si. Nous avons trouvé que les cellules solaires de type p-i-n avec des couches actives de GaPAsN non dopé présentaient de meilleures performances que les cellules solaires de type p-n avec des couches actives de GaPAsN dopé n. De plus, les cellules solaires avec une couche d'absorbeur en GaPAsN non dopé présentent de meilleures propriétés photoélectriques et des concentrations de défauts plus faibles que celles avec un absorbeur obtenu à partir de super-réseaux InP / GaPN. Plusieurs niveaux de défauts ont été détectés dans la bande interdite de ces matériaux et leurs paramètres ont été décrits en détail. Nous avons montré qu'un traitement de post-croissance approprié pouvait améliorer la qualité électronique des couches et des cellules solaires. Une cellule solaire à triple jonction a été fabriquée avec des couches actives d'absorbeurs de GaPAsN et de GaPN non dopées. La valeur élevée de la tension de circuit ouvert (>2,2V) atteste du fonctionnement des 3 sous-cellules, mais la performance globale est limitée par les faibles épaisseurs de couches d'absorbeurs.
Enfin, la troisième partie du travail est consacrée à l'étude de couches de GaP obtenues sur des substrats de Si à des températures inférieures à 400 ° C par une méthode originale de dépôt de couches atomiques assistée par plasma (PE-ALD). En effet, celle-ci utilise un équipement de dépôt chimique en phase vapeur assisté par plasma et elle repose sur l'interaction de la surface avec les atomes de Ga et P provenant respectivement du triméthylgallium et de la phosphine qui sont injectés alternativement. Nous avons également fait croître des couches en utilisant un processus continu (fournissant simultanément les atomes P et Ga) et observé que leurs propriétés électriques et structurelles étaient moins bonnes que celles obtenues par la méthode PE-ALD proposée. Nous avons exploré l'influence des conditions de croissance sur les hétérostructures GaP / Si. Nous avons constaté qu'une faible puissance de plasma RF conduit à de meilleures propriétés photoélectriques, structurelles et à moins de défauts, grâce à une meilleure passivation du substrat de silicium. En outre, nous avons démontré que, contrairement à des résultats de la littérature utilisant des procédés MBE, la technique PE-ALD n'affecte pas ou très peu les propriétés électroniques des substrats de silicium et aucune désactivation des dopants n'a été observée.

Title : Multijunction solar cells from monolithic integration of dilute nitrides on gallium arsenide (GaAs) and silicon (Si) wafers: defect studies

Keywords : solar cells, heterostructures, III-V compounds

Abstract : Multi-junction solar cells based on III-V compounds have reached very high power conversion efficiencies (46%). However, the fabrication methods that are generally used are complex and expensive for non-monolithic bonded and inverted solar cells. This thesis is devoted to the study of prospective methods to increase the efficiency of monolithic solar cells. The work is focused on the study of electronically active defects in the materials constituting the solar cells by means of photoelectric and capacitance techniques (admittance spectroscopy, DLTS,…) and it can be divided into three parts.

The first part deals with single-junction solar cells wherein the absorber is made of i-layers of 1 eV bandgap InGaAsN compounds with various thicknesses grown as sub-monolayer digital alloys (SDA) of InAs/GaAsN by molecular-beam epitaxy (MBE) on GaAs wafers. The cell with 900 nm thick InGaAsN exhibits the best photovoltaic performance and no defects could be evidenced from capacitance techniques. When the thickness is increased to 1200 nm, defects were detected, but their concentration is low so it did not strongly affect the photoelectric properties. Further increase to 1600 nm of the layer thickness was shown to lead to a higher defect concentration causing a change in the band diagram of the structure and lowering the lifetime of photogenerated carriers. This could explain the drastic drop of the external quantum efficiency, and the overall poor performance of the solar cell.

The second part is devoted to the study of single- and multi-junction solar cells with active layers of (In)GaP(As)N grown by molecular beam epitaxy (MBE) on GaP and Si wafers, respectively. More precisely, the active layers were either quaternary alloys of GaPAsN or SDAs of InP/GaPN. We found that p-i-n type solar cells with active layers of i-GaPAsN showed better performance than p-n type solar cells with active layers of n-GaPAsN due to higher EQE values. Moreover, solar cells with an i-GaPAsN absorber layer show better photoelectric properties and lower defect concentrations, than those with an SDA InP/GaPN absorber layer. Different defect levels were detected by capacitance methods in these materials and their parameters were described in detail. We showed that a suitable post-growth treatment could improve the electronic quality of the GaPAsN layer and the solar cell properties. Also, a triple-junction solar cell was fabricated with active layers of i-GaPAsN and i-GaPN. All subcells were found to be operating, leading to a large open circuit voltage (>2.2 V), but the overall performance is limited by the low value of the quantum efficiency due to low thicknesses of i-layers that should be increased for better absorption.

Finally, the third part is devoted to the study of GaP layers grown on Si wafers at temperatures below 400 °C using an original method called plasma-enhanced atomic-layer deposition (PE-ALD). Indeed, it uses a plasma-enhanced chemical vapor deposition equipment and it is based on the alternate interaction of the wafer surface with Ga and P atoms coming from injected trimethylgallium and phosphine, respectively. We also grew layers using a continuous process (providing simultaneously the P and Ga atoms) and observed that their electric and structural properties were poorer than that grown by the proposed PE-ALD method. The influence of growth conditions on the GaP/Si heterostructures was explored. We found that low RF-plasma power leads to better photoelectric, structural and defect-related properties, due to a better passivation of the silicon wafer. In addition, we demonstrated that, contrary to results reported in the literature using MBE processes, our growth process does not affect the electronic properties of phosphorous doped n-Si wafers, while slight changes were observed in boron-doped p-Si wafers containing Fe-related defects, however without deactivation of the doping nor strong degradation of the electronic properties.

Acknowledgements

This PhD thesis is the result of joint research of many persons in France and Russia so I'm happy to present them here. I want to thank Jean-Paul Kleider, my supervisor in GeePs, for his patient explanations of fundamental semiconductor physics, useful criticism in experimental work, his great help in my stay in Paris and hospitality. Also, I am grateful to Alexander Gudovskikh, my co-supervisor in Academic University, for my introduction in photovoltaics, infinite discussion of solar cells and belief in me. Therefore, I have always felt their support and scientific interest in our research.

I thank all my colleagues from GeePs, especially Arouna Darga for the experience in experimental methods and Sylvain Le Gall for useful criticism in theoretical issues, all professional technical staff and responsive administrative one for kind and working atmosphere in GeePs. Further, I appreciate all colleagues in Laboratory of Renewable Energy in Academic University, especially Dmitry Kudryashov, Ivan Morozov, Alexey Mozharov, Alexander Uvarov, for post-growth processing, Kirill Zelentsov and Anatoly Monastyrenko for working equipment. Also, gratitude goes to Laboratory on Nanoelectronics for grown structures.

Furthermore, I want to thank French government and Campus France (bourse Metchnikov) and Université Paris-Sud for financial and administrative support during PhD thesis under joint russian-french supervision. The study was carried out in the framework of the research project for young scientists RFBR #16-38-00791 and the PACSiFIC project funded by RFBR (#16-58-150006) and CNRS (PRC n°1062).

Last but not the least, I wish to thank my lovely family and dear friends from Paris and St Petersburg for their patience and support.

Content

Introduction

Nowadays, most sources of electric energy have different drawbacks: security (nuclear power), limited reserves of fossil fuels (oil, gas, coal), negative influence on the environment (hydropower), etc. Photovoltaics is a clean and powerful way to provide electricity and supply the growing demand of all countries. Indeed, it allows one to use an infinite source of energy that is available to everybody -the Sun- and directly converts it into electric energy.

Thus, my thesis is devoted to the investigation of new semiconductors for the fabrication of low-cost high-efficiency solar cells. The study is focused on multi-junction solar cells with active layers of III-V compounds grown on wafers of IV group elements. In Chapter I, the solar cell retrospective and modern concepts studied in the current work are presented. Then, the used methods of fabrication and characterization are described in Chapter II. Next three chapters are devoted to the study of different types of devices. Chapter III is related to the investigation of InGaAsN alloys grown by molecular beam epitaxy on GaAs and Ge wafers, Chapter IV concerns InGaPAsN grown on GaP and Si wafers by the same method, Chapter V deals with GaP grown on Si wafers by plasma-enhanced atomic-layer deposition. Finally, our studies are summarized in conclusion and some future works are suggested.

Chapter I

Bibliography

Introduction

In this Chapter, the literature review is presented for explored topic of thesis. Background is shown for modern and perspective MJSCs grown with using of III-V compounds on Si and Ge wafers. Problems and possible methods of their solution are given for different systems of semiconductors for photovoltaic application.

I.1 Retrospective

The era of semiconductor photovoltaics had started in the 1930s with results obtained on sulfur-thallium solar cells (SCs) at Ioffe Institute in Leningrad[1]. The study was carried out under the supervision of the founder of the Institute, academician A. F. Ioffe who firstly introduced a program for solar energy use by photovoltaic roofs to the USSR government. In 1940, another breakthrough event occurred in semiconductor technology: the first silicon p-n junction was unconsciously created. This discovery opened new possibilities for fabrication of transistors, light-emitting diodes and SCs for electricity production. On February 23, 1940, the American physicist Russell Ohl investigated a "strange" silicon sample whose current-voltage characteristics were erratic. It turned out that the sample reacted to light, and the degree of the observed photo-effect exceeded by one order of magnitude the photoelectric effect in traditional SCs. Consequently, Ohl accidentally obtained a semiconductor SC of a modern type patented in 1946. The principle of its operation is based on the absorption of radiation with energy close to the bandgap energy of the semiconductor and the formation of charge carriers creating a potential difference and a current. Ohl's colleague, Walter Brattain, guessed that the photoelectrical effect occurs on some invisible barrier between two silicon layers and the same barrier should straighten the alternating current. The layers were named p-type (positive, traces of boron were found in silicon) and n-type (negative, phosphorus was detected) by the type of doping, and the barrier area became known as the p-n junction. W. B. Shockley, W. Brattain and J. Bardeen in the American company Bell Laboratories discovered and described the field effect consisting in controlling the electrophysical parameters of the surface of a solid state with an electric field applied along the normal to the surface. On the basis of *p-n* junction, the same group fabricated the world's first semiconductor

transistor on 23th December of 1947, which is an important invention of the XXth century, since all modern electronics and nanoelectronics operate on the basis of field-effect transistors. On April 25, 1954, first silicon SCs were demonstrated at Bell Laboratories with an efficiency of about 6%[2]. Despite the low value of efficiency, the silicon SCs were used for serious purposes: in 1958 the first satellites equipped with such SCs - the Soviet “Sputnik-3” and the American “Avangard-1” were launched.

From the middle of the XXth century, the intensive development of silicon technology has contributed to the studies of silicon SCs around the world: it predetermined their widespread distribution observed today. The basis of technology for the silicon production, purification and processing have been developed in industry so it has been in the highest level among all semiconductor materials by now. However, since the 1950s new semiconductor materials called III-V compounds have started to be synthesized. It was initially binary and, later, multicomponent compounds including as a minimum one element of both III and V groups of the periodic table, for example, the well-known gallium arsenide (GaAs). Then, the first GaAs-based SC was fabricated, but it had lower performance compared to the silicon ones due to the material quality, since the GaAs technology had not yet been industrially worked out as for silicon. In the second half of the 1960s some pioneering work was carried out to obtain and study "ideal" heterojunctions in the AlAs-GaAs system that is used for the fabrication of wide-bandgap windows in SCs[3]. The idea relies on using a semiconductor with a larger bandgap energy (AlGaAs) than in the active region (GaAs) to reduce the recombination losses of charge carriers at surface states. It allowed to improve the SC characteristics, and their high radiation resistance have promoted the use of GaAs SCs in space by USSR in the “MIR” station in 1986[4].

Further developments of growth technologies have led to the improvement of SCs quality and increase of their efficiency. Until the 1980s, the main method of material growth was liquid-phase epitaxy (LPE) allowing to create simple SCs based on a *p-n* junction, but the development of modern epitaxial growth technologies like vapor-phase (VPE) and molecular-beam (MBE) epitaxy led to a strong increase in efficiency: it has become significantly higher than 20% in SCs based on the AlGaAs/GaAs system. On the other hand, new methods have been investigated for the fabrication of silicon SCs. The first one is the use of phosphorous diffusion into p-Si wafers for the fabrication of *p-n* junctions, and the other one is plasma-enhanced chemical vapor deposition (PECVD) of hydrogenated amorphous silicon (a-Si:H) on wafers because it allows one to create *p-n* junctions while providing outstanding passivation of the silicon surface. At present, the record efficiency is 28.8% and 26.7% for single-junction SCs based on GaAs (MOCVD)[5] and Si (PECVD)[6], respectively.

Since the 1960s, new ideas have originated: if a *p-n* junction of a semiconductor with a large bandgap is grown on another *p-n* junction with smaller bandgap, it would be possible to absorb a wider part of the solar radiation spectrum while limiting thermalization losses. Such solar cells are named multi-junction SCs (MJSC), and each constituent based on a *p-n* junction is named a subcell. The spectrum of solar radiation is heterogeneous as shown by Isaac Newton in an experiment on the light dispersion[7]. The single-junction SC absorbs only a part of the spectrum: radiation at photon energies larger than the bandgap energy of the semiconductor. According to the model of Shockley and Queisser[8], the maximum achievable efficiency for single-junction SCs is slightly larger than 30%. It is due to different intrinsic loss mechanisms in semiconductors[9] (Figure I.1a). Figure I.1b visualizes two main loss mechanisms for silicon SCs[10]: for photons energy lower and higher E_g, respectively. The first one is due to the absence of absorption for photons with energy lower than the bandgap. On the other hand, photons with higher energy can produce only one electron-hole pair so the excess energy compared to the bandgap energy is lost in thermalization of the created hot carriers.

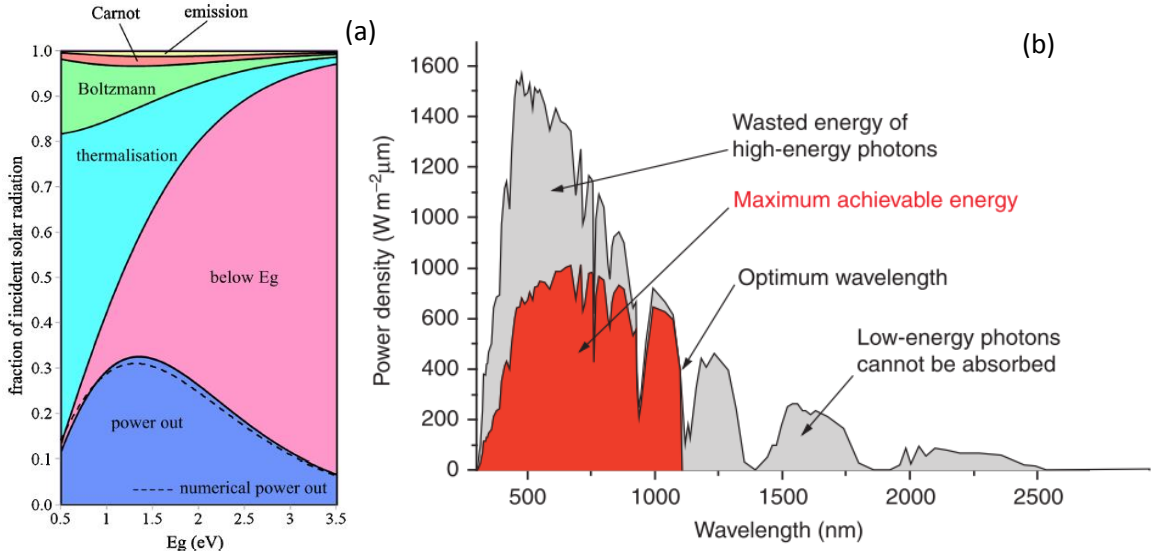

Figure I.1 a- intrinsic loss processes and conversion in outcoming power are shown to be dependent on the bandgap, E_g[9]; b- Spectral losses in a solar cell. The figure shows the maximum achievable energy of a silicon solar cell in relation to the sun spectrum (AM1.5)[10].

Therefore, in the end of the 1980s, many research groups concentrated their efforts on the development of various types of double-junction SCs. At the first stage, the best efficiencies were obtained in mechanically bonded SCs developed at NREL (USA). Both single-junction SCs were grown on germanium wafers with an active *p-n* junction of GaAs and GaInP lattice- matched to Ge by MOCVD as bottom and top junctions, respectively. Then the two *p-n* junctions are

mechanically bonded, and the upper Ge wafer is "shot back" by laser processing. As epitaxial technologies have been developed, many scientific groups have started to grow monolithic MJSCs on single wafers with three and more *p-n* junctions in one process. Further, the GaInP/GaAs/Ge system proves to be the simplest in production since the lattice constant of these materials is almost the same, and this is the most important parameter affecting the quality of grown semiconductor heterostructures. The efficiency of SCs based on this system exceeded 40% in 2007[11]. Furthermore, many attempts were made to increase the efficiency with the use of new inventions and post-growth methods in addition to the development of epitaxial technologies. Thus, in the 1980s, it was noted that SCs based on GaAs heterojunctions can more effectively work at high concentration of the sun light flux (several hundreds times) and it distinguishes them from silicon ones. At that time first SCs were fabricated for application under concentrator illumination[12].

Nowadays, almost all record values of efficiency are obtained for MJSCs based on III-V compounds using concentrating lenses, and the maximum efficiency today is 46%[13]. SCs with similar III-V compounds are used in space satellites and on the International Space Station (ISS) for electricity production where the most important properties of SCs are high efficiency and radiation resistance, while the high price is the main drawback for their use in terrestrial applications.

The main goal of this thesis is to study new approaches to enhance the efficiency and reduce the cost of MJSCs based on III-V compounds for both space and terrestrial applications. These approaches are based on new growth methods of III-V compounds for further application as active layers in MJSCs. Our work is focused on the study of electronically active defects using a set of complementary characterization techniques, the main emphasis being on admittance and capacitance techniques.

I.2 MJSCs on Ge and GaAs wafers

I.2.1 InGaAsN on Ge

MJSCs based on III-V compounds have the highest efficiency in the world and their record-efficiency has almost reached the psychological barrier of 50% for concentrator photovoltaics[13]. The four-junction SC based on the GaInP/GaAs/GaInAsP/GaInAs system[14] has the record efficiency of 46%[13], but it is fabricated by bonding of two structures grown on different wafers. The triple-junction SC based on the system InGaP/GaAs/InGaAs was metamorphic grown on a GaAs wafer and then it was inverted on a Si wafer: it has 44.4% efficiency[15]. However, these methods strongly limit the transfer to industry due to complicated technological steps, so monolithic MJSCs grown epitaxially without any mechanical processing steps are the most

interesting. Efficiency of such MJSCs is almost the same and the record is 45.7% for the four-junction SC based on the GaInP/GaAs/GaInAs/GaInAs system at a concentration of 294 suns[16]. According to previous studies two junctions based on GaInP (1.85 eV) and GaAs (1.42 eV) are the most common and industrially used for the SC fabrication based on III-V semiconductors[17]. Initially, the bottom *p-n* junction in the germanium wafer is used in combination with two other junctions in GaInP and GaAs to obtain triple-junction SCs. The bandgap energy of Ge is 0.67 eV[17], so the long-wavelength spectrum of sun radiation can be effectively absorbed. Moreover, the lattice- mismatch between Ge and GaAs is less than 0.1%, therefore there are possibilities for high-quality GaAs layers on Ge wafers (Figure I.2).

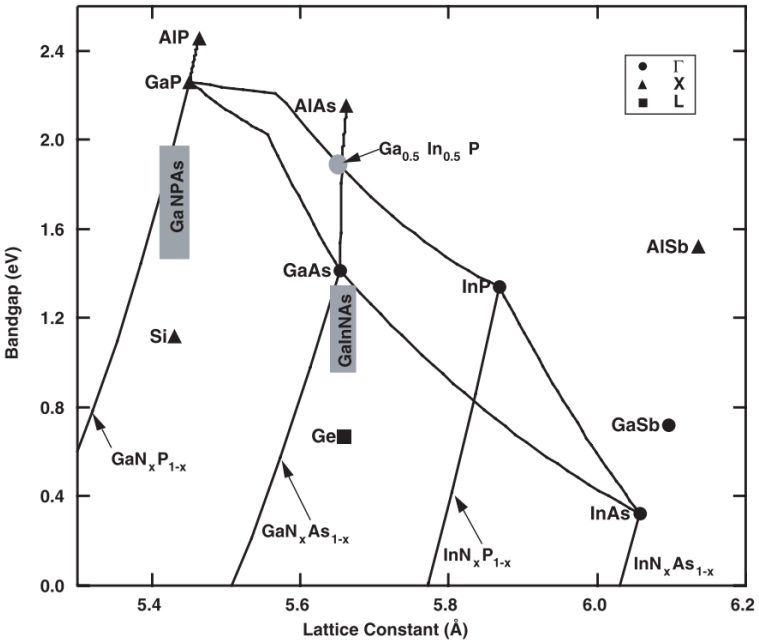

Figure I.2 Bandgap versus lattice constant. The grey boxes indicate nitrogen-containing alloys that have been grown lattice-matched to Ge and Si[18].

In addition, according to theoretical estimations the substitution of a germanium subcell with a subcell having a bandgap energy of 1 eV could increase the 3-junction SC efficiency by a few percent, and the addition such a subcell to a 3-junction grown on a Ge wafer will allow to reach 52% under concentration[19,20]. InGaAsNSb with small nitrogen content is the most prospective semiconductor for this goal. III-V-N alloys (GaPNAs, InGaNAs etc.) with nitrogen content less than 5% are called dilute nitrides. It has been shown that the small addition of nitrogen leads to the large bowing parameter for the bandgap in GaAsN alloys: adding only few percent of nitrogen reduces the bandgap by hundreds of meV[21]. Additional content of indium in $In_yGa_{1-y}N_xAs_{1-x}$ alloys is necessary for lattice-matching with Ge and GaAs when y=3x: it allows to epitaxially grow layers of InGaAsN on these wafers, and its bandgap energy can vary in a wide

interval and reach 1 eV[18] (Figure I.2). Such compounds like InGaAsN have been intensively investigated since the 1990s due to high interest in the fabrication of lasers for 1.3-1.55 μm wavelength on GaAs wafers[22]. However significant progress in the growth technology for photovoltaic applications has been reached only a few years ago due to the improvement in epitaxial equipment and methods. 44% is the record efficiency for the 3-junction SC grown by MBE with the bottom subcell based on the active layer of InGaAsNSb at 942 suns concentration[23]. A group from Finland obtained a value of 37-39% at 70 suns concentration for similar construction of 3-junction SCs grown by MBE with bottom InGaAsNSb subcell[24], they also reached an efficiency of 29% at AM0[25] for 3-junction SCs, where the bottom subcell based on InGaAsN was grown by MBE and top subcells were grown by VPE[26]. Despite the result achieved using growth of InGaAsN layers, MJSCs are limited by low lifetimes of charge carriers in these alloys[27]. It originates from an increased defect formation due to the incorporation of nitrogen into the lattice of GaAs at lower growth temperatures of InGaNAs in comparison with the growth of GaAs. It leads to the formation of centers of non-radiative recombination with high concentrations. It is known that the *p-i-n* junction is preferable to the *p-n* junction for active layers of SCs with low lifetimes of charge carriers, since the built-in electrical field reduces the recombination in the active region and improves the collection of charge carriers. Atoms of carbon and hydrogen can incorporate during the growth of III-V compounds by VPE: it leads to the unintentional background doping and the formation of various defects which have negative influence on the lifetimes in InGaNAs layers and on the efficiency of the SC[28]. Therefore, the equipment of MBE with RF- plasma source of nitrogen is more preferable for the growth of InGaAsN since it allows excluding the presence of C and H in the chamber. However, even MBE-grown InGaNAs layers have the concentration of the background doping up to 1×10^{17} cm^{-3} [29]: it leads to big changes in the band diagram for the i-layer, so the SC efficiency can significantly decrease if the charge carrier lifetime is low in active layers. The post-growth annealing is one of the ways to improve the quality of InGaNAs dilute nitrides [30–32]. Also, it has been proposed to use antimony (Sb) for the prevention of large defect formation and background doping during the growth because Sb is a good surfactant[33–36]. The authors showed the inhibition of the defect formation during the growth and a reduction of background doping concentration in the active layers of dilute nitrides. However, Sb has a significant disadvantage: due to deposition and accumulation on the walls inside the MBE chamber, it leads to undesirable background doping of layers in top subcells. Therefore, growth of MJSCs with Sb requires equipment with two growth chambers, but it significantly complicates the application of this technology in industry. Furthermore, the growth of such quinary alloys as InGaAsNSb is a difficult task due to the complexity of simultaneous control of material flows during the process.

In this work, the novel growth method of InGaAsN alloys by MBE without addition of antimony atoms is proposed to avoid the problems described above. It consists of using nanoheterostructures of an original design based on the InAs/GaAsN superlattice, where several InAs monolayers are separated by wide GaAsN barriers[37]. It opens the possibility of growth of semiconductor materials with the properties of quaternary solutions of InGaNAs with separated fluxes of indium and nitrogen. Thus, thick InAs layers of few monolayers compensate the elastic stresses arising during the growth of GaAsN on the GaAs wafer due to their lattice-mismatch. The semiconductor compound grown by the described method is called a sub-monolayer digital alloy (SDA). The method was successfully applied for the growth of III-V[38–40] and II-VI[41,42] compounds by MBE. Thus, in present work, the first task is the study of single-junction SCs with active layers of InGaAsN grown by SDA InAs/GaAsN on GaAs wafers.

I.3 MJSC on Si wafers

I.3.1 GaAs on Si

The wafer represents at least 50% of the cost of the SC so MJSCs grown on GaAs and Ge wafers are very expensive for terrestrial photovoltaic applications. The cost of the silicon wafer is the cheapest one compared to other semiconductor materials. Silicon is the second most abundant element on the Earth, after oxygen. Si accounts for 27.6-29.5% of the total mass of the earth's crust: sand is its simplest form. However, the reserves of pure silicon, suitable for nanoelectronics, are much smaller, and the technology requires high temperatures of 1100 °C. The silicon technology has been worked out much better than other ones, so about 90% of the SCs used in terrestrial applications are fabricated on monocrystalline silicon wafers with active layers of mono-, micro-crystalline and amorphous silicon. The record efficiency SC based on silicon is 26.7%[6] and it almost reaches the theoretical limit for the silicon single-junction SC.

Consequently, PV requires new approaches for high-efficiency and low-cost SCs, which can combine advantages of III-V MJSCs and silicon SCs. The fabrication of MJSCs with active layers of III-V compounds on silicon wafers is a prospective field for the photovoltaic industry. It is a real challenge for scientists, because this technology can also open ways for the fabrication of cheap optoelectronic integrated circuits with LEDs, lasers, HEMTs etc.

Historically, GaAs was the most common and most used material in the optoelectronic industry therefore it was the main reason for the development of monolithic growth technologies for this material on monocrystalline silicon wafers. Also, it was theoretically shown that single-junction and multi-junction GaAs-based SCs have the highest efficiency limit in the world [14]. Thus,

the majority of works about growth of III-V compounds on Si is devoted to the study of the GaAs growth on silicon wafers[43–59].

In 2008, Russian authors published a comprehensive and structured review of world research in this topic[43]. The growth of polar III-V compounds on a non-polar silicon wafer can lead to the formation of antiphase domains, but this problem could be solved by using disoriented wafers by 4°-6°[44]. Furthermore, the main fundamental problems of the GaAs growth on Si are the large mismatch of lattice constant (4%) and the difference in the coefficients of thermal expansion which have not been completely solved yet[17]. Two ideologically different groups of methods have been proposed to solve these problems.

The first approach provides attempts to grow GaAs directly on silicon wafers using different techniques: cyclic annealing[45], two-step growth[46,47], the use of surfactants, for example, hydrogen[48]. The most common method is the growth of a very thin nucleation layer at low temperature and the subsequent growth of active layers at higher temperatures. This technology allows one to obtain better structural properties of grown GaAs layers. The possible reason of this improvement is the higher mobility of the defects leading to their annihilation in the next growth steps.

A classical single-junction SC based on GaAs was grown on a silicon wafer with this two-step method. First, a buffer GaAs layer was grown by MBE at low temperature of 390 °C, then the sample was placed in a the VPE-chamber, where active GaAs layers were grown[46]. But the SC efficiency was only 11.17% due to the presence of a large number of defects near the edge of the bandgap in GaAs. In another work[47] the special process of annealing was carried out at a temperature of 600 °C to improve the layer characteristics after the growth of the buffer layer at a temperature of 150-300 °C. Then the SC was grown, the part of silicon wafer was shaped as an array of pyramids to reduce the effect of defects on the GaAs/Si heterointerface from the rear: it allowed to increase the efficiency from 8.7% to 10.6%. Previously, double-junction monolithic SCs based on GaAs/Si were grown in Japan by MOCVD[52], where the silicon homojunction acted as the bottom subcell, with an efficiency of 19.9%.

In recent years, novel methods of GaAs growth through holes in the buffer layer of dielectric materials covering silicon have emerged [53–55]. It allows avoiding the large number of antiphase domains on the Si/GaAs heterointerface in the first steps of growth. Further single crystals of GaAs would coalesce after passing through the entire thickness of the dielectric without dislocations formation. A French group has developed a method for the GaAs growth through holes in a silicon oxide (SiO_2) film with a thickness of 0.6 nm by the epitaxial lateral overgrowth method allowing to obtain III-V material of good quality[53]. Also, the improvement of structural properties of GaAs single crystals was obtained with an increase in the growth temperature from

550 to 575 °C[54]. SCs based on a GaAs *p-i-n* junction was grown in the holes of the SiO_2 film (its thickness was 200 nm) but it had an efficiency of less than 1%[55].

The second group of methods is based on the use of different thick buffer layers consisting of different materials (Ge, GaInP, GaAsP etc.) giving the possibility to grow a thick GaAs layer with high quality[49–51]. The metamorphic method consists in a smooth transition from the lattice constant of Si to GaAs or Ge. Thus, the silicon wafer is used as a template wafer for the subsequent growth of active semiconductor structures of GaAs. The buffer layer quality is not important in this method so dislocations can introduce in it. For photovoltaic application, the silicon wafer should be considered as an active layer for the bottom subcell in the ideal MJSC so the GaAs/Si interface must have high quality for a good transport of charge carriers through it. Thus, these methods are less preferable since defects and dislocations lead to significant recombination losses of charge carriers in buffer layers. Consequently, it does not permit to use silicon for high photovoltaic performance SCs.

As described above no successful approach has been found for monolithic epitaxial growth of GaAs on silicon wafers for optoelectronic applications like SCs. The mechanical bonding method was suggested to avoid direct growth of III-V compounds on the Si wafer. Two structures are grown on their different own wafers of GaAs and Si[56], then they are mechanically connected, and the top GaAs wafer is removed. As a result, a double-junction SC was fabricated with an efficiency of 19.1%. In this approach, the main efforts are focused on the development of a bonding technology allowing to reduce the effect of defect levels forming at the Si/GaAs heterointerface during the bonding process[57]. Nowadays, an efficiency of 27% was achieved for the tandem bonding SC based on the GaInP/Si system[58], and a triple-junction SC based on GaInP/GaAs/Si was grown[59]. However, the method of mechanical bonding is expensive and difficult to adapt to the industrial SC production.

To summarize, the monolithic epitaxial growth of GaAs on silicon is a very difficult task for modern optoelectronics due to the high lattice-mismatch between Si and GaAs. It leads to drastic degradation of the layer quality and low SC performance. Also, the bonding technology of GaAs/Si MJSC is very complex and inconvenient for low-cost mass-production. This is why novel semiconductor materials have been explored for a lattice-matched growth in top subcells of monolithic MJSCs on silicon wafers in one process without any mechanical steps.

I.3.2 GaP on Si

Gallium phosphide (GaP) is one of the best choices of III-V semiconductor to be grown on Si wafers. The lattice-mismatch between GaP and Si is only 0.37%[17] so it opens wide perspectives for the pseudomorphic epitaxial growth of layers based on GaP. Nowadays, there is a large number

of works devoted to the development of dislocation-free growth of GaP on silicon wafers[60–66]. However, problems occurring during the growth process are similar to the ones in the growth of GaAs on Si. Firstly, the growth of polar GaP compounds on a nonpolar Si wafer leads to the formation of antiphase domains[60]. Secondly, the requirement of high growth temperatures and different coefficients of temperature expansion of GaP and Si causes the formation of threading dislocations[61]. These reasons seriously complicate the growth process.

The methods for avoiding these problems coincide with that proposed above for the growth of GaAs on Si. First of all, the two-steps method is used with a nucleating layer grown at low temperature in a first step[62–64]. This growth method of the nucleation layer is called "MEE-migration enhanced epitaxy" for MBE. It consists in an alternate interaction of the gallium and the phosphorus fluxes with the wafer surface at low temperatures of 350-400 °C. In the second step, the growth of III-V materials occurs at high temperatures of 550-600 °C with continuous fluxes of atoms. According to SEM measurements much lower density of threading dislocations arises in the sample with nucleation layer of GaP[64] that positively impact the lifetime of charge carriers. Secondly, annealing procedures can also improve the quality of the GaP layers grown by MBE. For example, the multistage annealing at temperatures of 380-480 °C is preferable to the annealing at a constant temperature of 400 °C because crystal properties of GaP epilayers strongly improved[65]. Thirdly, the pre-epitaxial treatment of the wafer surface also can be used for optimizing the growth of GaP on Si. For instance, the silicon surface reconstructs in the growth chamber at temperatures of 700-800 °C under the gas flow of arsine (AsH_3) leading to better quality of GaP layers[66].

Despite the difficulties of the GaP growth on Si this concept is optimal for low-cost high-efficiency SC due to good passivation of Si by GaP and the possibility of growth of top subcells based on III-V alloys lattice-matched to GaP and Si as described below. Also, the efficiency of single-junction SCs based on the GaP/Si heterojunction should be by 1.1% higher than in a standard silicon diffusion homojunction, V_{OC} will be higher by 49 mV and can reach 0.7 V according to the theoretical estimations[67]. In 1980, the first SC based on a GaP/Si heterojunction was fabricated with high V_{OC}=0.66 V, but with it has low efficiency η=1.7% due to poor fill factor[68]. In 2015, similar SC with optimized contacts showed V_{OC}=0.634 V, and the efficiency reached 12.4 %[69].

I.3.3 InGaPAsN on Si

Through the relative success in the GaP growth on Si, new perspectives have opened in last few years for the growth of unusual kinds of semiconductors for the fabrication of MJSCs based on the integration of III-V compounds on silicon wafers. These modern materials are alloys

of In-Ga-P-As-N lattice-matched to GaP and Si with small nitrogen content. However, unlike the dilute nitrides of InGaAsN lattice-matched to GaAs and Ge described above, alloys of InGaPNAs are not investigated so far and their properties are poorly known (electron and hole mobility, lifetimes of charge carriers, effective density of states in the valence and conduction bands, etc.).

As known, GaP is an indirect semiconductor but the incorporation of nitrogen atoms leads to a significant change in the band structure of GaPN. The incorporation of just 0.43 % atomic fraction of nitrogen into the GaP lattice leads to the direct band transition, and the bandgap drastically decreases for increasing nitrogen content of few percent[70,71]. The theoretical description of the band diagram for dilute nitrides of InGaAsN and InGaPAsN will be described in detail in the next section, since it is a very important and extraordinary feature of these semiconductors. Furthermore, an addition of indium and (or) arsenic atoms allows one to vary the bandgap energy in a wide range of 1.5 to 2.1 eV while remaining lattice-matched to Si or GaP wafers[18] (Figure I.2).

The theoretical efficiency limit of double-junction SCs was simulated as a function of the bandgap energy of the bottom and top subcells[72]. According to such simulations 1.1 eV is the most optimal value of bandgap energy for the bottom subcell, and fortunately, it nicely corresponds to the value of silicon (E_g=1.12 eV)[17]. Further, the bandgap energy of InGaPAsN lattice-matched to Si varies in a wide range so 1.7 eV-InGaPNAs layers could be grown with good quality in the future. Such value is optimal for the top subcell in double-junction SCs. In this case the theoretical limit of the InGaPAsN/Si system achieves a value of 37.4% under AM1.5G[18]. The theoretical limit for double-junction SCs of GaInP/GaAs is only 35.1% and experimental samples have almost reached its record-efficiency value of 31.6% for monolithic SCs[73]. Furthermore, triple-junction SCs based on the InGaPAsN(1.8eV)/InGaPAsN(1.4eV)/Si system is preferable to the GaInP/GaAs/Ge system. The potentially achievable efficiency of a triple-junction SC based on the GaPNAs/GaPNAs/Si system (bandgap energy 2.0/1.5/1.2 eV) was theoretically calculated to be 44.5% when reaching a ~1ns minority carrier lifetime in GaPNAs[74]. The result of simulation creates promising background for the fabrication of high-efficiency MJSCs based on the InGaPAsN/Si system, and using cheap silicon wafers allows one to consider these SCs for future industrial production.

Attempts to synthesis of alloys with mixed anions such as $GaAs_{1-x}N_x$ and $GaP_{1-x}N_x$ started in the 60s of the XXth century. The main problem was the low nitrogen incorporation in InGaPAsN layers for obtaining significant nitrogen content of several percent. The nitrogen content had been obtained only at the level of the dopant until the mid-90s, so the semiconductors could not be considered as classical ternary alloys. Subsequent development of VPE and MBE technologies helped growing compounds with N content of few percents[75–77]. In contrast to (In)GaAsN alloys

InGaPAsN ones lattice-matched to GaP have not been popular in research so these compounds are weakly investigated. One of the first quaternary alloys of $GaP_{1-x-y}As_yN_x$ was grown on GaP wafers with contents of x=2% and y=0..19%[78] and the sample with multiple quantum wells with x=2% and y=12%[79] by MOVPE in Japan. In this article, the absence of dislocation was experimentally shown for compounds of GaPAsN and GaPN with different compositions and lattice-mismatch to GaP less than 0.3%. From this moment, properties of (In)GaPN(As) have begun to be investigated more deeply.

Nevertheless, the growth of InGaPAsN on Si and GaP wafers is still a challenge for researchers since there are many unsolved problems similar to the growth of InGaAsN on GaAs and Ge ones. First of all, growth of dilute nitrides layers occurs in non-equilibrium conditions at low temperature required for better nitrogen incorporation. Usually, it is less than 500 °C whereas the optimal growth temperature of GaAs and GaP is close to 600 °C. Secondly, a higher nitrogen content leads to the reduction of the bandgap energy of GaPN but in the same time it leads to a deterioration of the GaPN quality. According to previous studies, the photoluminescence intensity decreases drastically with increasing nitrogen concentration in GaPN; it decreases also in the same layers of dilute nitrides grown on Si instead of GaP wafers[71,80–82]. Moreover, the incorporation of nitrogen in the GaP lattice leads to the appearance of elastic stresses in pseudomorphic layers and lattice-mismatch with GaP and Si wafers. All this contributes to the appearance and increase of dislocations, appearance of antiphase domains and significant concentration of point defects (being non-radiative recombination centers) during the growth. Consequently, it can negatively impact the lifetime of charge carriers, the electron and hole mobility and other electrical properties that are crucial for optoelectronic devices. Nowadays, the number of studies concerned with defects in the InGaPNAs alloys isoperiodic to GaP is very small. The method of optically detected magnetic resonance (ODMR) has been used to find and describe a number of defects of the Ga_i type in GaPN(As) layers[83–85], but ODMR does not allow one to obtain useful information on its position in the band diagram, values of capture cross sections and concentration. These parameters are necessary for computer simulation of SC performance and defect influence on the lifetime of charge carriers in dilute nitrides. On the other hand, deep-level transient spectroscopy (DLTS) has been used to study defects in GaP:N layers (with a nitrogen concentration of $(3–8)\times10^{18}$ cm^{-3})[86–91] and $GaP_{0.991}N_{0.009}$ [92], but similar studies of InGaPAsN with higher nitrogen content have not been found.

Therefore, different ways were proposed to improve the quality of GaPN dilute nitrides, and they are similar to the ones for InGaAsN lattice-matched to GaAs. Rapid thermal annealing is often a powerful method for the improvement of semiconductors properties and it led to the passivation of some defects in GaPN[93]. Furthermore, additional incorporation of arsenic and

indium leads to the significant growth of the PL amplitude[81] and the inhibition of defect formation in dilute nitrides[85,94]. However, the quality of (In)GaPN(As) lattice-matched to GaP has still remained very poor so the fabrication of SCs with high efficiency is limited by low lifetimes in InGaPAsN materials.

There are only a few studies of SCs based on InGaPAsN lattice-matched to GaP or Si. In the early 2000s, a group from NREL firstly fabricated SCs with an active layer of a quaternary alloys of GaPAsN: single-junction lattice-matched to GaP wafers[95] and double-junction lattice-matched to Si wafers[96] by MOCVD. The best performance for single-junction SCs was shown in the sample with the undoped $GaP_{0.83}As_{0.14}N_{0.03}$ layer 0.64 μm thick and its important parameters are an open-circuit voltage value V_{OC}=1.12 V, a short-circuit current density J_{SC}=5.8 mA/cm^2 and a fill factor *FF*=60%, and the maximum of internal quantum efficiency was close to 70%. The double-junction SC had a low efficiency of 5.2% due to the bad quality of the GaPAsN. This can be caused by two reasons. The first one is a large number of threading dislocations rising during the growth on a silicon wafer (10^7 cm^{-2}) because their concentration is lower during growth on GaP wafers (10^5 cm^{-2}). The second one is the high nitrogen content of 4% in the quaternary alloy leading to a significant deterioration of its optical and electrical properties as described above.

For a long time they have remained the only SCs based on dilute nitrides InGaPAsN lattice-matched to GaP and Si. However, as for InGaAsN/GaAs the development of MBE opened good perspectives for the fabrication of SCs with active layers of InGaPAsN/GaP. In 2015, a single-junction SC was grown with an efficiency of 7.9% by MBE with RF-plasma source of nitrogen on GaP wafers[97]. It is based on elastically stressed $GaPN_{0.018}$ undoped layer 2μm thick and its photovoltaic parameters are V_{OC}=1.33 V, J_{SC}=8.53 mA/cm^2, *FF*=69%. Maximum of external quantum efficiency was 95% for the sample with anti-reflection coating. It is a great result for SCs based on GaPN that confirms possibilities of MBE equipment. Also, a single-junction SC was grown with the active layer of *i*-GaPAsN 300nm thick by MBE in France[98]. Its parameters are V_{OC}=0.82 V, J_{SC}=4.08 mA/cm^2, *FF*=52%. Recently, a Japanese group fabricated a single-junction SC based on a *p*-*i*-*n* junction of GaPAsN grown on an Si wafer by MBE but only the dark current-voltage characteristic of SC was presented[99].

Consequently, InGaPAsN dilute nitrides lattice-matched to GaP are attractive materials for the fabrication of high-efficiency MJSCs on silicon wafers. The development of MBE can improve the quality of these materials in comparison with structures grown by VPE like it was done for InGaAsN on GaAs wafers. Therefore, in the present work the second task is the study of single-junction SCs on GaP wafers and MJSCs on Si wafers with active layers of InGaPAsN grown by molecular-beam epitaxy.

I.3.4 Band structure and properties of dilute nitrides

The addition of nitrogen at only 0.43% changes the structure of the GaP from indirect to direct bandgap. Also, it strongly reduces the bandgap energy of GaPN and GaAsN compared with GaP and GaAs, respectively[70,71], although the bandgap energy of GaN is higher (E_g=4.2 eV) than that of GaP and GaAs. It is explained by the incorporation of highly electronegative atoms of nitrogen in the matrix of GaAs and GaP. Nitrogen produces a localized level in the band structure of GaAs (above the conduction band) and GaP (below the conduction band). While its concentration remains low there is not a strong influence on the band diagram of GaPN alloys, but when it exceeds 0.4% a significant modification is observed in the band structure. The model of band-anticrossing (BAC-model) was explored to describe the band structure of GaAsN and GaPN compounds. The authors described the interaction of a localized nitrogen level with the conduction band of GaP and GaAs, respectively[100,101]. As a result, there are two conduction subbands E_- and E_+, estimated by the formula[102]:

$$E_{\pm} = 0.5\{[E_C(k) + E_L] \pm [(E_C(k) - E_L)^2 + 4V^2x]^{0.5}\} \quad \text{(I.1)}$$

where $E_C(k)$ is the conduction band dispersion of the semiconductor which atoms are replaced, E_L is the energy of the localized states of the replacement atoms (here nitrogen), V_N is the hybridization parameter of the localized states and conduction-band states. According to the literature the nitrogen level is located at E_N(GaAs)=0.165eV[103] above the minimum of the GaAs Γ-valley and E_N(GaP)=0.03eV[102] below the minimum of the GaP X-valley.

The energy bandgap of quaternary alloys of $GaP_{1-x-y}As_yN_x$ can be estimated from the approximate equation with bowing parameter:

$$E_g(GaP_{1-x-y}As_yN_x) = (1-y)E_g(GaP_{1-x}N_x) + yE_g(GaAs_{1-x}N_x) - y(1-y)b_{GaPAs} \quad \text{(I.2)}$$

where b_{GaAsP}=-0.21 eV is the bowing parameter of the GaAsP ternary alloy[17]. The hybridization parameter V_N of GaNAs is 2.7 eV[102,104], and for GaPN a scatter of values is observed: 3.05 eV[105], 3.8 eV[102] and 4.38 eV[106]. It means that the BAC-model should be applied to GaPN alloys more carefully than to GaAsN ones due to different positions relative to the conduction band. Comparison of the experimental PL spectra of GaAsN and GaPN partially confirms this suggestion[107]. As a result, the energy transitions were clearly observed in GaAsN layers with E_- and E_+ values estimated from the BAC-model, but for GaPN only an approximate E_- value was detected. However, this partial discrepancy was explained by the exponential dependence of the

value of hybridization parameter in the BAC-model on the molar nitrogen fraction in $GaP_{1-x}N_x$ compounds[108]. Thus, the value of V_N is close to 4.38 eV and 3.05 eV for high (x>0.015) and low (x<0.007) nitrogen content, respectively.

The non-parabolic behavior of a conduction subband E_- can be explained by the larger electron effective mass (m_e) in dilute nitrides compared with GaAs and GaP. The value of m_e was explored in GaAsN/GaAs quantum wells with a nitrogen content of 0-2% by optically detected cyclotron resonance technique[109]. As a result, the value of m_e increases from $0.07m_0$ for GaAs up to $0.19m_0$ for GaAsN with 2% of nitrogen fraction. The BAC-model was applied for the theoretical estimation of an electron effective mass in $In_yGa_{1-y}As_{1-x}N_x$ lattice-matched to GaAs with high nitrogen content[70]. As a result, N-induced increase of m_e has been found in heavily n-type doped alloys and it reaches $0.40m_0$ for 3.3% of N and 8% of In. The effective mass of $GaN_{0.012}P_{0.988}$ was estimated as $0.38m_0$ in Ref.[102]. High value of m_e leads to a poor absorption in layers of dilute nitrides so they should be very thick to produce enough photo-generated current. It is a crucial issue since values of current must be matched for a bottom subcell of Si and a top subcell of InGaPAsN for high-efficiency MJSCs.

Moreover, SCs require the fabrication of a wide-bandgap window on the top of the structure for better performance. So GaP and GaAs layers can be considered as candidates for this application due to their higher band gap energy of 2.26 eV and 1.42 eV than in dilute nitrides InGaPAsN(1.5-2.1 eV) and InGaAsSbN (0.9-1.2 eV), respectively. Thus, the exact knowledge of band properties of InGaPAsN/GaP and InGaAsN/GaAs heterojunctions is necessary for SC design and simulation, especially their band offsets. However, there are only very few works where it was obtained from experiments. According to literature, most part of the band offset should be in the conduction band for both heterojunctions[110]. The conduction-band offset is 280 meV for the $GaN_{0.02}As_{0.12}P_{0.84}$/GaP heterojunction provided that bandgap energies are 2.34 eV and 2.0 eV for GaP and $GaN_{0.02}As_{0.12}P_{0.84}$ materials, respectively[79]. The valence band and conduction band offset of GaAsN/GaAs were measured by XPS to be -0.019eV/%N and -0.175eV/%N respectively,[111] corresponding to a predicted type II of the heterojunction[112]. With indium incorporation the valence band level of InGaAsN gets up and for a content larger than 9% the heterojunction changes from the staggered band of II type to the straddling band of I type[113]. The $In_{0.06}Ga_{0.94}As_{0.98}N_{0.02}$/GaAs heterojunction is of II type with a valence band offset of 0.13 eV and a conduction band offset of 0.30 eV[114].

According to the BAC-model electron (μ_e) and hole (μ_h) mobility should quickly fall with increasing nitrogen content. However, there are no experimental data for InGaPAsN lattice-matched to GaP as for GaPN. Electron and hole mobility was obtained from Hall measurements of n- and p-doped $In_{3x}Ga_{1-3x}As_{1-x}N_x$ layers lattice-matched to GaAs with nitrogen fraction of 0-

3%[115]. For nitrogen fraction of 3% μ_e and μ_h have values of 120 cm^2/Vs and 50 cm^2/Vs, respectively.

As noted above, incorporation of nitrogen leads to low lifetime of charge carriers in dilute nitrides due to a high concentration of non-radiative recombination centers. Most of the works have been devoted to the study of InGaAsN alloys on GaAs rather than of InGaPAsN on GaP so it has allowed to improve growth conditions of InGaAsN layers and their quality. Perhaps, it explains why the efficiency of SCs with dilute nitrides on GaAs wafers is much higher than on GaP wafers. The biggest part of this work is devoted to the study of the influence of defect levels in both types of dilute nitrides on the performance of SCs.

I.3.5 Alternative way for growth of GaP on Si

Nowadays, high-efficiency SCs lattice-matched to GaAs are produced on expensive wafers of GaAs or Ge, and SCs grown on silicon wafers have not reached high efficiencies. Modern methods of MBE and VPE require high temperatures of 500-800 °C for the growth of III-V compounds leading to unsatisfactory quality of heterointerfaces, layers deformation due to differences in thermal expansion coefficients, and deterioration of the bulk properties due to a large number of threading dislocations. In addition, the drastic drop of minority carrier lifetime was observed directly in the silicon wafer due to the annealing procedure of the wafer in the MOCVD chamber required for better growth of GaP layer[116]. It leads to a lower value of quantum efficiency in the long-wavelength region in the GaP/Si SC which can cause a significant drop in QE of the final MJSC in the future. Furthermore, high temperatures can lead to inter-diffusion of elements of the III, V and IV groups, which are doping impurities for each other, during the epitaxial growth process. Thus, the heterointerface is blurred, additional doping regions formed, and it negatively affects the photoelectric properties of structures. In addition to problems of scientific nature for epitaxial growth, there are economic ones due to strong requirements of ultra-high vacuum in chamber, ultra-pure source of atoms, more complicated maintenance of equipment etc. leading to price increase of SC production. It seriously limits the use of epitaxial SCs in terrestrial photovoltaic applications. Therefore, new and cheaper methods should be investigated for the growth of III-V compounds on silicon wafers for applications in high-efficiency MJSCs.

In this work, such a method, named plasma-enhanced atomic-layer deposition (PE-ALD), is presented for the low temperature growth of III-V GaP-based compounds using a plasma-enhanced chemical deposition process. It is based on the growth of GaP(N) layers on silicon wafers in a PECVD chamber at temperatures below 400 °C without using thermal annealing at high temperatures during the fabrication process. A similar approach is performed for a low-temperature growth of GaAs and GaP nucleation layers on silicon wafers in the above considered

two-steps MBE process. The method is also used in VPE and called atomic-layer epitaxy (ALE[117]). It consists of the alternate interaction of the wafer surface with the phosphorus and the gallium flows leading to atomically smooth layer-by-layer 2D-growth of GaP(N) without coalescence in islands for 3D- growth. Previously, the opportunity of ALE growth was demonstrated in the VPE chamber for GaP on Si[117], but the process required high temperatures (more than 500 °C) for precursor's decomposition limiting the use of low temperatures. This problem does not arise in the suggested method of PE-ALD since the decomposition occurs in a low-temperature plasma, and not on the wafer surface. On the other hand, the lack of requirement for ultra-high vacuum compared with MBE makes the growth by PE-ALD more attractive from the economic point of view; industrial mass production of SCs could thus be targeted.

The proposed growth method of GaP on Si wafers has never been investigated before, so the properties of the obtained GaP layers and GaP/Si heterojunctions are unknown. Therefore, in the present work the third task is to explore the properties of GaP/Si structures grown by plasma-enhanced atomic- layer deposition at low temperatures.

Summary

The retrospective of semiconductor SCs was reviewed in this section. Different approaches were presented for the fabrication of high-efficiency MJSCs for terrestrial and space applications. Special attention was paid to the description of existing MJSCs grown on wafers of IV group (Si, Ge) and possible ways for improvement of their performance and reduction of their cost. Therefore, this study can be separated in three different parts investigating novel methods and materials for the fabrication of SCs. In the two first approaches, molecular-beam epitaxy is used for the growth of SCs with active layers of original alloys like dilute nitrides. These semiconductors are III-V-N compounds with a small content of nitrogen. In the first part, structures with InGaAsN layers lattice-matched to GaAs are studied for future integration in MJSCs on GaAs and Ge wafers. Here, InGaAsN layers are grown by a new method as nanoheterostructures of an original design based on the InAs/GaAsN superlattice. In the second part, single-junction SCs on GaP wafers and MJSCs on Si wafers with active layers of InGaPAsN will be explored. Its investigation allows us to complete our knowledge on properties of semiconductors for their application in high-efficiency MJSCs on silicon wafers. In the third part, a novel method of plasma-enhanced atomic-layer deposition at low temperature is studied for the growth of III-V compounds on Si wafers. It is considered as a prospective method for the production of low-cost terrestrial SCs based on III-V/Si systems.

Chapter II

Experiments and methods

Introduction

The technological aspects of SC fabrication and methods of SC research are presented in this chapter. The study can be separated into four different steps: SC growth, post-growth processing, experimental research and theoretical simulation. SCs are grown by two methods: molecular-beam epitaxy and plasma-enhanced atomic-layer deposition. Then, grown structures are processed for fabrication of experimental samples depending on the characterization technique. Thereby it is a very demanding task using different methods of contact formation (vacuum evaporation, plasma- enhanced chemical- vapor deposition), thermal treatment (rapid thermal annealing, annealing on home-made heater), selective etching (wet, dry) for samples with desirable construction (e.g. mesa-structures). Photoelectrical properties of SCs are obtained from current-voltage characteristics and spectral response. A substantial part of the work is devoted to investigation of layers properties in structures by different capacitance methods (capacitance-voltage characteristics, admittance spectroscopy, deep-level transient spectroscopy). Also, different techniques (scanning and transmission electron microscopies, Raman spectroscopy) are used for characterization of structural properties. Finally, properties of SC are simulated by computer modeling.

II.1 Growth technology

The material growth is the most important part of SC fabrication since initial properties of layers directly depend on its conditions. However, this thesis is mostly devoted to post-growth and exploration of SCs properties so growth methods are described generally without all technological details.

II.1.1 Molecular-beam epitaxy

MBE is one of the most attractive and popular method for the growth of semiconductors with high quality. The main advantages are the high vacuum during growth and the purity of the source of elemental species involved constituent or doping elements leading to low background unintentional doping unlike in VPE leading to carbon and hydrogen incorporation. In this study, a

Gen III Veeco MBE system is used for the growth of photoelectric structures with active layers of dilute nitrides. This equipment has solid sources of Ga, In, P, As for III-V growth and sources of Be and Si for *p*- and *n*-type doping of layers, respectively. The setup features a source of atomic nitrogen based on the discharge of N_2 molecules by radio frequency (13.56 MHz) plasma for the creation of dilute nitrides. The schematic view of the setup is presented in Figure II.1.

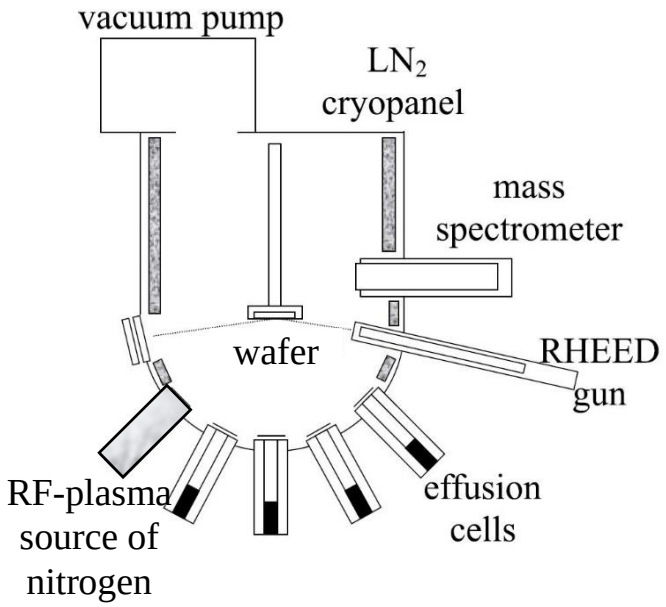

Figure II.1 The schematic view of MBE setup[118] with RF-plasma source of nitrogen.

We will present results obtained on three series of samples.

The first series of samples consist of single- junction SCs with active layers of undoped InGaAsN (E_g=1.03 eV) grown on n-GaAs wafers (Figure II.2a). The layers are made of nanoheterostructures of an original design based on the InAs/GaAsN superlattice (SL). The SL can be considered as multi-quantum wells where wells are grown as sub-monolayer digital alloys (SDA) with thickness of a few monolayers (MLs). For example, the InGaAs SDA is a SL with periods of $(InAs)_n/(GaAs)_m$ where n, m=1,2,3… are numbers of monolayers[39]. In such configuration, the InAs/GaAsN SL behaves as an InGaAsN quaternary alloy. Therefore, in our samples thin InAs layers of 1 ML (0.2-0.5 nm) should compensate the elastic stresses arising during the growth of GaAsN (7-12 nm) on the GaAs wafer due to lattice-mismatch. On the other hand, InAs has a tendency to coalesce leading to formation of 3D islands instead of the required 2D layer. Thereby the described method is very complex since thickness and composition parameters of GaAsN and InAs must be chosen and controlled very precisely for optimal performance of SCs. In the current work, three such structures were grown with different thicknesses of *i*-InGaAsN. Here and below, InAs/GaAsN is considered as InGaAsN so both names will be used.

The second series of samples consist of single- junction SCs with active layers of InGaPAsN grown on identical *n*-GaP wafers (Figure II.2b). Increasing nitrogen incorporation in GaP promotes the reduction of bandgap energy and lattice constant leading to lattice-mismatch with the silicon wafer. Therefore, the elastic stresses arising during the growth process must be compensated for better quality of dilute nitrides. An additional content of indium or arsenic is proposed for this task since the lattice constant of alloys should increase with the introduction of these atoms. The first grown SC has an active layer of *n*-doped quaternary alloys of GaPAsN with As content of 15% (E_g=1.9 eV), 1000 nm thick. Such thick layer is grown for better measurements of optical absorption of GaPAsN. Then, two similar SCs were grown with an undoped i-GaPAsN with larger As content (up to 30%, leading to E_g=1.7 eV) layer, 300 nm thick, with two different post-growth treatments in the MBE-chamber. These structures allow us comparing photoelectric properties of Si-doped and undoped dilute nitrides for their utilization in top subcells of MJSC. A fourth SC is based on undoped InGaPN (E_g=2.04 eV), 350 nm thick, grown as a SDA of InP(0.3nm)/GaPN(10nm). It is grown to compare the compensation ability of In and As in GaPN layers, the possible influence on defects formation and the photoelectrical properties.

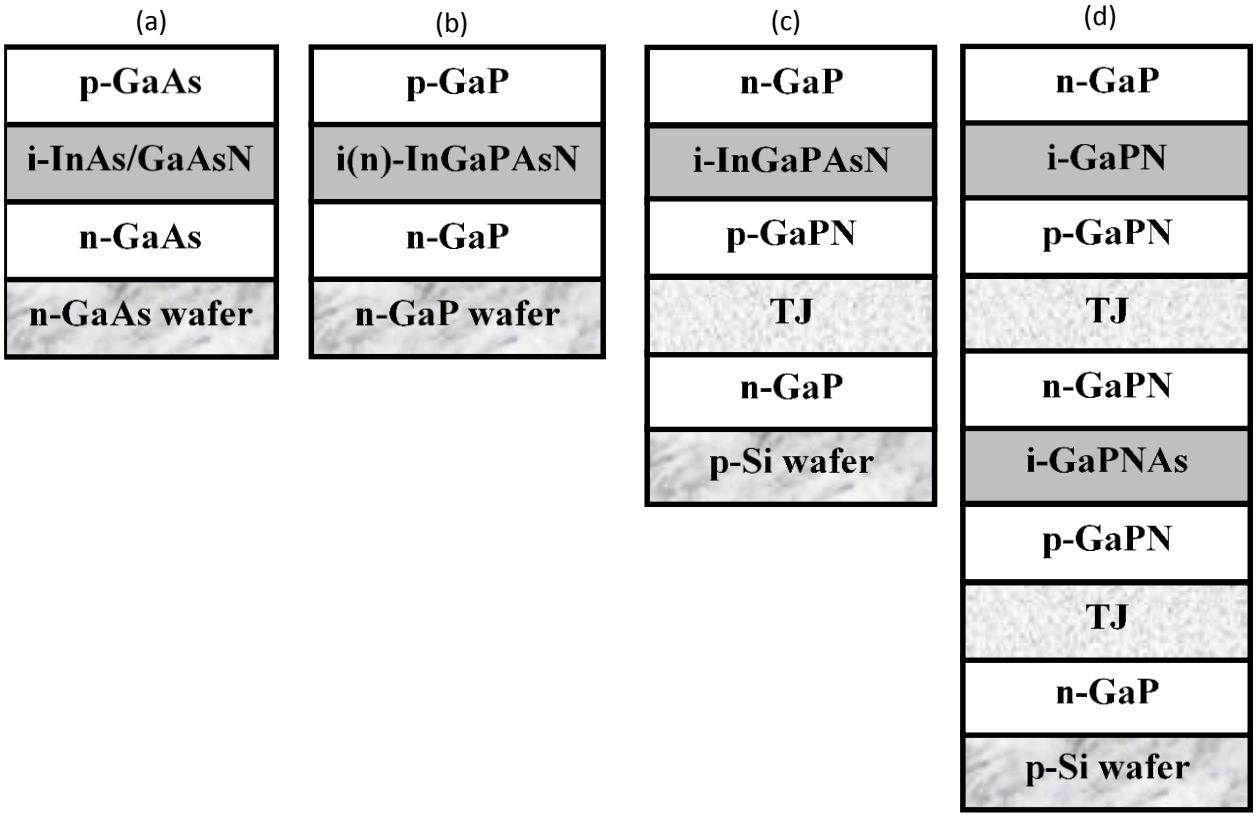

Figure II.2 Schematic view of solar cells with active layers of dilute nitrides grown by MBE. TJ stands for tunnel junction.

A third series of samples consist of MJSCs (3 double-junction (Figure II.2c) and 1 triple-junction (Figure II.2d) grown on *p*-type (concentration of acceptors $10^{16}cm^{-3}$) Si(100) wafers with top subcells based on active layers of undoped III-V compounds. Bottom subcells for all MJSC are formed by pre-growth thermal annealing of the wafer in a phosphorous flow during 10 minutes at 400-500 ˚C in the chamber. It leads to the formation of a *p*-*n* homojunction in the silicon wafer due to P atoms incorporation in the Si lattice leading to surface *n*-type doping. Then III-V layers are grown for the fabrication of tunnel junction (TJ) and top subcells. The first double- junction SC has a top subcell based on *i*-layer of $GaP_{0.70}As_{0.30}$, 400 nm thick. It is grown as a reference and to define the role of nitrogen in defect formation in III-V compounds. Then, two different structures are grown with active layers of undoped dilute nitrides lattice-matched to Si as the top subcell. As described before $GaP_{0.98}N_{0.02}$ is superlattice- matched to Si so it is a good candidate for an active layer in top subcells. However, problems of elastic stresses in ternary GaPN should be solved. Therefore, indium and arsenic are applied for the compensation of arising elastic stresses due to incorporation of nitrogen in the GaP lattice and for possible reduction of E_g. One double-junction SC has an undoped region based on an $InP/GaP_{0.99}N_{0.01}$ (10nm/0.3nm) SDA, 200 nm thick, with bandgap energy of 2.1 eV. Another one is grown with an undoped layer of $GaP_{0.882}As_{0.10}N_{0.018}$ (E_g=1.9 eV), 200 nm thick, with 10 percent of arsenic for a better incorporation of nitrogen and for providing a decrease of bandgap. The last sample is a triple-junction SC with two subcells based on active layers of undoped dilute nitrides grown on the Si wafer. Middle and top subcells are *p*-*i*-*n* junctions with active *i*-layers of $GaP_{0.882}As_{0.10}N_{0.018}$, 200 nm thick, and $GaP_{0.987}N_{0.013}$, 150 nm thick, respectively.

All SCs are grown without any antireflection coating.

II.1.2 Plasma-enhanced atomic-layer deposition (PE-ALD)

Plasma-enhanced chemical vapor deposition is the second growth technology used in this work. It is a popular technique for the fabrication of SC based on amorphous silicon layers. Its main advantages are lower cost of production and lower temperature of process than in MBE. The technology is based on material deposition from gas phase on solid wafer. Gas flows enter into the PECVD- chamber and molecules decompose under the influence of plasma (nitrogen, hydrogen, argon etc.). Different gases are used as sources of atoms in PECVD: phosphine (PH_3) for phosphorous (P), trimethylgallium (TMG) for gallium (Ga), silane (SiH_4) for silicon (Si), dimethylzinc (DMZn) for zinc (Zn). In this work, GaP layers with different thicknesses (50-100nm) are grown using an Oxford PlasmaLab System 100 (13.56 MHz) equipment on both *n*-type (phosphorus-doped, 2-7 Ω·cm) and *p*-type (boron-doped, 0.8-1.2 Ω·cm) silicon wafers at 380

°C. Therefore, grown samples are based on the GaP/Si heterojunction (Figure II.3). The schematic view of our setup is presented in Figure II.4.

Figure II.3 Schematic view of GaP/*p*-Si and GaP/*n*-Si samples grown by PECVD.

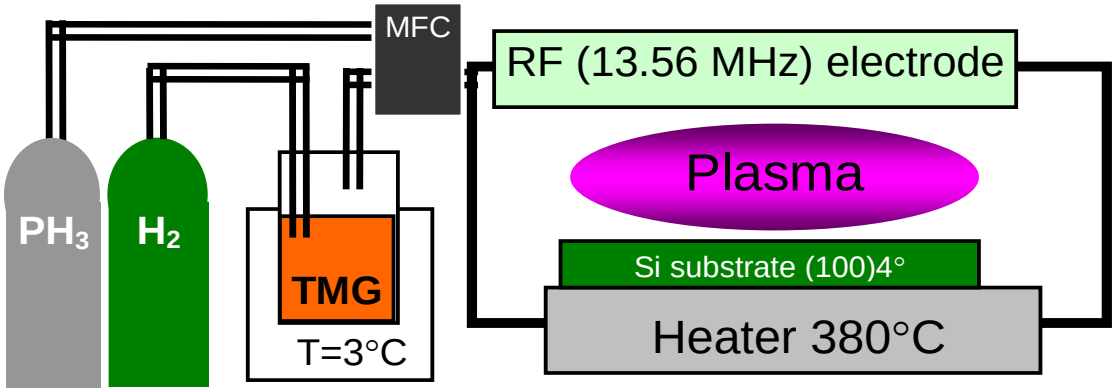

Figure II.4 Schematic view of PECVD setup[119].

If there are flows of TMG and PH_3 in the chamber at the same time, it will be called continuous growth of GaP. However, there are many different parameters controlled by the operator, that can modify or improve the growth process. In this work, the deposition process has been modified. Indeed, we have introduced only one type of gas at a time in the chamber, so that the gas flows of different molecules have been separated in time. For example, GaP consists of atoms of III (Ga) and V (P) groups so their flows are separated and at any moment atoms only of one group occupy the chamber. For example, in the first step, only the PH_3 source is opened and only P atoms interact with the silicon wafer. Then, its source is closed, the chamber is cleaned by a hydrogen plasma and P atoms migrate on the surface and try to find and stay at stable places. Afterwards the TMG flow enters the chamber and Ga atoms are adsorbed onto the phosphorus surface. They migrate, interact with P atoms and stay in position providing Ga-P bonds. Then the chamber is cleaned again by a H plasma and excess Ga atoms are emitted from the surface. The first cycle is then completed. All steps are then repeated again. Therefore, the method is called plasma- enhanced atomic-layer deposition. Eventually, GaP material is produced with atomic smooth surface and with the supposed GaP crystal lattice. The typical temperature of process is less than 400 ˚C. Such a process is similar to what is used in the initial step of MBE described in

Chapter I based on the concept of migration-enhanced epitaxy at low temperature for the growth of 2D smooth layers of GaP. Additional steps can be introduced for the desirable doping of GaP. For example, silane flow is added for *n*-type doping of GaP. A schematic view of typical GaP:Si growth is presented in Figure II.5.

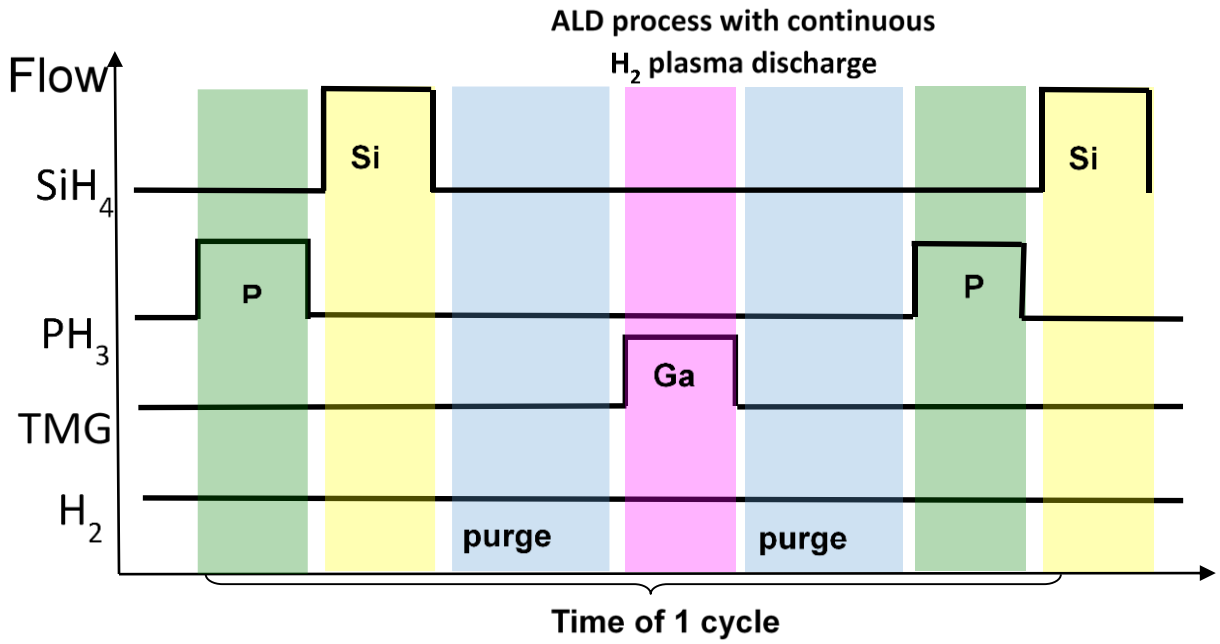

Figure II.5 Schematic view of atomic-layer deposition of GaP:Si.

II.2 Post-growth processing

Post-growth processing is applied for samples fabrication from as- grown structures for their experimental exploration. The main goal of this step is the creation of samples with good contact layer and desirable shape. Prepared samples can be divided into two groups: the first one consists in SCs for the investigation of photoelectric properties and the second one is mesa-structures for capacitance measurements. Therefore, there are three technological steps to this purpose: contact material deposition, temperature treatment and etching. All these processes strongly depend on the construction of grown samples and suggested experimental methods so many different ways are used it this work for samples fabrication. In this section, methods are described overall but each post-growth process will be described separately in the next chapters for each type of samples.

II.2.1 Contact fabrication

In this section, two different problems are investigated, namely the fabrication of ohmic contacts and of Schottky barriers to the layers. It is quite a difficult task to find the best contact materials and annealing temperature for each semiconductor. Usually, it takes a lot of time and many tests are required but electrical characterization cannot be accurate without suitable contact layers. So many technological approaches have been developed for the reliable formation of ohmic contacts to *n*-GaP, *p*-GaP, *n*-GaAs, *p*-GaAs grown by MBE, *n*-GaP grown by PE-ALD, *n*-Si and *p*-Si wafers as well as for Schottky barriers to *n*-GaP grown by PE-ALD, *n*-Si and *p*-Si wafers. Here, we describe the equipment used for this goal.

The vacuum evaporation method is used for the deposition of contact materials in the BOC Edwards Auto500 equipment. It is intended for the fabrication of metal films by thermal and electron beam sputtering, including high-purity films of metals with a high melting point. The equipment is a chamber with pressure below 10^{-5} mbar where sources of metal are located in the bottom part of the chamber while the structures are fixed to a rotated disc in the top part. Deposition occurs as a result of evaporator heating in two different ways, depending on the melting point of the metal:

1. Resistive evaporation (Ag, Au, In, etc.). The solid metal source is put in evaporators made of refractory metals with a high melting point like molybdenum or tantalum. An electric current is passed through them and due to heating the material almost instantly evaporates and is deposited on the disk. The mass of evaporated material defines the thickness of the deposited layer. The advantage of this method is its simplicity and the speed of the process but the drawback is its-rather poor control.

2. Evaporation by an electron beam (Pd, Cr, Ti, Ni, etc.). The electron beam heating method is used for evaporation of refractory metals: it is directed to the material in a graphite holder and heats the metal which evaporates at a certain rate. The thickness of the deposited layer on the structure is defined using an optical sensor inside the chamber. The beam power and deposition time allow us to control the thickness of the deposited layer. In this work, optimal deposition regime is selected at a rate of 1-3 nm/min. The disk uniformly rotates during the deposition process to achieve uniform deposition of material.

Our BOC Edwards Auto500 equipment allows us to deposit a few metals in one process for the fabrication of complex sandwich metal structures. Then, the Jipiec JetFirst 100 equipment is used for rapid thermal annealing (RTA) of deposited contacts. It allows to anneal semiconductor structures in N_2, Ar, N_2 + H_2 (3-5%) and air flow in the temperature range from 20 °C to 1300 °C with an accuracy of ± 2 °C. The setup has a computer software permitting to create recipes with

different parameters and monitor them in real time. Vacuum evaporation and subsequent RTA are used for the fabrication of ohmic contacts to all the III-V compounds and Schottky barriers to all the structures.

Also, we have developed low-temperature fabrication of ohmic contacts to silicon wafers. Hydrogenated amorphous silicon (a-Si:H) is deposited by PECVD method onto the wafer using an Oxford PlasmaLab System 100. Then silver is vacuum evaporated in BOC Edwards Auto500 system and samples are annealed on a home-made heater at air atmosphere at low (less than 200 °C) temperature.

II.2.2 Etching methods

After contact formation, an etching step is required for the fabrication of mesa-structures with desirable shape. Sometimes the surface of grown structures can be inhomogeneous and shunt currents can appear. Also, contact layers can have low conductivity leading to problems with the collection of charge carriers and low reliability of measured data due to areas that are not well defined. Furthermore, in DLTS samples must have small capacitance values for better measurements. Therefore, mesa-structures should be fabricated with well defined small areas. Precise etching has been used to this purpose. In the current work, both types of dry and wet etching processes are used depending on the structures and experimental characterization techniques. On the other hand, etching is a chemically active process leading to possible unwanted interactions of the etchant with metallic contacts or resistor used in photolithography. Below, we describe specific optimized recipes of etching for specific metal contacts.

II.2.2.1 Dry etching

Dry etching is carried out at the Oxford PlasmaLab 100 ICP380 equipment of reactive-ion etching (RIE) and inductively coupled plasma (ICP) etching. This equipment is designed for etching a wide range of different semiconductor materials. The etching principle is based on the chemical and mechanical interaction between ions from the plasma and the structure. Our equipment allows us to use ICP and RIE methods simultaneously and to use different etchant gases (Ar, O_2, CF_6, BCl_3, Cl_2 etc.). In our case, the technology of dry etching is optimized for III-V compounds and for silicon with deposited metal (In, Au) contacts without their degradation during the process. For III-V compounds etching is carried out with optimized powers in an atmosphere of chlorine (Cl_2) and boron trichloride (BCl_3) with a ratio of 3:1 at a temperature of 20 °C with controlled rate of 1 μm/min. Silicon etching is carried out with optimized powers in an atmosphere of sulfur hexafluoride (SF_6) and oxygen (O_2) with a ratio of 9:1 at a temperature of -10 °C with controlled rate of 0.5 μm/min. These developed recipes allow us to obtain good reproducibility

and controllability for the fabrication of mesa-structures with the desirable shape for our experiments without any high degradation of metal contacts. Nevertheless, dry etching has two disadvantages: possible degradation of the structure due to ion bombardment leading to defect formation and very high etching rate of 1 μm/min.

II.2.2.2 Wet etching

The wet etching is more preferable for a precise control because some samples require an accuracy of etching depth of 20 nm. However, it is a hard task to find a suitable etchant for III-V compounds weakly interacting with metal contacts and resists of lithography, especially for III-V-N alloys. A common solution based on sulfuric acid (H_2SO_4) of H_2SO_4:H_2O_2:H_2O=5:1:1 is used for the etching of SCs based on InGaAsN/GaAs layers since their top and bottom gold contacts remain stable in it. The etching rate of InGaAsN is 50-100 nm/min. On the other hand, one of the resist used for lithography in post-growth processing described below is strongly etched in this solution. Thereby we have found a very unusual and rare solution based on potassium iodate (KIO_3): KIO_3:HCl:H_2O=1:1:20 allowing us to perform the lithography for the fabrication of mesa-structures with the geometry described below. Its solution etches GaP-based dilute nitrides with a rate of 70-80 nm/min. It should be noted that wet etching is a complex task due to the high number of parameters and ambient conditions (temperature, atmosphere) affecting the process. For this reason, each etching rate must be precisely calibrated for each new solution. The etching properties of the solution can strongly depend on time since chemical reactions lead to big changes in its behavior. It is an important drawback unlike for dry ICP-etching that is stable with time.

II.2.3 Post-growth processing of SC

The grown structures and used experimental methods can impose very strong restrictions on the post-growth processing. The growth of good quality structures is only the first step to obtain adequate experimental data. Each experimental technique requires special fabrication and geometry of contacts. An ohmic contact grid must be created for photoelectric measurements under illumination, but for good capacitance measurements small dots should be formed by etching since the signal accuracy decreases with increasing contact area. Furthermore, bottom contacts to wafers must be always ohmic otherwise a potential barrier appears and leads to catastrophic deterioration of photoelectrical performance of solar cells.

Unfortunately, we experienced such problems at the initial stage of this thesis for single-junction SCs grown on GaP wafers. A wafer is normally heated by IR-radiation in the used MBE equipment, but GaP does not absorb at these wavelengths. Therefore, a titanium layer, 100 nm thick, was deposited by magnetron sputtering on one side of the *n*-GaP wafer to absorb IR radiation

in order to heat the wafer, and the other side of the wafer is used for the growth of dilute nitrides layers. In the first stage of our studies, it was found that titanium formed a Schottky barrier onto *n*-GaP so we found a procedure to remove the titanium layer. However, this procedure is quite complicated and not applicable for industrial applications so we also developed a post-growth technology in order to contact the *n*-GaP wafer from the front side, which allowed us to keep the titanium layer on the bottom side. So, in the proposed technology both contact electrodes, on the *n*-GaP wafer and on the *p*-GaP top layer, are taken on the front side of the wafer. In the future, it will allow to adapt the technology to the requirements of the planar industry.

Figure II.6 illustrates the principle of the post-growth process of mesa-structures fabrication, for example, for the *p-i-n* structure with an active layer of GaP(N) grown on an n-type silicon substrate. Initially, the front surface of the gallium phosphide is cleaned in HF:H_2O solution during 5 seconds to remove the oxide possibly formed on the GaP surface (Figure II.6a). Next, the resistive layer is applied to the front side of the sample. In this step, the lower PMGI resist is first applied and heated at 170 °C for 5 minutes, then the second resist AZ_MIR_701 is applied and baked for 90 seconds at 90 °C. Then the sample is exposed to UV light through the created mask with an intensity of 6 mW/cm^2 for 90 seconds. After this step, the resist is developed in solution of AZ_MIF_726 (2.5% tetramethylammonium hydroxide solution) for 90 seconds until a double border is formed (Figure II.6b). Then the top contact is vacuum deposited to the front layer of p-GaP (Figure II.6c). Then, the remaining resist is lift off by boiling in dimethylsulfoxide (DMSO) for 5 minutes at 170 °C to completely delete the resist from the sample surface (Figure II.6d). At the next stage, the resist layer AZ_1518 is applied and baked for 60 seconds at a temperature of 100 °C. Next, the sample is exposed for 30 seconds to a UV light intensity of 6 mW/cm^2 through a new mask with holes selected to exclude the interaction of the deposited metals with the etchant in the subsequent etching process. Resist is developed within 60 seconds in a solution of AZ_MIF_726 (Figure II.6e), afterwards the sample is etched in a wet solution of KIO_3: HCl: H_2O (Figure II.6f). The technology of the etching of diluted nitride layers of the GaP(N) type is a key step in the post-growth process, so it had been developed very long and scrupulously. Further remaining resist is removed in the DMSO under the previously described conditions (Figure II.6g). Then, the first step of resists application and their exposure to UV light is completely repeated using a new mask. The mask image was chosen to make safe cover of the formed SCs and mesa-structures as columns to prevent shunting of the active layers (Figure II.6h) during the subsequent vacuum deposition of the contact to the *n*-GaP bottom layer (wafer) in the form of concentric rings (Figure II.6i). In the final step, the resist is removed in the DMSO solution under the conditions described above (Figure II.6j). Thus, mesa-structures are fabricated for carrying out capacitance

measurements on structures with both electrodes drawn to the front side. The main advantage of the technology is the ability to adapt the contact geometry to any future experimental research.

For the requirements of the current work, it was necessary to fabricate mesa-structures for carrying out capacitance studies and SC for photoelectric measurements. Three different masks were created to this purpose: the first one (Figure II.7a) for the resulting lithography in Figure II.6b, the second one (Figure II.7b) for lithography in Figure II.6d, and the third one (Figure II.7c) for lithography in Figure II.6h. The fabricated sample with mesa-structures and SCs is presented in Figure II.8. Four dots in the form of crosses, visible in Figure II.8, are used for precision alignment of the mask position at different stages of the post-growth process. For convenience of visual perception, violet and red colors indicate the remaining resist, and the green is the surface of the sample in Figure II.7, all dimensions are indicated in mm.

The diameter of the contacts to the top *p*-GaP layer is 0.5 mm first and third rows in Figure II.8, while it is 1 mm for the second row. Such diameter values are well adapted to the capacitance measurements. The concentric geometry of the contacts allows us to achieve better collection of charge carriers in the experiments. It reduces the problem of interpretation of obtained results in case of the presence of lateral spreading in the sample layers. A contact grid design has been adapted to the circular contact geometry to measure photoelectric properties (4 series of circles in Figure II.7a and Figure II.8). Furthermore, contacts for transfer line measurements (TLM) are fabricated to investigate their ohmic behavior and estimate their resistivity. TLM contacts are also formed during the deposition of metals to the top (Figure II.6c) and to the bottom contact (Figure II.6i): in the photograph of the sample they are located in the first and third rows, respectively (Figure II.7 and Figure II.8).

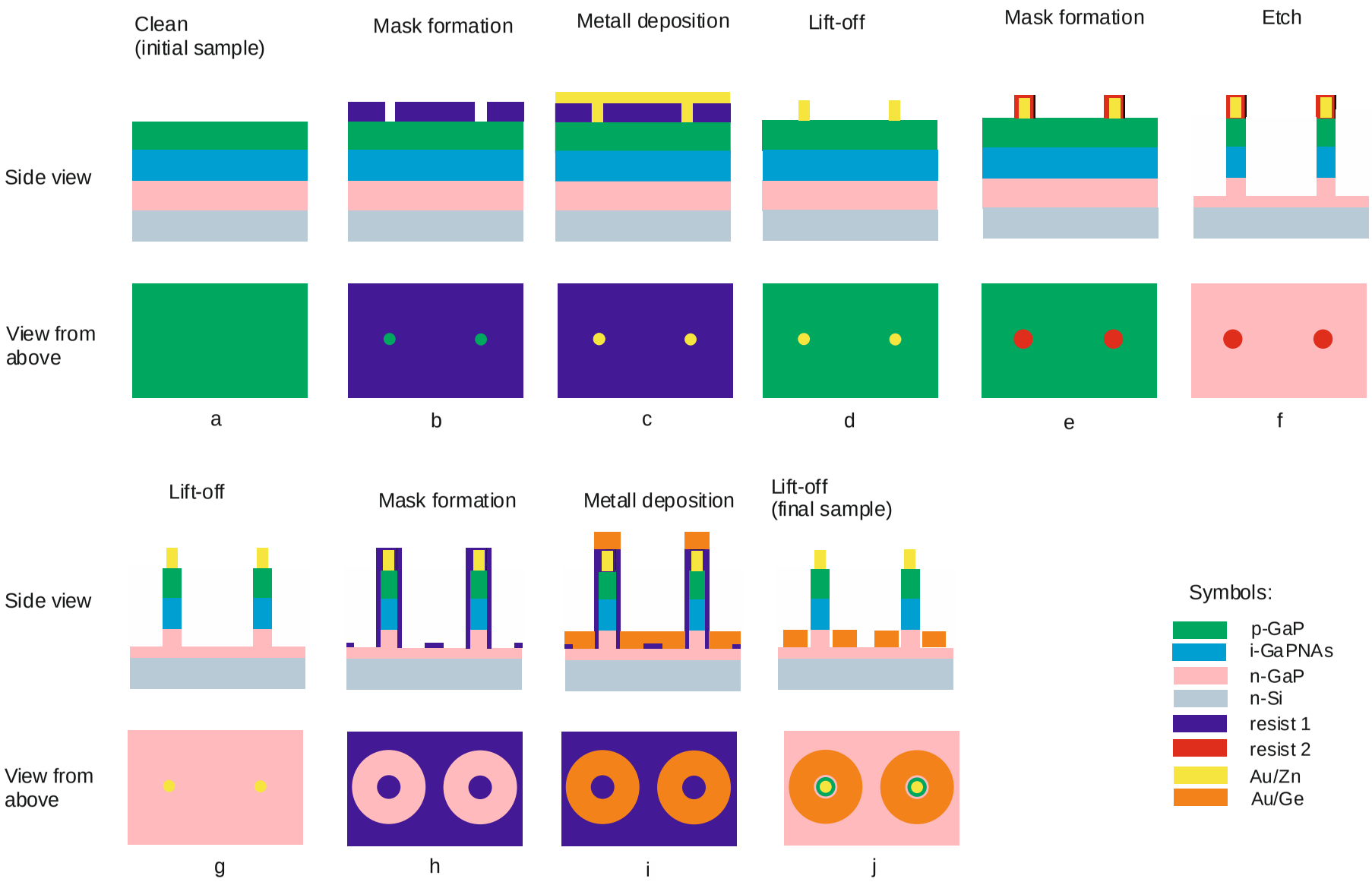

Figure II.6 Schematic view of post-growth technology of sample fabrication.

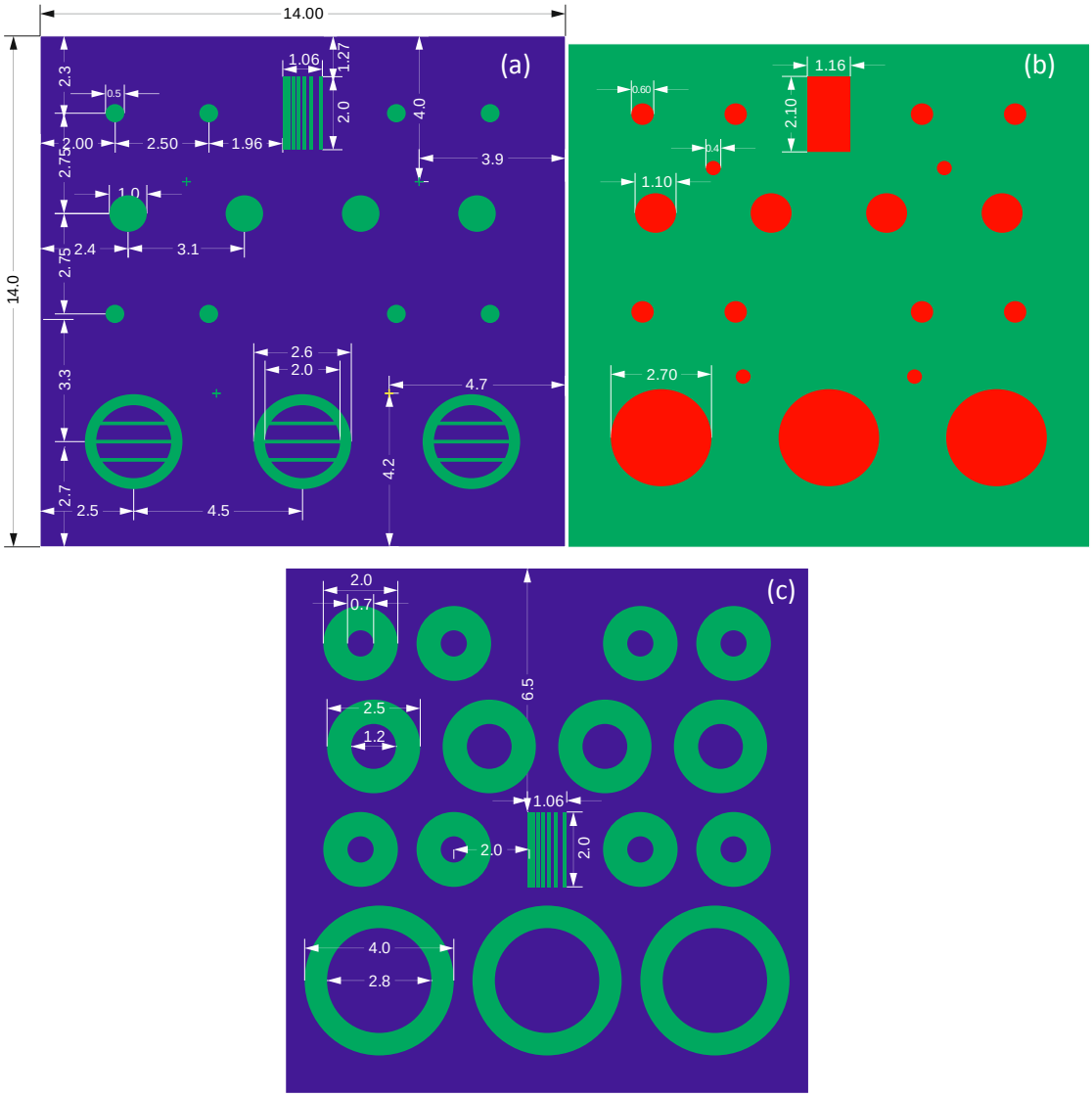

Figure II.7 (a, b, c). Mask for photolithography. Violet and red colors indicate the remaining resist after exposure, and the green is the surface of the sample. Dimensions are in mm.

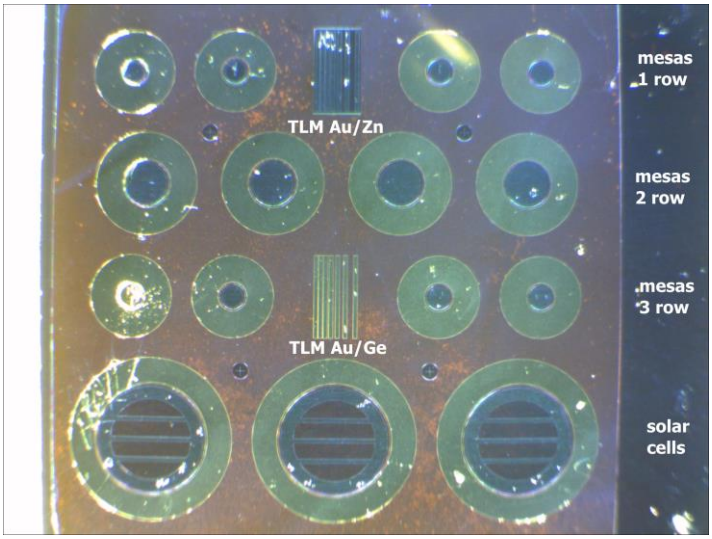

Figure II.8 Real fabricated sample for experimental research.

The developed post-growth technology is a universal planar method for the fabrication of mesa-structures and solar cells. However, developer and etchant solutions as well as resists should be found based on the composition of used semiconductors and metals. In this work, the method was successfully tested on single-junction SC grown on GaP wafers. It opened good perspective for the application of this method to MJSCs.

In double-junction SC there are two subcells and one tunnel junction (TJ). For example, consider our double-junction on a silicon wafer (Figure II.2c): the top subcell is a *p*-*i*-*n* junction based on InGaPNAs, the TJ is n^{++}-GaP(N)/p^{++}-GaP(N) and the bottom subcell is a *p*-*n* silicon homojunction. The problem is the direct capacitance measurement of the top subcell without influence of the bottom subcell. The proposed post-growth technology allows us to form metal contacts to the *p*-GaP layer and to the *n*-GaPN top layer allowing us to directly measure the photoelectric properties and the capacitance of the top subcell.

II.3 Experimental methods

Different techniques are developed to study SCs and dilute nitrides properties in the current work. First, photoelectric properties of SC are characterized by current-voltage characteristics in the dark and under illumination as well as spectral response measurements. Optical transmission and reflection are measured for the optical characterization of samples. However we will mainly focus on capacitance measurements that constitute the core of our characterization work. Capacitance techniques are used to provide a deeper study of external properties of dilute nitrides and GaP grown by PE-ALD. Capacitance-voltage measurements allow us to estimate the doping concentration in active layers of SCs. Admittance and deep-level transient spectroscopies provide information about defects in dilute nitrides. Furthermore, scanning electron, atomic-force, Raman, transmission electron microscopies are used for the characterization of structural properties of GaP grown by PE-ALD. Scanning electron microscopy is also used for measurements of mesa-structures after etching and to evaluate the geometric properties of structures.

II.3.1 Current –voltage characteristics

Current-voltage characteristics is the measurement of current between electrodes as a function of the applied voltage. The current-voltage characteristic of a standard p-n junction in the dark (Figure II.9) is described by the well-known modified Shockley law (II.1)[120]:

$$J = J_S \left[\exp\left(\frac{qV}{nk_BT}\right) - 1 \right] \quad \text{(II.1)}$$

where J is the net current flowing through the diode between the *p*-side and the *n*-side; J_S is the "dark saturation current", e.g. the diode leakage current density under reverse bias in the absence of light; V is the applied voltage across the terminals of the diode; q is the absolute value of electron charge; k_B is Boltzmann's constant; T is the temperature (K); n is the ideality factor.

The ideality factor is an important parameter giving information on the quality of the *p*-*n* junction. In ideal *p*-*n* junctions the current is driven by the diffusion of electrons and holes and n is equal to 1 in this case. When the current is driven by recombination of electrons and holes through deep centers in the space charge region of the *p*-*n* junction, n is equal to 2.

Under light, if the photon energy is larger than the bandgap ($h\nu \geq E_g$), photons are absorbed and create electron-hole pairs that are separated by the built-in electric field in the space charge region, leading to a photocurrent of opposite sign to the forward current in the dark and making the *p*-*n* junction an active device generating electric power.

The process of converting solar energy into electricity can be divided into four stages: 1) absorption of light; 2) generation of electron-hole pairs; 3) separation of charge carriers in a *p*-*n* junction; 4) collection of charge carriers on electrodes.

The total current under light is:

$$J = J_S \left[\exp\left(\frac{qV}{nk_BT}\right) - 1 \right] - J_{ph} \quad \text{(II.2)}$$

where J_{ph} is the photogenerated current.

In Figure II.9 the subsequent parameters of SC are shown: short-circuit current (J_{SC}), open-circuit voltage (V_{OC}), voltage (V_{PM}) and current (J_{PM}) at maximum power point $P_{PM} = V_{PM} J_{PM}$. To describe the shape of the I-V curve under illumination another parameter is used: the fill factor of the I-V characteristic (FF), defined as:

$$FF = \frac{P_{PM}}{V_{OC}J_{SC}} = \frac{V_{PM}J_{PM}}{V_{OC}J_{SC}} \quad \text{(II.3)}$$

If P_{in} is the input power of light illumination the SC efficiency can be written as:

$$\eta = \frac{P_{PM}}{P_{in}} = \frac{FFV_{OC}J_{SC}}{P_{in}} \quad \text{(II.4)}$$

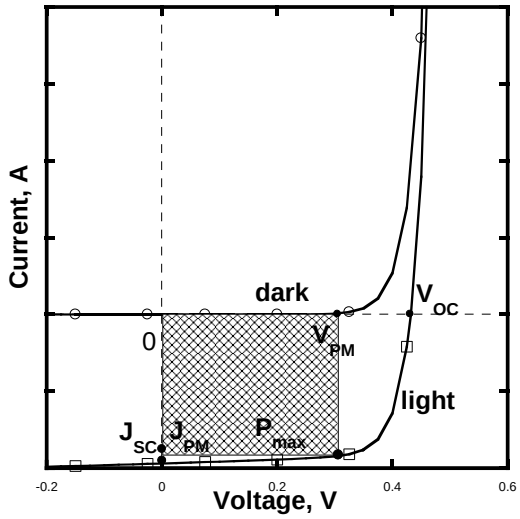

Figure II.9 Current –voltage curves of solar cell in the dark and under illumination.

In this work, I-V curves are measured for all SCs in the dark and under illumination (using either AM1.5G light from a solar simulator or white light from a halogen lamp) in a wide temperature range of 80..360 K.

II.3.2 Quantum efficiency and optical measurements

The external quantum efficiency (EQE) is the ratio of the number of carriers collected by the SC to the number of photons with a fixed energy that hit the SC. The EQE spectrum is the dependence of EQE on photon energy (or wavelength). The EQE is zero for photons with energy lower than E_g since they are not absorbed. If all photons at a given wavelength are absorbed and create one electron-hole pair, and if all photogenerated carriers are collected the EQE is unity at this wavelength.

In this work, the external quantum efficiency is measured by a home-made setup called "Spectrum-SC". Short-circuit regime is used for measurements of EQE for single- junction SCs. Illumination from a light source (halogen lamp) passes through an optomechanical modulator (chopper) and through a monochromator. Then, monochromatic light with fixed wavelength is concentrated on the sample. Light is absorbed in the sample, and the current signal is synchronized at the modulator's speed. We also measure the current signal of a reference SC (based on Si, GaSb) with known EQE. The EQE of the studied SC is then obtained by normalizing the current to that

of the reference SC. The wavelength is changed by the monochromator at a step of 5 nm. Finally, the EQE spectrum is obtained in a wide wavelength range, between 300 and 1200 nm.

The method is successfully applied for the characterization of single- junction solar cells. However, in MJSC it is also necessary to measure EQE for each subcell separately since it gives useful information on the material quality. As described above, a MJSC is a cascade of single-junction SCs with different bandgap values of the active layer and each subcell is responsible for the absorption of part of the solar spectrum. The MJSC is considered as a series connection of the subcells. Thereby for measuring a single subcell the influence of the rest should be excluded, for example, the corresponding *p-n* junctions could be saturated. In this case, current through saturated subcells do not depend on applied monochromatic light. It means that the corresponding diodes can be substituted by a shunt resistor. Illumination by additional light source is a powerful method to reach this goal.

In this work, double- junction SCs with bandgap energies of 1.8-2.1 eV and 1.1 eV (Si) in top-GaPN and bottom-Si subcells, respectively have been studied. The top subcell is not sensitive to infra-red (IR) illumination due to high bandgap, and the bottom one is not sensitive to ultra-violet (UV) illumination which is absorbed by the top sub-cell. Firstly, IR LED illuminates the silicon subcell for EQE measurement top subcells (short- circuit regime). Secondly, an UV LED illuminates the GaPN-subcell for QE measurement only of silicon subcells (short- circuit regime). As a result, EQE is obtained for both subcells separately. In case of triple- junction SC, two of the three subcells are saturated and another one is explored in short- circuit regime. However, it is not easy to obtain good experimental data when the bandgap energy of the middle subcell is close to that of the top one. Furthermore, if the quality of the top subcells is low it is a very difficult task to distinguish a small current signal from the high current of the saturated bottom diode. Nevertheless, EQE is measured in this work for single-, double and triple- junction SCs. J_{SC} can be estimated directly from EQE by:

$$J_{SC} = \frac{q}{hc}\int_{\lambda_{max}}^{\lambda_{min}} EQE(\lambda)P(\lambda)\lambda d\lambda \qquad \text{(II.5)}$$

where h is Planck's constant, c is the light velocity, λ is the wavelength, and $P(\lambda)$ is the spectral irradiance of sunlight (AM0, AM1.5, etc.).

Therefore, EQE directly affects the SC short circuit current and its value should reach unity for optimal performance. However, there are many reasons of losses in EQE. They are separated in two groups: optical losses and internal losses. The first one is associated with insufficient

absorption of incident light due to reflection, weak material absorption and transmission through SC. The second one is associated with insufficient collection of electron-hole pairs in the structure due to bulk and surface recombination, serial and parallel parasitic resistance and thermalisation of charge carriers. All explored SCs are grown without AR-coating so the setup was also used for measurements of their transmission and reflection to define their influence on EQE. It allows one to obtain the value of internal quantum efficiency (IQE) that characterizes the response of the SC to the only absorbed photons. Thus IQE can be affected only by internal losses associated with bad collection of charge carriers in the structure. Different capacitance methods allow us to understand the nature of internal losses in SCs and to provide some recommendation for the improvement of IQE in future experiments.

II.3.3 Capacitance-voltage method

The capacitance- voltage (C-V) method is a simple and common way to obtain information on internal properties of semiconductor layers in p-n junctions. It is based on measurements of the p-n junction capacitance change as function of the applied voltage. The width of the space charge region (SCR), *W*, is estimated for a *p*-*n* homojunction without applied voltage by[120] :

$$W = \sqrt{\frac{2\varepsilon_s\varepsilon_0}{q}\left(\frac{N_A + N_D}{N_A N_D}\right)V_{bi}} \tag{II.6}$$

where N_D is the donor concentration in the *n*-side, N_A is the acceptor concentration in the *p*-side, V_{bi} is the built-in voltage, ε_s is the relative dielectric permittivity. In case of an abrupt asymmetric *p*-*n* junction (e.g. $N_A >> N_D$) its equation can be simplified to:

$$W = \sqrt{\frac{2\varepsilon_s\varepsilon_0 V_{bi}}{qN_D}} \tag{II.7}$$

In a more accurate estimation taking into account the contribution of majority carriers to the space charge density, a correction factor k_BT/q has to be introduced. So V_{bi} should be replaced by V_{bi}-kT/q in equation:

$$W = \sqrt{\frac{2\varepsilon_s\varepsilon_0}{qN_D}(V_{bi} - k_BT/q)}\,. \tag{II.8}$$

If a reverse voltage is applied to such a p^+-n junction the magnitude of the electric field in the SCR grows and the width of the SCR increases due to the additional charge in the SCR as:

$$W = \sqrt{\frac{2\varepsilon_s\varepsilon_0}{qN_D}(V_{bi} - V_a - k_BT/q)}, \tag{II.9}$$

where V_a is the applied voltage. The semiconductor charge is given by:

$$Q_s = qS\int_0^W N_D dx\,, \tag{II.10}$$

where S is the surface area of the p-n junction. Therefore, the p-n junction acts as a capacitor since voltage variation leads to charge variation. Furthermore, we can apply both a dc voltage and an ac voltage with a small amplitude. As a result, the capacitance can be estimated from:

$$C \equiv -\frac{dQ_s}{dV_a} = -qS\frac{d}{dV_a}\int_0^W N_D dx = -qSN_D\frac{dW}{dV_a} = \sqrt{\frac{q\varepsilon_s\varepsilon_0 S^2 N_B}{2(V_{bi} - V_a - \frac{k_BT}{q})}}, \tag{II.11}$$

where V_a is the applied voltage. A typical capacitance-voltage curve is plotted for an abrupt p^+-n junction in Figure II.10a. From Eq (II.11) we find:

$$\frac{1}{C^2} = \frac{2}{q\varepsilon_s\varepsilon_0 S^2 N_D}(V_{bi} - V_a - k_BT/q)\,. \tag{II.12}$$

For an abrupt p^+-n junction with homogeneous doping the dependence of $1/C^2$ on applied voltage V should be linear (Mott-Schottky plot). Its slope defines the donor concentration in the n-region (N_D), the extrapolation to the voltage axis ($1/C^2=0$) gives the value of V_{bi}-k_BT/q (Figure II.10b).

More generally, the profile of the dopant concentration in the n-region can be deduced from:

$$N_D(W) = \frac{2}{q\varepsilon_s\varepsilon_0 S^2}\left(\frac{d\left(\frac{1}{C^2}\right)}{dV}\right)^{-1}, \tag{II.13}$$

with $$W = \frac{\varepsilon_s\varepsilon_0 S}{C}. \tag{II.14}$$

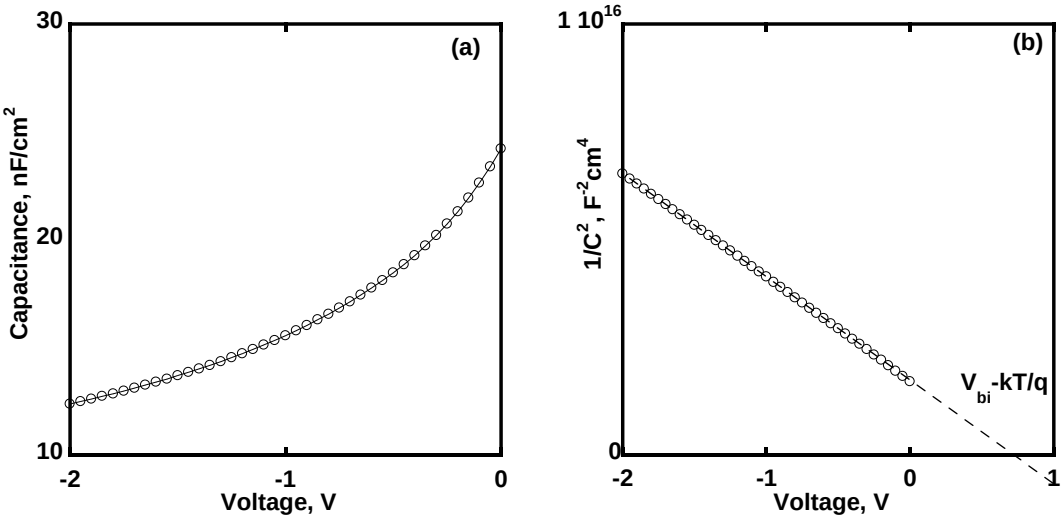

Figure II.10 Capacitance-voltage curve C(V)- a, and Mott-Schottky plot *1/C²(V)*- b.

In principle, all equations described in this section can be also applied to Schottky diodes (metal/semiconductor) and abrupt heterojunctions where space charge layers exist due to the energy barrier at the junction. However, we would like to emphasize that there are two main issues regarding the extraction of the built-in voltage V_{bi} from the intercept of the linear extrapolation of $1/C^2$ to the voltage axis and the determination of the doping density from the slope of $1/C^2$.

Firstly, for highly asymmetric *p-n* junctions or heterojunctions, when the band bending at the junction is so pronounced that a strong inversion layer builds at the surface of the lowly doped semiconductor, the intercept of the linear extrapolation of $1/C^2$ does not yield the correct value of the built-in voltage. Indeed, it has been shown that this intercept value corresponds to the equilibrium potential difference of only the depleted part of the space charge region, and does not integrate the part in the strong inversion layer[121]. This is particularly important if, in the case of

heterojunctions, one uses this intercept voltage as the built-in voltage to deduce band offsets at the heterojunction as proposed in some works[122], since it can lead to significant errors[123].

Secondly, in the above equations the charge in the SCR comes from the ionized donor density, which is compensated by free carriers outside the SCR where charge neutrality prevails. The charges that actually move in response to the ac voltage are the free electrons, not the ions. Hence, the capacitance-voltage profiling technique should determine the free carrier density rather than the doping density. It has been shown in the literature that, in case of non uniform doping, what is actually measured is an apparent or effective carrier density, which is close to the actual free carrier density, and designated by N_{CV} [124]. Another issue also related to the apparent effective density comes from defect levels that may be present in the semiconductor. Indeed, the energy levels in the bandgap related to intentional doping are generally so shallow that they can be considered as fully ionized above 100 K. However, levels that are not so shallow (e.g. 100 meV or more from the band edge) may also be partly ionized depending on the temperature, which can thus provide a temperature dependent contribution to N_{CV}. So, the *C*-*V* measurements typically allow one to determine some effective doping or carrier density but in order to study deep defects other popular methods are used: admittance spectroscopy and deep-level transient spectroscopy. These will be recalled in the following.

II.3.4 Admittance spectroscopy

The admittance spectroscopy (AS) consists in carrying out measurements of capacitance and conductance as a function of temperature and frequency. AS is widely used for the determination of the electronic properties of defects in the semiconductor layers of Schottky barriers, *p*-*n* and *p*-*i*-*n* junction structures. One of the first works on this subject was published in 1975[125]. It provides a simple way to determine different properties of defect levels interacting with majority-carriers in semiconductor materials: energy position of the level E_T, capture-cross section σ, concentration N_T.

Let us take again the example of a p^+-*n* junction or Schottky barrier onto a *n*-type semiconductor. Under the application of the alternative small signal of applied voltage at the frequency *f*, one can describe things by considering that the position of the electron (majority carrier) Fermi level is oscillating in the Schottky barrier structure or abrupt p^+-*n* junction (Figure II.11). If the electron Fermi level crosses some defect levels in the bandgap, this produces a modulation of the occupancy of these states. It results in an alternative capture and emission process of electrons in the states, provided the time constant of these processes is lower than the period of the alternating signal. This gives an additional contribution to the charge variation.

Consequently, compared to the defect free case, the junction capacitance is increased due to the additional charge variation associated with the capture and emission in the localized states.

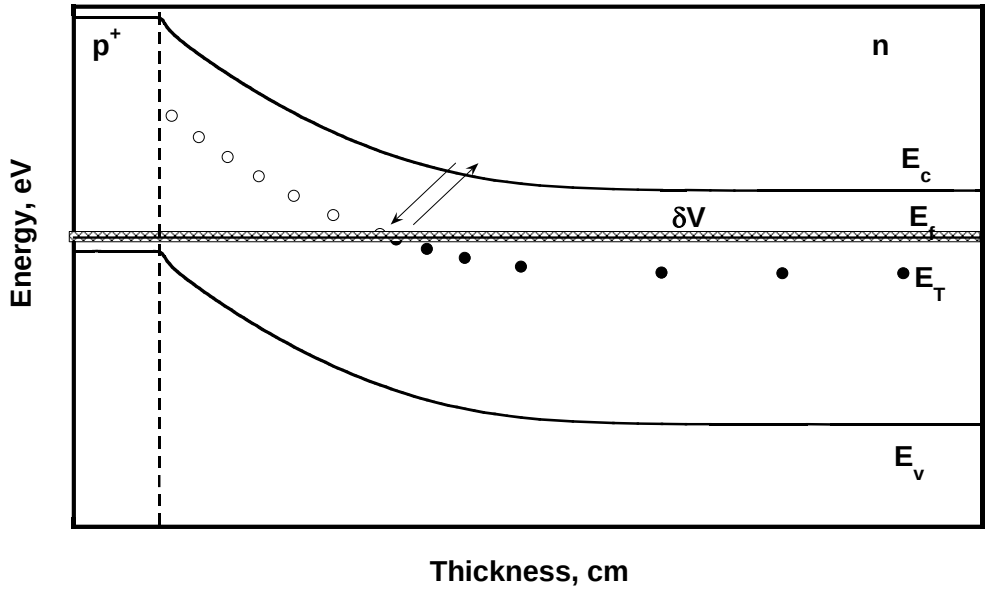

Figure II.11 Schematic illustration of a p^+-n junction or Schottky barrier onto an n-type semiconductor with a defect level at energy E_T. The arrows indicate the capture and emission of electrons from the defect.

Since emission and capture frequencies are equal at the Fermi level, the charge variation at the defect level can occur if the angular frequency of the ac signal ω (equal to $2\pi f$, where f is the frequency of the ac signal) is less than $2e_n$, where e_n is the emission electron rate defined by:

$$e_n(T) = c_n N_C e^{\frac{E-E_C}{k_B T}}, \tag{II.15}$$

where c_n is the capture coefficient of electrons and N_C is the effective density of states in the conduction band. Thus, one can define a characteristic temperature T_0 and a characteristic angular frequency response ω_0 for the response of the defect state, that are linked through

$$2e_n(T_0) = \omega_0 . \tag{II.16}$$

When the temperature is lower than T_0 or the angular frequency is higher than ω_0, there is no response from defect levels, and we are in the so-called freeze-out regime. Thus, the measured capacitance is the usual depletion capacitance described before. When the temperature increases

or the frequency decreases, the capacitance *C(T,f)* starts to increase and a capacitance step appears on *C(T,f)* graphs. A step in the capacitance curve corresponds to a peak in the conductance curve *G(T,f)* and in the capacitance derivative *dC/dT(T,f)*[125,126]. Since e_n is an increasing function of temperature, a frequency increase leads to an increase of T_0 and to the shift of the capacitance step to higher temperatures on the *C*(*T*) curves. Similarly, on *C*(ω) curves, the step shifts to higher frequencies with increasing temperature.

A schematic capacitance dependence on frequency and temperature is shown in Figure II.12. Capacitance steps are accompanied by peaks in the conductance and in the capacitance derivative. In the current work both types of representations are used. According to (II.15) and (II.16), the dependence of T_0 on ω_0 is given by:

$$2e_n(E_a) = 2c_n N_C e^{\frac{-E_a}{k_B T_0}} = \omega_0 \,, \tag{II.17}$$

where E_a=E_c-E_T will be called the activation energy of the level. The capture coefficient of electrons is related to the electron capture cross-section c_n=$\sigma_n \upsilon_{th}$ where υ_{th} is thermal velocity of electrons. It should be noted that the position of the capacitance step depends on the capture cross-section of defect levels while the amplitude of the step is directly dependent on the number of defects regardless of the capture cross-section.

Thus,

$$f_0 = \frac{\sigma_n \upsilon_{th} N_C}{\pi} e^{\frac{-E_a}{k_B T_0}} \,, \tag{II.18}$$

where the effective density of states and thermal velocity generally depend on temperature as $\sim T^{3/2}$and $\sim T^{1/2}$, respectively, so the equation can be rewritten as:

$$f_0 = A T_0^2 e^{\frac{-E_a}{k_B T_0}} \,, \tag{II.19}$$

where *A* is supposed to be independent on temperature:

$$A = \frac{\upsilon_{300} N_{300} \sigma_n}{\pi (300)^2} \tag{II.20}$$

where N_{300} and υ_{300} are the effective density of states and thermal velocity at 300 K, respectively. As a result, a defect activation energy E_a can be extracted from the dependence of $ln(f_0/T_0^2)$ on inverse temperature or on $1000/T_0$. This graph is called an Arrhenius plot and its schematic representation is shown in Figure II.13. The pre-exponential factor is estimated from extrapolation of the curve to infinite temperature ($1000/T_0=0$ in the graph). The capture-cross section can then be calculated from (II.20).

The value of defect concentration can be estimated by the method suggested by Walter [127]. It is based on the capacitance derivative with respect to angular frequency. The defect distributions in energy, or density of states (DOS) can be reconstructed by this method for both *p-n* and *p-i-n* junction. According to Eq (II.17), each angular frequency corresponds to a certain energy at fixed temperature:

$$E_\omega = k_B T ln \frac{c_n N_C}{\omega}. \tag{II.21}$$

Then, the DOS is estimated for a *p-i-n* junction by[127]:

$$N_T(E_\omega) = -\frac{V_{bi}^2}{W\left[qV_{bi} - \left(E_{fn\infty} - E_\omega\right)\right]} \frac{dC}{d\omega} \frac{\omega}{k_B T}, \tag{II.22}$$

where $E_{fn\infty}$ is the energy position of Fermi level with respect to the valence band edge in the *n*-layer of the *p-i-n* junction. Also, for asymmetric p^+-*n* and *p*-n^+ junctions the energy distribution of defects is estimated by:

$$N_T(E_\omega) = -\frac{2V_{bi}^{\frac{3}{2}}}{W\sqrt{q}\sqrt{qV_{bi} - \left(E_g - E_\omega\right)}} \frac{dC}{d\omega} \frac{\omega}{k_B T}. \tag{II.23}$$

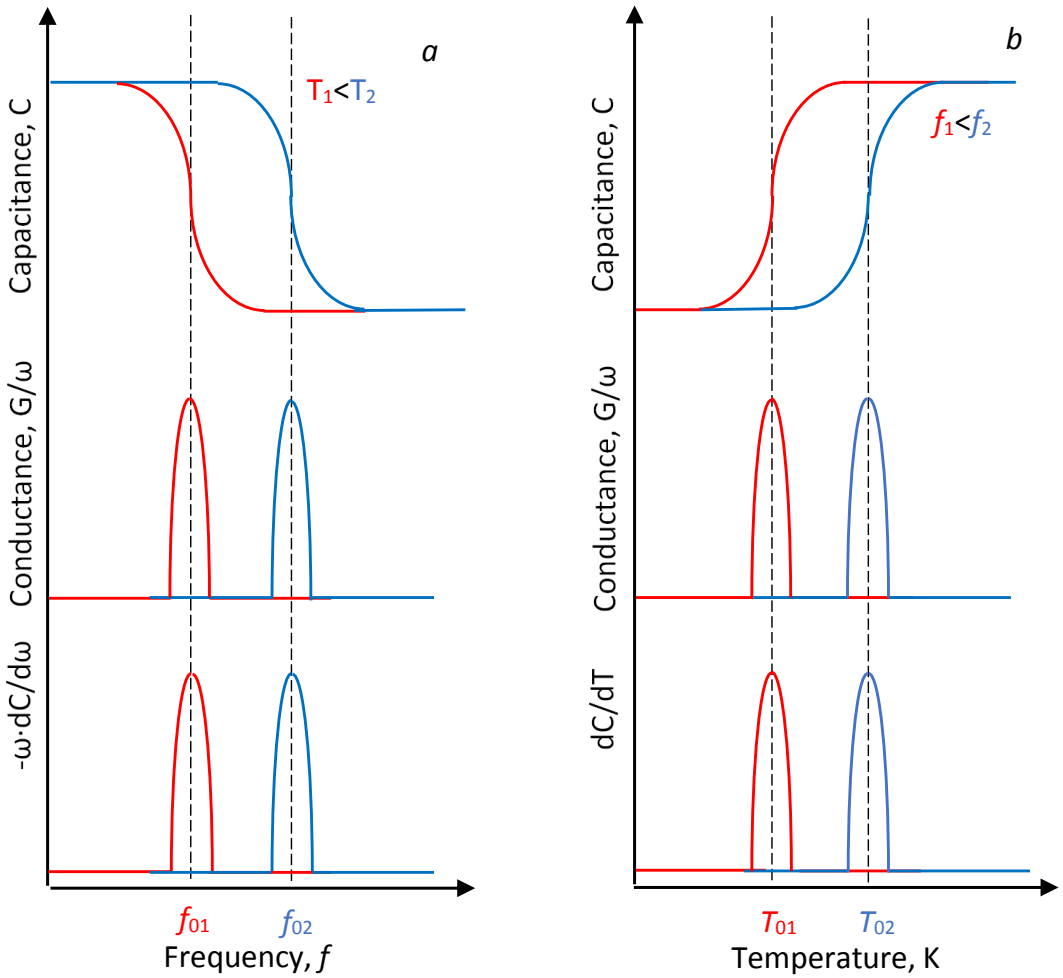

Figure II.12 a- Schematic dependence of the capacitance and conductance on frequency for two temperatures; b- Schematic dependence of the capacitance and conductivity on temperature for two frequencies.

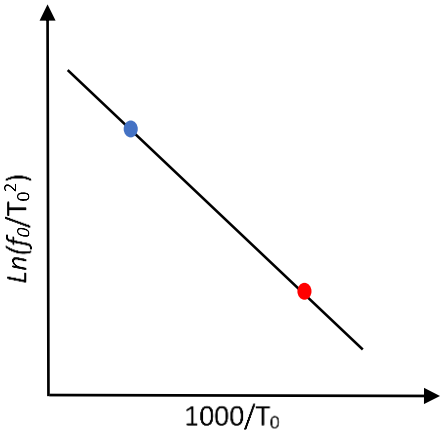

Figure II.13 Arrhenius plot of $ln(f_0/T_0^2)$ as a function of characteristic temperature.

In this work, admittance measurements are performed in a liquid nitrogen cryostat in the temperature range from 80 K to 400 K and at frequencies from 20 Hz to 1 MHz using a RLC-meter Agilent E4980A in GeePs, France and RLC-meter E7-20 in SPbAU, Russia. The dc voltage can be also applied and changed through the RLC-meter.

II.3.5 Deep-level transient spectroscopy

Deep-level transient spectroscopy (DLTS) is another very powerful method for the study of active defects in semiconductors. DLTS was proposed in 1974 by D.V. Lang as a method to study deep levels in semiconductor structures having a SCR like Schottky diodes or *p-n* junctions[128]. It is a transient method that is based on the measurement of the junction capacitance versus time following a change in applied voltage, as illustrated in Figure II.14. To briefly present the physical background of DLTS, let us consider an abrupt p^+-*n* junction under an applied reverse bias voltage V_0, and assume there is a defect level lying at an energy E_T above midgap.

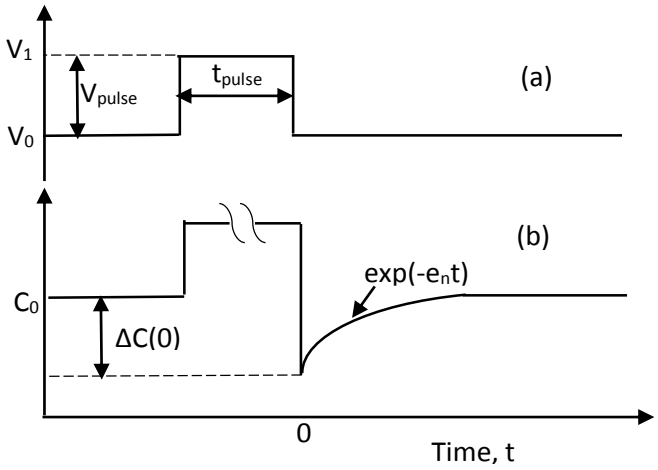

Figure II.14 a- time dependence of bias voltage, and b- typical time dependence of the junction capacitance for majority-carrier traps.

Under steady-state, in the region where the level E_T lays above the electron quasi-Fermi level, states are empty, while in the region where the level E_T lays below the electron quasi-Fermi level, states are occupied by electrons (Figure II.15a). Under such steady-state conditions, the junction capacitance is C_0 and the width of the SCR is W_0. A positive bias pulse with amplitude V_{pulse} and duration t_{pulse}, called the filling pulse, is then applied so that the total bias voltage changes to V_1. This induces a shrinking of the SCR, and electrons flow into what was previously part of the depletion region, so that some traps previously empty can capture electrons. If V_{pulse} is large enough so that $V_1>0$, holes can also be introduced in this part of the SCR so that some traps may possibly also be filled with holes. The degree of trap filling depends on t_{pulse} and on the capture coefficients c_n and c_p for electrons and holes, respectively, that are proportional to the capture

cross-section for the corresponding type of charge carriers. If the pulse width t_{pulse} is large enough one may reach the steady-state at V_1 and some levels are then completely filled so that $n_T=N_T$, n_T being the concentration of traps being occupied by electrons and N_T the concentration of traps (Figure II.15b). Following the filling pulse, the bias is changed to its initial reverse bias V_0. Therefore, the states that were previously filled with electrons release their electrons that are emitted to the conduction band and swept out of the SCR by the electric field. So the occupied trap concentration changes with time, $n_T(t)$, which also implies a time dependence of the SCR, $W_0+\Delta W(t)$, $\Delta W(t)$ going to zero when steady-state is reached again.

Following Shockley and Read[129], and Hall[130], and since we neglect capture events during the transient under reverse bias, n_T is given by equation:

$$\frac{dn_T}{dt} = (N_T - n_T)e_p - n_T e_n \,, \tag{II.24}$$

where e_n and e_p are the emission frequencies for electron and holes, respectively. The steady-state electron occupation of a level is:

$$n_T = \frac{e_p}{e_p + e_n} N_T \,. \tag{II.25}$$

This allows one to define so-called electron traps if $e_n>>e_p$ (majority-carrier in *n*-type, $n_T=0$) and hole traps if $e_p>>e_n$ (minority-carrier in *n*-type, $n_T=N_T$), the demarcation being roughly at midgap. With the initial condition $n_T(0)=N_T$ the solution of (II.24) is given by:

$$n_T(t) = \left[\frac{e_p}{e_p + e_n} N_T + \frac{e_n}{e_p + e_n} N_T exp\big(-(e_p + e_n)t\big)\right]. \tag{II.26}$$

Thus n_T decreases exponentially versus time. In case of $e_n>>e_p$:

$$n_T(t) = N_T exp(-e_n t) \,. \tag{II.27}$$

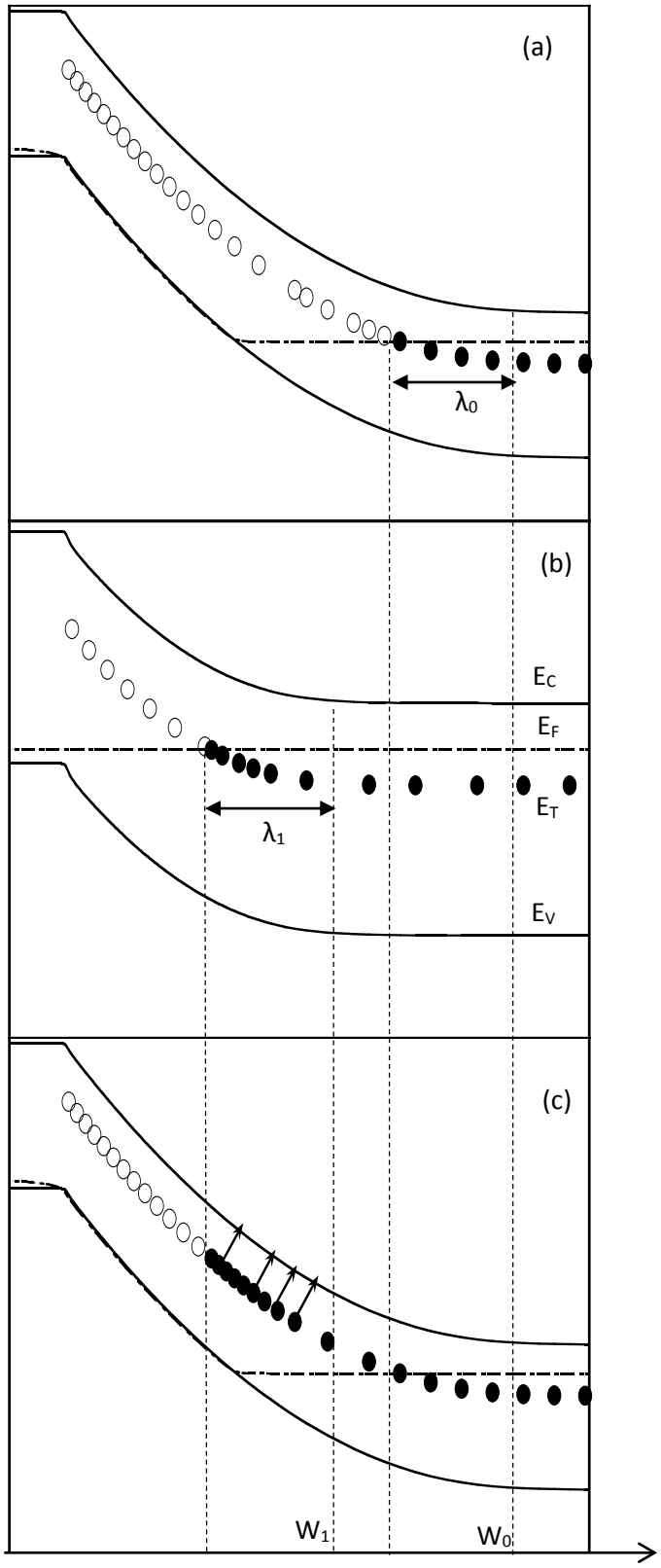

Figure II.15 Spatial distribution of full and empty traps at a given defect level E_T in an abrupt p^+-n junction: a- at steady-state reverse bias V_0, b- at bias $V_1=V_0+V_{pulse}$ during the filling pulse, c- after the pulse when the bias has been set at V_0 again. Arrows indicate trapped electrons that will be re-emitted to the conduction band.

Such a dependence directly relates the time-dependent occupied trap concentration to the electron emission rate and thus to the defect properties (energy level, electron capture cross section). However, unfortunately, it is impossible to directly measure the trapped electron concentration. This is why it was proposed to use the junction capacitance that is associated with the occupancy changes. The capacitance of a p^+-n or Schottky junction is defined by Eq (II.11) so the capacitance relaxation to its steady-state value C_0 can be defined by differences in the width of the SCR. In case of low defect concentration, $N_T << N_D$, the change in capacitance referred to the steady-state value, $\Delta C = C(t) - C_0$, is related to the change in space charge width $\Delta W(t)$ by:

$$\frac{\Delta C(t)}{C_0} = -\frac{\Delta W(t)}{W_0}. \tag{II.28}$$

The emission of electrons from traps after they have been filled by the filling pulse leads to the relaxation of the SCR to its initial value of W_0 due to neutralization of ionized donors by electrons at the edge of the SCR. The bias being kept constant, one can obtain the following equation[131]:

$$\int_{W_0}^{W_0+\Delta W(t)} N_D(z) \cdot z dz = \int_{W_1-\lambda_1}^{W_0-\lambda_0} n_T(t,z) \cdot z dz . \tag{II.29}$$

If the concentrations of donor impurities and traps are constant, integration of the preceding equation gives:

$$\frac{\Delta W(t)}{W_0} = \frac{n_T(t)}{2N_D} \frac{(W_0-\lambda_0)^2 - (W_1-\lambda_1)^2}{{W_0}^2}. \tag{II.30}$$

Together with equation (II.28):

$$\frac{\Delta C(t)}{C_0} = -\frac{n_T(t)}{2N_D} \frac{(W_0-\lambda_0)^2 - (W_1-\lambda_1)^2}{{W_0}^2}. \tag{II.31}$$

In case of $W_0 >> W_1 >> \lambda_{0,1}$, this simplifies into:

$$\frac{\Delta C(t)}{C_0} \approx -\frac{n_T(t)}{2N_D}. \tag{II.32}$$

Together with Eq (II.27), the capacitance relaxation can be estimated by:

$$\frac{\Delta C(t)}{C_0} = -\frac{N_T}{2N_D}\exp(-e_n t)\,. \tag{II.33}$$

Thus, the capacitance *C(t)* at reverse bias V_0 after the filling pulse is described by:

$$C(t) = C_0\left[1 - \frac{N_T}{2N_D}\exp(-e_n t)\right]. \tag{II.34}$$

The typical capacitance dependence is presented for majority-carrier traps in Figure II.14b. In case of minority-carrier traps e_n and $-\frac{N_T}{2N_D}$ are replaced by e_p and $+\frac{N_T}{2N_D}$, respectively[128]. So, during the transient the capacitance increases for majority-carrier traps and decreases for minority-carrier traps. Thus, the emission rate and trap concentration can be estimated from the dependence of the capacitance on time at a given temperature. However, in case of overlapping of emissions from different defect levels at the same temperature the analysis becomes more complicated and it can be difficult to distinguish between several contributions. Therefore, a method was presented by Lang to better separate the responses of various defects in one temperature region and to obtain information on the properties of detected defects in a simple way by using a temperature scan. When the filling pulse ends, the applied voltage returns to the initial value V_0 and the experimental setup starts to measure the capacitance transient by a fast-response capacitance bridge. This procedure is repeated for each temperature with a certain temperature step. Then data are processed by a dedicated mathematic function to associate each temperature to an emission rate. In the classical DLTS analysis the spectral function *S*(*T*) is defined as the difference between capacitance values at two fixed times, t_1 and t_2. Depending on the authors, *S*(*t*) is defined as $C(t_1)-C(t_2)$ or $C(t_2)-C(t_1)$ with $t_2 > t_1$. In this work, *S(T)* is defined as:

$$S(T) \equiv C(t_2) - C(t_1) = \Delta C_0[\exp(-e_n t_1) - \exp(-e_n t_2]\,, \tag{II.35}$$

where ΔC_0 is the capacitance change immediately after the end of the pulse, at time t=0. Typical behavior of *S*(*T*) is presented in case of a single majority-carrier trap in structure[132] in Figure II.16.

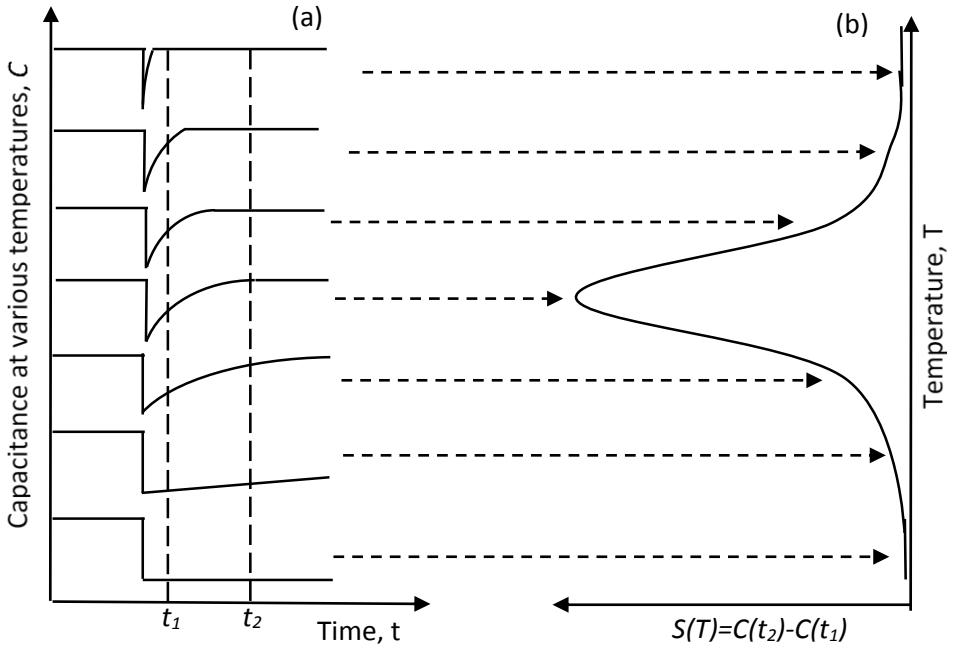

Figure II.16 Qualitative illustration of the temperature dependence of the DLTS spectrum, *S(T)* (b) calculated as the difference of capacitance at the two times t_1 and t_2 that define the rate window (a).

As described above the electron emission rate of a deep level is strongly temperature dependent:

$$e_n = \sigma_n \upsilon_{th} N_C e^{\frac{-E_a}{k_B T}} . \tag{II.36}$$

Therefore, the physical nature of the maximum in *S*(*T*) spectrum can be fairly well understood. At low temperature, the capacitance transient is very slow so $C(t_2)$ is almost equal to $C(t_1)$ and *S* is almost zero. When the temperature increases, $C(t_2)$ starts increase before $C(t_1)$ leading to an increase in *S*(*T*). At a certain temperature *S* has a maximum value. For higher temperature, $C(t_2)$ stays almost the same but $C(t_1)$ is now also increasing and approaching the steady-state value. So *S*(*T*) decreases and finally goes toward zero at high temperature when the transient is much faster than both t_1 and t_2. In this way, each time window t_1 and t_2 is associated with a certain maximum position of *S*(*T*). The value of emission rate e_n can be estimated from the derivation of (II.35) by equation:

$$e_n(T_{max}) = \frac{\ln t_2/t_1}{t_2 - t_1}. \quad \text{(II.37)}$$

Therefore, each time window defines the so-called DLTS rate window, i.e. the emission rate e_n at temperature position T_{max}.

Then, it is necessary to change the time window t_1 and t_2 and to find new pairs of emission rate and temperature. Finally, the dependence of $ln(e_n/T_{max}^2)$ on the inverse characteristic temperature $1000/T_{max}$ is plotted. Like in admittance spectroscopy, from such Arrhenius plot the activation energy and capture cross-section can be estimated. Moreover, from Eq (II.35) the value of $S_{\max}$ is proportional to ΔC_0 and therefore to the defect level concentration N_T. If t_{pulse} is large enough to fill all defect levels and the duration of the emission phase is large enough to allow for all captured electrons to be emitted again, the defect concentration can be estimated from S_{max} (in case of a single defect level) by:

$$N_T = \frac{S_{max}}{C_0} \frac{2r^{r/(r-1)}}{r-1} N_D \,, \quad \text{(II.38)}$$

where $r=t_1/t_2$.

Here, we described the classical DLTS method for an abrupt p-n junction with a single defect level. In real experiments, many causes lead to complications in the detected signal and difficulties in its interpretation for instance because of non-exponential behaviors. It is due to the overlapping of point defect responses with close energy positions or extended defects associated to distributions in energy. In this case, the shape of *S(T)* changes and becomes broader. A more detailed description of extended defects nature is given in the next chapters where experimental results are presented.

Sometimes, in case of overlapping of two point defect responses a modified method called Laplace-DLTS can help to distinguish them. It is a mathematical method of analyzing the capacitance transient. The Laplace-DLTS is based on the precise measurement of the capacitance transient at fixed temperature many times (in this work, it is measured 2000-10000 times) with very high resolution (frequency of sample measurement). In order to use the Laplace-DLTS method the capacitance transient needs to be fully completed, meaning that the capacitance reaches the steady-state value corresponding to the reverse bias V_0. Then, the quantitative description of

non-exponential behavior in the capacitance transients is to assume that they are characterized by a spectrum of emission rates:

$$f(t) = \int_0^\infty F(s)e^{-st}ds\,, \tag{II.39}$$

where *f(t)* is the recorded transient and *F(s)* is the spectral density function[133]. To find a real spectrum of the emission rates in the transient it is necessary to use a unique mathematical algorithm estimating an inverse Laplace transform for the function *f(t)*, yielding a spectrum of delta-like peaks for multi-, mono-exponential transients, or a spectrum with overlapping broad peaks for defects with an energy distribution. It means that the algorithm tries to approximate the capacitance transient *C(t)* by many exponential transients. As a result, Laplace-DLTS gives an output function of emission rates corresponding to the response from the defect levels. The algorithm is considered as "good" for structure analysis if peaks on *F(s)* are very narrow. Then, the spectrum *F(s)* should be found for a few temperature points and the Arrhenius plot can be obtained. Laplace-DLTS is a very powerful method to distinguish point defects if they have very close activation energies. However, the transient must be measured very precisely and the increase in defect concentration leads to the deterioration of estimated *F(s)*. Therefore, Laplace-DLTS is almost not applicable for measurements of extended defects due to the very long transient and overlapping of many responses. In this work, commercial software “Laplace Transient Processor” is used for Laplace-DLTS measurements[133].

Finally, DLTS is one of the most useful methods for studying defect properties in semiconductor materials so it has been intensively used in the current thesis. The automated installation based on a Boonton-7200B capacitance bridge is used for measurements of capacitance transients for classical DLTS and Laplace-DLTS methods. Experiments are performed at high frequency (1 MHz) at temperatures from 78 to 400 K.

II.3.6 Structural methods

Although the main goal of this work is to study photoelectric properties and defects in solar cells, we also used various methods to study structural properties. Basically, these methods are used for the study of GaP layers grown by PE-ALD on silicon wafers since this material is quite new and its properties have not been investigated so far.

The first method is scanning electron microscopy (SEM). It is based on the interaction of a focused electron beam with the sample, giving information about the sample's surface topography and composition. It is a common method for determining layer thicknesses and

investigating interface and surface quality in semiconductor structures. In the current work, it is used for characterization of surface quality of GaP grown by PE-ALD at different conditions. Also, it is used for the precise determination of thicknesses in single-junction and double-junction SCs since it is a very critical issue for controlled wet etching. Then classical and high resolution transmission electron microscopies (TEM and HRTEM) are performed to study properties of materials at the atomic scale. These methods are based on the analysis of the transmitted electrons beam through the sample. HRTEM allows one to improve spatial resolution of SEM images and to obtain maps of atoms in the lattice and at interfaces. Therefore, it is a very fruitful method to study structural properties at a scale of 0.1 nm. Initial information about chemical content of grown GaP based layers is obtained from Raman spectroscopy data. This technique consists in the measurement of vibrational, rotational, and other low-frequency modes in a semiconductor layer since these modes are fingerprints by which molecules can be identified.

II.4 Simulation

Computer simulation is a very powerful tool to help analyzing new experimental data, especially for semiconductor device physics. In the current work, software AFORS-HET (Automat FOR Simulation of HETero structures) 2.5 is used for the simulation of SC performance[134]. It is necessary to define the stacking of layers and enter electronic, optical and defect parameters of each layer. Then the program solves Poisson's equation together with continuity equations using drift and diffusion currents, and we can draw band diagrams and extract carrier concentrations, etc. Different external conditions can be changed: applied ac or dc voltage, illumination spectrum at different wavelengths, etc. The program also allows us to simulate measured data curves like I-V, C-V, C-T, EQE, etc. Furthermore, the interface of the program is very clear and simple to use.

Summary

In this Chapter we have given the description of the growth of materials, post-growth processing and experimental studies. Structures can be separated in two groups: solar cells grown by MBE (single-junctions on GaAs wafer, single-junctions on GaP wafer, multi-junctions on Si wafer) and GaP/Si heterostructures grown by PE-ALD. Different aspects of metal contact formation with required properties are developed. We also gave an overview of photoelectric (I-V, EQE) and capacitance (C-V, AS, DLTS) methods used to study our samples and structures. Finally, we mentioned the simulation software that will be used to analyze the device physics of our structures.

Chapter III

InGaAsN

Introduction

In this chapter, we describe the results obtained on single-junction solar cells grown on GaAs wafers by MBE with active layers of SDA *i*-InGaAsN with different thicknesses. Photoelectric and electric properties are investigated at different conditions. Moreover, different capacitance methods (AS, DLTS, C-V) are used to characterize the defects in the layers. Finally, simulations are performed to help analyzing the data.

III.1 Samples preparation

Single-junction SCs based on *p*-*i*-*n* heterostructures were grown by MBE. They consist in three samples with a bottom *n*-type GaAs layer (200 nm thick, doping density of 3×10^{18} cm^{-3}) first grown onto (100) *n*-type GaAs wafers, followed by the growth of undoped (*i*) InAs/GaAsN SL with different thicknesses of the active *i*-layer (900 nm, 1200 nm, 1600 nm). Practically, the InAs/GaAsN SL is obtained by the growth of ternary GaAsN, 7-12 nm thick, followed by the growth of binary InAs, 0.2-0.5 nm thick (1 ML), and repeated in order to reach the targeted thickness. The top *p*-type layer is made of a 200 nm thick GaAs layer with a doping density of 1×10^{19} cm^{-3}. The schematic cross-section of the samples is presented in Figure III.1. All samples were grown without any antireflection coating.

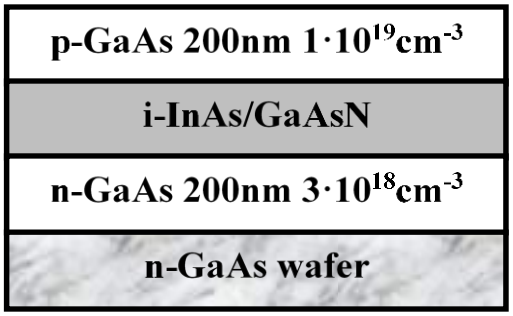

Figure III.1 Schematic view of the p-i-n structures with *i*-InAs/GaAsN active layers.

Contacts were fabricated using photolithography and vacuum evaporation of metals. Au/Ge was used for the *n*-type bottom contact and Au/Zn was used for the *p*-type top contact[135].

The ohmic behavior of the current- voltage characteristics for contacts was obtained after rapid thermal annealing using a JIPelec JetFirst 100 equipment at 380 °C. For photoelectric measurements the top contact consisted in a grid, while for capacitance measurements circular contacts with diameters of 0.5 and 1 mm were used on the front side, then mesa-structures were formed by wet etching down to the wafer.

III.2 Photoelectric properties

The photoluminescence (PL) spectra of the InGaAsN samples measured at room temperature are displayed in Figure III.2. They were measured using an instrument from Accent RPM Sigma (Accent Optical Technologies) with a semiconductor laser (λ=778 nm) as the pumping source. The bandgap energy of InGaAsN is 1.03 eV whatever the sample thickness. However, we observe that the intensity of photoluminescence strongly decreases when the thickness increases. Perhaps, it is explained by rising of defect density in InGaAsN layers. Indeed, deep defects could act as non-radiative recombination centers that reduce the free carrier concentrations, thus also reducing the band-to-band PL signal.

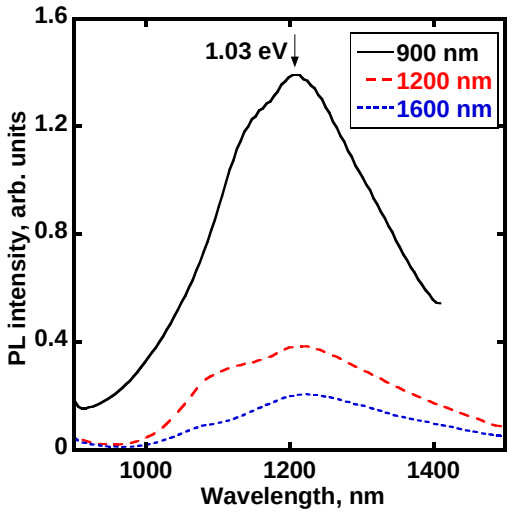

Figure III.2 Photoluminescence spectra of the 900 nm, 1200 nm and 1600 nm thick *i*-InGaAsN samples.

Then, the external quantum efficiency and reflection were measured at a temperature of 25 °C to study photoelectric and optical properties of the structures (Figure III.3). Value of QE exceeds 50 % for 900 nm InGaAsN sample without AR coating so the quantum efficiency can reach 75% in case of absence of reflection losses. Obviously, when the thickness of the *i*-layer increases from 900 nm to 1200 nm, the quantum efficiency decreases slightly in the short wavelength range due to possible recombination losses while it slightly increases in the long

wavelength range because of enhanced absorption with the thickness increase. Further thickness increase to 1600 nm leads to a catastrophic decrease of quantum efficiency of SC in short wavelength region due to high recombination losses caused by centers of non-radiative recombination. It is important to note the specific shape of QE curve for sample with 1600 nm thick InGaAsN at long wavelength values remain almost the same unlike in short wavelength region. Possible reasons of such behavior are discussed below.

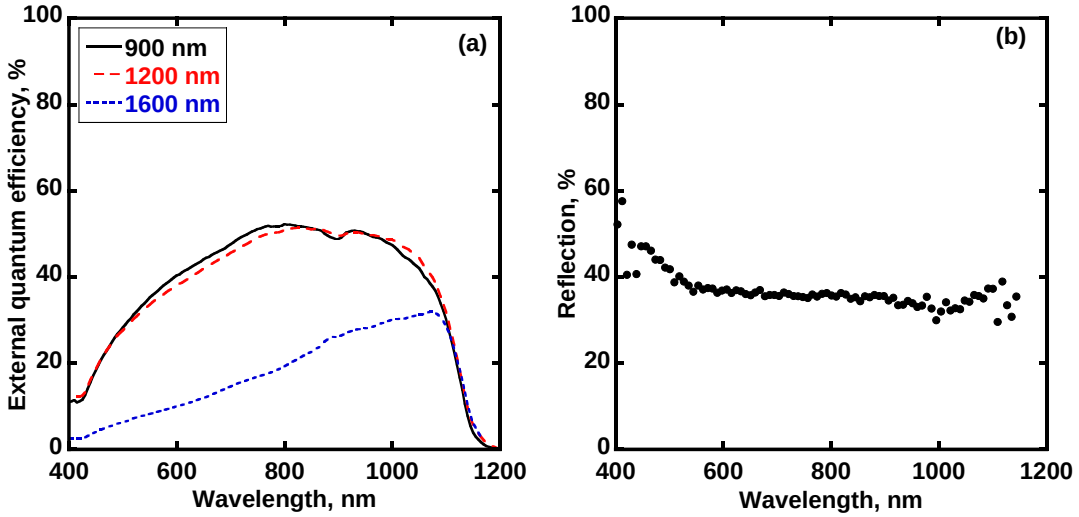

Figure III.3 External quantum efficiency (a) and reflection (b) of single-junction SCs with *i*-InGaAsN.

Then, current-voltage curves are presented in Figure III.4 for two cases: I-V under illumination of AM1.5G for SCs and dark I-V for mesa-structures. The sample with 900 nm-InGaAsN shows the best performance with V_{OC}=0.40 V and J_{SC}=15.5 mA/cm^2. Although these values are not very large they are quite promising in the perspective of transferring this *p-i-n* junction to MJSC. Making the InGaAsN layer thicker (1200 nm) leads to a decrease in V_{OC}, whereas a further increase in the thickness up to 1600 nm causes a catastrophic drop in J_{SC}. I-V curves in the dark have the conventional exponential dependence corresponding to semiconductor junction as confirmed for mesa-structures in semilogarithmic scale in Figure III.4b: straight line at forward bias voltage, and saturation at high voltage due to serial resistance in the sample. In addition, the current value is low at reverse bias voltage so samples are suitable for capacitance investigation.

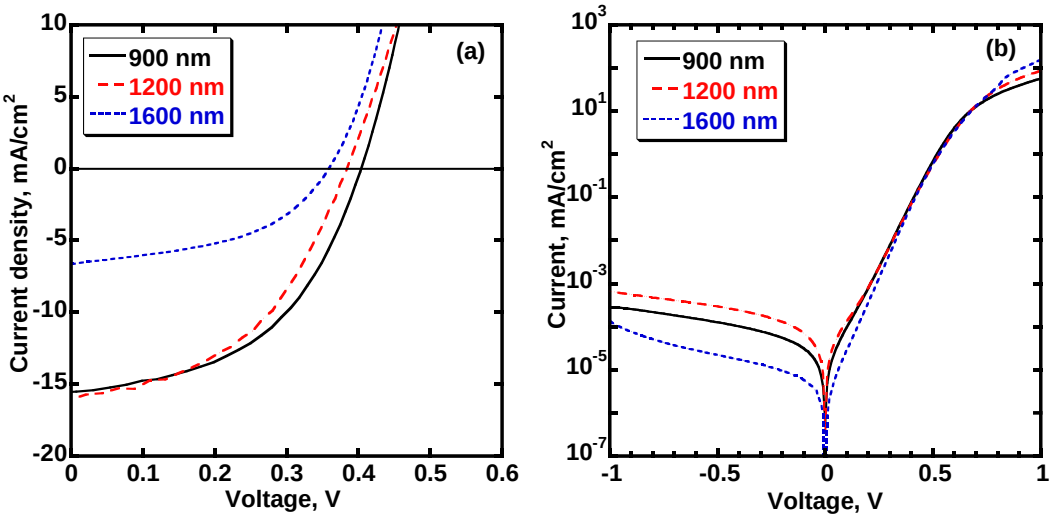

Figure III.4 Current-voltage characteristics under illumination for solar cells (a) and in the dark for mesa-structures (b).

Therefore, photoelectric properties of single-junction solar cells degrade with increasing the thickness of the active *i*-InGaAsN layer due to higher defect concentration. Thus, capacitance methods are used to explore this suggestion.

III.3 Capacitance measurements

III.3.1 Quasi steady-state capacitance measurements

The *C-V* dependence was measured at reverse bias in the interval [-1V, 0V] at 1 MHz and at 300 K for the three InGaAsN samples. C-V curves of 1200 and 1600 nm thick InGaAsN samples are presented at Figure III.5.

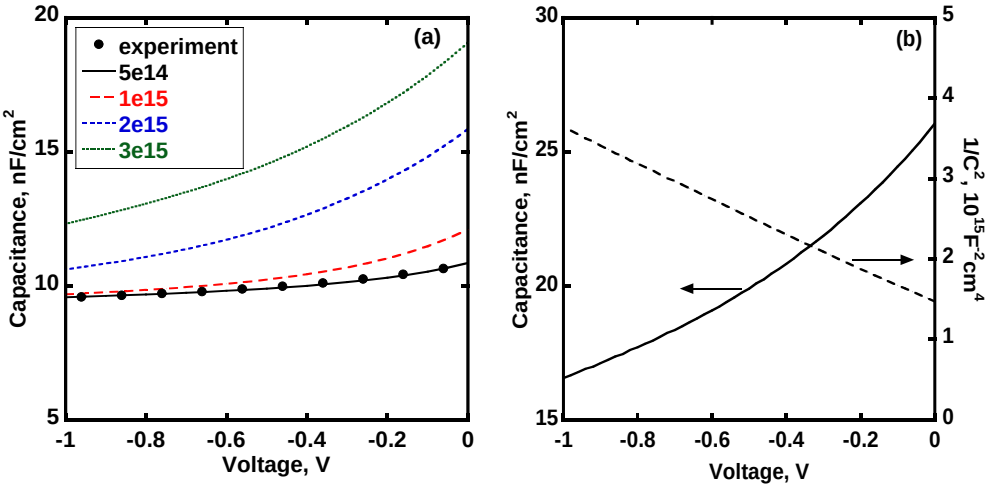

Figure III.5 Capacitance-voltage (*C-V*) characteristics measured for the 1.2 µm thick InGaAsN sample and simulated with varying doping concentration (a), *C-V* and Mott-Schottky plot for the 1.6 µm thick InGaAsN sample (b).

The capacitance of the sample with 900 nm thick InGaAsN was found independent of applied voltage, meaning that the effective width of SCR, d_{eff}, probed by the capacitance measurement, defined as $d_{eff} = \varepsilon/C$, ε being the dielectric permittivity, is equal to the *i*-layer thickness. So the *i*-layer is fully depleted in the 900 nm thick InGaAsN sample. As can be seen (Figure III.5a), for the 1200 nm thick InGaAsN sample, the capacitance also tends to become constant at reverse bias, and only a very small increase is observed towards 0V. We note that a capacitance of 10 nF/cm^2 corresponds to a value of d_{eff} of 1.15 μm if we take the permittivity $\varepsilon = 1.15\times10^{-12}$ F·cm^{-1} of GaAs, which is indeed close to the thickness of the *i*-InGaAsN layer. This indicates that there is no strong unintentional or residual doping in the *i*-layer of both 900 nm and 1200 nm thick samples. The small bias dependence on the 1200 nm thick sample does not allow us to determine the unintentional/residual doping concentration reliably from a Mott-Schottky plot. To estimate the doping concentration, we have performed electrical modeling of the sample with 1200 nm thick InGaAsN in order to simulate the *C-V* curves. From the simulated *C-V* curves with varying doping concentration (*p*-type, see below), we can deduce that the non-intentional doping concentration should be less than 1.0×10^{15} cm^{-3}. For the 1.6 μm thick InGaAsN sample, however, the capacitance is bias dependent. The experimental Mott-Schottky plot for this structure shown in Figure III.5b exhibits a linear behavior of $1/C^2$ as a function of the applied voltage, as expected in the depletion regime of a *p-n* junction. According to the slope, the effective doping concentration value is estimated at 5.0×10^{15} cm^{-3} at 300 K. Note that a such doping concentration value would have been detected even in the sample with the thinnest *i*-layer since the depletion capacitance would have been much larger than the geometrical capacitance because the effective space charge layer thickness would have been significantly smaller than 900 nm. In conclusion of the *C-V* measurements at room temperature, the sample with a 1600 nm thick *i*-layer exhibits significant higher effective background doping than the samples with thinner *i*-layers. We also performed *C-V* measurements at 77 K and found that the dependence of the capacitance on applied voltage was much less pronounced, indicating that deep defects also contribute to the effective doping at 300 K. From computer simulations that will be presented below, it is found that this background doping is of acceptor type. It is worth noting that a p-type background doping is typical for *i*-layers of dilute nitrides (In)GaAsN grown by MBE[28,29]. Usually, it is associated with non-equilibrium growth conditions at low temperatures that lead to the formation of gallium vacancies and nitrogen-related defects of acceptor type in dilute nitrides but a complete description and explanation of background doping in InGaAsN layers should be investigated in further experiments. Nevertheless, in our InAs/GaAsN layers the background doping values are several times lower than those found for InGaAsN layers grown by MBE without Sb in the articles cited above (more than 1.0×10^{16} cm^{-3}). Low background doping of the *i*-layer is necessary for better

collection and transport of charge carriers in dilute nitrides with low lifetimes[34,96,136]. Consequently, the SDA InAs/GaAsN is preferable to InGaAsN compounds grown continuously by MBE. This might be due to the ionization of defect levels giving an additional contribution to the net doping, as discussed below.

As described above the admittance spectroscopy is based on the measurement of the capacitance and conductance of *p-n* or *p-i-n* junctions using a small signal alternating voltage at different frequencies and at various temperatures. If the Fermi level (or quasi Fermi level) crosses the defect level in the space charge region we may detect an additional contribution to the capacitance provided that $\omega\tau < 1$, τ the time response of the defect, sum of the capture and emission frequencies which are equal at the quasi Fermi level. Therefore, admittance spectroscopy can detect responses coming from the *i*-InAs/GaAsN layer, even if the layer is fully depleted, the high frequency/low temperature capacitance value being then determined by the *i*-layer thickness. The step position in *C(f)* and *C(T)*, or turn-on, is defined as $\omega_0\tau=1$ (Eq. (II.17)). The step in the capacitance is also accompanied by a maximum in the conductance, which is a simple way to clearly identify the turn-on angular frequency, ω_0. However, the maximum in the conductance is often hidden by the parasitic shunt conductance or the dc conductance related to the current flow across the junction that increases with temperature. This is why conductance values will not be presented here. The turn-on position can then be determined at a given temperature in a capacitance vs frequency plot, by the maximum of the capacitance derivative d*C*/d*f* or preferentially the maximum of the so-called differential capacitance d*C*/d(Ln[*f*]). The measured temperature (*T*) and frequency (*f*) dependences of the raw and differential capacitance are shown in Figure III.6 for zero bias voltage. The capacitance of the sample with the 1200 nm thick InGaAsN layer exhibits two steps (Figure III.6a) that are evidenced in the peaks of the differential capacitance $f \times dC/df$ (Figure III.6c). We can observe a first step on *C(f)* leading to a peak on $f \times dC/df$ at low temperatures 100-280 K and a second one at higher temperatures 320-360 K (series of steps are indicated by arrows). These steps can be caused either by interface states at InGaAsN/GaAs heterojunctions or by bulk defect levels in the *i*-layer. The *C(T,f)* curves were measured at different applied bias voltages (measurements are not shown here) and the step position in *C(f)* curves does not change: it indicates that the response originates from bulk defects rather than from the interface. Further increase in thickness of the InGaAsN layer up to 1600 nm leads to a drastic enlargement of the amplitude of the first step while the second step in *C(f)* curves remains the same (Figure III.6b).

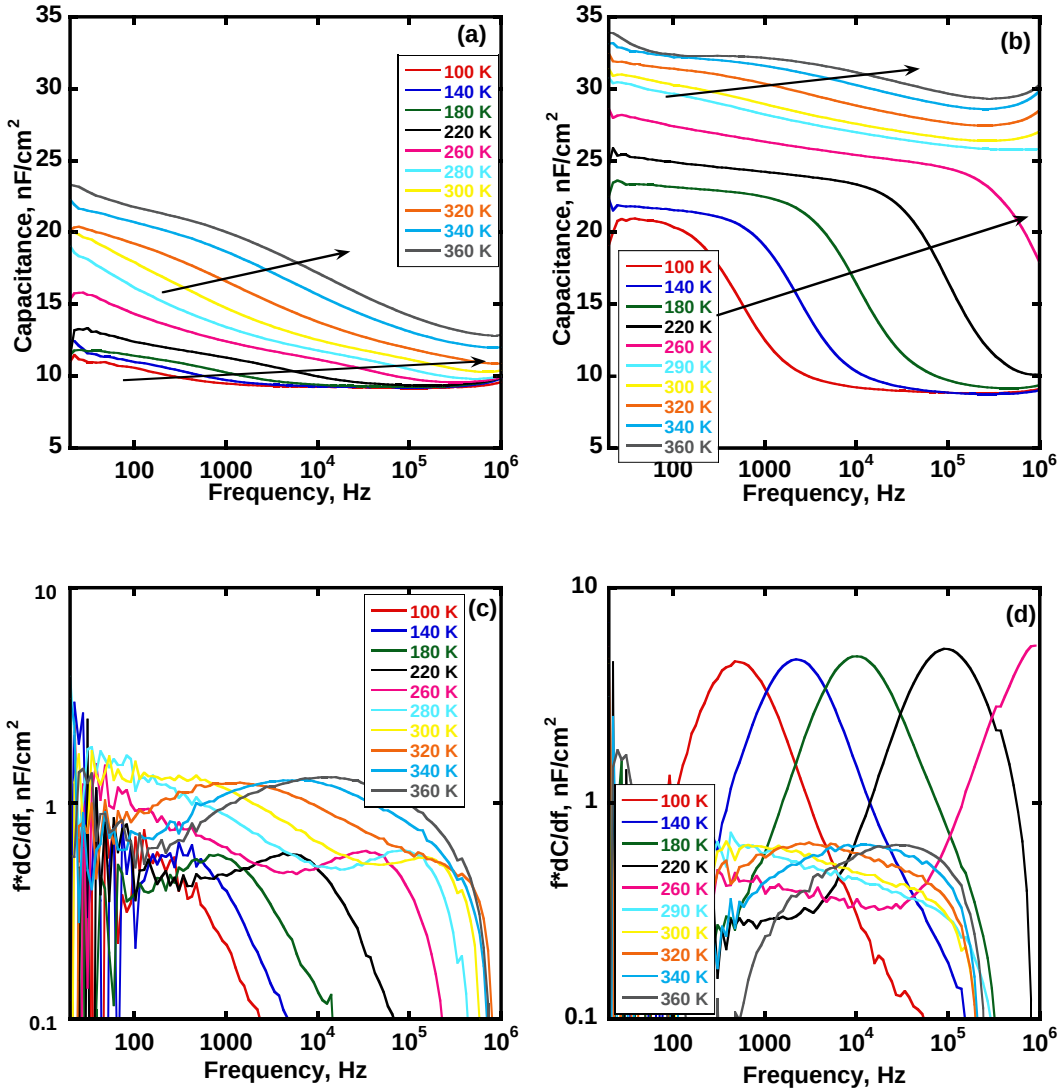

Figure III.6 Frequency dependent capacitance, C, (top) and differential capacitance, $f \times dC/df$, (bottom) at various temperatures, measured on from SC with InGaAsN active layers with thickness of 1200 nm (a, c), and 1600 nm (b, d).

Defect parameters, Ea and σ, in InAs/GaAsN were extracted from linear fit of f_0/T_0^2 in Arrhenius plots, where f_0 and T_0 being the characteristic turn-on frequency and temperature, respectively. Note that, while the error in the energy determination can be evaluated at ±0.05 eV, the error in the determination of σ is quite large due to the extraction procedure (a small change in the slope of the linear fit induces a strong change in σ). In addition, the values of thermal velocity and effective density of states in the band are not well known in these new III-V compounds, but they are calculated from effective mass of $m_e=0.1m_0$ and $m_h=0.47m_0$ for InGaAsN compounds. The characteristic Arrhenius plots for extraction of defect parameters in our samples are shown in Figure III.7.

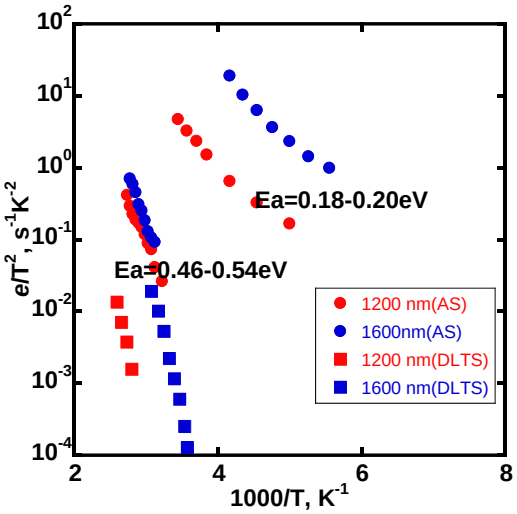

Figure III.7 Characteristic Arrhenius plots for extraction of defect parameters by AS (circles) and DLTS (squares) for the InAs/GaAsN samples with thickness of 1200 nm (red symbols) and 1600 nm (blue symbols).

For the sample with *i*-layer thickness of 1200 nm, the defect level revealed at low temperature has characteristic values E_a=0.20 eV and $\sigma=3\times10^{-17}$ cm^2, while the defect revealed at high temperature has parameters E_a=0.46 eV and $\sigma=1.4\times10^{-15}$ cm^2. The observed non-linear behavior of Arrhenius plot for 0.20 eV defect is explained by imperfect thermal contact with sample at low temperature so it produced differences between real temperature of sample and temperature of cryostat. However, it quickly decreases with heating and at high temperatures a linear behavior is observed. For the sample with a 1600 nm thick *i*-layer we find E_a=0.18 eV and $\sigma=1.4\times10^{-16}$ cm^2 for the low-temperature defect level, while for the high-temperature one we find E_a=0.54 eV and $\sigma=3.4\times10^{-14}$ cm^2. The defect parameters are presented in Table III.1. Taking into account the above mentioned uncertainties in the extracted defect parameter values we can conclude that the defects detected in both 1200 nm and 1600 nm thick samples are likely to be the same and constitute a characteristic feature of the *i*-InGaAsN layer based on the InAs/GaAsN SDA.

According to measured *C(T, f)* data we can conclude that layers of InGaAsN grown using InAs/GaAsN SDA do not exhibit any response from defects so their concentration is below the detection limit of the AS technique up to at least a thickness of 900 nm (not shown here). Further, when the thickness is increased to 1200 nm, conditions become more favorable for the formation of defects in InGaAsN but their concentration is still low, so it does not lead to a drastic change in the capacitance curves (Figure III.6a). However, the defect concentration drastically increases when the thickness is increased to 1600 nm, leading to huge changes in the capacitance-frequency curves (Figure III.6b). Such a behavior for defects in epitaxial multilayers which have small lattice

misfit with substrate was widely discussed[137,138]. It was shown that a misfit will be accommodated by uniform elastic strain until a critical film thickness is reached. Thereafter, it is energetically favorable for misfit to be shared between dislocations and strain. Thus we can propose that 900 nm thick layer is strained and has low defect concentration while increase of the layer thickness to 1200 nm leads to dislocations formation and therefore defect responses are detected.

In the following, we estimate the concentration of detected defects in samples with *i*-InGaAsN thickness of 1200 nm and 1600 nm. To this purpose, the method suggested by Walter was used[127]. It is based on the use of the capacitance derivative with respect to angular frequency. The density of states (DOS) can be reconstructed by this method for both *p-n* and *p-i-n* junctions. In Figure III.8 we present the DOS corresponding to the detected defects. The total defect concentration (N_T) was estimated for the *p-i-n* junction case from the integration of the DOS over the defect distribution around 0.18-0.20 eV. We found N_T=5×10^{14} cm^{-3} and N_T=3.5×10^{15} cm^{-3} for samples with *i*-InGaAsN 1200 nm and 1600 nm thick, respectively (Table III.1). These values are close to that of the effective doping concentrations estimated from *C-V* measurements at 300 K. Consequently, the observed shallow defects completely ionize at temperatures above 260 K introducing an additional charge that can explain the observed increase of the effective doping concentration at 300 K in the sample with the largest thickness. A peak in the DOS is also obtained around 0.50 eV, as shown in Figure III.8. The estimated defect concentration is slightly lower for sample with InGaAsN 1200 nm thick (8.4×10^{14}cm^{-3}) than with 1600 nm (1.3×10^{15}cm^{-3}) (Table III.1).

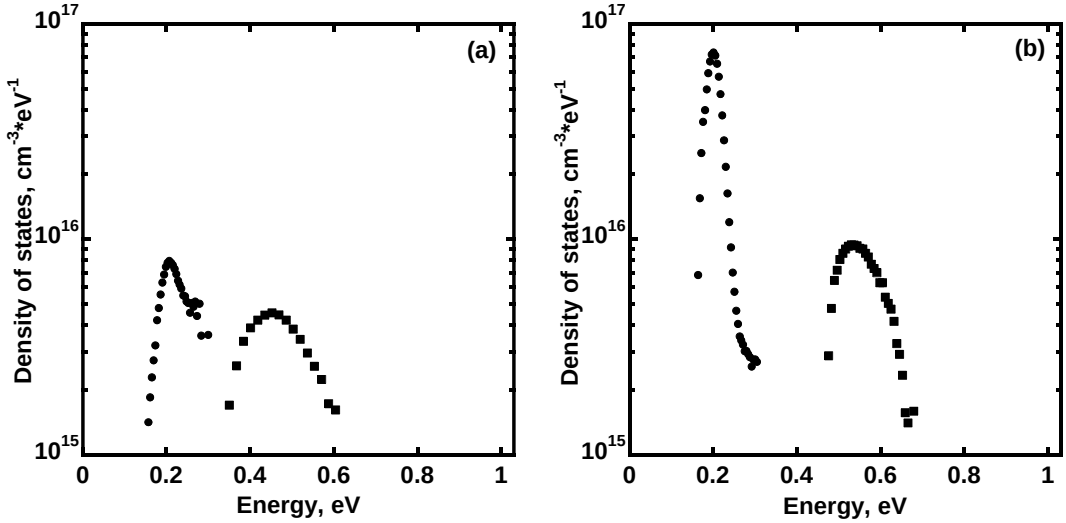

Figure III.8 Density of states in the energy bandgap for low (circles) and high (squares) temperature defects detected by admittance spectroscopy for 1200 nm (a) and 1600 nm (b) thick *i*-InGaAsN layers.

III.3.2 DLTS measurements

The samples were also explored by the DLTS technique with the following conditions: the amplitude of the reverse bias voltage was V_{rev}=-1V, the amplitude of the filling pulse was V_{pulse}=+1V (i.e., the voltage during the filling pulse was 0V), the filling pulse duration was t_{pulse}=40 ms. The DLTS spectra *S(T)* for different rate windows is shown in Figure III.9. No peaks are detected in the DLTS spectrum for the used temperature range in the 900 nm thick InGaAsN sample (Figure III.9a). On the other hand, peaks of the capacitance are observed for the 1200 nm thick sample at temperatures above 360 K and high emission rates (Figure III.9b). The position of the peaks shifts toward higher temperatures when the rate window is increased, but their amplitude also substantially increases and their shape is quite broad. A series of broad peaks with a much larger amplitude is observed in the 1600 nm thick sample at temperatures 280-360 K. Such broad peaks are usually assigned to extended defects such as dislocations rather than to point defects[139].

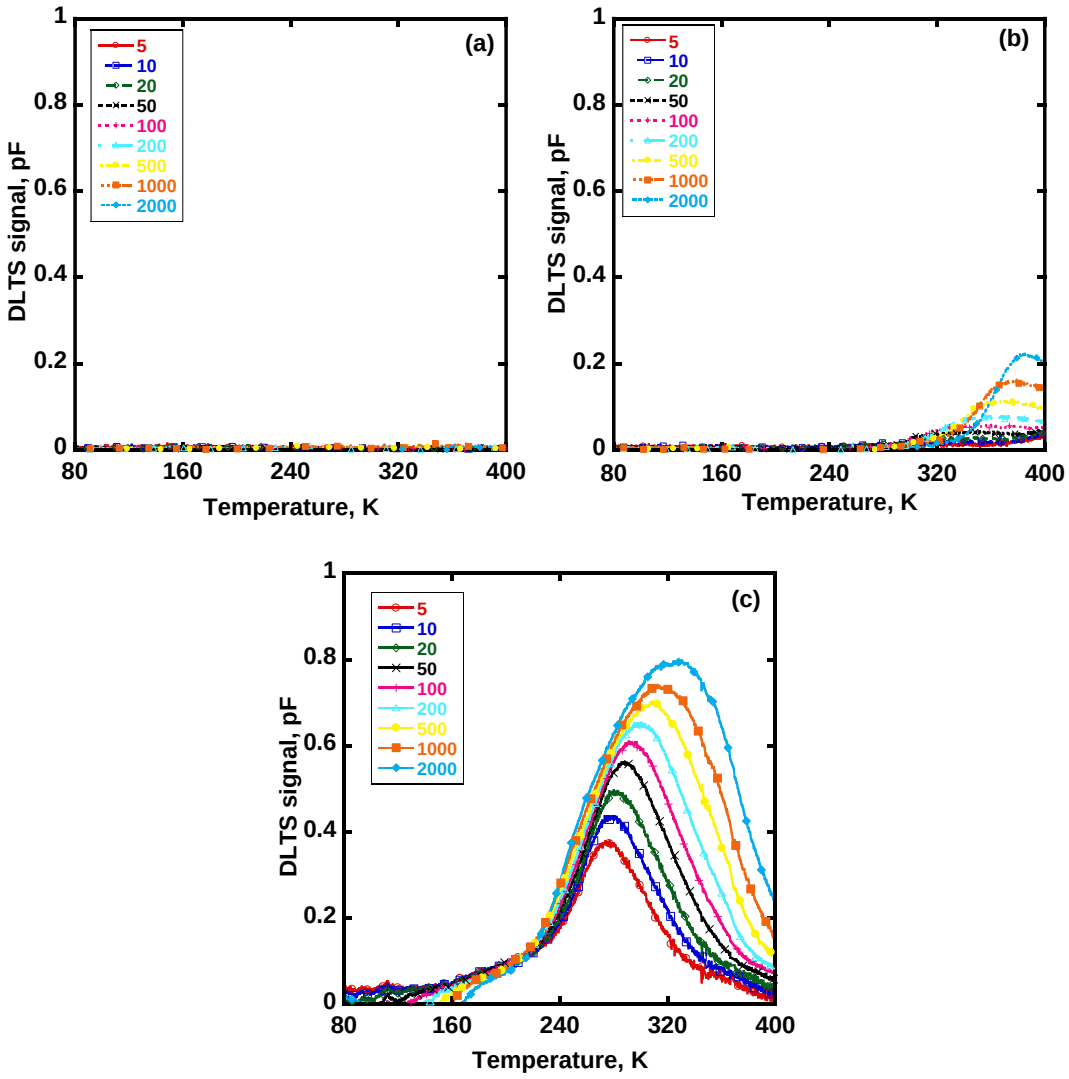

Figure III.9 DLTS spectra S(T) on solar cell structures made of active layers of InAs/GaAsN with thickness of 900 nm (a), 1200 nm (b) and 1600 nm (c) for different rate windows (in s^{-1}).

The Arrhenius plots of defects obtained from the DLTS spectra are shown in Figure III.7 in order to compare with the AS data. The defect parameters extracted from both techniques are presented in Table III.1. The important difference in AS and DLTS measurements is the different used range of emission rates, because the DLTS setup with Boonton-7200 allows to accurately measure capacitance transients with relatively low emission rates, e<2000 s^{-1}, unlike AS that can better reveal higher emission rates. From DLTS measurement, we found an activation energy around E_a~0.8 eV and a cross section around $\sigma \sim 10^{-15}$ cm^2 for defect state. We could relate this defect state to that deep-defect one measured using AS. However, the difference between the values of E_a measured by the two techniques (~0.8 eV *vs* ~0.5 eV using DLTS and AS respectively) is large and remains unclear. Using DLTS, such a high activation energy had already been detected in similar materials[140,141], but no explanation about the large E_a value (larger than half of the bandgap) was given. Further research should be done to resolve why the activation energy evaluated from DLTS is much higher than midgap. It is an unexpected and unusual result which forces to consider DLTS data carefully and with a critical view. Admittance spectroscopy is likely to be more suitable to extract defect parameters in our layers where doping is low, unintentional, and related to shallow defects. Indeed, in DLTS the dopant concentration should be higher than the deep defect concentration for correct interpretation of the data. This may explain the discrepancy between the defect parameters extracted from AS and DLTS, along with the unexpected large activation energies from DLTS.

Thickness, nm	E_a, eV	σ, cm^2	N_T, cm^{-3}	Method
1200	0.20	3.0×10^{-17}	5.0×10^{14}	AS
	0.46	1.4×10^{-15}	8.4×10^{14}	AS
	0.82	4.5×10^{-13}	n/e	DLTS
1600	0.18	1.4×10^{-16}	3.5×10^{15}	AS
	0.54	3.4×10^{-14}	1.3×10^{15}	AS
	0.78	1.9×10^{-11}	1.0×10^{15}	DLTS

Table III.1 Parameters of defects detected in *i*-InAs/GaAsN samples.

The absence of responses from the low-temperature level on the DLTS spectra can be explained by the principle of DLTS measurement in case of fully depleted *i*-InAs/GaAsN in *p*-*i*-*n* junctions at low temperature for all samples. In this case, when the applied voltage returns at reverse value following the filling pulse, the space charge region must extend in adjacent layers in the structure. But the cover layer of *p*- and *n*-GaAs have very high doping concentration (1×10^{19}

cm^{-3} and 3×10^{18} cm^{-3}) so the DLTS signal should be low because although it is proportional to the defect density, it is also inversely proportional to the doping density at the edge of the space charge layer[30]. This may also explain the absence of high temperature response in the sample with 1200 nm thick *i*-InGaAsN layer in DLTS spectra. However, the sample with 1600 nm thick InGaAsN rather behaves as a p-n junction at temperatures above 240 K due to additional ionization of shallow defects. Nevertheless, the low activation energy of this defect (E_a=0.20 eV) does not allow considering it as an effective center of non-radiative recombination that could be responsible for low lifetimes in the layers of dilute nitrides InAs/GaAsN (see below).

On the contrary, defects detected at high temperature (E_a=0.45-0.55 eV) are close to the middle of the bandgap of the InGaAsN (E_g=1.03 eV) and have large capture cross sections so they can have strong influence on the charge carriers lifetimes in active layers of SC. Defects with similar parameters were previously observed in many works[29,140,142,143]. Broad DLTS peaks in Figure III.9c mean non-exponential response compared to the classical case of DLTS spectra for a point defect, so the interpretation of data should be considered more carefully. Broad shape and increasing amplitude of peaks can be due to different causes: local fluctuations in the composition of the compounds[144], overlap of responses from several discrete defect levels with small separation in energy, defects having an energy density of states (e. g. Gaussian distribution, extended defects with unknown energy distribution), dislocations etc. In the work[139] the convenient method was proposed for analyzing such responses from extended defects (not point defect with discrete energy level) that exist with localized and band-like states. For the InGaAsN alloys grown by MBE with a RF-plasma source of nitrogen the analysis shows logarithmic enlargement of the peak amplitude without any temperature shift when the duration of filling pulse is increased until up to 10 ms for the same rate window: such a behavior is typical for localized states[29]. However, saturation occurs at t_{pulse} larger than 10 ms and the peak amplitude remains constant like in case of a point defect. Probably, in the case of dilute nitrides, a strong fluctuation in composition occurs due to non-equilibrium growth conditions and the tendency of nitrogen clusterization leads to the transformation of point defects into extended ones with some energy distribution.

III.4 Structural properties

Further correlation to previous measurements supporting the increase of defects with increasing thickness is provided by X-ray diffraction measurements (Figure III.10). The main peak is related to the response from the GaAs wafer, and the peak at slightly smaller angle is attributed to the InGaAsN layer. This indicates that InGaAsN is under compressive stress and exhibits a slightly larger average lattice constant than GaAs. We observe that the shift of the peak is increased

with the thickness, especially for the 1600 nm thick layer, where it becomes strongly broadened, indicating partial relaxation and formation of defects and dislocations. Formation of dislocations and other defects are known to occur in thick strained layers when it exceeds the critical thickness in heteroepitaxial growth[145,146].

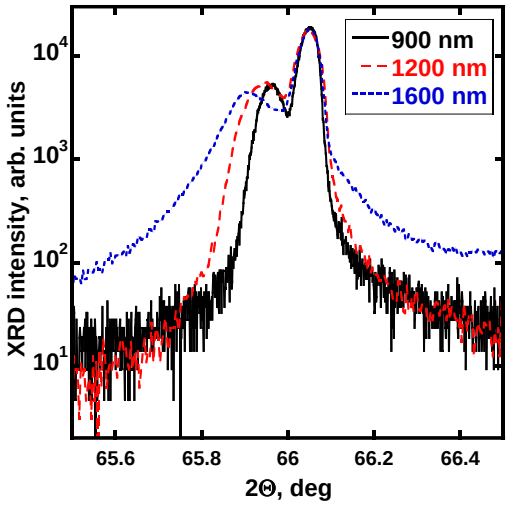

Figure III.10 X-ray-diffraction rocking curves of the 900 nm, 1200 nm and 1600 nm thick InGaAsN samples.

III.5 Simulation of external quantum efficiency

As shown above the external quantum efficiency of the solar cell with an active layer of InGaAsN drastically drops when the layer thickness increases from 1200 nm to 1600 nm (Figure III.3a). It occurs when photogenerated electron-hole pairs cannot effectively reach the highly doped GaAs layers and recombine in the InGaAsN active one. In principle, in a p^+-i-n^+ structure the built-in electric field in the active i-layer improves the separation and collection of charge carriers and reduces recombination in the active region of the solar cell. However, the presence of a background doping and of charged defects which were revealed in our layers from the capacitance measurements tends to replace the p^+-i-n^+ structure by either a p^+-n-n^+ or a p^+-p-n^+ structure. In the first case, the p-n junction is the top p^+-GaAs/n-InGaAsN junction while in the second case it is the bottom p-InGaAsN/n^+-GaAs junction. In order to investigate these two possibilities, we performed numerical simulations using AFORS-HET 2.5. To simulate either the n-InGaAsN case or the p-InGaAsN case, we introduce either a donor type defect at 0.18 eV below the conduction band or an acceptor type defect at 0.18 eV above the valence band (as detected from admittance spectroscopy) with a concentration of 5×10^{15} cm^{-3} (that was obtained from the C-V analysis at 300 K of the 1600 nm thick InGaAsN sample). Simulated band diagrams for n- and

p-InGaAsN are presented in Figure III.11a and Figure III.11b, respectively. Also, the EQE curves were calculated taking into account the reflection losses that were measured on solar cells (Figure III.3b). We introduced a bulk defect level located at 0.5 eV below the conduction band in *n*-InGaAsN (above the valence band edge in *p*-InGaAsN), with capture cross sections of electrons and holes equal to 2×10^{-13} cm^2 and 2×10^{-14} cm^2, respectively. As noted above, m_e in InGaAsN is in 5-10 times lower than m_h so electron σ should be in 5-10 times higher than hole σ for the same value of pre-exponential factor estimated from Arrhenius plot. The defect concentration was varied for both cases (Figure III.11c and Figure III.11d, respectively). In the first case, the separation of charge carriers generated at short wavelength will occur more efficiently, since the regions of high built-in electric field and high absorption (close to the front surface) coincide. In the second case, these regions are spatially separated. As a consequence, the EQE is more affected in the second case due to enhanced recombination of electron-hole pairs and the shape of the EQE curve is different. The big drop in EQE observed in the 1600 nm-InGaAsN sample is more pronounced at short wavelength, where light is absorbed in a narrow depth close to the p^+-GaAs/*i*-InGaAsN interface. This behavior is well reproduced in the simulation if the InGaAsN layer is of *p*-type. This suggests that the InGaAsN layer has a *p*-type background doping and that the *p*-*n* junction is located at the bottom side. Therefore, all detected defects from AS and DLTS are traps for holes because they are majority-carrier traps in *p*-InGaAsN. Another consequence is that the defects in the 1600 nm thick sample were detected at the bottom side of InGaAsN, indicating that increasing the thickness from 900 nm to 1600 nm has not produced defects only in the upper part of the layer, but the defects are likely to be distributed all over the thickness.

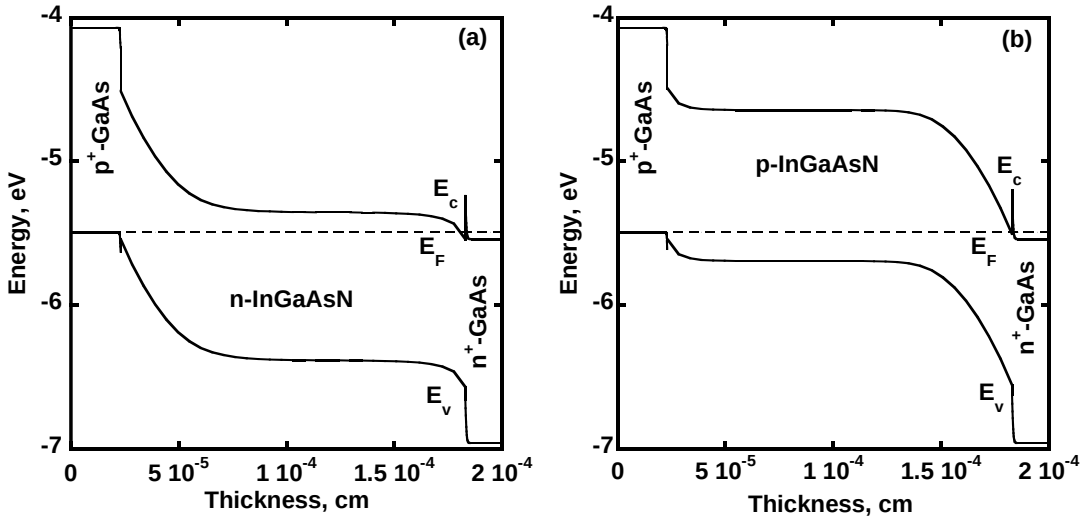

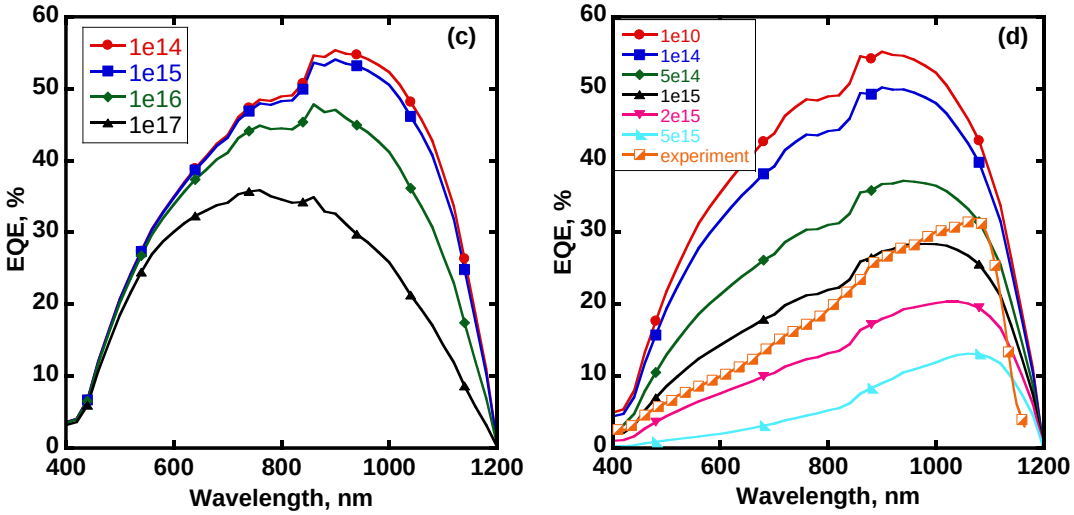

Figure III.11 Band diagram of modeled p^+-GaAs/n-InGaAsN/n^+-GaAs (a) and p^+-GaAs/p-InGaAsN/n^+-GaAs (b) structures with 1600 nm thick InGaAsN layer, and corresponding external quantum efficiency for various deep defect concentrations ((c) and (d)). The experimental curve is also shown in (d).

Taking now the InGaAsN layer to be *p*-type, we also simulated the EQE curve for various deep defect concentrations for 900 nm and 1200 nm thick samples (Figure III.12). An increase in the thickness of the InGaAsN layer from 900 nm to 1200 nm leads to only very small changes in the EQE curve: a small increase in the long-wavelength range because of enhanced absorption. The increase of the defect concentration up to 0.5×10^{15} cm^{-3} induces a small decrease of EQE because the electric field is strong enough in the InGaAsN layer to separate the carrier and to allow them to be collected before they recombine. On the contrary, for the 1600 nm thick InGaAsN layer the EQE curve exhibits the drastic decrease at short wavelength and the same shape as observed experimentally when the defect concentration is above 0.5×10^{15} cm^{-3}. Therefore, the concentration of $(0.5\text{-}2.0)\times10^{15}$ cm^{-3} estimated from AS and DLTS allows to achieve good qualitative and quantitative correlation between experiments and simulations.

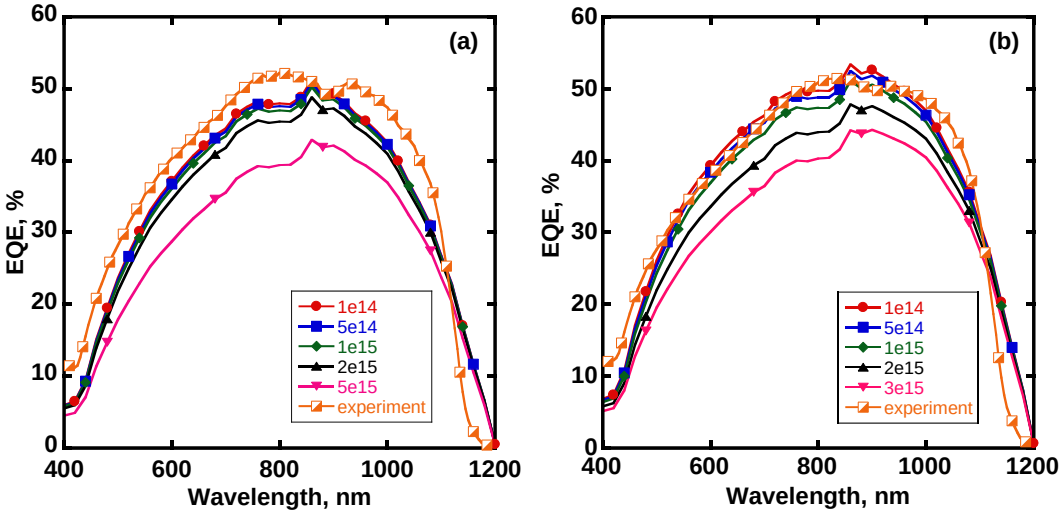

Figure III.12 Measured and simulated external quantum efficiency curves of the *p-i-n* structures with InGaAsN 900 nm (a) and 1200 nm (b) thick for various deep defect concentrations.

Consequently, the relation was demonstrated between the thickness of *i*-InGaAsN active layer grown by MBE in the form of SDA InAs/GaAsN in solar cells and their photoelectric and internal properties. An increase in the thickness of the active layer leads to formation of defects that are centers of non-radiative recombination, responsible for a strong drop in EQE in the short-wavelength region.

Summary

In Chapter III, sub-monolayer digital alloys of InAs/GaAsN were grown on GaAs wafers by molecular-beam epitaxy for application in single-junction solar cells with undoped active layer of InGaAsN with bandgap closed to 1 eV. The influence of its thickness on their photoelectric and internal properties was explored by different techniques. According to experimental data and simulation following conclusion were declared:

- Technology of SDA InAs/GaAsN allows to grow intrinsic 900 nm thick InGaAsN with low free carriers concentration at room temperature without Sb (less 1×10^{15} cm^{-3}). Also, deep defects were not observed for this sample.
- Increasing of its thickness up to 1200 nm leads to formation of majority carriers traps with energy activation of 0.20 eV (5×10^{14} cm^{-3}) and 0.50 eV (8×10^{14} cm^{-3}). So background doping concentration remains low at room temperature and deep levels do not have significantly effect on photoelectric properties
- Further layer thickening, up to 1600 nm, leads to significant increase of 0.20 eV-level concentration to 5×10^{15} cm^{-3}. InAs/GaAsN becomes *p*-type doped at room

temperature due to their ionization and band diagram of *p*-GaAs/*i*-InGaAsN/*n*-GaAs changes.

- Observed defects with E_a=0.50 eV are non-radiative recombination centers leading to extreme drop of external quantum efficiency in the InAs/GaAsN sample of 1600 nm thickness.

Chapter IV

InGaPAsN

Introduction

In this Chapter, single-junction SCs grown on GaP wafers and MJSCs grown on Si wafers with active layers of InGaPAsN are explored. The parameters of SCs are presented in Table IV.1.

Photoelectric and electric properties are investigated at different conditions. Further, different capacitance methods (AS, DLTS, C-V) are performed for the characterization of defect and doping properties. The main problem of these studies was the absence of post-growth processing of grown structures in the initial steps of our work. This is why we have developed different methods of contact formation and etching for our structures that are described in Appendix.

Type of SC	#Sample	Wafer	Active junction in bottom subcell of MJSC	Active layer in single-junction SC/ top subcell of MJSC	Active layer thickness, nm	Front layer
Single	1	*n*-GaP	-	*n*-GaPAsN	1000	*p*-GaP
	2	*n*-GaP	-	*i*-GaPAsN	300	*p*-GaP
	3	*n*-GaP	-	*i*-GaPAsN	300	*p*-GaP
	4	*n*-GaP	-	*i*-InP/GaPN	350	*p*-GaP
Double	5	*p*-Si	*p*-Si/n^+-Si	*i*-GaPAs	400	*n*-GaPAs
	6	*p*-Si	*p*-Si/n^+-Si	*i*-InP/GaPN	200	*n*-GaP
	7	*p*-Si	*p*-Si/n^+-Si	*i*-GaPAsN	200	*n*-GaP
Triple	8	*p*-Si	*p*-Si/n^+-Si	*i*-GaPNAs *i*-GaPN	200 150	*n*-GaP

Table IV.1 Parameters of SCs grown on GaP and Si wafers.

IV.1Single-junction grown on GaP wafers

IV.1.1Samples description

Studies of SC based on dilute nitrides, InGaPAsN, have started from single-junction SCs grown on *n*-type GaP wafers. The first one is a structure with an active layer of *n*-type 1000 nm thick $GaP_{0.832}As_{0.15}N_{0.018}$, and with a 100 nm thick highly doped *p*-type GaP front contact layer, so the SC is based on a *p*-*n* junction where *p*-GaP is the emitter/wide bandgap window and *n*-GaPAsN is the photoactive base layer (sample #1, Figure IV.1a). Here, *n*-GaPAsN has the same composition over the layer thickness. The second SC is based on a *p*–*i*–*n* structure with an undoped 300 nm thick GaPNAs layer confined between two symmetric *p*- and *n*-type GaPAsN layers, and also with a 100 nm thick front *p*-GaP layer as a wide bandgap window (sample #2, Figure IV.1b). The third SC has the same layers as in the second structure but it was treated in another post-growth processing in MBE-chamber including growth of additional cover layer of a 80 nm thick p^+-GaP (sample #3, Figure IV.1c). In these two samples the arsenic content varies in the range 15-30% in quaternary GaPAsN alloy for better nitrogen incorporation. The fourth sample is also a *p*–*i*–*n* structure with 350 nm thick undoped InP/GaPN (0.3 nm/10 nm) SDA confined between *p*- and *n*-type GaPN layers, and with a 100 nm thick front *p*-GaP layer as a wide bandgap (sample #4, Figure IV.1d).

Before description of the experimental studies it is necessary to observe qualitative differences in the band diagrams for SCs based on single *p*-*n* (sample #1, Figure IV.2a) and *p*-*i*-*n* (sample #3, Figure IV.2b) junctions in the equilibrium conditions. Qualitative behavior of all *p*-*i*-*n* structures investigated in the work is almost the same so any of them can be compared with sample #1. The main difference lies in the separation and collection of generated charge carriers in the SC base. In case of the *p*-*i*-*n* structure, absorbed photons generate electron-holes pairs which are effectively separated by the electric field acting on the entire thickness of the undoped layer. Its configuration is usually used when lifetime of charge carriers is low. For *p*-*n* structure, the electric field takes place only in the SCR, the carriers moving by diffusion outside the region. Thus, if the quality of the material is poor and its thickness exceeds the value of diffusion length, l_{diff}, charge carriers can recombine in the thick doped layer and do not reach highly doped regions, so carrier collection becomes ineffective. For investigated *p*-*n* junctions value of l_{diff} should of the order of 1 μm or more for high performance of SC. According to the literature, the quality of dilute nitrides lattice-matched to GaP is very poor so rather poor photoelectric properties of sample #1 are expected.

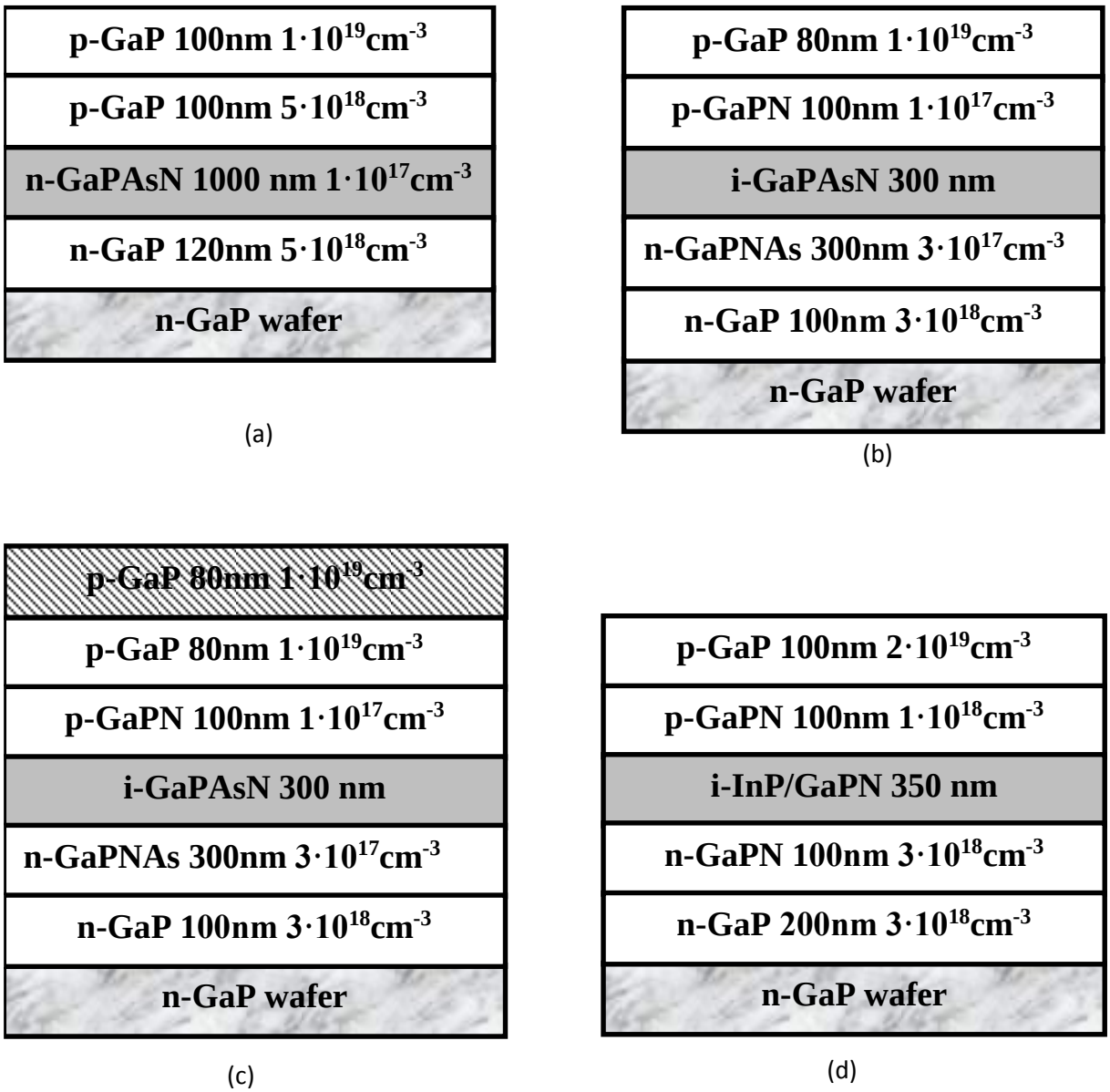

Figure IV.1 Schematic view of single-junction solar cells grown on *n*-GaP wafers: sample #1 (a), sample #2 (b), sample #3 (c), sample #4 (d).

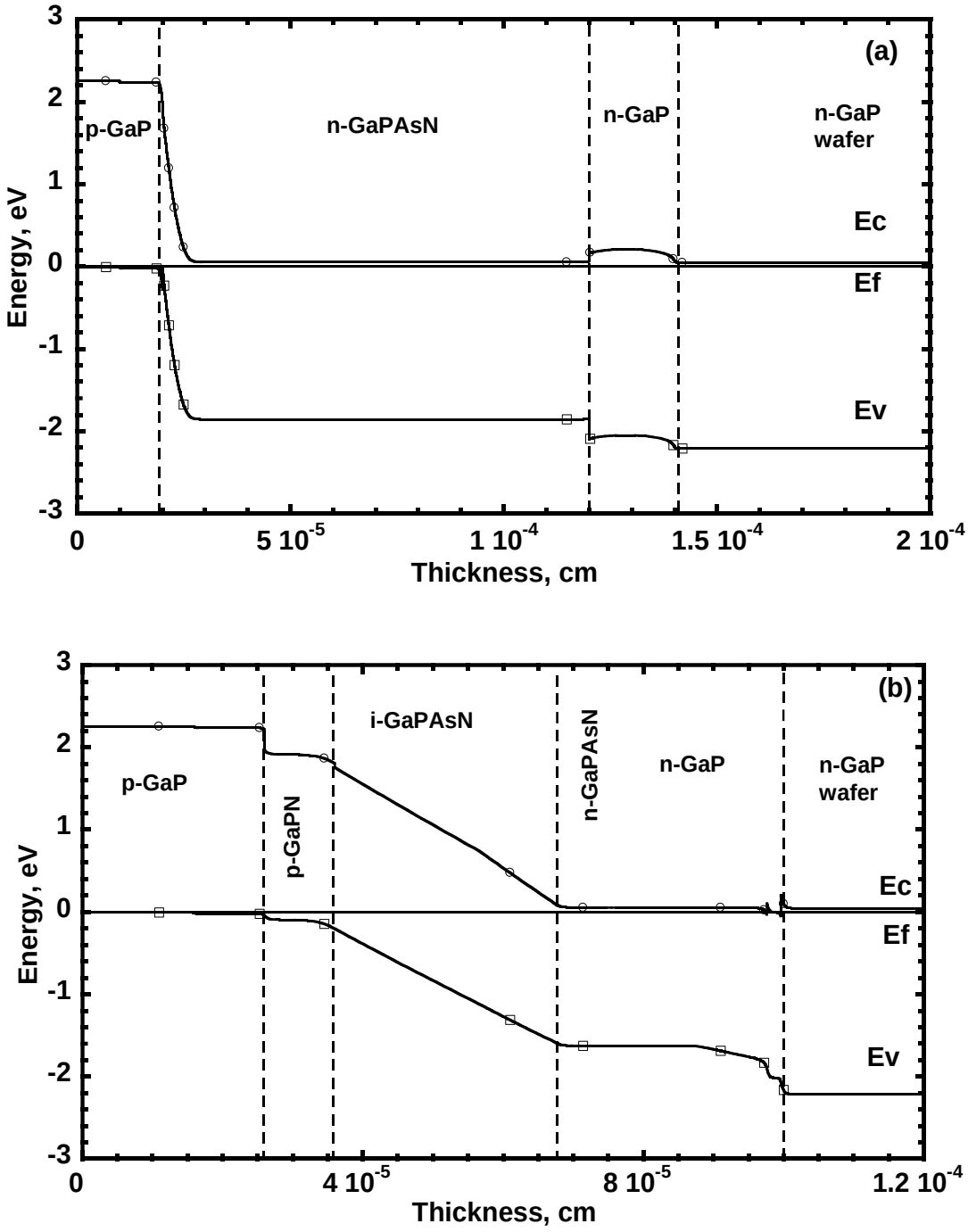

Figure IV.2 Band diagram of SC with single *p-n* (a) and *p-i-n* (b) junctions.

For further electrical and capacitance measurements ohmic contacts were fabricated to the top and the bottom sides of samples. The detailed description of this technology is presented in Appendix A.

IV.1.2 Quantum efficiency and current-voltage measurements of single-junction solar cells

Unfortunately, there are many differences in our single-junction SCs, but it is possible to designate the most important factors acting on their photoelectrical properties. Usually, the quality of active layers has the strongest influence on their performance. In our case, there are three samples with an active GaPAsN layer: one with *n*-type doped base and two with an undoped base, so the influence of the doping level can be defined. Secondly, the fourth sample has an undoped layer of GaPN/InP with almost the same thickness so it is possible to study the influence of layer composition on photoelectric properties of the SC. Furthermore, both *p-i-n* structures with undoped GaPAsN differ from each other only by the post-growth processing in MBE-chamber including growth of additional cover layer of p^+-GaP 80 nm thick. Figure IV.3a shows the current-voltage characteristics of all structures measured under AM1.5G illumination.

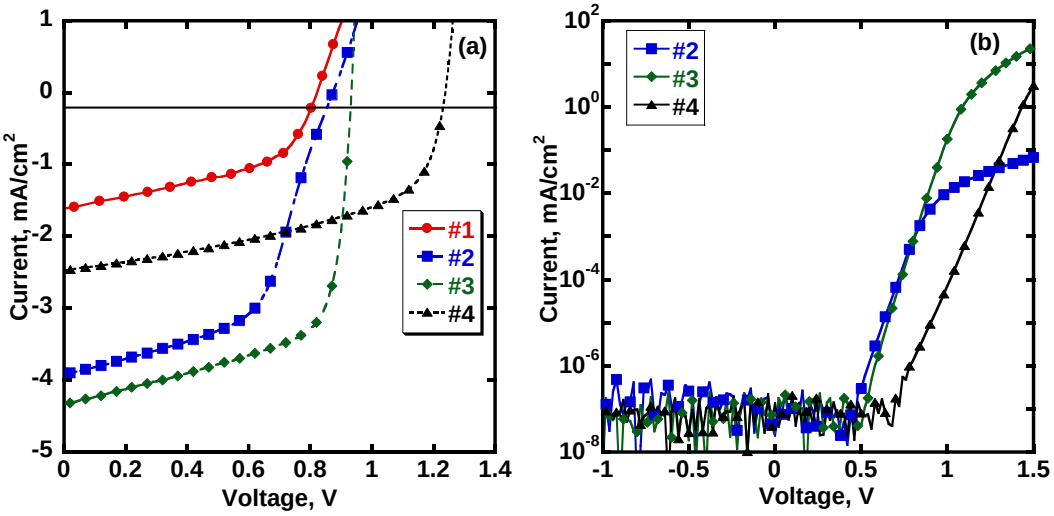

Figure IV.3 Current- voltage characteristic of solar cells under AM1.5G (a) and of mesa-structures in the dark (b), 25°C.

Sample	*layer*	V_{OC}, *V*	J_{SC}, mA/cm^2	*FF*, %	η, %	*n*	R_s, $\Omega \cdot cm^2$	R_{sh}, $\Omega \cdot cm^2$
#1	*n*-GaPNAs	0.82	1.61	48	0.63	n/e	n/e	n/e
#2	*i*-GaPNAs	0.87	3.93	54	1.84	1.46	n/e	n/e
#3	*i*-GaPNAs	0.93	4.34	65	2.60	1.37	0.70	915
#4	*i*-InP/GaPN	1.24	2.47	52	1.59	1.86	n/e (low)	1358

Table IV.2 Parameters of solar cells performance on GaP (n/e - not estimated).

Small values of the filling factor for these I–V curves are explained primarily by large ohmic losses related to imperfect upper contact grid. The sample #1 with a *p–n* junction is characterized by poorer performance (especially, extremely low short-circuit current) than SCs with a *p-i-n* junction. This fact is indicative of a more effective collection of generated charge carriers in the short-circuit regime in the case a *p–i–n* structure, which can be related to the presence of a pulling electric field in the undoped GaPAsN layer. Despite the fact that E_g of *i*-GaPAsN (1.7 eV) is smaller than *n*-GaPAsN (1.9 eV), V_{OC} is also higher for sample #2 (0.87 V) than in sample #1 (0.82 V). Change in post-growth treatment process leads to significant improvement of the I-V curve for *p-i-n* sample #3. First of all, the fill factor has much higher value 65% compared to 54% for sample #2. Possibly, it comes from the additional contact layer of p^+-GaP grown after annealing in MBE-chamber since it improves the GaP/metal contact. Short-circuit current also increases and reaches a value of 4.34 mA/cm^2 in sample #3. Sample #4 shows the highest open-circuit voltage of 1.24 V for single-junction SCs grown on GaP wafer due to high bandgap energy of 2.03 eV. However, its short-circuit current is lower than the value in the sample with *i*-GaPAsN and higher than in *n*-GaPAsN. Consequently, using an undoped layer of GaPAsN is much more preferable than using *n*-type layer for photovoltaic applications[136]. For this reason, we are mostly focusing in the detailed study of I-V curves for *p-i-n* structures.

I-V curves in the dark are presented in Figure IV.3b for samples #2-#4 with active *i*-layer. First, the reverse current is low for all mesa-structures so it will be possible to apply capacitance methods for deeper investigations. All *p-i-n* samples show exponential dependence of the current on the forward applied voltage (straight line in logarithmic scale). However, it exhibits clear that the slope of sample #4 is the smallest incline and slope of sample #3 is slightly sharper than in sample #2. It means differences in value of ideality factor *n* in *p-i-n* junctions thus it was estimated for each sample from classical equation for dark I-V dependence: n_2=1.46, n_3=1.37 and n_4=1.86. Value of ideality factor describes what is determining for the transport mechanism in junction: diffusion (*n*=1) or recombination (*n*=2). For ideal *p-n* junctions without any recombination in the SCR transport is defined only by diffusion. When the defect concentration increases, charge carriers start to recombine in SCR and the recombination current also grows. According to Shockley-Read-Hall theory if the defect level is placed in the middle of the bandgap the ideality factor is equal of 2. In practice, transport is defined by both mechanisms so *n* takes values from 1 to 2 like in the considered samples. Therefore, the first conclusion is the existence of recombination issues in *p-i-n* junctions based on dilute nitrides InGaPAsN. Then, the ideality factor of sample #4 with *i*-InP/GaPN layer is much closer to 2 than in samples #2 and #3 with GaPAsN. It means higher recombination influence on carriers transport in InP/GaPN thus the defect concentration should be higher in this layer. The deviation from exponential voltage dependence at high current

for samples #2 and #3 is caused by a series resistance which value is higher for sample #2. It comes from a better quality of the cover contact *p*-GaP layer in sample #3 due to a change of post-growth processing in the MBE-chamber.

The current-voltage characteristics of an ideal SC is described by equation (II.2), where the photocurrent is subtracted from the dark current of the ideal diode. However, the performance of real SC is affected by resistive effects reducing the efficiency by dissipating power in the resistances. The most common parasitic resistances are series R_s and shunt R_{sh} resistances. The SC circuit including resistances is shown in Figure IV.4.

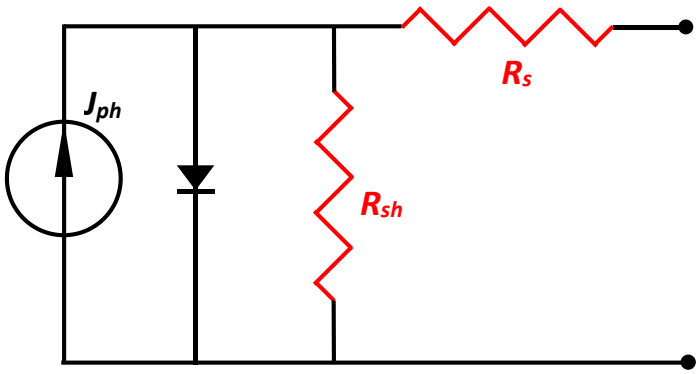

Figure IV.4 Parasitic series and shunt resistances in a solar cell circuit.

Series resistance in SCs has three causes: the transport of charge carriers through the emitter and base of the SC, the contact resistance on the metal/semiconductor interface, and the resistance of metal contact to the top and bottom sides of SCs. Series resistance leads to deterioration of fill factor since the slope of the I-V curve becomes less steep in the region near to open-circuit voltage. The low shunt resistance causes power losses in solar cells by providing an alternate path for the current. It reduces the amount of current flowing through the SC junction and the voltage across SC. The effect of a shunt resistance is strongly observed at low light levels, and at low voltages where the equivalent resistance of the junction is high. Shunt resistance appears due to poor manufacturing process rather than SC design. It leads to deterioration of fill factor: horizontal line of I-V curve for ideal SC in the short-circuit region starts to tilt and reduces *FF*. Consequently, the realistic parameter of ideality factor and resistances of SC can be estimated by the equation:

$$J = J_S\left[\exp\left(\frac{q(V - JR_s)}{nk_BT}\right) - 1\right] - J_{ph} + \frac{V - JR_s}{R_{sh}} \qquad \text{(IV.1)}$$

For sample #2 the deviation from the conventional behavior is observed close to the open-circuit voltage regime (Figure IV.3a). The bending of the curve can be due to high series resistance caused by low quality of contact layers and the metal/GaP interface. It is also confirmed by analysis of dark I-V curve of sample #2 (Figure IV.3b) where it changes its behavior from exponential (diode) to linear (resistance) at lower voltage and the value of series resistance is higher (slope of I-V curve in linear scale) than for sample #3. The reason of such a behavior is the difference in post-growth treatment in the MBE-chamber. In this case, it is difficult to estimate a precise value of R_{sh} and R_s in sample #2. But it was successfully done for samples #3 and #4: parameters are shown in Table IV.2.

In result, some points can be concluded from the data. Series resistance is lower for SC with InP/GaPN but the fill factor is larger for *p-i-n* SC with GaPAsN. The ideality factor of SC with InP/GaPN is higher (and much closer to 2) than with GaPAsN layers. It leads to lower short-circuit current and lower efficiency even with higher open circuit-voltage in sample #4. Furthermore, the dependence of open-circuit voltage on temperature was measured for samples #3 and #4 (Figure IV.5). $V_{OC}(T)$ behavior is similar for both samples and it decreases with increasing temperature with a coefficient of 2mV/K.

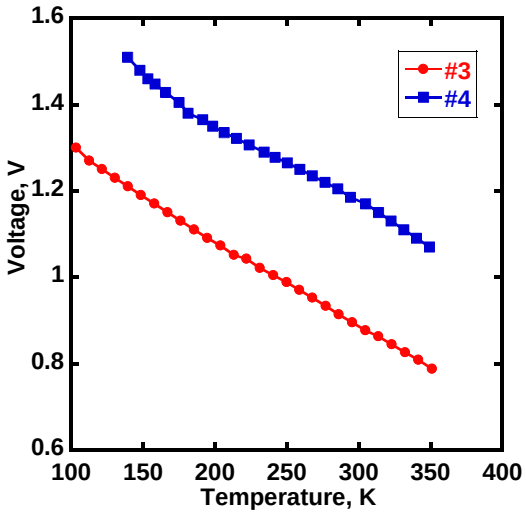

Figure IV.5 Temperature dependence of open-circuit voltage in two SCs.

The external quantum efficiency was also measured for structures #1-#4 (Figure IV.6). For all samples, it is possible to distinguish two peaks in the EQE curve. This can be explained by the peculiar structure of the conduction band in InGaPAsN dilute nitrides where two conduction subbands may exist. The detailed investigation of this phenomenon is addressed in Appendix B. Let us focus here on the comparison of the EQE curves of the four samples.

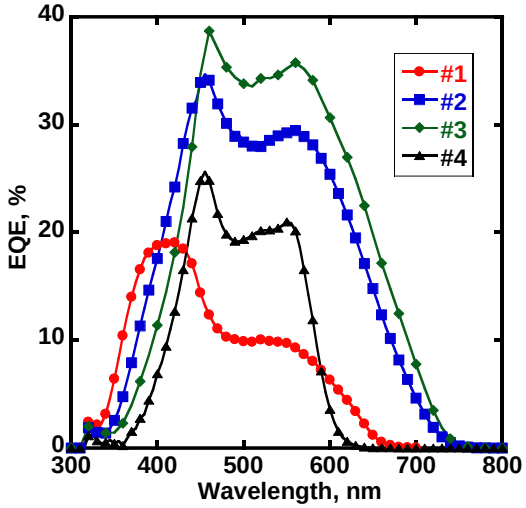

Figure IV.6 External quantum efficiency of single-junction SCs grown on *n*-GaP wafer.

The value of EQE is much larger for sample #2 with the *p*-*i*-*n* structure based on GaPAsN than in sample #1 based on the *p*-*n* junction. It means a more efficient collection of generated charge carriers in the short-circuit regime for the *p*–*i*–*n* structure. As can be seen, the *p*–*i*–*n* structure exhibits a higher EQE with respect to both the peak (35%) and the integral (area under curve) values as compared to those of the *p*–*n* structure which is in agreement with larger value of J_{SC} (Table IV.2). In addition, the quantum efficiency significantly increases in the long wavelength region, which is related to lower recombination losses in the undoped layer. These differences may be due to larger lifetimes of carriers in the undoped layer of the GaPAsN quaternary alloy as compared to that in doped layers. It should be noted that the studied structures are not provided with antireflection coatings. However, even with allowance for the reflection losses (in the range of 20-40%), the values of quantum efficiency obtained in the *p*–*i*–*n* structure are yet insufficient for its effective operation in the top junction of MJSC. In order to further improve the efficiency, it is necessary to increase the thickness and, hence, the level of absorption in the undoped region.

Comparing now with sample #2, we first remember that sample #4 with undoped layer of SDA InP/GaPN was grown for comparison of two fabrication methods for improvement of the photoelectric quality of GaPN. Introducing nitrogen leads to lattice-mismatch with the GaP wafer as described before and elastic stresses increase. The SDA method had been shown to be able to provide stress compensation by adding one monolayer of InAs in GaAsN grown on GaAs wafers. Consequently, this growth procedure can be applied for compensating stresses between GaP and GaPN by adding some monolayers of InP. According to the spectral response, sample #2 with GaPAsN layer has higher peak and integral EQE values than sample #4 with InP/GaPN (the same tendency was observed for J_{SC} above). It means lower lifetime charge carriers in the InP/GaPN material than in GaPAsN due to the existence of higher defect concentration as suggested from the

ideality factor in InP/GaPN close to 2. It confirms conclusion suggested by other authors[80] about better compensation of elastic stresses by arsenic than by indium. Nitrogen is a V-group element so it tries to take place in the sublattice of V-group atoms in the GaP lattice (phosphorus sites). Arsenic is also a V-group element so it also stands in phosphorus sites and it leads to more effective stress compensation than indium incorporation since the latter is a III-group element. We also observe that the shape of quantum efficiency has a more abrupt slope in the long-wavelength region in InP/GaPN than in all sample with GaPAsN. A possible reason is the smaller nitrogen content in the active layer of sample #4 since nitrogen has a tendency to clusterization leading to local inhomogeneous composition of materials.

Finally, comparing sample #2 and #3, we observe a significant improvement in the EQE for sample #3 as was already noticed in the I-V curve under illumination. Sample #3 has the best photovoltaic properties among the studied samples. However its EQE is still very low (<40%). This could be explained by low lifetimes of carriers related to defect leading to recombination, which deserves further studies of defect properties in such dilute nitride layers. This will be the focus of next section using capacitance techniques.

IV.1.3 Admittance spectroscopy

In this section, the study of solar cells is performed by admittance spectroscopy. Measurements were made with a Janis VPF-100 nitrogen vacuum cryostat at temperatures *T* in the range from 80 to 360 K and an E7-20 RLC-meter at frequencies *f* in the range from 20 Hz to 1 MHz.

Figure IV.7 shows the temperature dependence of the capacitance at different frequencies, *C(T,f)*, for the single-junction solar cells (samples #1-#4) grown on GaP wafers. The steps observed in the capacitance curve with increasing temperature evidence the response of a defect level in the bulk, or at the interface, or the presence of a potential barrier in the (In)GaPN(As)/GaP heterojunction. An analysis of theoretical band diagrams and of the run of the experimental current-voltage characteristics, which have no bends, suggests that the features observed in the admittance spectra are not associated with parasitic potential barriers at interfaces. Measurements of *C(T,f)* at different bias voltages demonstrated that the peak and step positions are independent of the applied bias voltage, which is evidence of the response of defect levels in the bulk of the material, rather than at the interface.

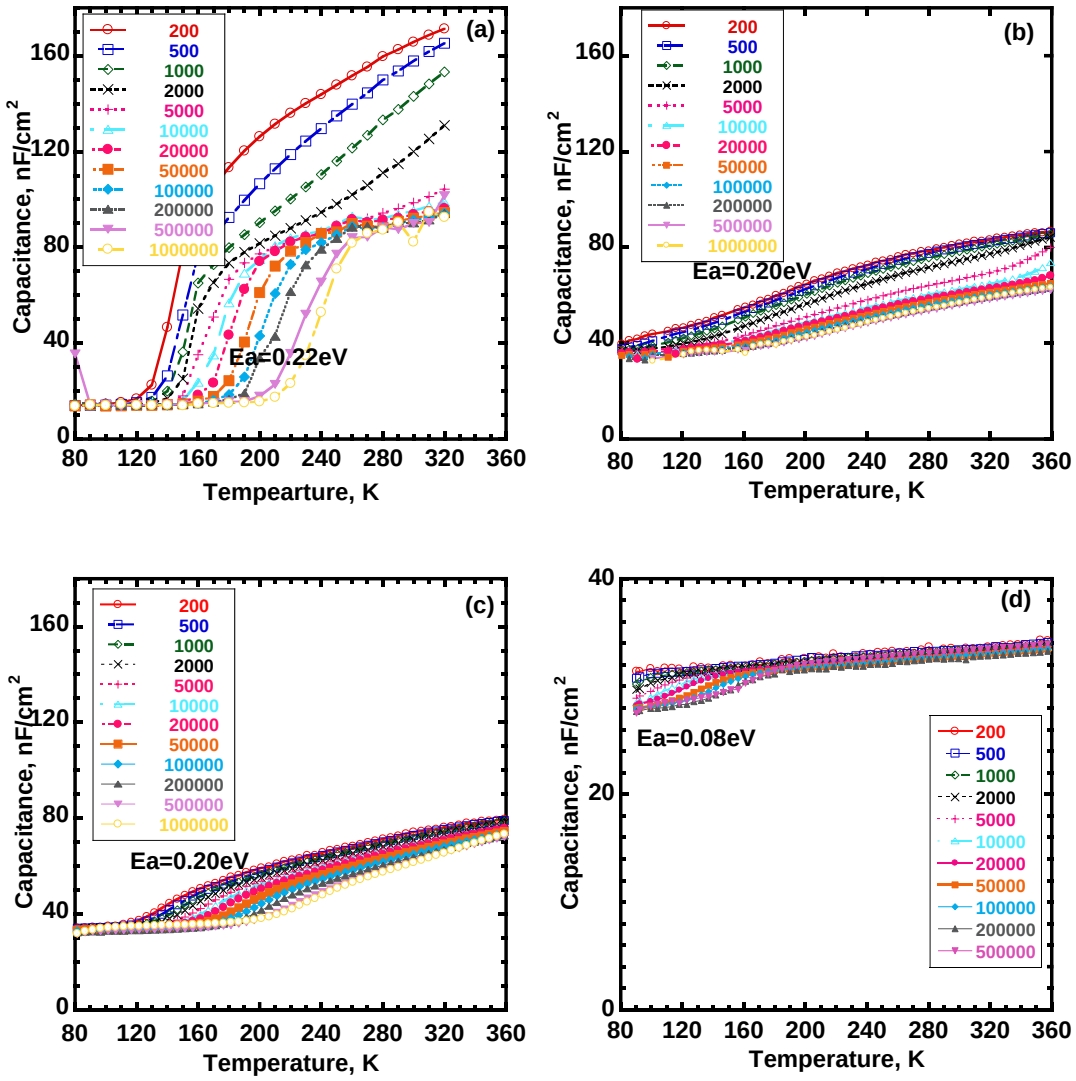

Figure IV.7 Experimental dependence of the capacitance upon temperature at various frequencies (indicating in Hz) for sample #1(a), #2(b), #3(c) and #4(d).

For the grown *p–n* structure (sample #1) on the GaP wafer, a clearly discernible capacitance step are observed at temperatures of 100–200 K (Figure IV.7a), which corresponds to a defect level with an activation energy of E_a=0.22 eV and capture cross section $\sigma=2.4\times10^{-15}$ cm^2 (Figure IV.8). One more step with a low activation energy of 0.04–0.1 eV can be seen at a higher temperature in the admittance spectra. It is difficult to determine this value more precisely because of the overlapping of both responses falling within the same temperature range. Further, samples #2 (Figure IV.7b) and #3 (Figure IV.7c) show similar capacitance dependence: the same low temperature step overlapping with another high temperature response. The parameters extracted from the low temperature step are E_a=0.20 eV and $\sigma=1.7\times10^{-15}$ cm^2 (Figure IV.8), but the amplitude of the step is much lower than in the *p-n* structure. Unfortunately, parameters for defects responding at higher temperature could not be estimated in both samples. In sample #2 responses from defects strongly overlap for low frequencies, but for high frequencies (higher than 5 kHz) the

temperature range does not allow to measure useful points at temperatures above 360 K, so it is impossible to define properly the parameters of this defect.

For sample #4 with *i*-InP/GaPN capacitance curves have low temperature series of blurred steps and then monotonous growth of capacitance without any feature (Figure IV.7d). According to the Arrhenius plot (Figure IV.8), these steps correspond to a response with a thermal activation energy E_a=0.08 eV and a capture cross section $\sigma=1.45\times10^{-16}$ cm^2. Possibly, this defect could be a donor-type point defect formed by silicon atoms at the site of gallium in the GaP lattice (Si_{Ga}) at a position of E_C-0.09 eV. This defect was also observed in undoped GaP:N layers grown by VPE[90]. However, since it is a shallow impurity center, it should not be very active in recombination and thus not affect the lifetime of charge carriers in the material. At temperatures above 160 K, the capacitance is almost independent on frequency and slowly grows with heating up to 360 K, so there are no response from defective levels in the explored temperature range for AS measurements.

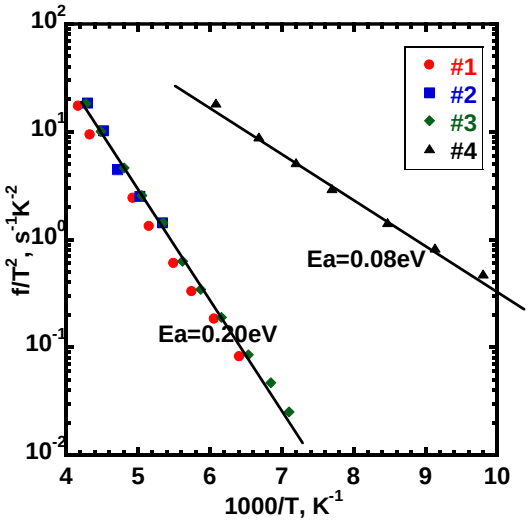

Figure IV.8 Arrhenius plot of the capacitance step for sample #1-#4.

Let us discuss the defect level with an activation energy of 0.22 eV, observed in *p–n* structures. According to a previous studies[86,88,89], the T1 level with a close activation energy and capture cross section is observed in the GaP:N material doped with silicon. This defect is a $Si_{Ga}+V_P$ complex, which appears under non-equilibrium growth conditions when a large number of gallium and phosphorus vacancies are formed and Si occupies their substitutional sites. The *n*-GaPAsN layer under study was also intentionally doped with silicon with significant concentration. For the structures with *i*-GaPAsN, a similar response is also observed but the step amplitude is extremely low. It means that this defect has much lower concentration but its existence can be associated with unintentional background doping of *i*-GaPNAs by silicon during the growth process.

Therefore, admittance spectroscopy allowed to detect defect with low activation energy which can be associated with silicon incorporation in dilute nitrides and, perhaps, responsible for unintentional doping of these layers. However, their low values of E_a and σ do not allow us to consider them as effective centers of non-radiative recombination in InGaPAsN. Consequently, DLTS will be used for exploration of deep levels. However, *p-i-n* structures show better photoelectric properties so only samples #2-#4 with *i*-layer are studied by this method.

IV.1.4 Capacitance- voltage measurements

The section is devoted to the study of single-junction solar cells with *p-i-n* junction grown on GaP wafers by the capacitance-voltage method to define the background doping in the *i*-layer of dilute nitrides. As shown above by AS there is no contribution from defect levels in the capacitance value at high frequency and at low temperature (Figure IV.7). Therefore, *C-V* curves were measured for all samples in reverse voltage range of 0..3 V at a frequency of 1MHz at 80 K (Figure IV.9a). Obviously, the capacitance decreases versus reverse voltage in all samples but the decrease rate is different. Sample #2 has the strongest dependence of capacitance on bias voltage and quickly decreases, sample #3 shows slight capacitance drop and sample #4 exhibits almost no capacitance change. According to Eq. (II.14), the width of SCR can be estimated from the capacitance value. The estimated dependence of the space charge width on applied reverse voltage is shown in Figure IV.9b.

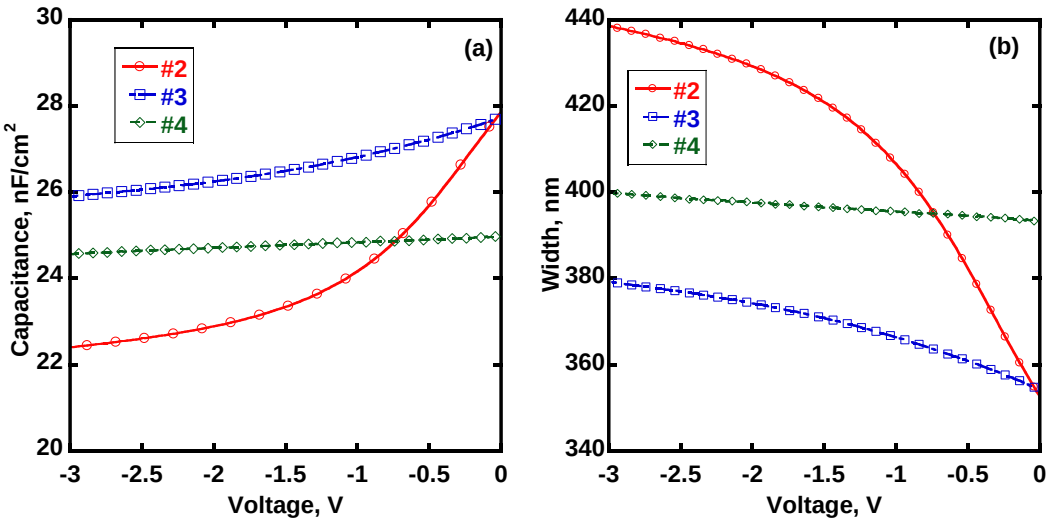

Figure IV.9 Capacitance-voltage characteristics (a) and width- voltage dependences (b) for solar cells with single *p-i-n* junction at 80 K.

According to the growth recipe, the *i*-layer of dilute nitrides must be undoped so the width of SCR must be equal to the thickness of the *i*-layer at reverse applied voltage in the classical case

of ideal *p*-*i*-*n* junction where doping concentration in *p*- and *n*-layers is much higher than in the undoped *i*-layer. However, background doping in *i*-layers yields to differences compared to the ideal case. It leads to the formation of a classical *p*-*n* junction instead of the expected "*p*-*i*-*n*" structure. Thus, the capacitance can depend on the applied voltage since the SCR extends inside the less doped supposed "i"-layer. In addition, the presence of silicon related defects in the i-layers suggests that the background doping should be of *n*-type.

The SCR width is almost independent of the applied bias voltage in sample #4 and its estimated thickness is approximately 390 nm. It is close to the value of 350 nm estimated from the growth process, so the *i*-InP/GaPN layer must be fully depleted; the discrepancy can come from the unknown value of dielectric permittivity in dilute nitrides or (and) an error in the area estimation. Further voltage increase does not lead to an extension of SCR in the adjacent *p*- and *n*-layers since they have very high doping concentration that is confirmed by the growth recipe (3×10^{18} cm^{-3} and 1×10^{18} cm^{-3} for the *n*- and *p*- layer, respectively). According to the computer simulation of *C*-*V*, the background *n*-type doping concentration should be lower than 1×10^{16} cm^{-3} in sample #4 (Figure IV.10c).

Both samples with *i*-GaPAsN exhibit a change of the capacitance with increasing of voltage, and the estimated SCR width is larger than the value of 300 nm announced from the growth procedure. It means that the SCR extends in adjacent layers, and the stronger *C*-*V* dependence of sample #2 suggests that the two samples should have different doping concentrations. In the simulation, we varied the doping concentration in the *i*-layer (*n*-type) and in the adjacent *p*- and *n*-layers. The best correlation with experiments was obtained when *n*- and *p*-type layers have the doping concentration of 3×10^{17} cm^{-3} and 1×10^{17} cm^{-3} in sample #2. These values correspond to that announced from the growth recipe. However, they are slightly higher in sample #3: 5×10^{17} cm^{-3} and 4×10^{17} for *n*- and *p*-layers. The simulated *C*-*V* dependences are shown in Figure IV.10 for different concentrations of *n*-doping *i*-layer at 80 K. From the comparison with experimental data, we can estimate the *n*-type doping concentration at 3×10^{16} cm^{-3} and 1×10^{16} cm^{-3} in sample #2 and #3, respectively.

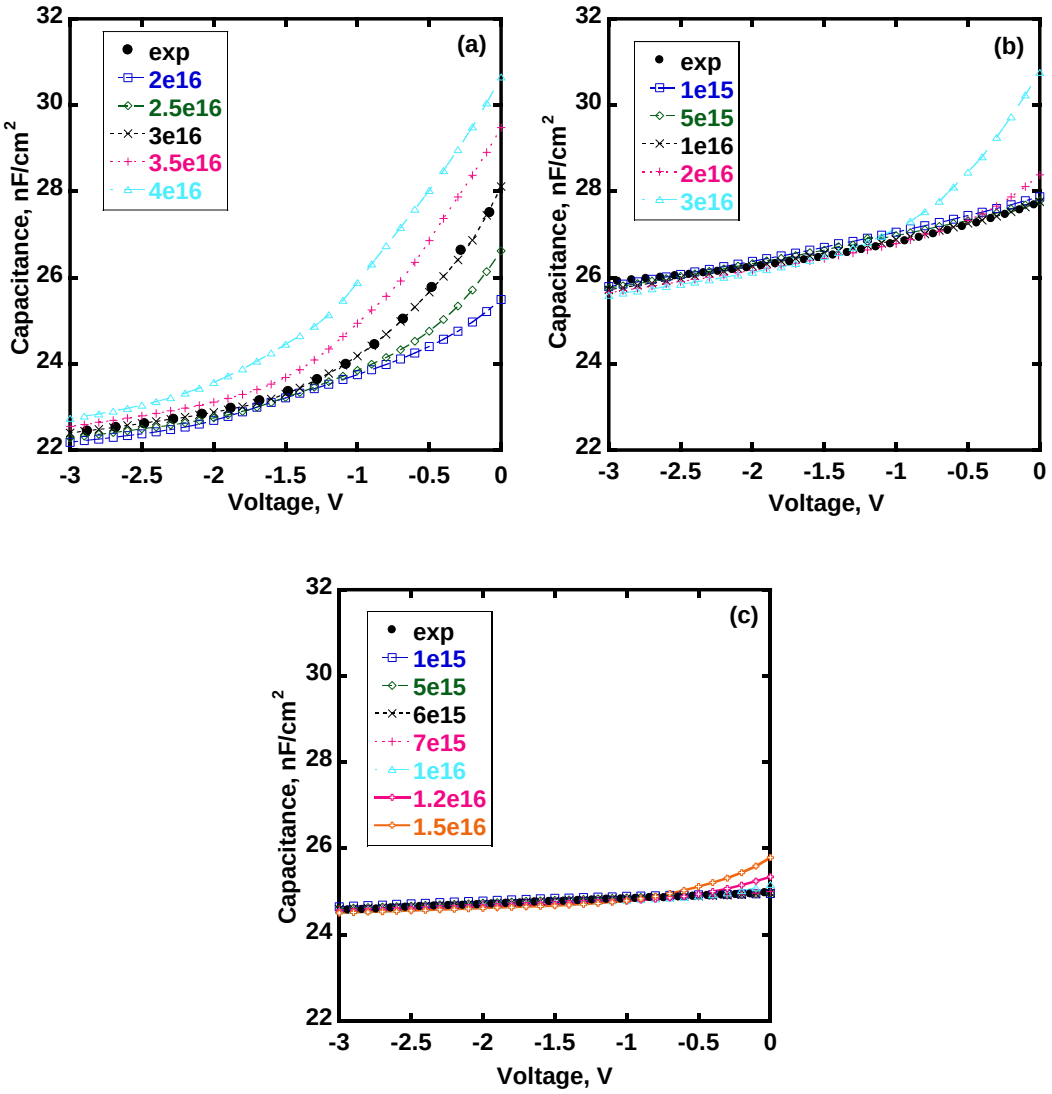

Figure IV.10 Simulated capacitance-voltage characteristics for sample #2(a), #3(b) and #4(c) with single *p*-*i*-*n* junction at 80 K for different concentration of *n*-type doping in *i*-layer.

Simulated band diagrams at zero bias voltage are presented in Figure IV.11 for all three samples. The space charge region is divided between *i*- and cover *p*- layer of 100 nm in sample #2 due to their comparable doping concentration (3×10^{16} cm^{-3} and 1×10^{17} cm^{-3} respectively) in ratio 3.5:1 at zero voltage so it is *p*-*n* junction. Further, the SCR extends simultaneously in both layers and at the final value of -3 V they become almost fully depleted. In sample #3 the SCR also extends in the *p*-layer at equilibrium conditions, but due to the high concentration ratio (more than one order of magnitude) almost total SCR is lying in the *i*-layer so it is almost fully depleted even at zero bias voltage because its thickness is almost coinciding with the SCR width. The increase of reverse voltage up to 3 V leads only to a slight extension of SCR of 10 nm thus sample #3 can be considered as a *p*-*i*-*n* junction. The sample #4 shows a band diagram similar to that of an ideal *p*-*i*-*n* junction since the electric field extends all across the width of *i*-GaPAsN layer. Low doping in *i*-layer and high doping in cover *p*-layer lead to full depletion of *i*-GaPAsN and negligible width

of SCR in cover *p*-layer. Consequently, GaPAsN alloys seen to be more unintentionally doped (1-3×10^{16} cm^{-3}) than InP/GaPN for the current growth processes. If *i*-GaPAsN is used as an active layer in SC based on *p*-*i*-*n* junction, cover layers must be highly doped and minimal value of doping can be estimated for suggested thickness of *i*-layer. However, reasons of background doping in InGaPAsN also must be explored by fabrication of special structures where doping value can be estimated directly from experimental data, and not from simulation. This information could help to decrease concentration doping in dilute nitrides lattice-matched to GaP and Si.

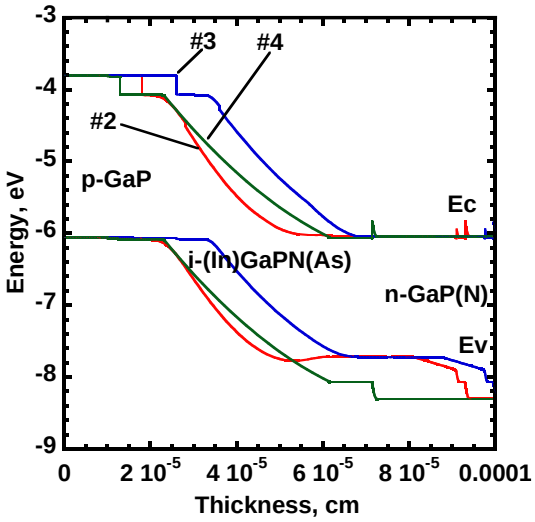

Figure IV.11 Simulated band diagram for solar cells with single *p*-*i*-*n* junction at 80 K.

IV.1.5 Deep-level transient spectroscopy

The samples were studied by the deep-level transient spectroscopy technique to explore deep defects in the *i*-layer of dilute nitrides.

IV.1.5.1 GaPAsN layer of sample #2

For sample #2 the DLTS spectra *S(T)* was measured for different rate windows under the following conditions: V_{rev}=-2 V, V_{pulse}=+1.5 V, t_{pulse}=100 ms (Figure IV.12a). The *S(T)* spectra have two clear series of peaks associated with responses from majority-carrier traps. First series is placed in the temperature range 80-120 K and it corresponds to a defect level with activation energy E_a=0.18 eV and capture-cross section σ=3.1×10^{-15} cm^2 estimated from Arrhenius plot in Figure IV.12b. These values correlate well with parameters of a similar defect detected by admittance spectroscopy above. Afterwards, a clear series is detected in the temperature range of 200-280 K and it corresponds to a deep defect with parameters of E_a=0.58 eV and σ=6.9×10^{-13} cm^2.

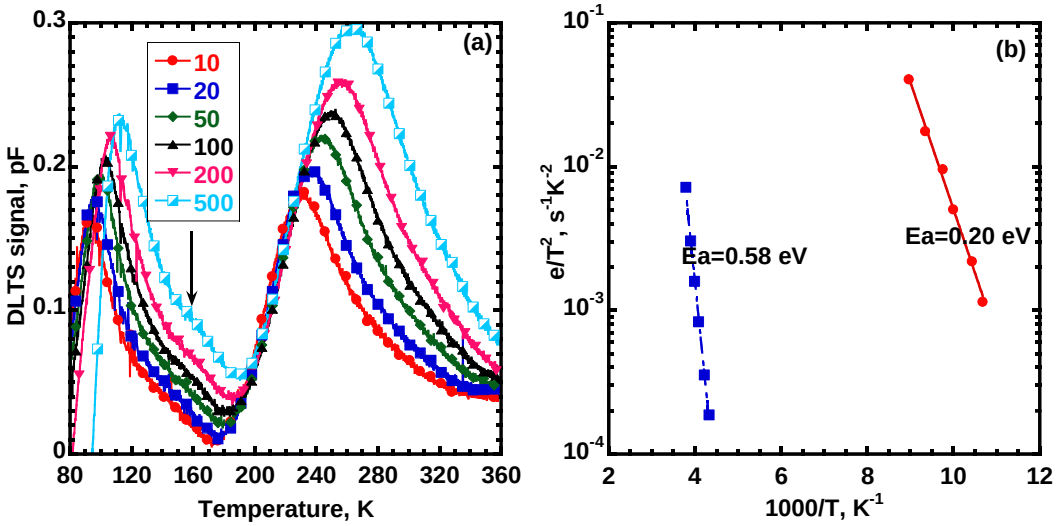

Figure IV.12 a- DLTS spectra *S(T)* for sample #2 (with layer of GaPAsN) for different rate windows (in s^{-1}) with the following conditions: (a)- V_{rev}=-2 V, V_{pulse}=+1.5 V. b- Arrhenius plot of detected responses.

Nevertheless, spectra *S(T)* also have some feature (shown as arrow in Figure IV.12a for e_r=500 s^{-1}) in the high-T side of peaks related to defect at 0.18 eV in the temperature range 120-160 K: it can suggest the existence of one additional defect with lower amplitude. Also, in the temperature range 140-200 K the shape of *S(T)* can suggest the existence of the response from a trap for minority carriers. However, the sample was always under reverse bias even during the filling pulse, meaning that a response from minority carrier traps could hardly be in the *i*-layer. A correct estimation of the parameters for these two responses is impossible due to their low peak amplitude and overlapping with the responses from the main defects with an activation energy 0.18 eV and 0.58 eV. As described above sample #2 has a *p*-*n* junction lying in the *i*-layer and in cover *p*-layer so its band diagram is different from the usual Schottky so the DLTS data should be analyzed and interpreted for a correct estimation of defect concentration and clear understanding of processes occurring during the measurements. Figure IV.13 presents the simulated band diagram at a value of applied voltage of -0.5 V (during the filling pulse) and -2 V (initial and after filling pulse state) in sample #2.

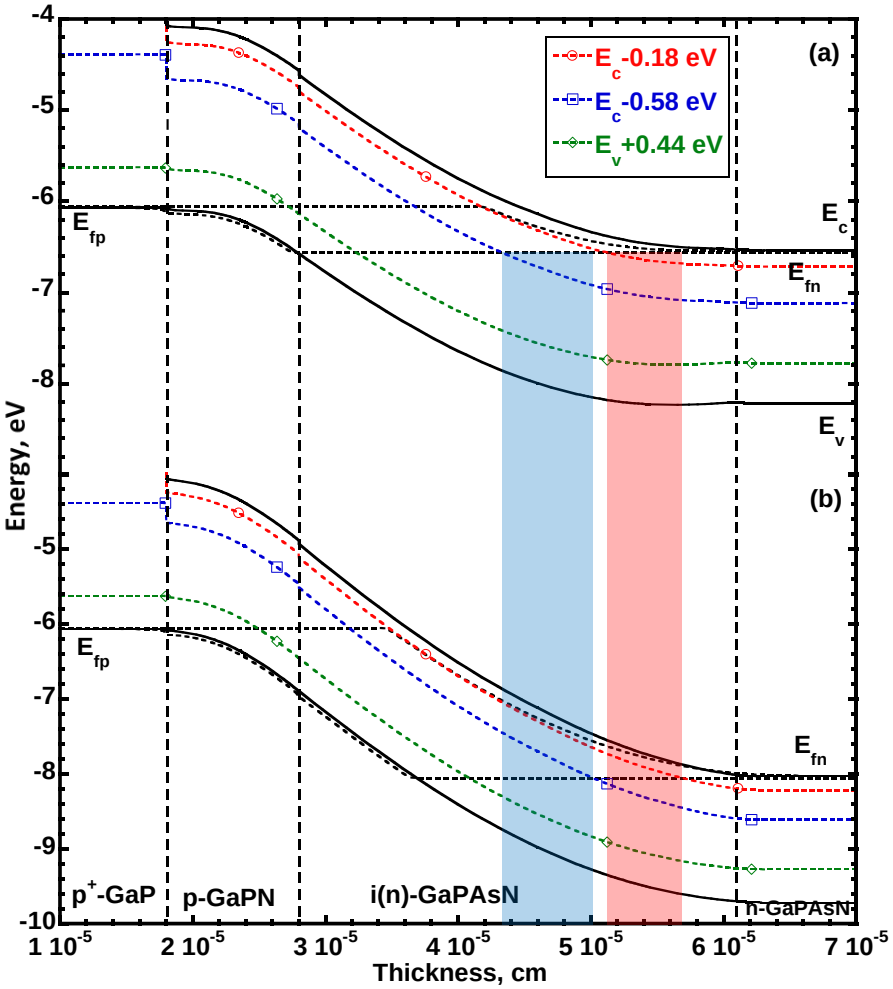

Figure IV.13 Band diagram of sample #2 at -0.5 V(a) and -2 V(b).

The band diagram consists of valence and conduction bands, electron and hole quasi*-*Fermi levels, position of electron traps at an energy 0.18 eV and 0.58 eV below conduction band, and a suggested hole trap at position E_v+0.44 eV. Here and further, *i*-layer of InGaPAsN is considered as *n*-type layer. According to the simulation, at the reverse bias of -2 V (Figure IV.13b) the electron *quasi*-Fermi level essentially shifts only in the *i*-layer unlike adjacent layers where it almost remains constant. In this case, the electron traps must be empty above the electron quasi Fermi level and filled below but each trap level crosses the quasi Fermi level at its own point in the SCR (Figure IV.13b). The quantity denoted λ in the theory of DLTS is difference between the border of the SCR and the position of this intercept point. When the positive filling pulse (final voltage is -0.5 V) is applied the electron quasi Fermi level is pushed towards the conduction band only in part of the *i*-layer and some empty traps could capture electrons (Figure IV.13a). When the sample returns to its initial state at V_{rev}=-2V the electron quasi Fermi level is placed below the defect states filled with electrons in a narrow region where electrons are emitted thus yielding the capacitance

transient that is measured by DLTS. This region defines the number of defects contributing to the DLTS response so it must be taken into consideration for a correct estimation of defect concentration. Each region is shown as a rectangle of the corresponding color for each defect level in the band diagram (Figure IV.13). According to equation (II.38) the defect concentration was estimated under the condition of N_D=3×10^{16} cm^{-3} as from the C-V measurements and we find value of 2×10^{15} cm^{-3} and 4×10^{15} cm^{-3} for defects at E_c-0.18 eV and E_c-0.58 eV, respectively. For the latter we could also estimate the capture time which is of the order of 10^{-11} s assuming a thermal velocity value of 10^7 cm/s. It is extremely small value for the *i*-GaPAsN layer that can lead to low EQE in SC (Figure IV.6). Consequently, we must study this defect carefully in future experiments since lifetimes in dilute nitrides must be higher than 10^{-9} s for sufficient performance of MJSC[74].

The DLTS technique also allows to detect minority-carrier traps. To this purpose, minority carriers (holes in our undoped *i*-GaPAsN) must be injected in the space charge region during the filling pulse. However, holes and electrons are then simultaneously injected in the SCR so in DLTS spectra responses can be observed from both majority- and minority- carrier traps. It leads to the overlapping of responses and the analysis becomes more complicated. Holes can be injected by light or by applying a forward bias voltage. The second method is used in our measurements. Therefore, the DLTS spectrum *S(T)* was measured for different rate windows under the following conditions: V_{init}=+0.2V, V_{pulse} = +0.8V, t_{pulse} = 50 ms (Figure IV.14a).

Significant differences are observed when comparing spectra *S(T)* in Figure IV.12a and Figure IV.14a in the temperature range below 200 K. *S(T)* starts to decrease from 80 K and has a negative value: it indicates a response from minority-carrier traps. Thereby, series of close negative peaks are detected in the temperature range 160..180 K. Existence of this defect leads to quenching of the response from the defect at E_c-0.18 eV in the range 80..120 K due to potentially higher concentration. Nevertheless, there are positive peaks on *S(T)* similar to peaks associated with the responses from the defect level at E_c-0.58 eV in previous measurements. Series of both peaks are very close so some overlapping is observed. Since peaks have opposite signal (positive for majority-carrier trap and negative for minority-carrier trap) the shape of *S(T)* becomes complicated to analyze. Nevertheless, it was done in our case but obtained values must be checked in future experiments for minority trap. Negative peak of *S(T)* for rate window 10 s^{-1} is 156 K (Figure IV.14a), and *S(T)* of 10 s^{-1} associated with response from E_c-0.58 eV starts to increase at 172 K in previous measurements (Figure IV.12a). It suggests that the majority-carriers trap has no influence on the peak position from minority-carrier trap for emission rate 10 s^{-1}. Similar situation is observed for the rest rate windows. Therefore, parameters of this defect level are estimated from the Arrhenius plot (Figure IV.14b): E_a=0.44 eV, which corresponds to a level position of

E_v+0.44eV, and σ=2.6×10^{-11} cm^2. The defect concentration is 2×10^{15} cm^{-3}. The defect can also be considered as an effective center of non-radiative recombination.

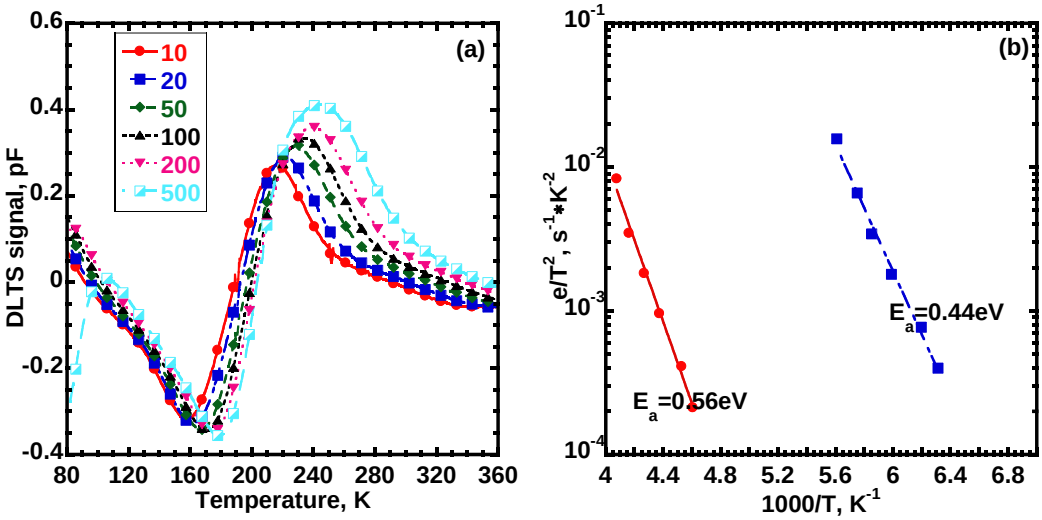

Figure IV.14 a- DLTS spectra *S(T)* for sample #2 with layer GaPAsN for different rate windows (in ms) with the following conditions: V_{init}=+0.2 V, V_{pulse}=+0.8 V. b- Arrhenius plot of detected responses.

The appearance of responses from E_v+0.44eV can be explained by the band diagrams at the corresponding bias conditions of this experiment (Figure IV.15). For majority-carrier traps, the behavior remains the same as in measurements at reverse bias voltage but the spatial region giving rise to a response changes. All equation for the DLTS describing the method were obtained under assumption of uniform distribution of traps and impurities but it can be incorrect in real samples. It can also lead to differences in *S(T)* spectra for different regions of SCR since the obtained trap concentration describes only the width between W_1-λ_1 and W_0-λ_0. However, the main distinction between the two experiments is the region where holes emit in valence band after the end of the filling pulse. It corresponds to a part of cover *p*-layer in Figure IV.13, and part of the *i*-GaPAsN layer in Figure IV.15. Therefore, in the second experiment the response from E_v+0.44eV leads to strong changes as holes contribute in the capacitance value of the *p*-*i*-*n* junction. Furthermore, for both experiments *S(T)* decreases at temperatures above 240 K up to the measurement limit of 360 K for all rate windows. This indicates absence of other responses from minority- and majority-carrier traps, so it suggests the absence of defect levels with higher activation energy in the considered layer of *i*-GaPAsN.

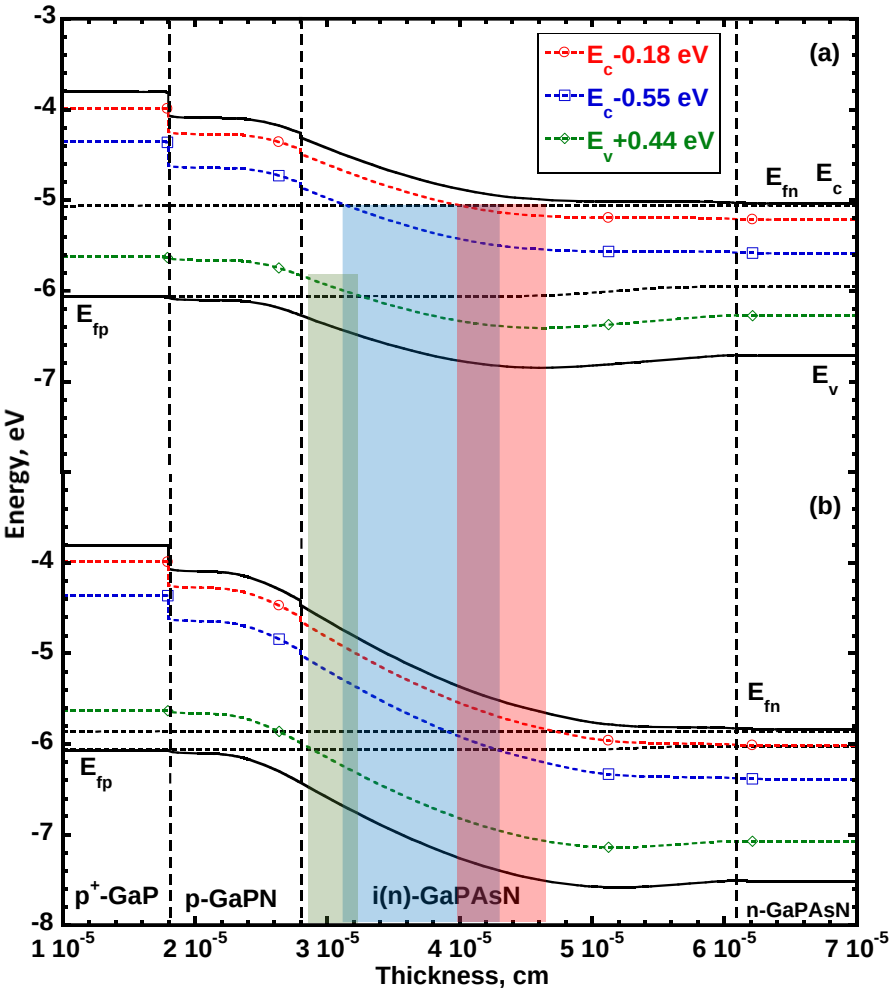

Figure IV.15 Band diagram of sample #2 at +0.2 V(a) and +1.0 V(b).

Let us now discuss another issue related to the *S(T)* spectra of Figure IV.12a. Usually point-defects with known activation energy lead to responses as narrow peaks on *S(T)* spectra. However, own peaks are broadened, especially for E_c-0.58 eV. Also, the peak amplitude increases with the rate window. It suggests a non-exponential behavior of responses from defect levels due to different possible reasons. It can come from the dependence of the capture cross section on temperature[147], an energy distribution of the defect position in the bandgap due to alloying of GaPAsN[144], or responses from various closely separated defect levels. Furthermore, another possible reason is the response from extended[148] defects rather than from point defects. The useful method to distinguish between point and extended defects is the measurement of the dependence of the peak amplitude on the duration of filling pulse at fixed temperatures. The isothermal dependence of the peak amplitude at fixed temperature is described for point defects by [149,150]:

$$S_{peak}(t_p) = C_1(1 - e^{-N_{CV}\nu_{th}\sigma_n t_p}) + C_2\ln(C_3 t_p), \quad \text{(IV.2)}$$

where C_1, C_2 and C_3 are constants. These parameters can be estimated by fitting of experimental $S_{peak}(t_p)$ curves. Moreover, in the case of an extended defect, the peak amplitude of the DLTS signal versus duration of filling pulse width is a logarithmic function[151]:

$$S_{peak}(t_p) = B\ln t_p \quad \text{(IV.3)}$$

where B is a constant. In general, the key distinction is the saturation of the peak amplitude in case of point defects unlike in extended states. Spectra $S(T)$ and the dependence $S_{peak}(t_p)$ are presented in Figure IV.16 and Figure IV.17 for E_c-0.18 eV and E_c-0.58 eV, respectively.

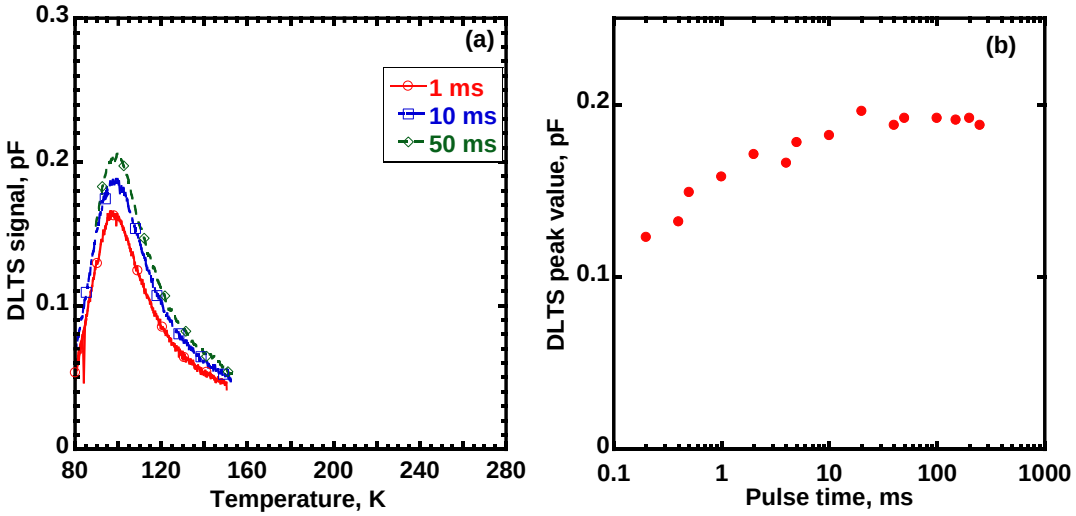

Figure IV.16 (a)- spectra $S(T)$ of the defect at E_c-0.18 eV for rate window of 50 s^{-1} for different filling pulse duration in sample #2, (b)- dependence of the peaks value on filling pulse duration.

For both defect levels the dependence of the peak value on filling pulse duration is observed. Both curves saturate for t_{pulse}>100 ms so responses from point defects can be suggested for the detected levels in sample #2. The width of the peak for the defect at E_c-0.18 eV is smaller and saturation occurs earlier than for the one at E_c-0.58 eV.

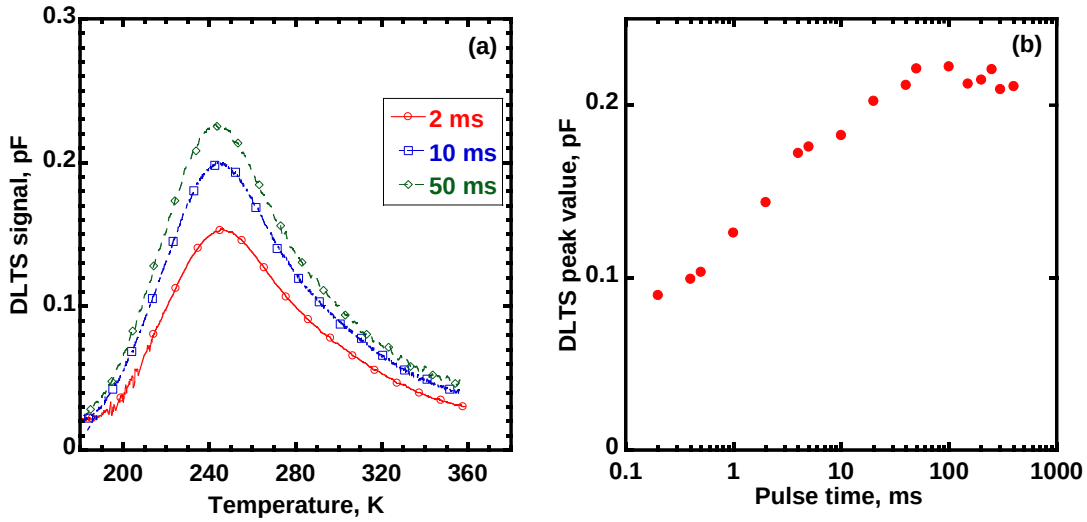

Figure IV.17 (a)- spectra *S(T)* of the defect at E_c-0.58 eV for rate window of 50 s^{-1} for different filling pulse duration in sample #2, (b)- dependence of the peak value on filling pulse duration.

The most probable reason for the non-exponential behavior in the considered materials originates from alloying. Probably, in the case of dilute nitrides, a strong fluctuation in composition occurs due to non-equilibrium growth conditions and to the tendency of nitrogen clusterization leads to the transformation of point defects into extended ones with some little energy distribution. Furthermore, high arsenic content of 15-30% can also lead to some energy distribution for the defect level. Therefore, estimated values of capture cross section and activation energy can be considered as "average" parameters for detected defect levels. Peak value is the crucial parameter since the defect concentration is estimated from its value so the filling pulse duration must be carefully chosen for DLTS measurements. In our case, the defect concentration was estimated from the peak value associated with e_r=500 s^{-1} with t_{pulse}=100 ms (Figure IV.12) since it is in the saturation region in the $S_{peak}(t_p)$ curve and all traps should contribute to the capacitance transient.

In summary, in sample #2 we detected two majority-carrier traps (E_c-0.18 eV and E_c-0.58 eV) and one minority-carrier trap (E_v+0.44 eV). They should be point defects with some energy distribution leading to broadened peaks on DLTS spectra. It can be explained by composition fluctuation of the GaPAsN quaternary alloy due to nitrogen clusterization and high arsenic content of 15-30%. Future experiments could be focused on deeper study of parameters of energy distribution of the defects to define their nature and the role of N and As in their formation.

IV.1.5.2 GaPAsN layer of sample #3

The DLTS method was applied to sample #3 having an *i*-layer of GaPAsN with simulated donor concentration of 1.0×10^{16} cm^{-3}. As described above, this structure is closer to an ideal *p*-*i*-*n* junction due to lower doping of the *i*-layer and higher doping of cover *p*- and *n*-layers. In the first

step, the DLTS spectra *S(T)* were measured for different rate windows under the following conditions: V_{rev}=-2.0 V, V_{pulse}=+1.5 V, t_{pulse}=50 ms and V_{rev}=-3.0 V, V_{pulse} =+2.5V, t_{pulse}=50 ms (Figure IV.18). We observe that the shape of the curves is very strange and different from spectra *S(T)* for sample #2 obtained with similar parameters of experiments (Figure IV.12a).

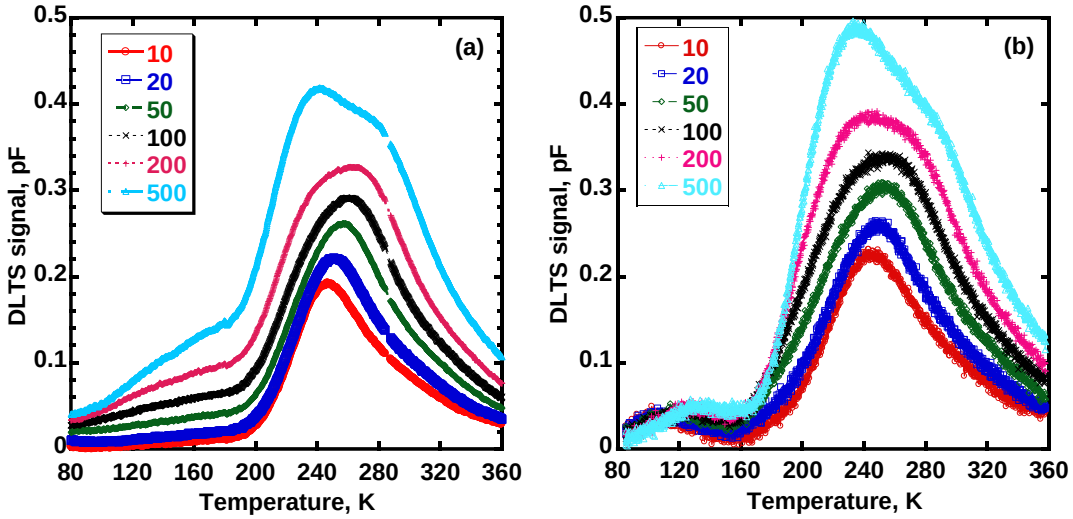

Figure IV.18 DLTS spectra *S(T)* for sample #3 (with GaPAsN layer) for different rate windows (in s^{-1}) with the following conditions: (a)- V_{rev}=-2.0 V, V_{pulse}=+1.5 V and (b)- V_{rev}=-3.0 V, V_{pulse}=+2.5 V.

According to these experiments, there is a capacitance transient that does not depend on temperature. It is very rapid so it leads to the appearance of an additional high peak on *S(T)* spectra for high rate windows at temperature 240 K. Possible, the gate window (t_1 and t_2) corresponding to high rate windows is located close to start of capacitance transient that leads to the instability of the signal in this region. Nevertheless, a series of peaks for low rate windows is observed in the temperature range 220..280 K similar to responses from the defect at E_c-0.58 eV detected in sample #2. However, estimation of its parameters in sample #3 is impossible due to the overlapping with the temperature independent high peak of unknown nature. Also, responses from the defect level at E_c-0.18 eV are not observed but they were detected by admittance spectroscopy (Figure IV.8) for this sample #3 and by DLTS in previous sample #2 in the low temperature range 80..160 K. In Figure IV.18a this region could not properly explored due to the influence of the capacitance transient described before, but in Figure IV.18b a series of peak is observed with very low amplitude and large width. It could be associated to responses from the defect at E_c-0.18 eV. The low peak amplitude can be partly explained by the band diagram for sample #3 during the DLTS measurements for V_{rev}=-3.0 V, V_{pulse}=+2.5 V (Figure IV.19b). The values of λ are very small (15 nm and 40 nm for -3 V and -0.5 V, respectively) so the thickness of *i*-GaPAsN from which

electrons can emit is thin (only 25 nm). The width of SCR is almost the same at all applied reverse bias voltage since the *i*-GaPAsN layer is fully depleted. Therefore, value of correction factor associated with λ in equation (II.31) is 0.14 which is three times less than in sample #2 so the amplitude of *S(T)* is also lower. Furthermore, *S(T)* is inversely proportional to N_D which is equal to the doping concentration in the cover layer of *n*-GaP (5×10^{17} cm^{-3}) in sample #3 unlike in sample #2, where it is the unintentional doping concentration in *i*-GaPAsN (3×10^{16} cm^{-3}).

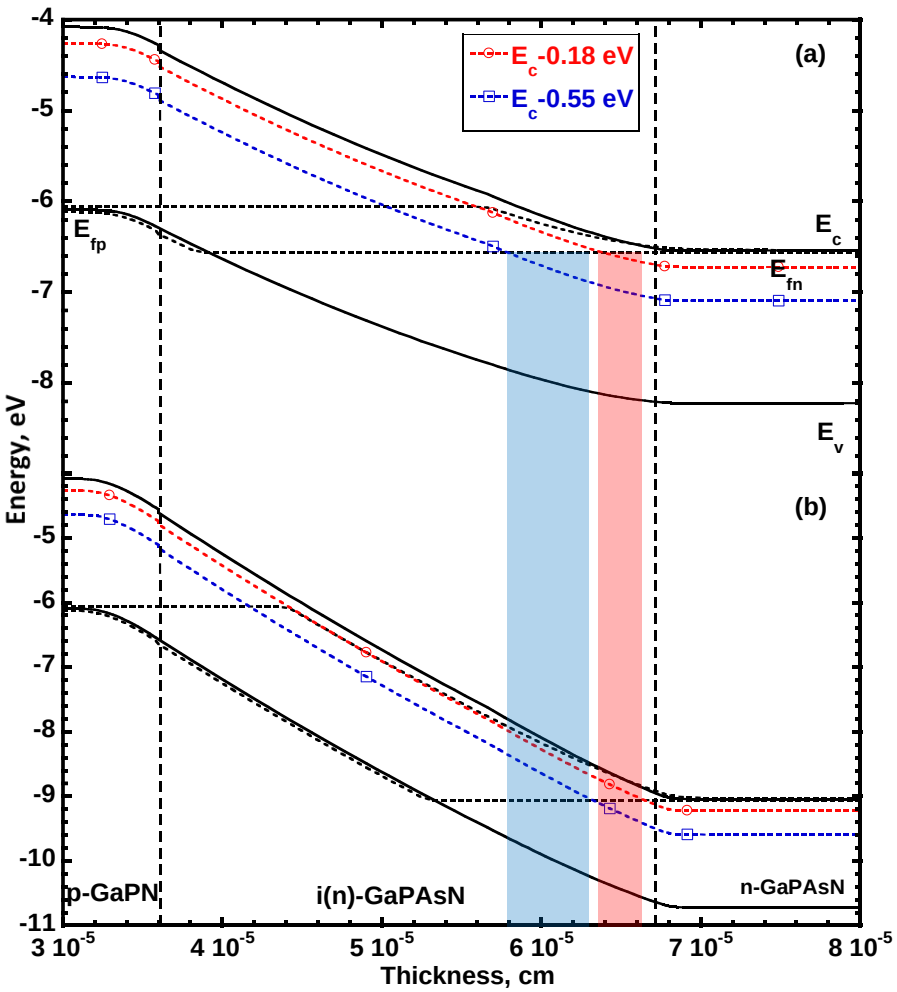

Figure IV.19 Band diagram of sample #3 at -0.5 V(a) and -3.0 V(b).

Interpretation of experiments described above is complicated due to difficult applicability of classical DLTS theory to *p-i-n* junctions with fully depleted *i*-layer. This is why, forward bias was applied to fill traps inside the *i*-layer and detect their responses. The DLTS spectra *S(T)* were measured for different rate windows under the following conditions: V_{init}=+0.2 V, V_{pulse}=+0.5 V, t_{pulse}=50 ms (Figure IV.20). Band diagrams corresponding to the bias conditions are shown in Figure IV.21.

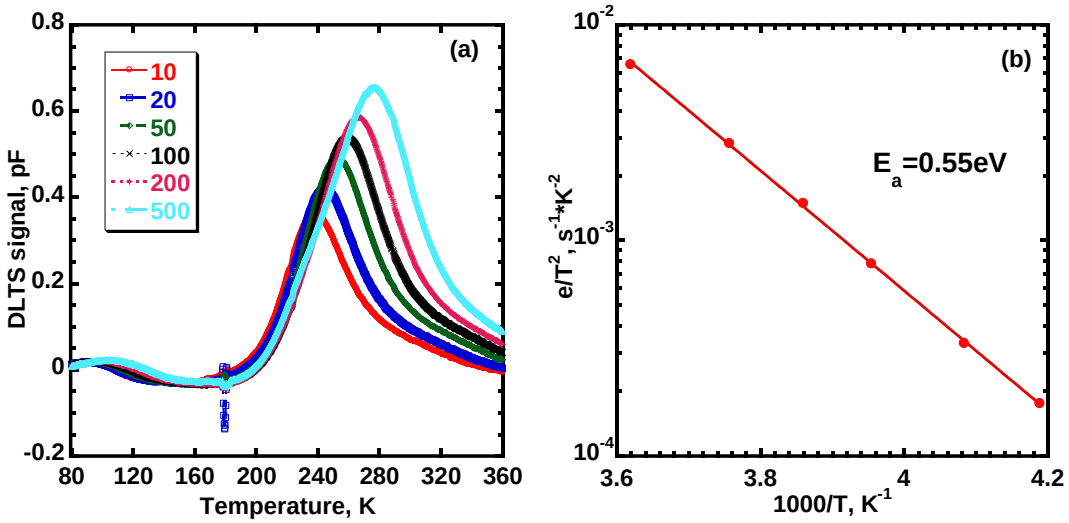

Figure IV.20 (a) - DLTS spectra *S(T)* for sample #3 (with GaPAsN layer) for different rate windows (in s^{-1}) with the following conditions: V_{init}=+0.2V, V_{pulse}=+0.5V. (b)- Arrhenius plot of detected responses.

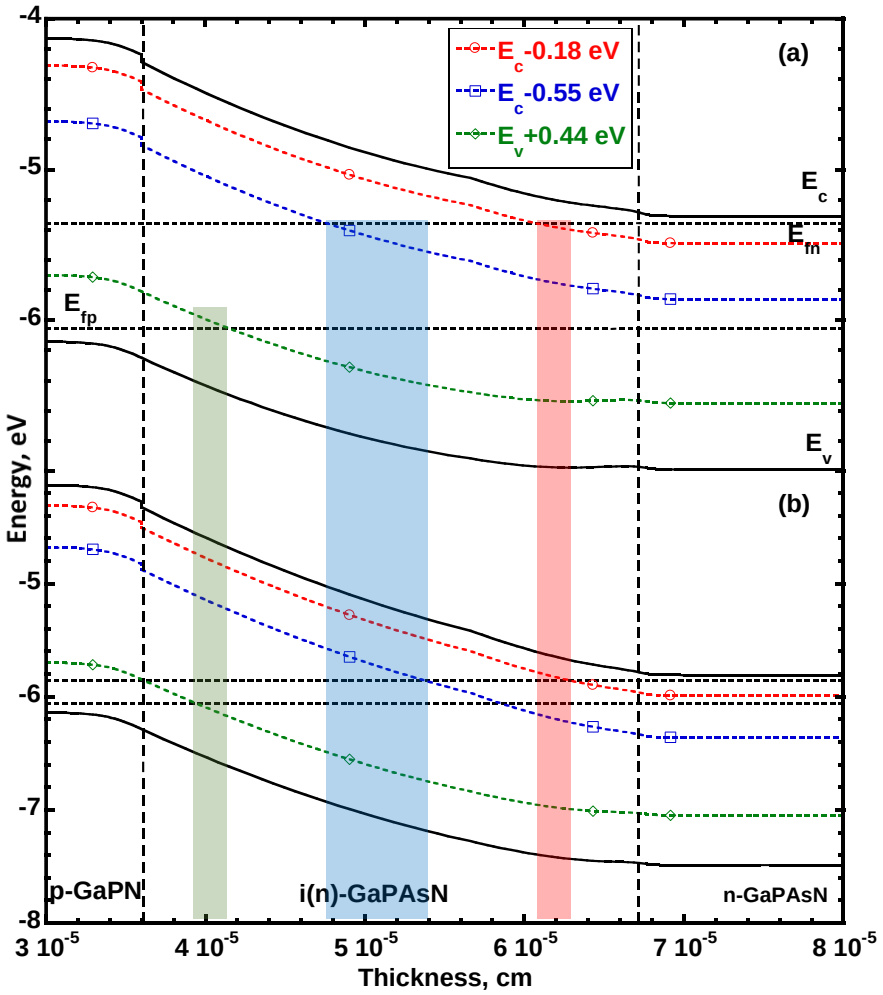

Figure IV.21 Band diagram of sample #3 at +0.7 V(a) and +0.2 V(b).

In this case, spectra *S(T)* show normal behavior with series of peaks corresponding to a defect level with an activation energy of E_a=0.55 eV and a capture-cross section $\sigma=3.1\times10^{-15}$ cm^2 estimated from the Arrhenius plot in Figure IV.20b. These values are close to that of the defect at E_c-0.58 eV in sample #2 so it can be considered as the same defect. The defect concentration was estimated with condition of $N_D=1\times10^{16}$ cm^{-3} and we found a value of 2×10^{15} cm^{-3}, which is lower than for the similar defect in sample #2. Figure IV.22 presents spectra *S(T)* for two different t_{pulse} values and the dependence of peak amplitude for e_r=50 s^{-1} corresponding to the defect level E_c-0.55 eV on filling pulse duration. The peak amplitude for 50 s^{-1} increases with t_{pulse} and saturates at t_{pulse}>50 ms. Similar behavior was observed in sample #2 for the defect at E_c-0.58 eV, that we attributed to a point defect with some energy distribution due to composition fluctuation in the quaternary alloy of GaPAsN. Obviously, there is also a response in the temperature range 120..170 K associated with minority-carrier traps similar to that in sample #2, and the peak value is again lower than in sample #2. The lower concentration of both majority- and minority-carrier traps detected in sample #3 as compared to sample #2 correlate well with the better photovoltaic performance and better EQE curve that were previously observed.

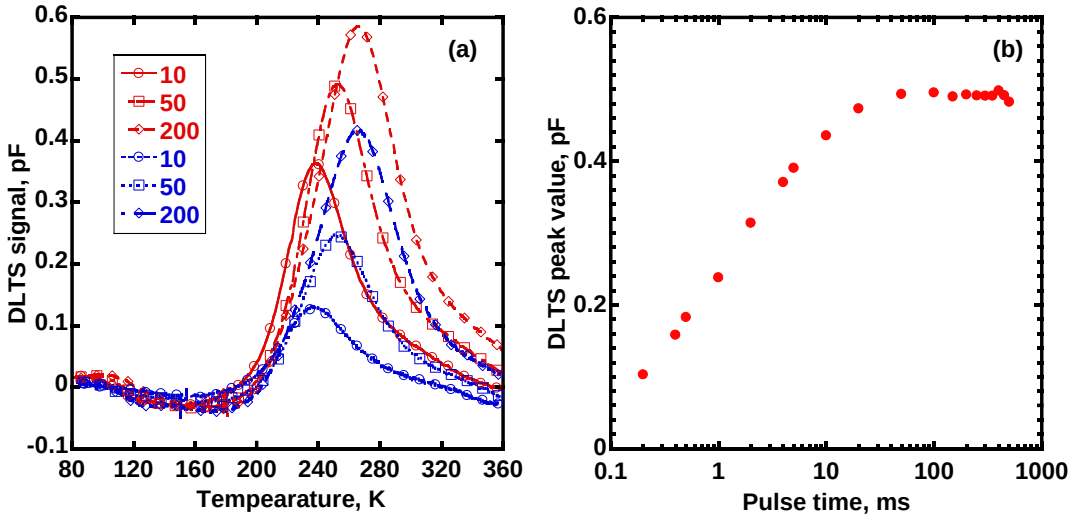

Figure IV.22 (a)- spectra *S(T)* of the defect at E_c-0.55 eV for filling pulse duration of 1 ms (blue) and 50 ms (red) in sample #2, (b)- dependence of the peak value for e_r=50 s^{-1} on filling pulse duration.

IV.1.5.3 InP/GaPN layer of sample #4

The DLTS spectra *S(T)* were on sample #4 measured for different rate windows under the following conditions: V_{rev}=-3V, V_{pulse}=+2.5V, t_{pulse}=50 ms (Figure IV.23a).

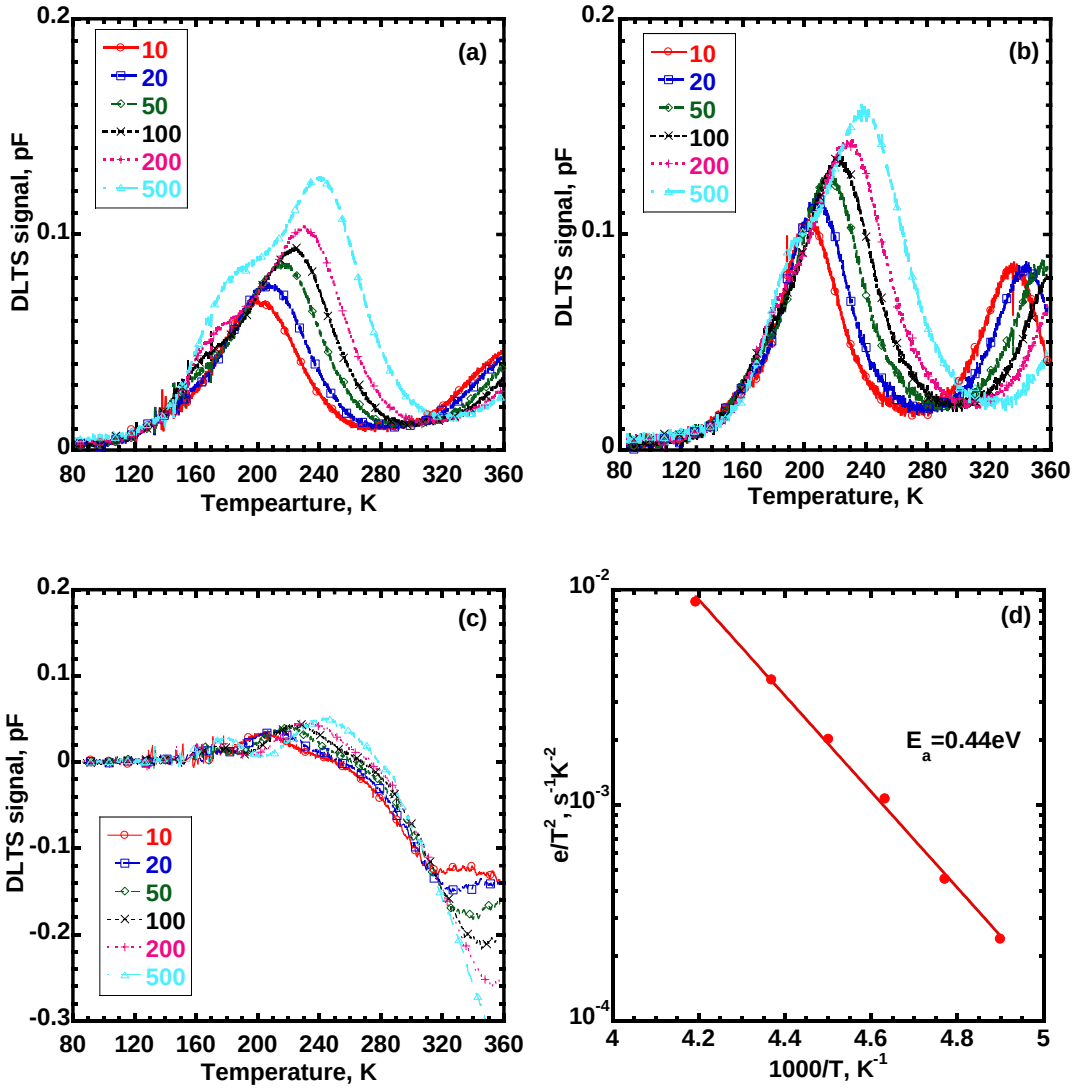

Figure IV.23 DLTS spectra *S(T)* for sample #4 (with InP/GaPN layer) for different rate windows (in s^{-1}) with the following conditions: (a)- V_{rev}=-3V, V_{pulse}=+2.5V, (b)- V_{rev}=-3V, V_{pulse}=+4.0V, (c)- V_{init}=0.2 V, V_{pulse}=1.2 V. (d)- Arrhenius plot for responses detected in (b).

In the temperature range 200..260 K positive peaks correspond to the response from a majority-carrier trap. However, correct estimation of its parameters is difficult due to overlapping *S(T)* with an unknown peak at temperatures 160..200 K which does not shift with the rate window. It leads to the appearance of a shoulder in the low-*T* side of peaks for high emission rates like in Figure IV.18 for DLTS spectra of sample #3. As suggested before, it can be associated with measurement problems in the start of capacitance transient since t_1 and t_2 are short. Also, *S(T)* starts to increase again at temperatures above 280..300 K up to the temperature limit of the used setup (360 K). This suggests the existence of another majority-carrier trap, but measurements up to 420 K in another setup also did not allow obtaining the level parameters due to monotonous DLTS signal increase and absence of maxima in *S(T)* spectra even for low e_r at high temperature. Therefore, this can be attributed to the response from a defect with large activation energy and

with a high peak amplitude and broad width of *S(T)* spectra. This behavior suggests the presence of a broadened defect with a high activation energy. A similar response was observed early for unintentionally doped layers of GaP:N[152], where it was associated with EL2 defect typical for GaAs[153]. Future experiments could be focused on the modification of the setup in order to be able to heat the sample up to 600 K for a correct estimation of defect parameters.

An attempt was made to improve the DLTS spectra by amplification of the defect response to exclude the influence of the unknown peak for high rate windows so DLTS was performed at the filling pulse value of +4 V instead of +2.5 V (Figure IV.23b). It leads to a deeper extension region inside the InP/GaPN layer during the filling pulse and emission from more defects after its end so the peak amplitude increases. Similar approach was used for DLTS measurements in sample #3 when forward bias voltage was applied (Figure IV.20a). Band diagram at these experimental conditions is presented in Figure IV.24 for sample #4.

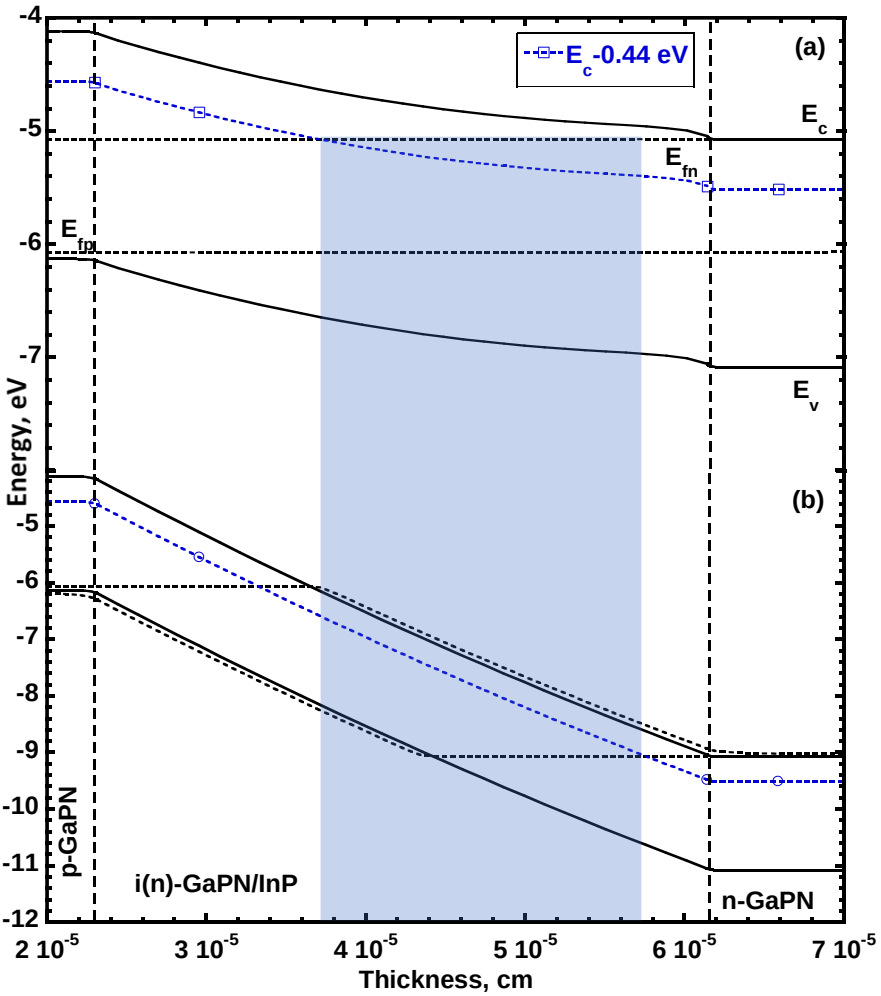

Figure IV.24 Band diagram of sample #4 at +1.0 V(a) and -3.0 V(b).

Series of clear *S(T)* peaks is observed in the temperature range of 200..260 K like in previous measurements (Figure IV.23a), but their amplitude is higher and the influence of the unknown peak can be neglected. According the Arrhenius plot (Figure IV.23c), these peaks correspond to the response from a defect level with an activation energy E_a=0.44 eV, and a capture-cross section $\sigma=1.7\times10^{14}$ cm^2. A defect with similar parameters was early observed in the GaPN[92] and GaP:N[86–88] layers grown on GaP wafers. This defect was a majority- carrier trap in similar *n*-type layers in these works so it indirectly indicates background doping of *n*-type in our *i*-InP/GaPN layer. Possible structure of defect was proposed previously as the complex based on a pair of nitrogen atoms at the phosphorus sites (N_P-N_P) and the vacancy of gallium V_{Ga}, arising as a result of displacement of gallium due to incorporation of nitrogen in the GaP lattice. Another interesting question is the nature of the defect at E_c-0.55 eV in samples #2 and #3 with *i*-layers of GaPAsN. The similar temperature region of detected peaks on DLTS spectra *S(T)* and values of parameters suggest a correlation between this defect and the defect at E_c-0.44 eV detected in InP/GaPN. Perhaps, the latter transforms into the former due to additional arsenic content in the alloy. This suggestion should be considered in future studies.

The peaks on *S(T)* spectra associated with the defect at E_c-0.44 eV are broadened and their peak value increases versus rate window. Also, the peak value increases with increasing filling pulse duration from 1 ms to 50 ms (Figure IV.25a). On the other hand, the peak value saturates for filling pulse duration longer than 100 ms (Figure IV.25b). Consequently, it suggests that point defects based on N_P-N_P and V_{Ga} with E_a=0.44 eV can transform into extended defects with some energy distribution in compounds of dilute nitrides (In)GaPN. It is caused by higher nitrogen incorporation than in GaP:N semiconductors and local composition fluctuation in alloys due to possible nitrogen clusterization. The similar behavior of DLTS spectra *S(T)* was obtained for defects detected in previous samples with dilute nitrides in this study. The defect concentration was estimated with condition of $N_D=7\times10^{15}$ cm^{-3} and we found a value of 2×10^{14} cm^{-3}.

The lack of response from the defect detected by admittance spectroscopy in Figure IV.23b is explained by the low value of activation energy E_a=0.08 eV, since its peak on DLTS spectra *S(T)* should be at temperatures below 80 K. On the other hand, clear high-temperature peaks appear in the spectra *S(T)* when V_{pulse} is set to +4 V corresponding to forward bias voltage of +1V during the filling pulse (Figure IV.23b). We suggest these peaks are the sum of responses from deep minority- and majority-carrier traps since holes are injected in the SCR in this regime. Thus, simultaneous emissions are observed after return to V_{rev}=-3 V from both traps at high temperatures. Initially *S(T)* increases due to the response from an electron trap, but further the response from a hole trap rapidly rises leading to negative contribution in *S*(*T*) and it decreases: we observe local "false" peaks in *S(T)* spectra. To confirm the existence of minority-carrier traps DLTS was

measured under the following conditions: V_{init}=0.2 V, V_{pulse}=1.2 V, t_{pulse}=50 ms (Figure IV.23c) to enhance hole injection in the SCR. As a result, spectra *S(T)* remain almost the same at temperatures below 160 K, but at higher temperature the *S(T)* curve strongly decreases due to the contribution of a minority-carrier trap. The estimation of its parameters is impossible since the peaks are not observed in the used temperature range. Thus, according the experiments there are deep traps with high activation energy for holes and electrons in the *i*-InP/GaPN layer of sample #4, but the precise estimation of their parameters is impossible due to overlapping of their responses and to the limited available temperature range (below 400 K).

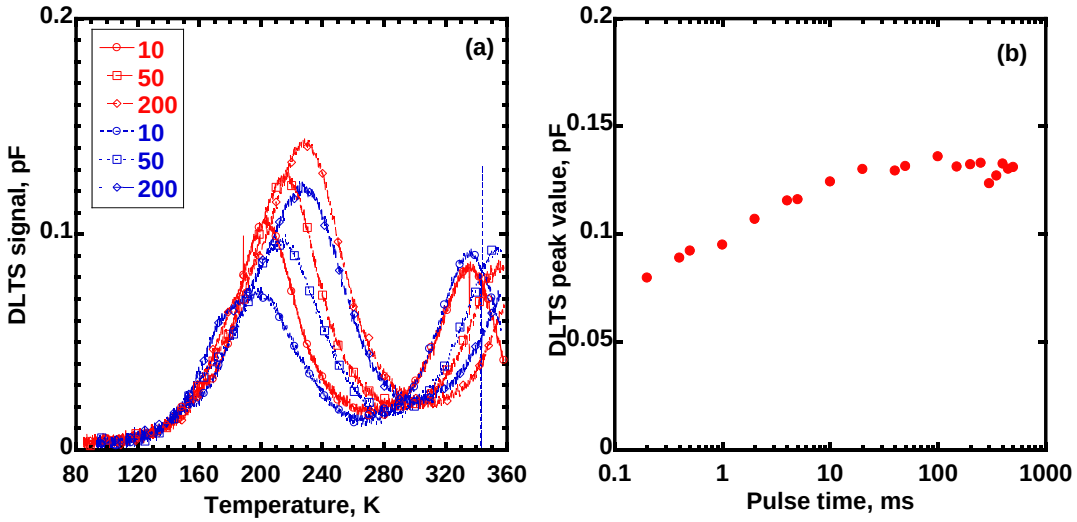

Figure IV.25 (a)- spectra *S(T)* of the defect at E_c-0.44 eV for filling pulse duration of 1 ms (blue) and 50 ms (red) in sample #4, (b)- dependence of peak value for e_r=50 s^{-1} on filling pulse duration.

Finally, the DLTS method allowed us to detect deep levels in the *i*-layer of InGaPAsN. Sample #2 has responses from the defect levels at E_c-0.18 eV (that is also detected by AS), E_c-0.55 eV and E_v+0.44 eV. The concentration of the latter was strongly reduced after post-growth treatment in sample #3, and the concentration of the defect level at E_c-0.55 eV was also slightly reduced. This may explain the better photovoltaic properties of sample #3 compared to sample #2 since both defects affect the lifetime in dilute nitrides. In addition, sample #4 (with *i*-InP/GaPN layer) exhibits the defect level at E_c-0.44 eV, which has a similar nature as E_c-0.55 eV in *i*-GaPAsN. Furthermore, we suggest the existence of deep-level traps near to the middle of the bandgap in the InP/GaPN layer, which can be considered as centers of non-radiative recombination. On the other hand, such responses were not observed in samples #2 and #3 with *i*-GaPAsN (in the explored temperature range). This may explain the poorer photoelectric properties of SCs with *i*-InP/GaPN (#4) compared to that with *i*-GaPAsN (#2, #3) layers. Therefore, *i*-

GaPAsN with post-growth treatment (sample #3) is considered as the most suitable for photovoltaic applications and should be studied in more details in future works.

IV.2 Double-junction solar cells on Si wafers

IV.2.1 Samples description

Fabrication of multi*-i*-junction solar cells with active layers of III-V compounds on silicon wafers is an attractive challenge for researchers. However, as described above there are not many studies of structures with good quality and high efficiency due to growth problems. Therefore, this work presents some investigation of MJSC grown on silicon wafers with active layers of dilute nitrides by the MBE method. Principle scheme of studied double-junction SCs is presented in Figure IV.26. Triple-junction SC is formed by the addition of a subcell similar to the top subcell in double-junction SC but with larger bandgap energy of *i*-layer.

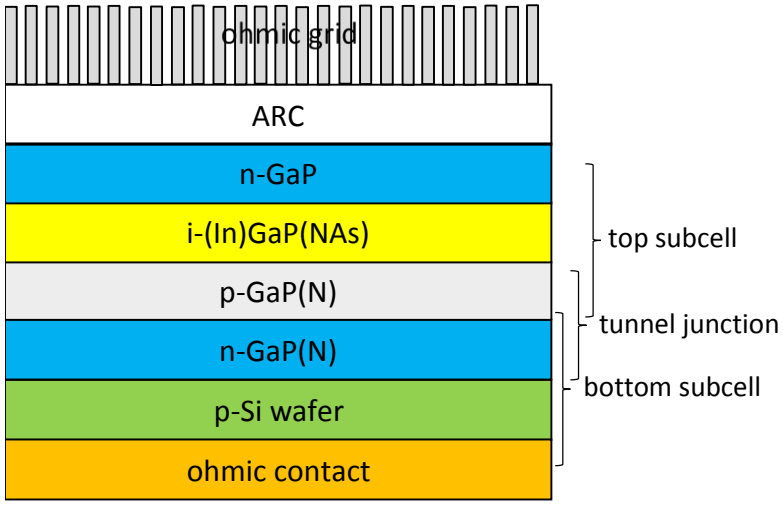

Figure IV.26 Schematic view of double-junction GaP(AsN)/Si solar cells.

The present SCs consist of two subcells: bottom with silicon junction (E_g=1.12 eV) and top with GaP(AsN) junction (E_g=1.8-2.0 eV). According to the study of single-junction solar cells presented above, the top subcell should be based on a *p-i-n* junction with undoped layer of dilute nitrides. However, the structure can be grown on both *n*- or *p*-type silicon wafer, furthermore the bottom junction can be formed as a silicon homojunction or a GaP/Si heterojunction. All these features were explored in detail in our previous work[154]. Here, only the main conclusions are presented. Three single-junction SCs were grown by MBE on silicon wafer with subsequent junction: *p*-GaP/*n*-Si, *n*-GaP/*p*-Si and *n*-GaP/*n*-Si/*p*-Si. In the last one *n*-Si layer was fabricated by pre-growth wafer annealing in phosphorus flow. The *p*-GaP/*n*-Si heterojunction shows the worst performance due to limitation of carrier transport by the potential barrier for holes caused by the

high valence band offset of 0.8-1.0 eV[67,155]. Further, the *n*-GaP/*n*-Si/*p*-Si isotype heterostructure is preferable for photovoltaic application compared to the anisotype *n*-GaP/*p*-Si heterojunction since quantum efficiency of the first one is higher. Reason for the difference is the defective layer formed in silicon wafer near to the interface. In *n*-GaP/*n*-Si/*p*-Si it lies in the highly doped *n*-Si emitter, but in *n*-GaP/*p*-Si it lies in lowly doped *p*-Si base. In the second case, defects have much higher influence on the SC performance due to higher impact of non-radiative recombination in the base. Consequently, the isotype structure of *n*-GaP/*n*-Si/*p*-Si shows the best performance and it is used in all MJSC in the current work. The phosphorous flux was being directed on the *p*-type (p=1.0×10^{16}cm^{-3}) silicon wafer for 10 minutes at 500 °C without growth. Then the migration-enhanced epitaxy was used for the growth of a thin nucleation layer of GaP as an initial step for the improvement of the quality of subsequently grown III-V compounds. More information can be read about growth conditions of *n*-GaP on *p*-type silicon wafer elsewhere[64].

Afterwards, tunnel junctions were grown and subsequent *p*-*i*-*n* junction as a top subcell. Three double-junction SCs were grown with undoped *i*-layer of III-V compounds with different composition. Sample #5 (Figure IV.27a) is grown with a *i*-layer of $GaP_{0.70}As_{0.30}$ 400 nm thick as a test structure for studies of structural properties of III-V alloys on silicon wafers. Thickness of top *n*-GaPAs contact layer is 250 nm. As described above atoms of In and As are used for improvement of GaPN quality. For this reason, double-junction SC with ternary alloy was not grown. Thus, indium is added for compensation of elastic stresses in GaPN and SDA *i*-InP/GaPN (200nm) is used in sample #6 (Figure IV.27c). In sample #7 (Figure IV.27d) *i*-$GaP_{0.882}As_{0.10}N_{0.018}$ layer 200 nm thick is grown with additional arsenic content for compensation of elastic stresses in GaPN. Therefore, top subcells of sample #6 and sample #7 correspond to single-junction SCs #4 and #3 that were described and studied in preceding sections. Finally, triple-junction SC (sample #8, Figure IV.27e) is formed by addition of the top *p*-*i*-*n* subcell with *i*-$GaP_{0.987}N_{0.013}$ 150 nm thick to sample #7. Thickness of top *n*-GaP contact layer is 200 nm for #6- #8 samples. Studied sample #8 is the first triple-junction SC with active layers of dilute nitrides grown on silicon wafers since, to the best of our knowledge, there are no data published in literature about such SC.

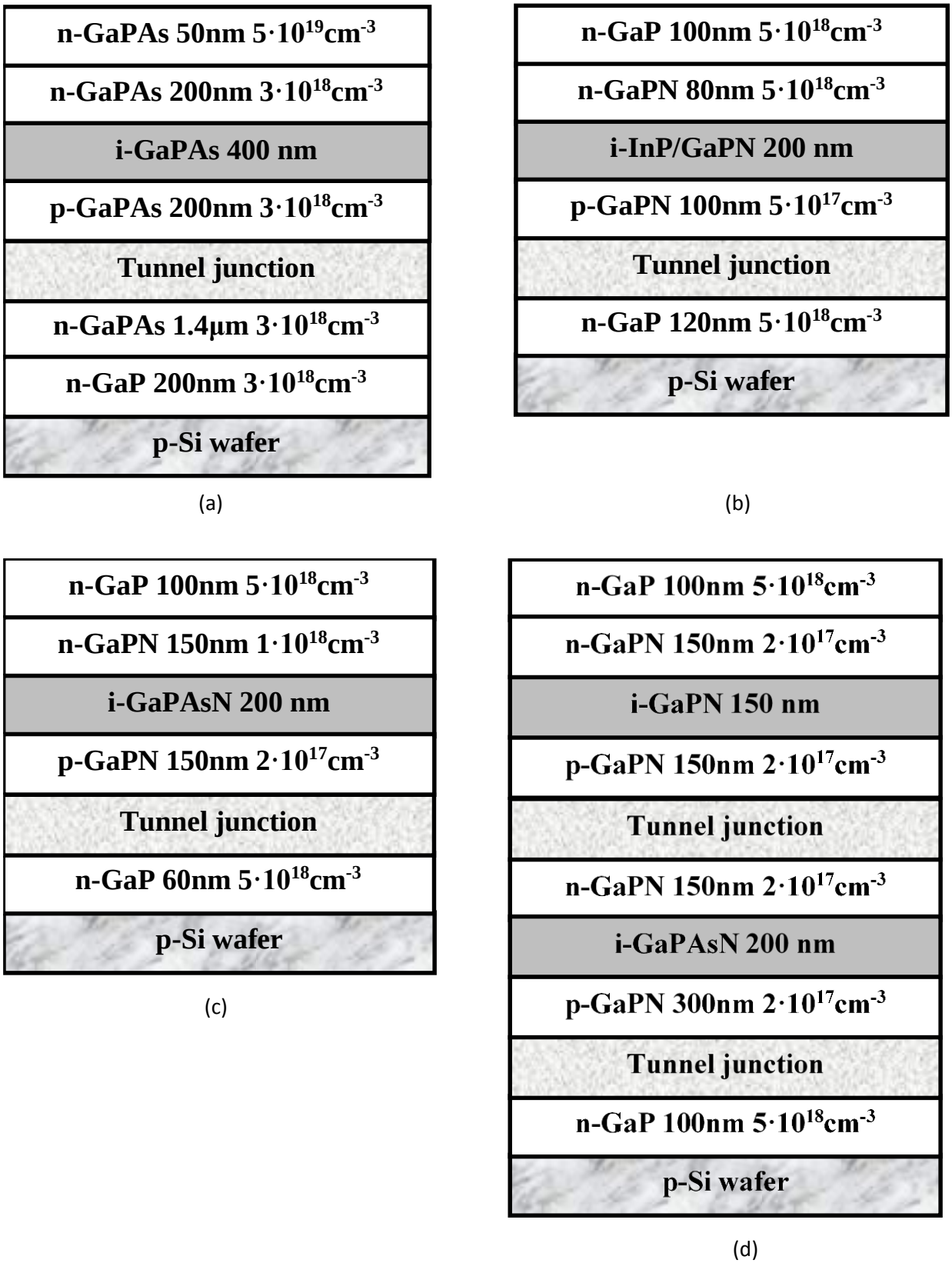

Figure IV.27 Schematic view of multi-junction solar cells grown on *p*-Si wafers: sample #5 (a), sample #6 (b), sample #7 (c), sample #8 (d).

For further electrical and capacitance measurements ohmic contacts were fabricated to the top and the bottom side of samples. The detailed description of this technology is presented in Appendix C.

IV.2.2 Quantum efficiency and I-V curves

Current-voltage characteristics under illumination are presented in Figure IV.28 for MJSC. Their important parameters are presented in Table IV.3. The MJSC based on ternary alloys of GaPAs has very low value of short-circuit current of 0.79 mA/cm^2 and open-circuit voltage of 0.89 V. It means very poor quality of materials and layers in this structure. However, sample #6 with InP/GaPN shows much higher V_{OC} at 1.59 V meaning that both subcells contribute in this value since it is higher by 0.35 V than for single-junction SC with the same active layer of InP/GaPN. The short-circuit current (J_{SC}=1.29 mA/cm^2) is higher than in sample #5, but it is lower than in single-junction SC #4, possibly, due to smaller *i*-InP/GaPN thickness of 200 nm. The substitution of InP/GaPN by GaPAsN in sample #7 leads to a drop of open-circuit voltage down to 1.39 V due to lower bandgap energy and increase of short-circuit current up to 2.1 mA/cm^2 in the same time. The bending on I-V curve of sample with *i*-GaPAsN can be due to non-optimized front contact. Nevertheless, both samples #6 and #7 have low fill factor so the technology of front contact fabrication must be developed and optimized in future experiments. The I-V curve of triple-junction SC shows J_{SC}=1.02 mA/cm^2 and V_{OC}=2.23 V so all three subcells work, but it has bending and poor fill factor of 54% due to non-optimized front contact.

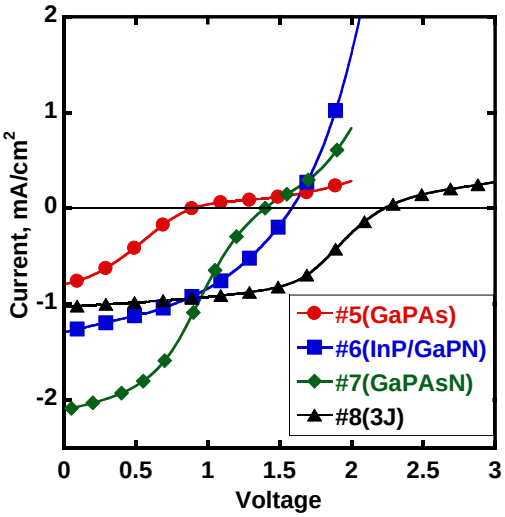

Figure IV.28 Current- voltage characteristic of multi-junction solar cells under illumination of solar simulator at 1 sun, 25°C.

Sample	*i-layer*	V_{OC}, V	J_{SC}, mA/cm^2	*FF*, %
#5	GaPAs	0.89	0.79	38
#6	InP/GaPN	1.59	1.29	40
#7	GaPAsN	1.39	2.1	38
#8	3J	2.23	1.02	54

Table IV.3 Parameters of multi-junction solar cells performance.

The external quantum efficiency was measured by the method described in Chapter II for MJSC. Additional illumination of infrared and ultra-violet diode is used for measurements of EQE in top subcells and bottom subcells, respectively. Result of experiments are presented in Figure IV.29 for all samples. Firstly, integral and peak values of EQE in the bottom silicon subcell are much higher than in the top subcell for all structures. It is due to the lower bandgap energy (1.12 eV) and much better quality of crystalline silicon. In this case, the photogenerated current is much higher in the bottom subcell and it reaches a value of 20 mA/cm^2. It is well-known, that the total current of a MJSC is equal to the smallest current value for all subcells in series. Therefore, the current of the top subcell with dilute nitrides limits the performance of the overall structures due to very low quantum efficiency.

EQE of sample #5 with $GaP_{0.70}As_{0.30}$ exhibits a single peak, but its integral value is very low due to the high bandgap energy of 2.26 eV. The shape of the EQE curve of sample #6 is similar to that of the single-junction SC with InP/GaPN (sample #4) and has two characteristic peaks corresponding to two transitions with E_- and E_+ energies. The integral and maximal value of EQE is larger than in GaPAs even if the thickness of GaPAs is 400 nm and thickness of InP/GaPN is only 200 nm. Therefore, dilute nitrides are more favorable for photovoltaic application than GaPAs. Unfortunately, the lower thickness leads to lower EQE than in the single-junction SC (sample #4) where the thickness was 350 nm. Utilization of quaternary alloy of GaPAsN (sample #7) allows to enhance the quantum efficiency of the top subcell and it becomes larger than in sample #6 (maximal value reaches 21%). EQE curves of the top subcell in samples #5-#7 are shown in one graph for more comfortable perception (Figure IV.29e). Consequently, GaPAsN is the most preferable composition of dilute nitrides for utilization in active *i*-layers of top *p*-*i*-*n* subcells in MJSC grown on silicon wafers. The same conclusion was suggested for single-junction SCs grown on GaP wafers in the previous section.

Fabrication of a triple-junction SC is not only a complicated growth task but also leads to measurement problems for the quantum efficiency. Suggested bandgap energies are very close between top (E_g=2.06 eV) and middle (E_g=1.90 eV) subcells so it is necessary to be very careful and accurate to distinguish responses from them separately. Standard UV illumination was used

for the measurement of the silicon subcell and a good curve was obtained. Further, reasonable measurements of the top subcell is obtained under simultaneous illumination of IR diode (900 nm) for saturation of the bottom subcell and red diode (650 nm) for saturation of the middle subcell. As a result, the shape of the curve has the behavior with two peaks typical for dilute nitrides. Integral and peak values of this curve are comparable with those obtained in double-junction SCs with InP/GaPN and GaPAsN. It means that it is technologically possible to grow a third subcell with photoelectrical properties similar to that of the active layers in the top subcell of double-junction SCs. The measurement of the middle subcell is the most difficult task in the observed sample #8 due to close bandgap energies of active layers in wide-gap subcells so they are photosensitive in almost the same region of the solar spectrum. Illumination of UV diode is used for saturation of the top subcell, but the low thickness of its undoped *i*-GaPN cannot fully absorb the light leading to undesirable absorption in the middle subcell. Thus, the latter involves the contribution of an additional current therefore a reverse bias voltage of 1.6 V was applied to compensate its influence. Also, illumination of IR diode is used for the saturation of the bottom silicon subcell simultaneously. As a result, the EQE of the middle subcell could not be precisely measured in the short wavelengths region but long-wavelength side of the curve was successfully obtained. Its edge corresponds to the bandgap energy of the $GaP_{0.882}As_{0.10}N_{0.018}$ active layer of the middle *p-i-n* junction so it generates electron-hole pairs and demonstrates photovoltaic properties. Consequently, the quantum efficiency of triple- junction SC was measured for each subcell and all three subcells work.

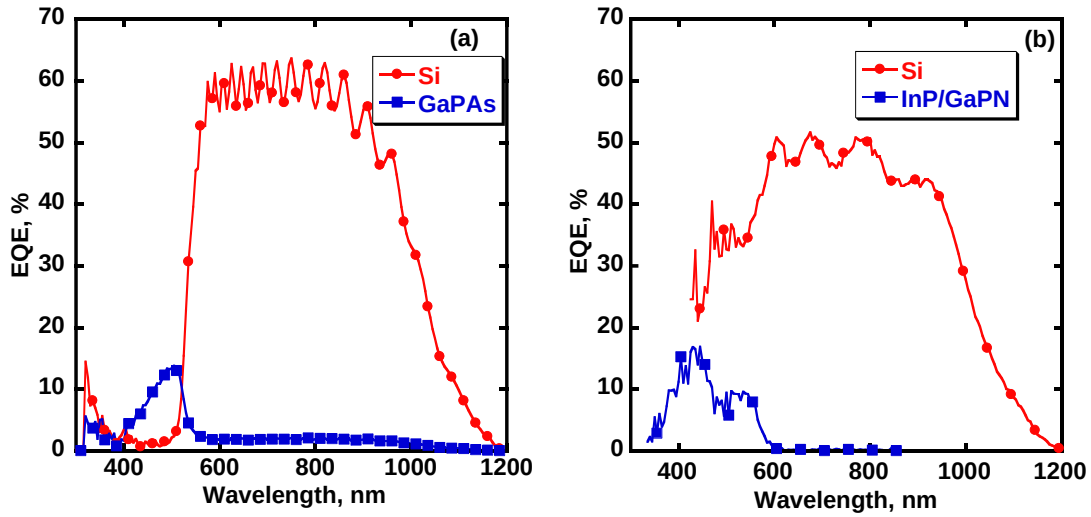

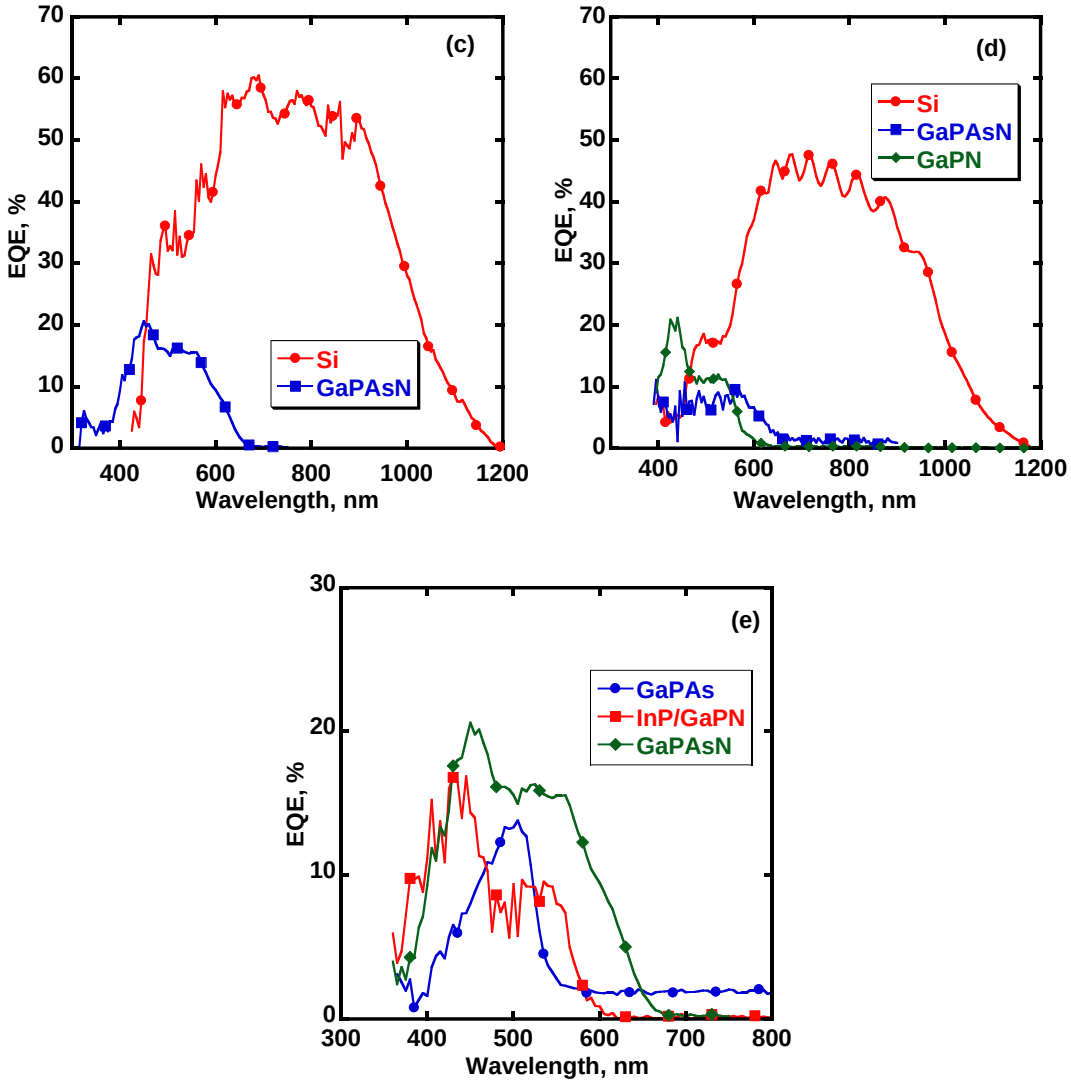

Figure IV.29 External quantum efficiency of double-junction solar cells with an active layer of GaPAs(a), InP/GaPN(b), GaPAsN(c) and triple- junction solar cell (d); e- zoom on the response of top subcells.

IV.2.3 Capacitance measurements of double-junction solar cells

In this section, capacitance methods are applied to study double-junction SCs. It is not so simple as in single-junctions since there are two junctions in series in the structures: bottom p-n^+ homojunction in the Si wafer and top p-i-n junction based on III-V alloys. Thus, we can detect defect responses from both junctions. For this reason, firstly we grown a special structure n-GaP/ n^+-Si/p-Si identical to the bottom subcell in MJSCs and the DLTS spectra $S(T)$ were measured for different rate windows under the following conditions: V_{rev} = -3.0 V, V_{pulse} = +2.8 V, t_{pulse}= 20 ms (Figure IV.30).

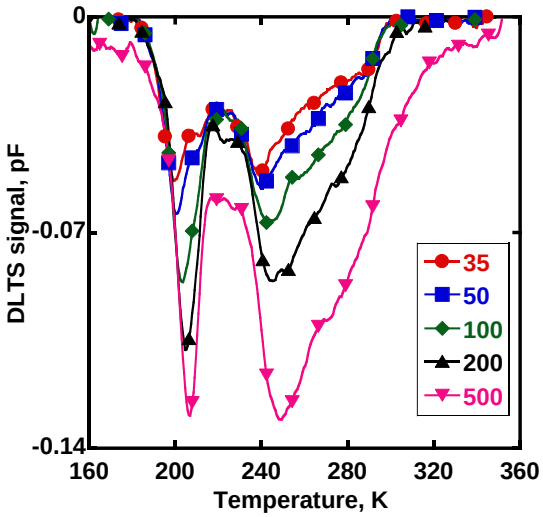

Figure IV.30 DLTS spectra *S(T)* for a test *n*-GaP/ *n*+-Si/*p*-Si sample for different rate windows (in s^{-1}) with the following conditions: V_{rev}= -3.0 V, V_{pulse}=+2.8 V.

DLTS spectra have features in the temperature range of 200-300 K which can be associated with overlapping responses from possible minority-carrier traps. However, the DLTS signal is low and noisy so it is impossible to correctly estimate defect parameters. Also, responses from minority-carrier traps are surprising since we used only reverse bias voltages in the experiments and according to the DLTS theory we should detect only majority-carrier responses. For this reason, DLTS data should be considered very critically. Nevertheless, DLTS spectra do not show any high positive peaks associated with responses in *p*-Si from majority-carrier traps. Consequently, if the DLTS spectra exhibit positive peaks in double-junction SCs, they must be associated with responses from defects in the top *p-i-n* junction, not in the bottom *p-n* silicon homojunction.

Consequently, in the current section, mesa-structures of double-junction SCs with active layer of GaPAs (#5), InP/GaPN (#6) and GaPAsN (#7) were fabricated (see Appendix C.2) and investigated by admittance spectroscopy, DLTS and Laplace-DLTS. Results are subsequently shown for each method for the three samples and then a discussion is presented for all detected defects.

First, the measured temperature dependences of the capacitance *C(T,f)* are shown in

Figure IV.31. The steps in the capacitance (which are accompanied by conductance peaks) observed for the samples are shifted toward higher frequency when the measurement temperature is increased. Such steps are characteristic for the response of gap states and may be caused either by bulk defect levels in the undoped layer or by interface states at the III-V-N/GaP(N) heterojunctions. The measurements of *C(T,f)* at different bias voltages (not shown here)

demonstrate that the step positions are independent of the applied bias voltage indicating that the response originates from bulk defects rather than from the interface.

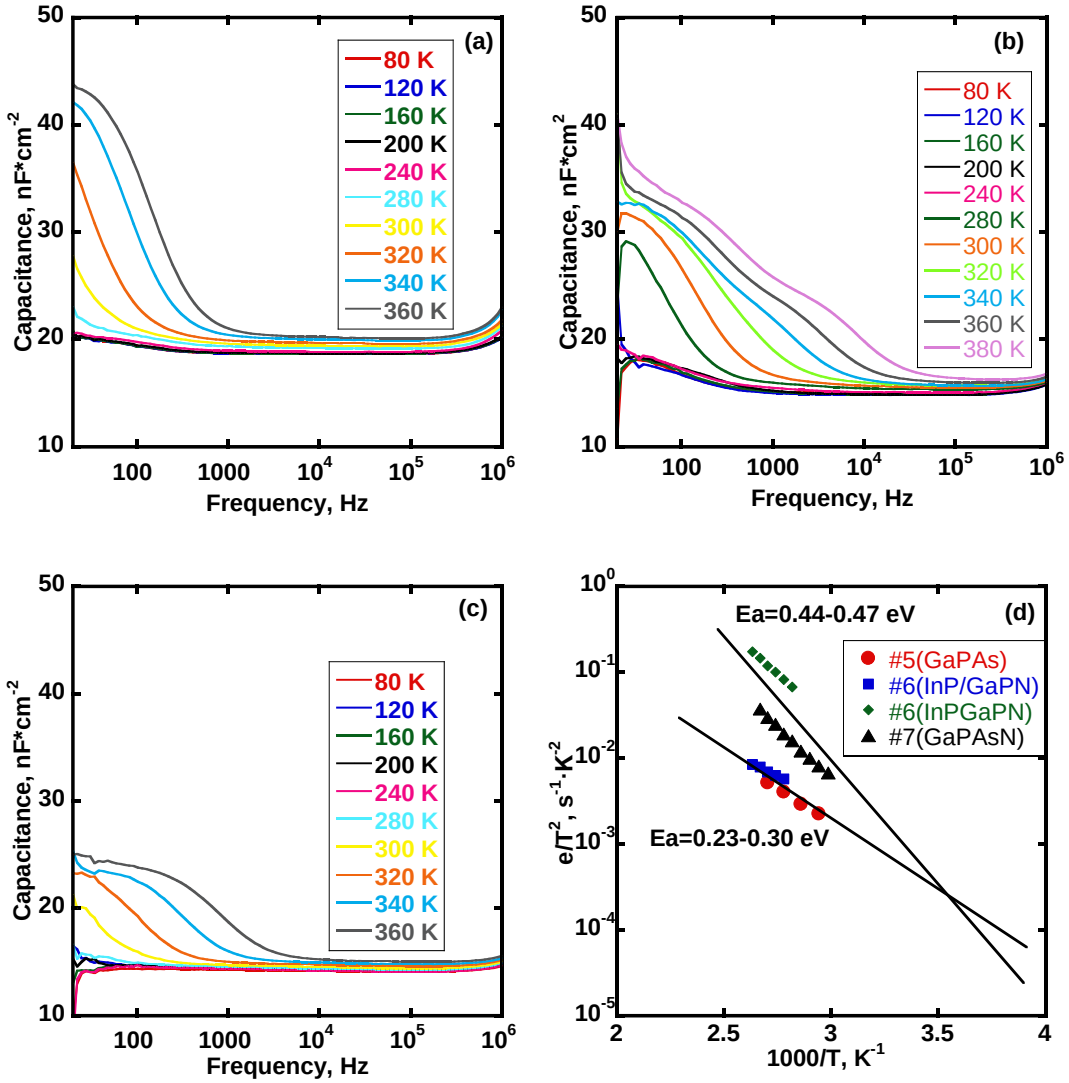

Figure IV.31 Capacitance spectrum *C(T,f)* for a- sample #5 with GaPAs, b- sample #6 with GaPN/InP, c- sample #7 with GaPAsN. d- Arrhenius plot of e/T^2 for the defects identified by admittance spectroscopy.

Sample #5 with an active layer of GaPAs exhibits a pronounced step in the capacitance curves at high temperatures 320-360 K (

Figure IV.31a). The Arrhenius plots are shown in

Figure IV.31d for all structures. For the GaPAs layer only one defect level with activation energy of 0.30 eV and low capture cross-section of $\sigma=3.8\cdot10^{-19}$cm^2 was observed. For the sample #6 *C(T,f)* curves (

Figure IV.31b) suggest the overlapping of several defect responses for the GaPN/InP layer. Detailed analysis of the *C(T,f)* derivative and *G(T,f)* curves (not presented here) has allowed us to

distinguish two capacitance steps (conductance peaks) that correspond to the response from two different defect levels, which are presented in

Figure IV.31d. While the exact determination of the activation energy and capture cross section is difficult for this structure, the first defect level seems to have the parameters E_a=0.23 eV and $\sigma=1.8\cdot10^{-20}$cm^2 and it looks similar to the defect observed for GaPAs sample #5 according to the Arrhenius plot. The second defect level with E_a=0.44 eV and $\sigma=1.3\cdot10^{-16}$cm^2 has similar parameters to the sample #7 (GaPNAs), which according to

Figure IV.31c exhibits only one defect response with E_a=0.47 eV and $\sigma=2.0\cdot10^{-16}$cm^2.

Further, the DLTS spectra *S(T)* were measured on mesa-structures for different rate windows under the following conditions: V_{rev}=-1.0 V, V_{pulse} = +1.0V, t_{pulse}=50 ms (Figure IV.32a-c). Arrhenius plots for the detected responses are also presented (Figure IV.32d).

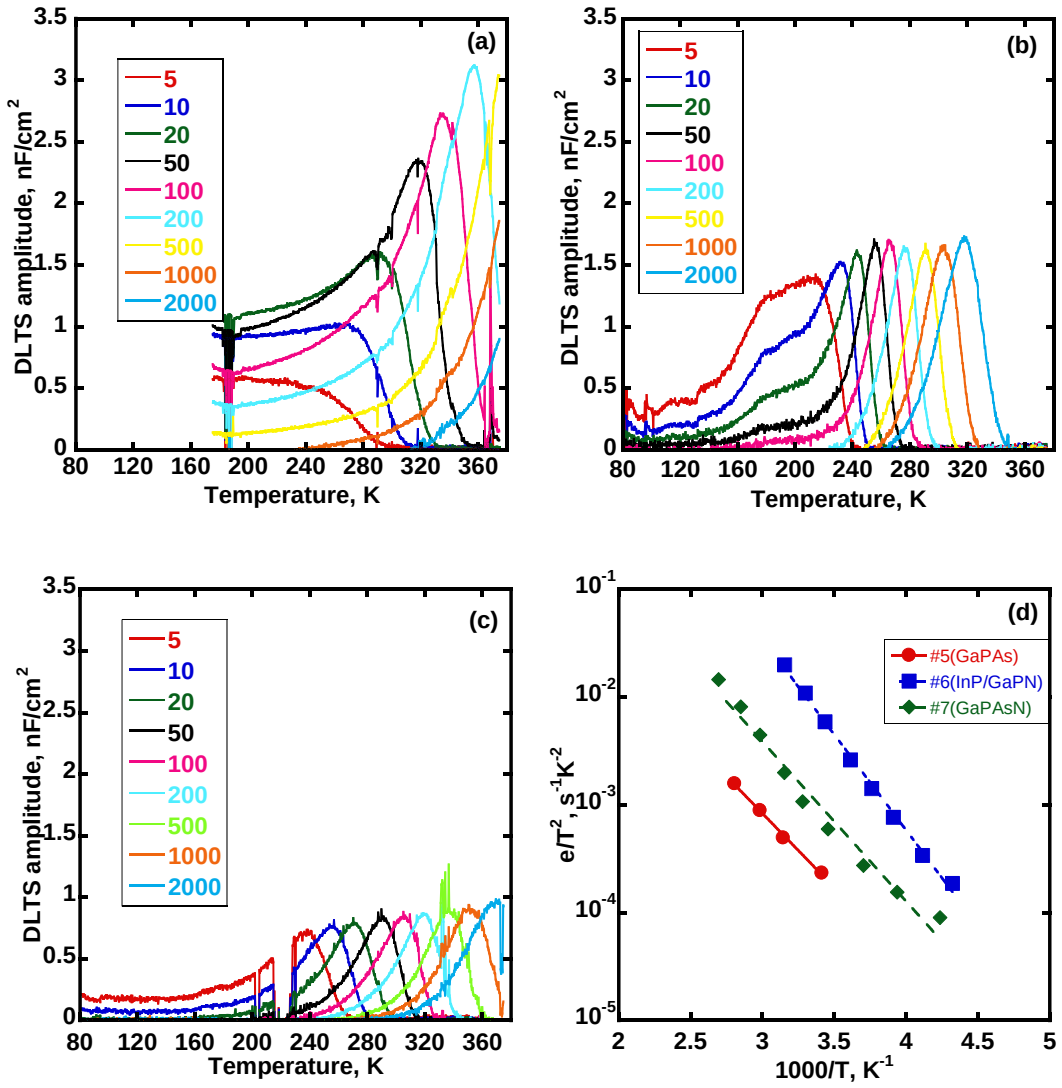

Figure IV.32 DLTS spectra *S(T)* for samples: (a)- #5, (b)- #6 and (c)- #7 for different rate windows (in s^{-1}) with the following conditions: V_{rev}=-1 V, V_{pulse}=+1 V. (d)- Arrhenius plot of e/T^2 for the defects identified by DLTS for samples.

A series of broadened peaks with high positive amplitude is observed in spectra *S(T)* of sample #5 (with GaPAs) at temperatures above 300 K. It corresponds to a defect level with E_a=0.27 eV and $\sigma=1.0\cdot10^{-20}cm^2$. Measured data at low temperature are very noisy and unstable so they are not presented here, but there are not any responses detected in this region. The sample #6 with InP/GaPN also has some measurement problem. It is the shoulder on the *S(T)* spectra at a temperature of 180 K for low rate windows. But it does not affect the useful signal of responses from a defect level in the temperature range of 240..330 K. It allows to estimate parameters of this level: E_a=0.37 eV and $\sigma=1.5\cdot10^{-17}cm^2$. The sample #7 also has one series of positive peaks in the temperature range of 240..350 K. However, its data on the Arrhenius plot are not a straight line in all the range. It can indicate the existence of responses from two defect levels in the same time but estimation of parameters for the defect at lower energy is impossible due to the higher responses from the defect detected at high temperatures. Thereby, the parameters of the latter are estimated from data in the straight part of the Arrhenius plot: E_a=0.40 eV and $\sigma=4.5\cdot10^{-18}$ cm^2. According to the Arrhenius plots, it can be concluded the similar nature of detected defects by DLTS, but it is not true. It is clear that behavior of spectra *S(T)* of sample #5 is strongly different from responses in sample #6 and #7 since their peaks are narrow and close to each other. It means existence of point defect in InP/GaPN and GaPAsN. The higher peak amplitude means higher defect concentration in GaPAs layer than in other both samples. But peak amplitude is lower in sample #7 than in #6 so GaPAsN should have better quality than InP/GaPN. Furthermore, it is not observed growth of *S(T)* value at high temperature after peaks in both samples so it suggests absence of responses from defect levels with higher activation energy in this layers. Thereby, detected responses should be single and they can be considered as centers of non-radiative recombination responsible for lifetime charge carriers.

According to admittance spectroscopy, InP/GaPN layer has two defect levels, and GaPNAs also should have two overlapping responses in DLTS spectra *S(T)*. Consequently, the Laplace-DLTS method was used to obtain additional information about defects in considered structures. The Laplace-DLTS spectra for different temperatures for samples and Arrhenius plot for detected defects are presented in Figure IV.33.

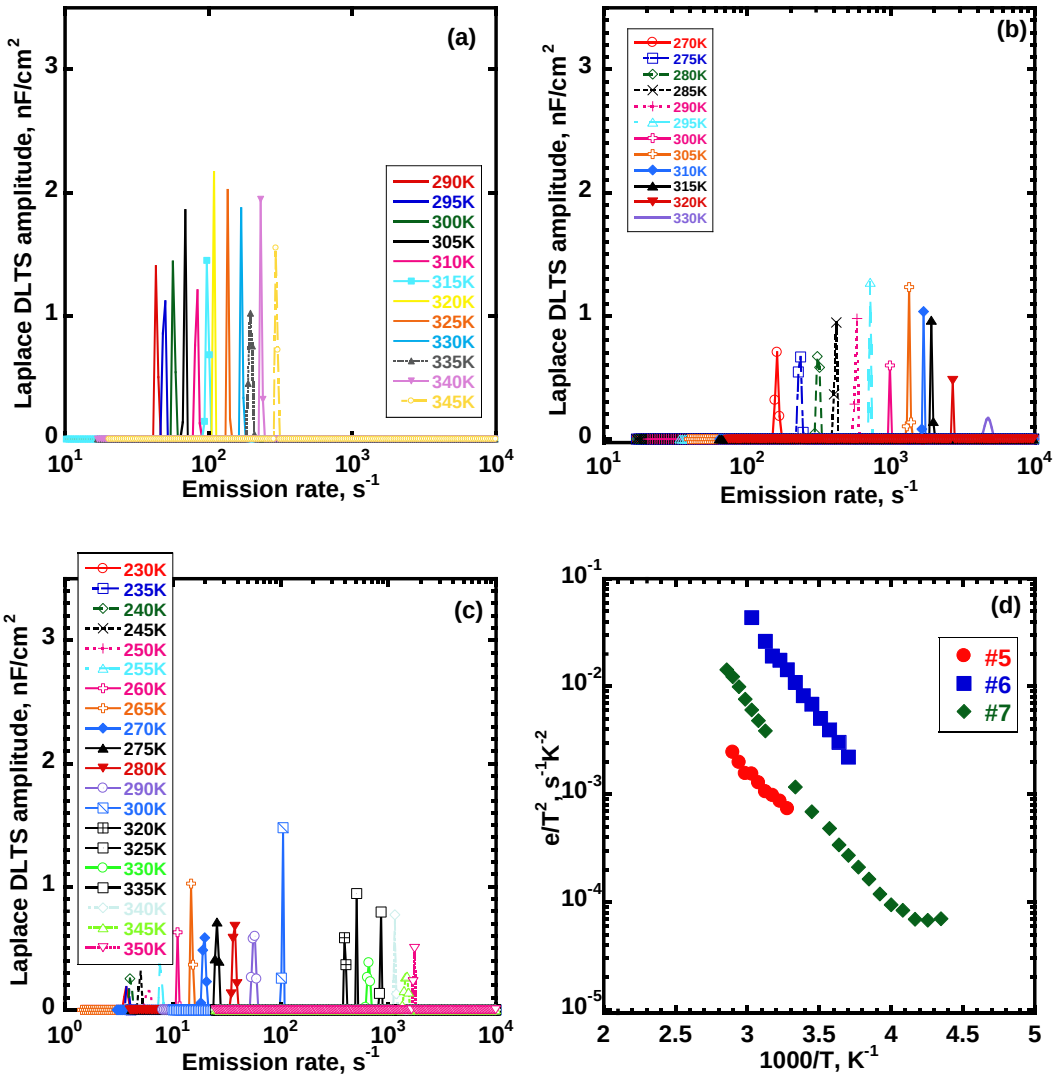

Figure IV.33 Laplace DLTS spectra *S(T)* for samples: (a)- #5, (b)- #6 and (c)- #7 at different temperatures. (d)- Arrhenius plot of e/T^2 for the defects identified by Laplace DLTS for samples.

Sample #5 with GaPAs has one series of peaks corresponding to defect level with following parameters: E_a=0.26 eV and $\sigma=1.3\times10^{-20}$ cm^2. These parameters correlates with defect detected by classical DLTS and admittance spectroscopy. Then, sample #6 has only one series in Laplace DLTS spectra associated with defect with higher values of parameters than in sample #5: E_a=0.37 eV and $\sigma=1.5\times10^{-17}$ cm^2. Therefore, it is the same response detected by classical DLTS for this sample. However, in sample #7 non-linear behavior of graph is observed in range 3.7..4.5 of 1000/*T* on Arrhenius plot. Absolutely the same situation is observed as in classical DLTS experiments for this sample. It suggests responses from two defect levels, and Laplace DLTS should distinguish them but other peak series are not found in spectra *S(T)*. Possible explanation is complex nature of defect and additional temperature dependence of pre-exponential factor in Arrhenius equation due to composition fluctuation in alloy of dilute nitrides. Parameters of defect was estimated in linear region for high temperatures: E_a=0.50 eV and $\sigma=2.7\times10^{-14}$ cm^2.

Finally, Arrhenius data obtained by the three methods were summarized for each sample and are shown in Figure IV.34.

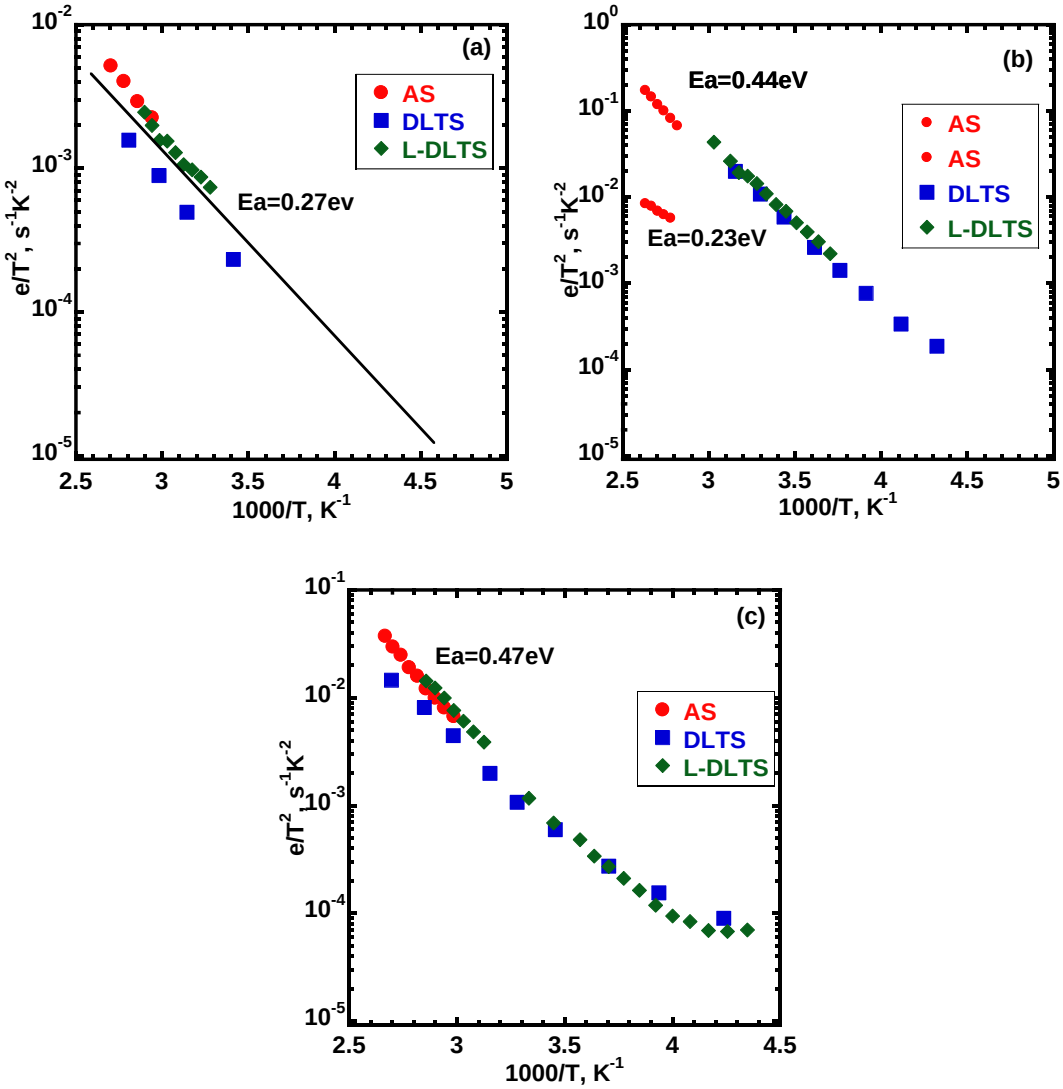

Figure IV.34 Arrhenius plot of e/T^2 identified in capacitance measurements in samples: a- #5, b- #6, c- #7.

Obviously, only one defect level with *Ea*=0.27 eV and $\sigma=2.0\times10^{-20}$ cm^2 was detected in sample #5 with GaPAs *i*-layer. It is confirmed by three independent experimental methods. It has higher concentration than another defect detected in sample #6 and #7, possible, due to big arsenic content of 30% in the ternary alloy. It leads to fluctuation of composition and favorable conditions for defect formation during the growth process so the quantum efficiency of this solar cell is lower than in samples #6 and #7. Estimated value of capture cross section is low and it should not strongly affect the lifetime of charge carriers, but non-exponential behavior of capacitance transient can lead to error in the estimation of its parameters. Unfortunately, the used temperature range does not allow to explore other possible defect levels, but the response from *Ec*-0.27 eV is

so strong that they would not be clearly observed even at higher temperature due to overlapping with it.

For sample #6, result of classical DLTS coincide with that of Laplace DLTS, and according to them only one defect should exist in the *i*-InP/GaPN layer. Also, the capacitance-frequency dependence has only one knee in

Figure IV.31b at temperature below 340 K suggesting response from only one single defect level. Therefore, all results show the same behavior at temperatures below 340 K. On the other hand, admittance spectroscopy for mesa-structures allowed to distinguish two responses at temperatures above 350 K (1000/T<3 in graph) unlike DLTS methods. Possibly, there are two defects with such parameters leading to strong overlapping of their responses at temperatures below 340 K corresponding to low emission rates for both methods of DLTS and admittance spectroscopy. Separation of responses is observed only at temperature above 340 K corresponding to emission rates more 5000 s^{-1}. It is a very high value so the capacitance transient occurs extremely quickly for this response and it cannot be correctly detected by the DLTS methods in the used equipment. Therefore, only precise high frequency admittance spectroscopy at high temperature allowed to distinguish responses from two defects and their parameters are estimated from its Arrhenius plot in

Figure IV.31d.

The Arrhenius plot shows almost the same dependence for all data obtained by the three methods in sample #7 with quaternary alloy of GaPAsN. First of all, there is a clear response corresponding to a deep defect level with parameters of E_a=0.47..0.50 eV and σ=(1-20)×10^{-15} cm^2. Also, responses from another defect is suggested at low temperature (region of 3.7..4.2 on Arrhenius plot), but it does not influence the dominant series of peaks associated with E_c-0.50 eV. Perhaps, it is also an overlapping of responses from two different levels like in sample #6. But measurements up to 380 K did not allow to detect another response nor appearance of additional features on capacitance-frequency curves. Thereby, other defects with low activation energy like 0.27 eV in GaPAs and 0.23 eV in InP/GaPN were not detected in the *i*-GaPAsN layer. Furthermore, amplitude of capacitance step and height of DLTS peaks are lower in sample #7 than in sample #6 so the defect concentration is lower in the GaPAsN layer than in InP/GaPN. In the same time, the quantum efficiency of top subcells with GaPAsN is better than with InP/GaPN. Thereby, the detected defects can be centers of non- radiative recombination leading to low lifetime of charge carriers in dilute nitrides. Consequently, layers of GaPAsN with 10% of arsenic are more suitable for application as a top subcell of double-junction solar cells than layers of InP/GaPN.

The defect with an activation energy of 0.44..0.47 eV is detected in sample #6 with the *i*-layer of InP/GaPN and sample #7 with *i*-GaPAsN, and it is not found in sample #5 with GaPAs layer. It suggests that nitrogen (N) plays a key role in the defect origin in the growth process. This defect has similar parameters with defect detected in single-junction solar cell #4 with *i*-InP/GaPN. As described above, it is associated with the formation of paired atoms of nitrogen in place of phosphorus in the GaP lattice (N_P-N_P) and gallium vacancy V_{Ga}. The observation the energy level at E_c-0.44 eV demonstrates a perfect correlation between properties of material in single- and double-junction solar cells based on dilute nitrides since it confirms that detected responses in double-junction SC come from the active layer of the top subcell with *i*-InP/GaPN unlike the bottom silicon subcell. Parameters of defect detected at low temperature in *i*-InP/GaPN look similar to those of defect detected in GaPAs so they can have similar nature of formation but this suggestion should be checked in future experiments.

However, InP/GaPN is better matched to the silicon wafer (mismatch is only 0.19 %) compared to GaPAsN (0.42%). On the other hand, local mismatch can be extremely higher due to formation of nitrogen clusters: it leads to a decrease in the lattice constant because of nitrogen atoms being incorporated in phosphorus sites. Additional content of As and In compensates the elastic stresses since it increases the lattice constant in the local area. It improves internal characteristics and photoluminescence of quaternary alloys of dilute nitrides compared to ternary alloys of GaPN[80,85,94] even if it is more lattice-mismatched to the GaP wafer. Also, according to photoluminescence measurements[80] indium incorporation into III-V-N alloys without As leads to higher non-radiative recombination losses than in III-V-N alloys containing As without indium. Indium being a III-group element is less efficient to compensate elastic stresses in the sub-lattice of V-group elements compared to arsenic in phosphorus sites (both being V-group elements). Therefore, additional content of arsenic leads to lower defect formation in studied solar cells and better photovoltaic performance than indium.

Consequently, mesa-structures of double-junction solar cells were explored by different capacitance methods. Sample #5 with GaPAs has the highest concentration of defect with activation energy of 0.22 eV. Two responses were explored in sample #6 with *i*-InP/GaPN: the defect with E_a=0.23 eV is similar to that in GaPAs, and another defect with E_a=0.44 eV associated with complexes of N_P-N_P and V_{Ga}. Sample #7 with GaPAsN has only one defect level at E_c-0.50 eV and lower concentration than in sample #6 since As better compensates elastic stresses in GaPN alloys. The defects at E_c-0.44 eV and E_c-0.50 eV can be considered as the main centers of non-radiative recombination in these layers since there are not other detected responses at high temperature up to the limit of our equipment.

IV.3 Influence of post-growth thermal annealing on solar cells

The results of photoelectrical measurements (low value of quantum efficiency and small short-circuit current) indicate insufficient lifetime of minority charge carriers for the fabrication of high-efficiency multi-junction solar cells, which is attributed to the high defect formation in (In)GaP(NAs) layers partially detected in the previous section. Thus, the study of the influence of growth conditions and post-growth methods on the behavior of defects in GaP(NAs) layers is an important task for optimization of the technological process for their fabrication in order to improve their quality. In this section, the attention is focused on the exploration of the influence of post-growth methods - thermal annealing on the properties of the structures. It is known that post-growth annealing can lead to an improvement of the layers quality of As-rich dilute nitrides[30–32]. Furthermore, the intensity of photoluminescence in GaP(N) layers grown on GaP wafers significantly increased after thermal annealing[156]. Therefore, the section presents the results of investigations of the influence of the post-growth annealing outside the MBE- chamber on the properties of defect levels in GaPAsN layers.

To this purpose, sample #1 with *n*-GaPAsN on GaP wafer and sample #7 with *i*-GaPAsN on silicon wafer were chosen. Sample #1 was annealed in a phosphorus flow at a temperature of 700 °C, and sample #7 was annealed at temperatures of 500 and 600 °C in a nitrogen ambient. Ohmic contacts to sample #1 and #7 were fabricated by methods described in Appendix A.1 and C.1, respectively. Further, structures are explored by admittance spectroscopy and their quantum efficiency was measured at conditions described above. The temperature dependences of the capacitance *C(T,f)* of samples for different frequencies are shown in Figure IV.35 and Figure IV.36 for samples #1 and #7, respectively.

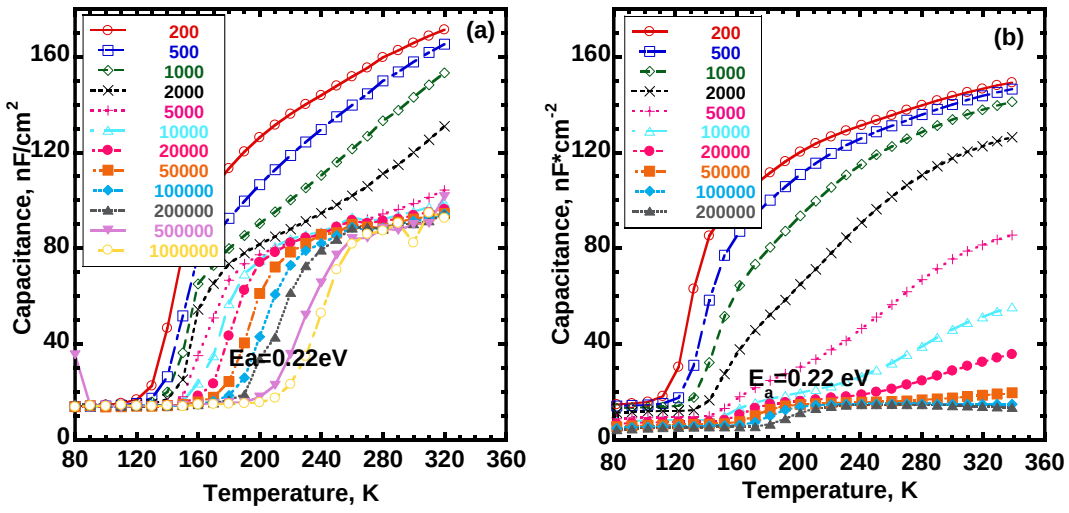

Figure IV.35. Experimental dependences of the capacitance upon temperature at various frequencies (indicating in Hz) for initial (a) and annealed (b) sample #1.

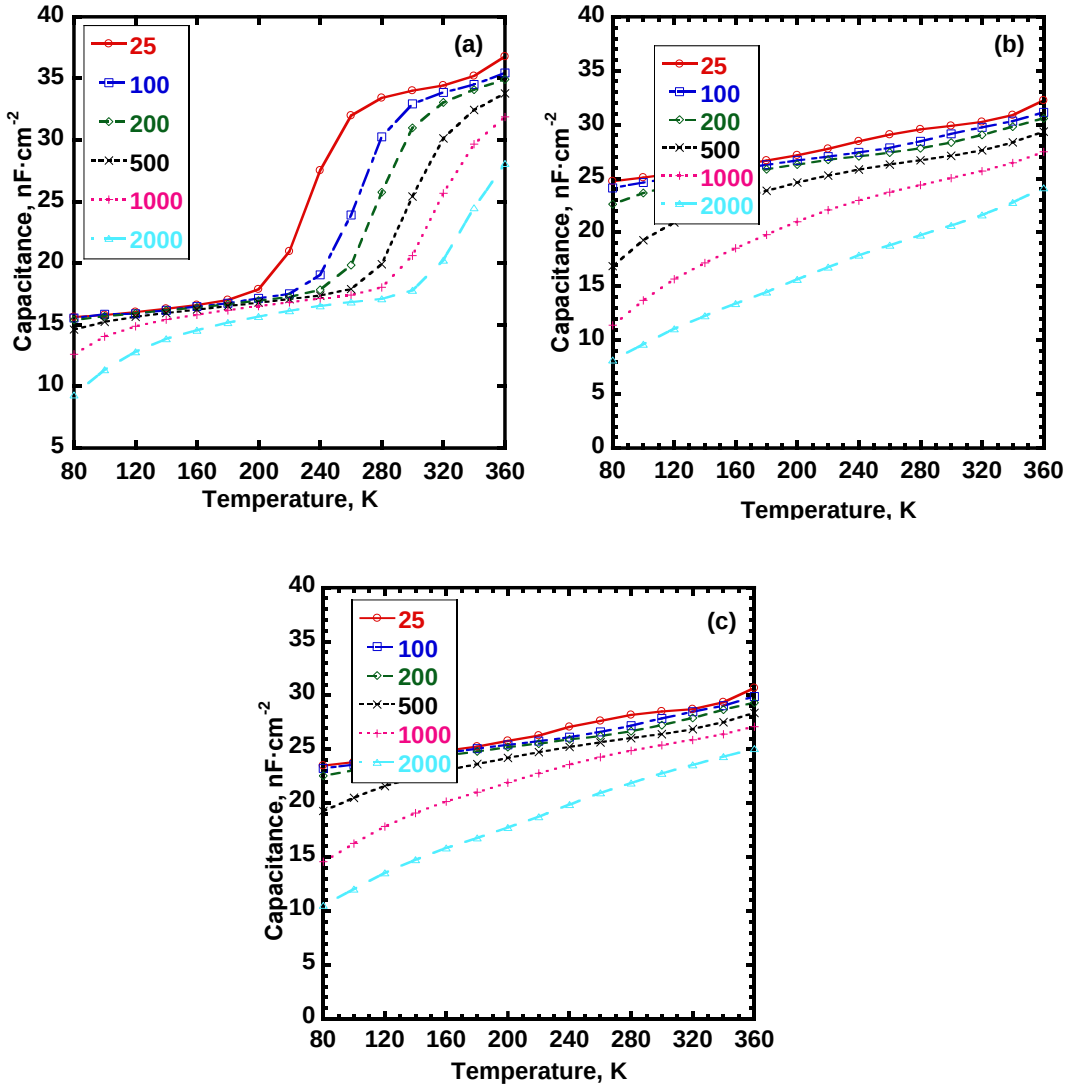

Figure IV.36 Experimental dependences of the capacitance upon temperature at various frequencies (indicating in Hz) for initial (a), annealed at 500 °C (b) and annealed at 600 °C (c) sample #7.

Figure IV.35a is the same as Figure IV.7a where *C(T,f)* curves are presented for the initial structure with *n*-GaPAsN grown on GaP. As described above, the detected defect at 0.22 eV corresponds to defect T1[89] with composition of $Si_{Ga}+V_P$. After the thermal annealing procedure (Figure IV.35b), the amplitude of the capacitance step corresponding to the response from this defect is significantly reduced for high frequencies (10 kHz and 50 kHz), which can indicate a drastical drop of their concentration in the *n*-GaPAsN layer. According to computer modeling, the number of T1 defects decreased by a factor of four and it became ~$5.0 \cdot 10^{16}$ cm^{-3} after thermal annealing. At the same time, no changes were detected for the concentration of defects responsible for the blurred high-temperature capacitance step.

Figure IV.36a shows *C(T,f)* curves for the initial *p*-*i*-*n* structure with *i*-GaPAsN layer grown on a Si wafer. The defect with an activation energy of 0.23 eV was detected in the temperature range 220-300 K in the initial sample as described above. Further, it can be seen that the *C(T,f)* behavior strongly changes: the amplitude of the step decreases and it becomes more blurred upon annealing at 500 °C for the whole frequency range (Figure IV.36b). Perhaps, we observe the modification of the defect level in GaPAsN leading to a drop of its concentration to ~10^{15} cm^{-3} according to simulation. Upon annealing at 600 °C (Figure IV.36c), the shape of *C(T,f)* curves remains the same without high steps as in initial structure. Therefore, thermal annealing leads to a drop of defect concentration detected by admittance spectroscopy in layers of dilute nitrides in considered structures.

Further, the EQE was measured before and after thermal annealing for the considered structures (Figure IV.37). The EQE of both samples significantly increases in whole wavelength region after thermal annealing. However, for sample #7 grown on silicon wafer, the quantum efficiency does not change with an increase in annealing temperature from 500 °C to 600 °C (Figure IV.37b). Consequently, it can be suggested that thermal annealing improves of the internal properties of the active GaP(NAs) layers. Consequently, such annealing is a technologically simple and effective method for improvement of the material quality in dilute nitrides of InGaPAsN alloys lattice-matched to GaP and Si.

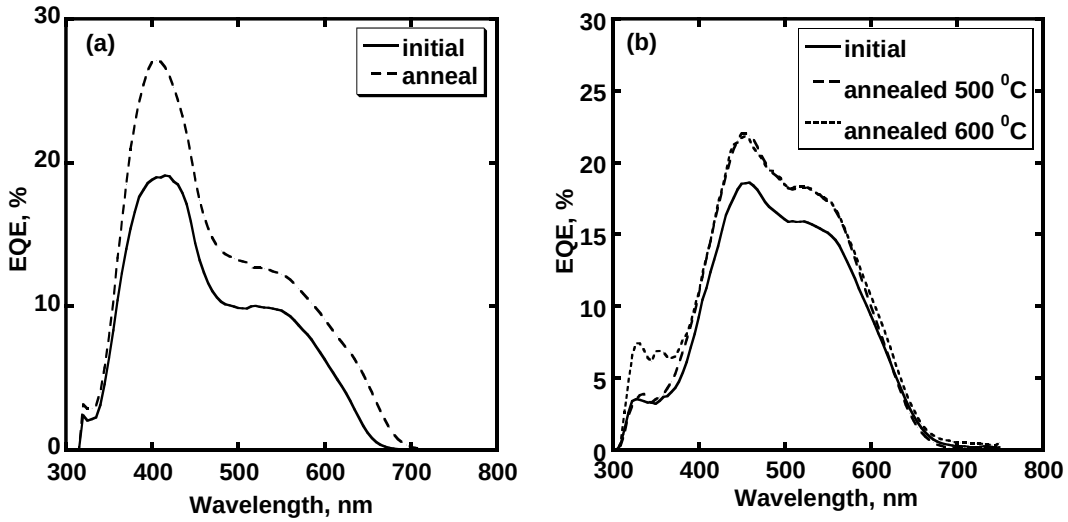

Figure IV.37 External quantum efficiency of sample #1 (a) and sample #7 (b) with GaPAsN layer before and after post-growth thermal annealing.

Summary

In Chapter IV, solar cells with layers of dilute nitrides grown by MBE on GaP and Si wafers were explored by different methods. According to experimental data following conclusions could be drawn:

- Undoped *i*-layer of dilute nitrides is more suitable for photovoltaic applications than *n*-type layers.
- SCs with active layers of *i*-GaPAsN alloys have higher short-circuit current, than those with *i*-InP/GaPN.
- Two peaks on quantum efficiency spectra are explained by the peculiar band structure of dilute nitrides with two conduction subbands leading to two light absorption mechanisms.
- Post-growth treatment improves photoelectrical and external properties of SC based on GaPAsN layers.
- Additional As content is preferable for SC compared to In since it leads to lower defect formation in *i*-layers and increase of quantum efficiency.
- Different defects were explored by capacitance methods. Some of them are centers of non-radiative recombination responsible for low lifetime of charge carriers in dilute nitrides.

Chapter V

PE-ALD growth

Introduction

As described in previous sections, epitaxial technologies require high temperatures for the pre-growth treatment of silicon wafers and growth of III-V compounds. It leads to different problems in the grown structures: deterioration of wafer quality, interdiffusion of atoms etc. Therefore we explored another route, with GaP layers grown by a low-temperature method in a plasma-enhanced chemical vapor deposition equipment for application in multi-junction solar cells. This is the topic of this chapter.

Structural properties of grown GaP are explored by scanning electron, Raman, and transmission electron microscopies. The electrical properties GaP/Si heterojunction structures are investigated. Then, capacitance techniques (C-V profiling and DLTS) are used to explore internal properties of grown layers. Finally, the influence of PE-ALD process on the quality of silicon wafers is explored by capacitance methods.

V.1 Growth of structures

Thin films of GaP with thickness of 50-75 nm were grown at 380 °C on *p*-type (boron-doped, 0.8-1.2 Ω·cm) and *n*-type (phosphorus-doped, 2-7 Ω·cm) (100) silicon wafers by continuous and PE-ALD methods using an Oxford PlasmaLab System 100 PECVD (13.56 MHz) setup. In the PE-ALD method phosphine (PH_3) and trimethylgallium (TMG) were alternatively changed with continuous plasma discharge due to constant hydrogen (H_2) flow during the growth and purge steps. On the contrary, flows of PH_3 and TMG occurred simultaneously in continuous process. The total flow and pressure were kept constant and equal to 100 sccm and 350 mTorr, respectively. Detailed description of technological process is given elsewhere[157]. In this study, one sample (#1) was grown by continuous method at RF plasma power of 100 W. Second sample was grown by PE-ALD method at constant RF plasma power of 20 W (#2) during the process. Then, it was increased to 100 W (sample #3) only during steps of TMG and PH_3. Schematic view of this process is shown in Figure V.1. The Table V.1 gives the general description and key differences of samples.

As described in a preceding chapter, the *n*-GaP/*p*-Si structure is more suitable for photovoltaics than the *p*-GaP/*n*-Si one due to the high valence band offset. Our main goal is to obtain *n*-GaP layers because the *n*-GaP/*p*-Si heterojunction can form a bottom subcell in perspective of multi-junction solar cells. To have *n*-type doping in GaP, silicon can be a good candidate, thus we introduced an additional step with a flow of silane in the PECVD reactor (Figure V.1). If silicon provides an effective *n*-type doping of GaP the GaP:Si/*p*-Si heterojunction should be a *n*-*p* junction, while the GaP:Si/*p*-Si heterojunction should be an isotype heterojunction (Figure V.2).

Sample	Growth process	RF plasma power, W	Type of GaP
#1	Continuous	100	amorphous
#2	PE-ALD	20	amorphous
#3	PE-ALD	100	microcrystalline

Table V.1 Description of GaP/Si samples grown in the PECVD chamber.

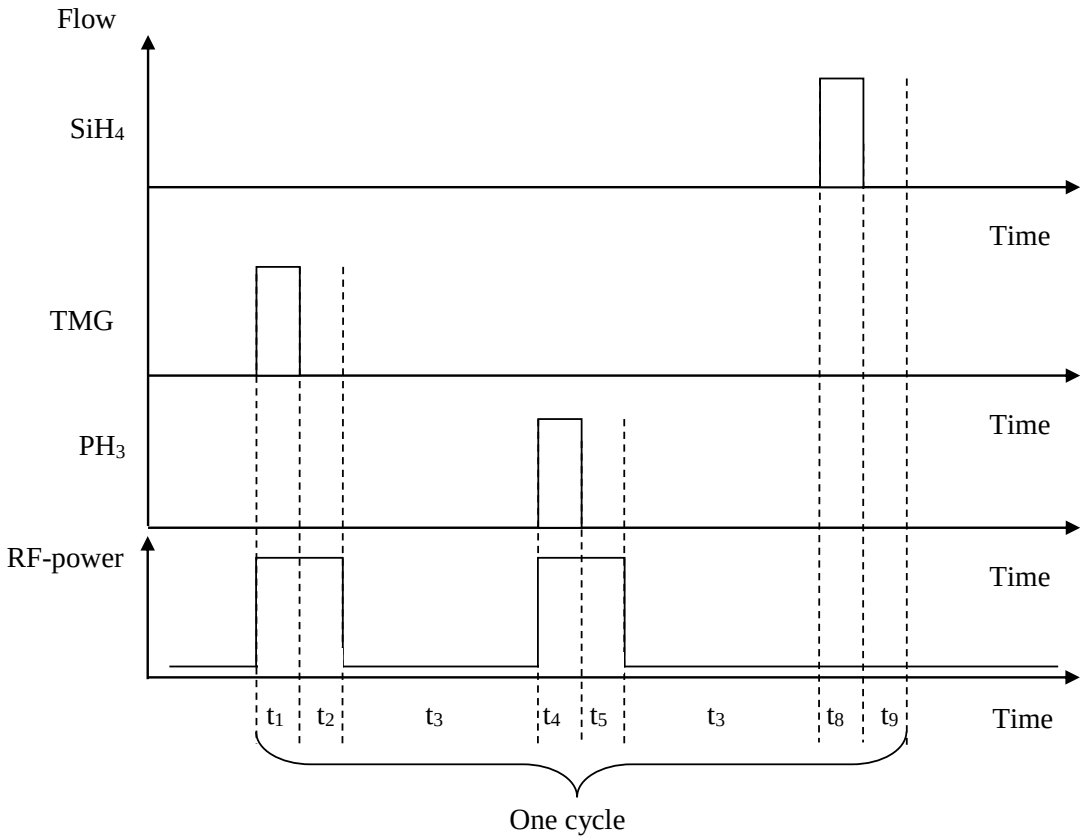

Figure V.1 Schematic view of PE-ALD growth of GaP:Si of sample #3. For sample #2, the RF power is kept constant all over the time.

Figure V.2 GaP:Si/*p*-Si and GaP:Si/*n*-Si structures. The first should act as an *n-p* junction while the second should be an anisotype junction.

V.2 Structural properties

Initial structural properties were explored by classical scanning electron microscopy: SEM-images are presented in Figure V.3. The interface of sample #1 is not flat and the GaP thickness depends on the considered region (Figure V.3a). Also, its surface is totally inhomogeneous: there are many crystallites with absolutely different sizes located in chaotic order and a high number of deep holes which can lead to degradation of the sample quality and of the properties of the GaP layer. On the contrary, for samples grown by PE-ALD the thickness of GaP has almost the same value everywhere so it can be estimated without any difficulties. However, the surface morphology depends on the deposition parameters. Despite homogeneous surfaces, they have different view for samples. The surface of GaP grown at an RF plasma power of 20 W is smooth (Figure V.3b) unlike that of another sample grown at 100 W where a lot of small nanocrystallites are visible (Figure V.3c). Higher plasma power may lead to preferable formation of crystalline structures due to higher migration of atoms on the surface. On the other hand, low plasma power does not transfer enough energy to atoms so they rather stay where they are absorbed which provides a smooth and homogeneous surface. Owing to the poor interface quality and structural properties of the GaP layer grown by continuous PECVD we are focused in this work on samples grown by the PE-ALD technique.

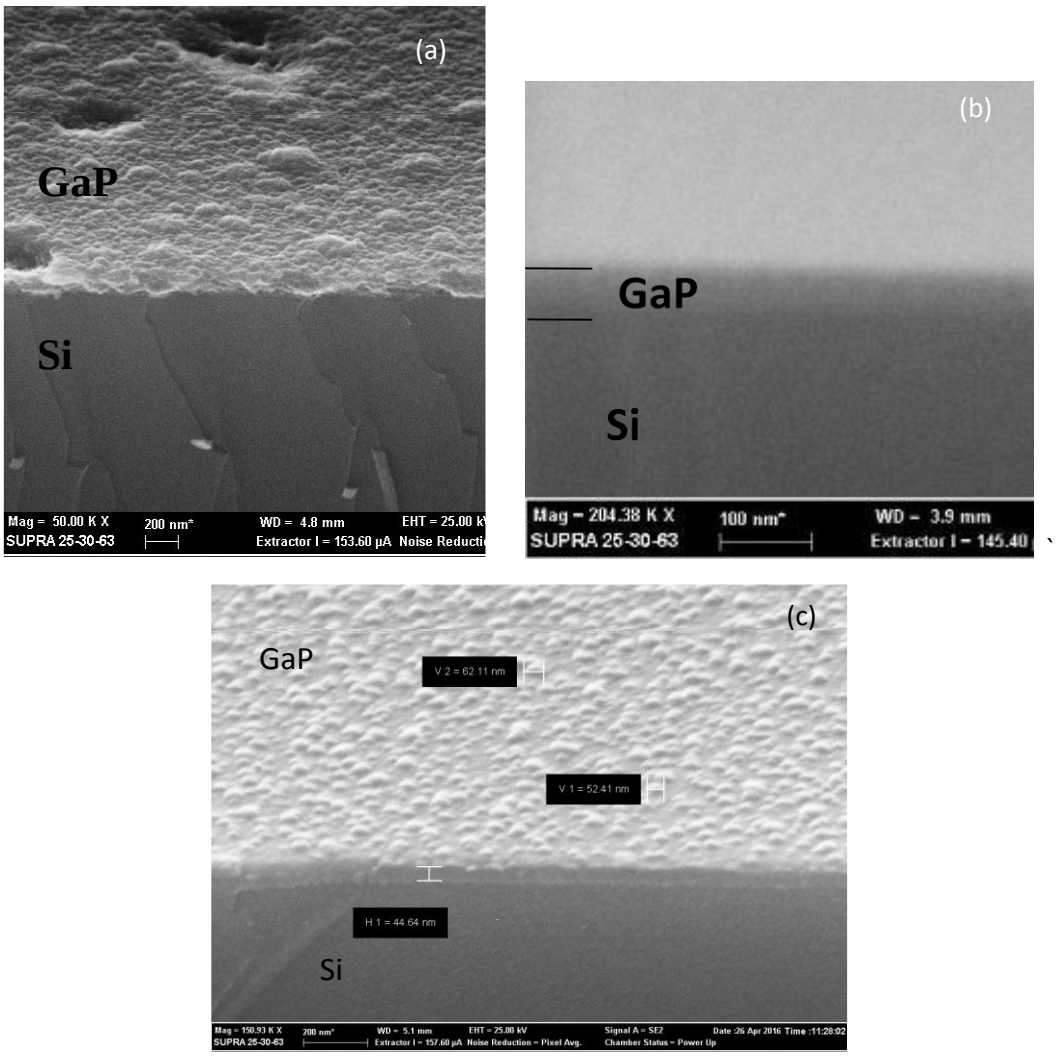

Figure V.3 SEM-image of GaP layer grown on silicon wafer by continuous (#1, a) and PE-ALD methods at RF plasma power of 20 W (#2, b) and 100 W (#3, c).

Raman spectra for samples #2 and #3 are presented in Figure V.4. The high peak at 309 cm^{-1} corresponds to the response from the silicon wafer and it has a similar shape in both curves. A major difference between the two samples can be seen in the graph in the region of 350-420 cm^{-1}. A broad feature at 360 cm^{-1} is detected in sample #2. It corresponds to the response from amorphous GaP[158] suggesting that the GaP layer grown at 20 W plasma power has an amorphous structure, so it will be called a-GaP in the following. On the contrary, two clear peaks can be distinguished at 365 and 402 cm^{-1} in sample #3. According to literature, these correspond to TO and LO phonon positions in microcrystalline GaP[159] suggesting that the GaP layer grown at 100 W plasma power has a microcrystalline structure, so it will be called µc-GaP in the following.

Therefore, the structure of GaP changes from amorphous to microcrystalline with increasing the RF plasma power from 20 W up to 100 W, while other growth conditions remain the same.

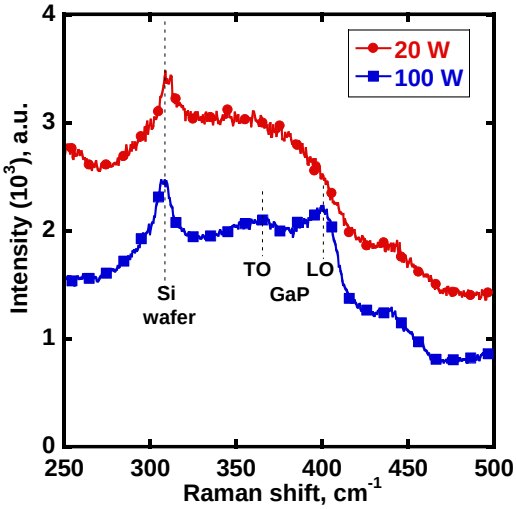

Figure V.4 Raman spectra of GaP films deposited by PE-ALD method at RF plasma power of 20 W (#2) and 100 W (#3).

Transmission electron microscopy (TEM) has also been performed on these samples. TEM-images are shown in Figure V.5.

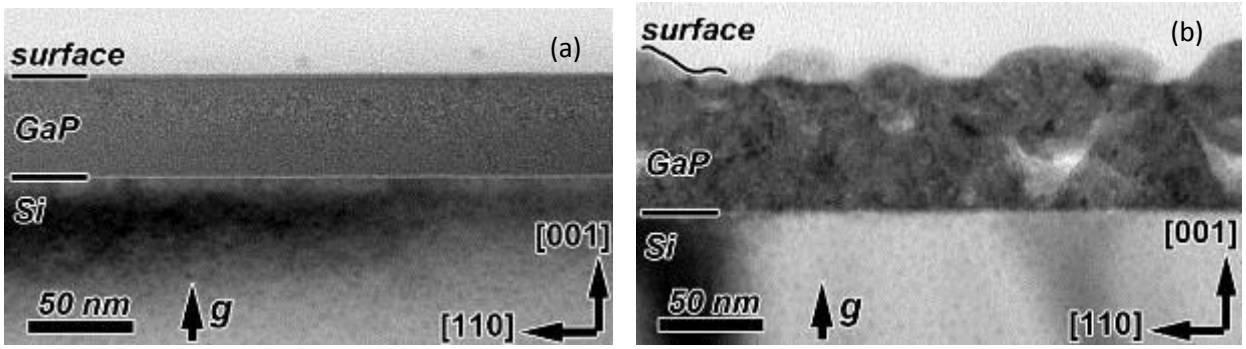

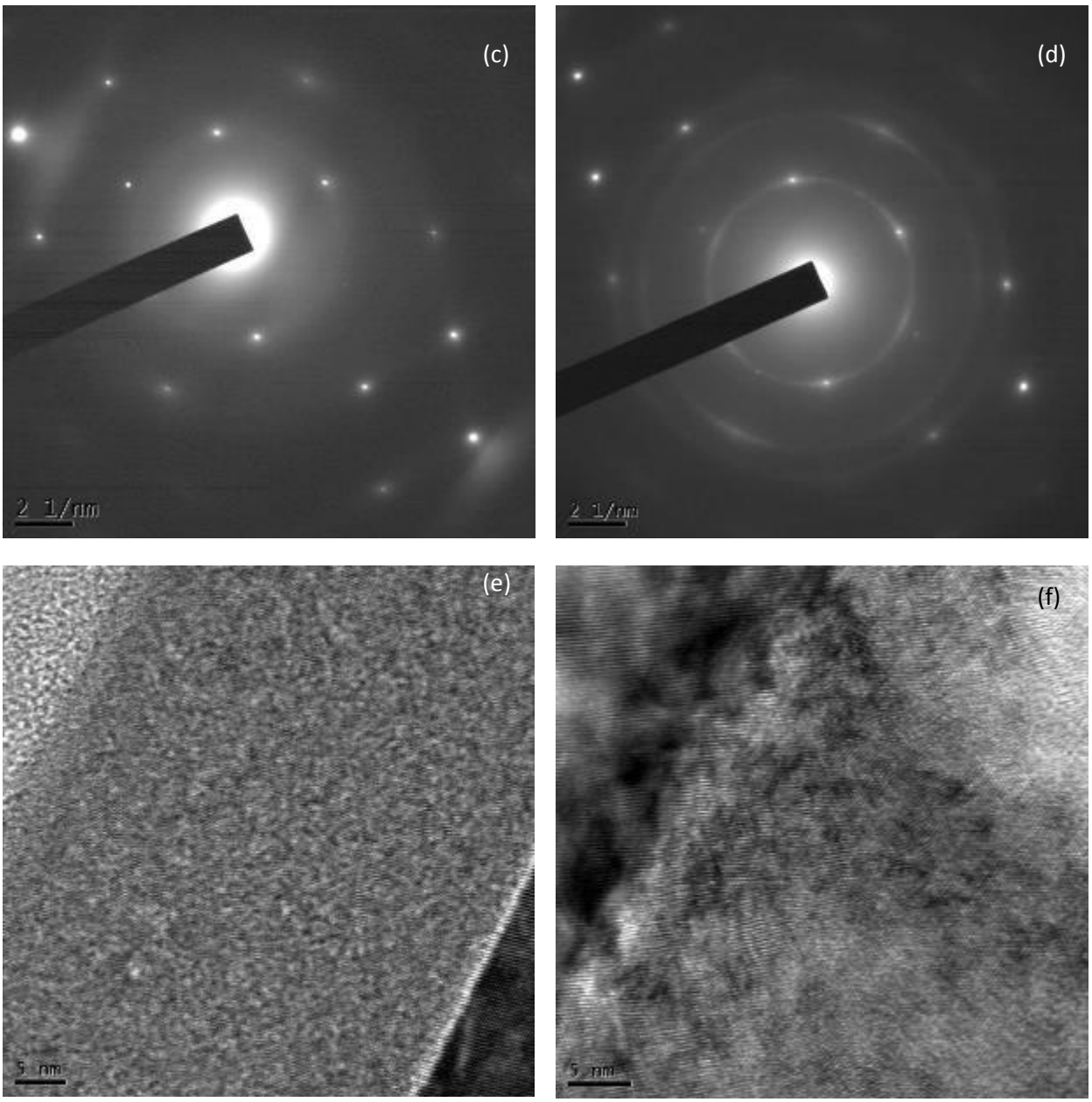

Figure V.5 TEM- images of a GaP layer grown onto a silicon wafer by the PE-ALD method at an RF plasma power of 20 W (left) and 100 W (right) for bright field modes (a, b), microdiffraction pattern (c, d) and high-resolution (e, f).

According to the images of bright field mode, a similar picture as from SEM measurements is observed. Sample #2 has flat surface and homogeneous composition without any feature (Figure V.5a). On the contrary, sample #3 has rough surface with high numbers of different objects on it and inside the GaP layer. It is possible to distinguish antiphase domains in the Figure V.5b revealing the existence of some crystalline growth in sample #3. In the microdiffraction pattern, both samples have diffraction spots coming from the monocrystalline silicon wafer. Then, sample #3 has three rings corresponding to diffraction on different crystal planes, {111}, {220} and {311}. Diffraction spots coming from silicon are lying in the ring since the lattice constant of GaP

coincides with that of Si. Consequently, according to the classification sample #3 appears as a polycrystalline (microcrystalline) GaP semiconductor. On the other hand, sample #2 shows mean substrate diffraction spots between central halo and diffused ring. These diffused rings mean that the structure of this sample grown at an RF plasma power of 20 W is amorphous. High-resolution TEM also confirms the observed differences between samples. Crystalline order and oriented features can be distinguished in the image for μc-GaP (Figure V.5f). It suggests that the silicon wafer defines the direction of growth in this process so it can be considered as crystalline growth. It is an attractive conclusion because the crystalline structure was obtained even at low growth temperature (380 °C). On the contrary, such a behavior is not observed in sample #2 where atoms grow in the same direction in strongly short distances so it has an amorphous nature. On the other hand, the interface region of sample #3 shows alignments of the {111} Si and GaP atomic planes through the interface. This indicates epitaxial relationship. Even if microcrystalline, the GaP layer is locally epitaxially oriented, in such manner it is elastically strained, even if presence of grain boundaries and differently oriented interfaces of adjacent grains make more complex the situation than for a monocrystalline interface. However, it is observed the absence of elastic stresses in sample #2 because of the GaP amorphous state.

In conclusion, all structural characterizations indicate that the GaP layer is amorphous for an RF plasma power of 20 W, and microcrystalline for 100 W. Therefore, the RF plasma power is an important parameter affecting the crystalline properties of the GaP layer.

V.3 Electrical properties

Since GaP/*p*-Si is suggested as a solar cell structure, ohmic contacts must be formed to GaP and *p*-Si. The isotype structure GaP/*n*-Si is also interesting for experiments because properties of the GaP layer and heterointerface can be explored from C-V measurements if a Schottky diode is formed on GaP, and an ohmic contact to *n*-Si. Ohmic contacts to *p*-Si can be achieved by methods described in the previous Chapter in double-junction solar cells: using indium and iron soldering, or deposition of amorphous *p*-Si, vacuum evaporation of silver and subsequent annealing at low temperature. Also, ohmic contacts to the *n*-Si wafer can be formed by the latter procedure where amorphous *p*-Si is replaced by *n*-Si.

The structural difference between layers of GaP grown by PE-ALD and MBE is a crucial issue for the fabrication of Schottky barriers and ohmic contacts to GaP. PE-ALD samples can be either amorphous or microcrystalline. Unfortunately, by now, there are no well documented articles on the fabrication of Schottky barriers and ohmic contacts to layers of amorphous gallium phosphide. Indeed, there are only a few papers devoted to the study of amorphous GaP, performed

in Japan at the end of the XXth century[160–163]. However, the problem of Schottky barriers and ohmic contacts were not explored. In these works the authors deposited gold[161] on the grown GaP layer to measure current-voltage characteristics in the structures: the gold contact was indicated as a "usual" electrode without investigation of its behavior. In our work, we used literature data and the experience gained for GaP layers grown by epitaxial technologies.

At the first stage of Schottky barriers investigation, the values of the barriers formed between metals and epitaxial *n*-GaP were found in literature[164]. A wide range of metals forms high-energy barriers on monocrystalline *n*-GaP. The most widely used for capacitance techniques are silver[165], gold[88] and nickel[89].

The difference between our layers and the epitaxial GaP layers may significantly affect the height of the barrier for the same metal, and hence the quality of the Schottky diode. The optimal Schottky diode has a current-voltage characteristic where the current is small and saturates at reverse bias voltages, but it increases exponentially versus forward bias voltage. Five metals were chosen to form contacts to our samples: in addition to silver, gold and nickel, we also tested palladium and a chromium/gold stack. The materials were deposited through a mask with circular holes of 2, 1, 0.5 and 0.25 mm in diameter. The hole diameters are selected according to requirements for capacitance values which must be less than some hundreds of picofarads for precise and reliable measurements. The thickness of the deposited metals was in range 80-100 nm. Figure V.6a presents dark I-V curves obtained with a dot diameter of 0.5 mm from different metals.

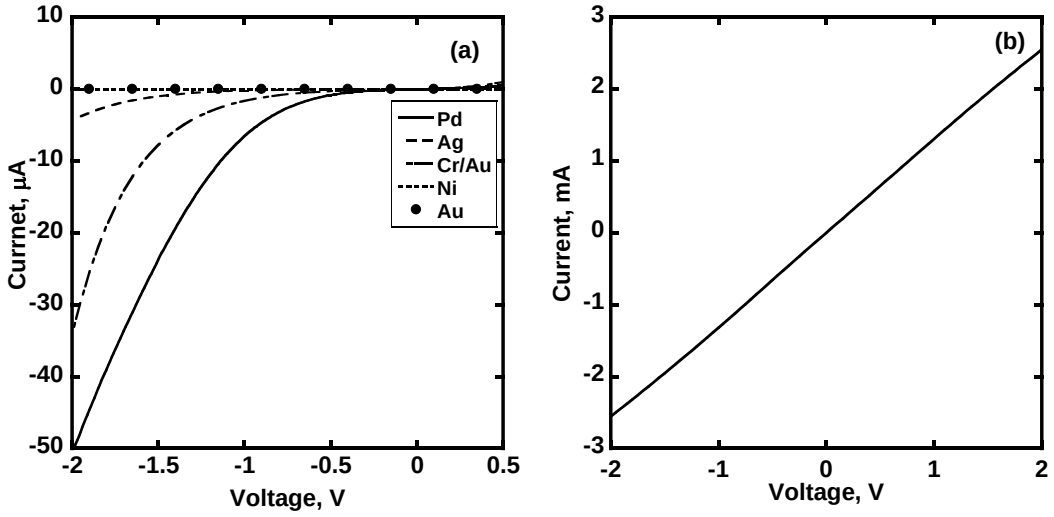

Figure V.6 (a)- current-voltage characteristic of Schottky diode to GaP/*n*-Si structures at reverse bias voltage for different metals. (b)- current-voltage characteristic between Ti/Ag contacts deposited on *n*-GaP.

According to these curves, nickel and gold are preferable for barrier formation to our GaP samples since the value of dark current at reverse voltage is low and remains constant even at high voltage amplitude. Samples with gold contact have shown stable behavior before and after applying reverse voltage larger than 2 V compared to that with nickel contact. Furthermore, nickel has tendency to oxidation leading to change of Schottky diode properties over the time. Thereby, gold was chosen as the main metal for Schottky diode fabrication to GaP/*n*-Si heterojunctions.

As described above, properties of PE-ALD GaP can be different from that of GaP grown by epitaxial methods so we should also check if ohmic contacts could also be obtained on our samples using methods that normally provide ohmic contacts on epitaxially grown GaP. In the previous Chapter, In and alloys of Au/Ge were used for ohmic contact fabrication to epitaxial *n*-GaP. But indium is fragile and unstable, and Au/Ge requires temperature annealing that can lead to shunts due to germanium diffusion through the thin layer of GaP. Furthermore, structures are grown at temperatures below 400 °C so the contact should be fabricated at low temperature above deposition one to avoid changes in sample properties. A Ti/Ag alloy was evaporated as a top contact onto *n*-GaP. The I-V curve between two adjacent contacts is presented in Figure V.6b. It shows a nice linear behavior corresponding to an ohmic contact.

We also fabricated Schottky diodes on both types of silicon wafer after removal of the GaP layer (to test if GaP deposition could create defects in the c-Si wafers). To this purpose, gold and titanium were used for *n*- and *p*-type, respectively. After contact fabrication, selective etching was used for creation and separation of mesa-structures. GaP layers were wet etched, and silicon wafers were dry etched in the ICP chamber at conditions described in Chapter II.

Figure V.7 presents the schematic view of preparation of all samples explored in this study. The first type consists in samples with a gold Schottky barrier on isotype GaP/*n*-Si heterojunctions (Figure V.7a). In a first step, 50 nm of *n*-type amorphous silicon was deposited on the bottom of the silicon wafer by PECVD. Then silver was evaporated onto a-Si:H to form the bottom contact. This bottom contact became ohmic after thermal annealing during 20 min at 170 °C in the air atmosphere. Gold contact dots with diameter of 0.5 and 1 mm were evaporated on the top of the structures to form Schottky barrier (SB) diodes to GaP. Finally, mesa-structures were formed by dry etching of the GaP layer and of 2 μm of silicon using an Oxford PlasmaLab System 100 ICP 380. A photograph of such samples is presented in Figure V.8a.

The second type of samples consists in solar cells with front Ti/Ag ohmic contact to anisotype GaP/*p*-Si heterojunctions (Figure V.7c). In the first step, the Ti/Ag alloy was deposited on GaP by vacuum evaporation as a contact grid for photoelectric measurements. Then, silicon was dry etched at the same condition. Finally, an indium ohmic contact was formed to *p*-Si. The photograph of such samples is shown in Figure V.8b.

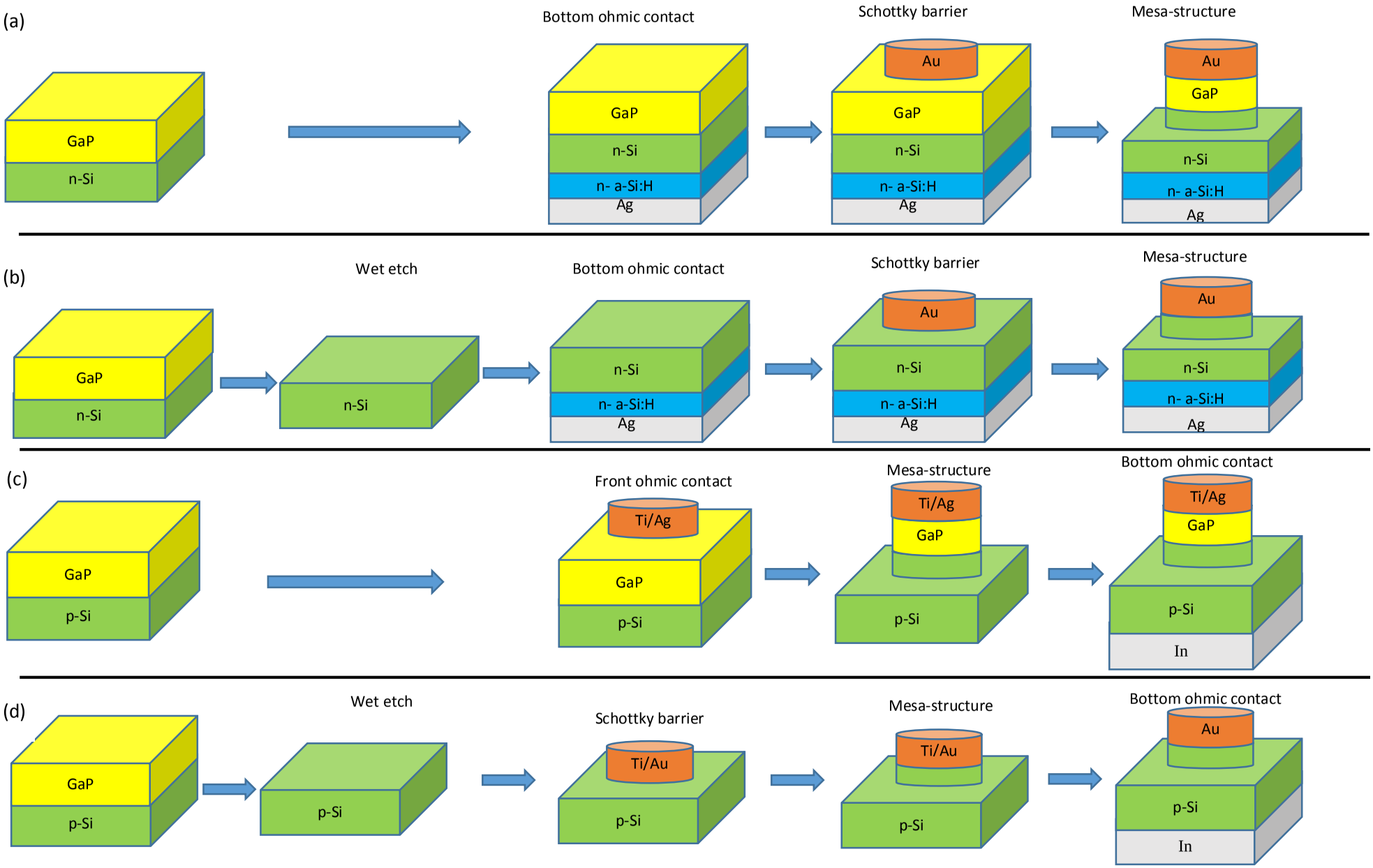

Figure V.7 Technological fabrication process of samples with: Schottky diode to GaP/*n*-Si (a), Schottky diode to *n*-Si (b), ohmic contacts to GaP/*p*-Si (c) and Schottky diode to *p*-Si (d).

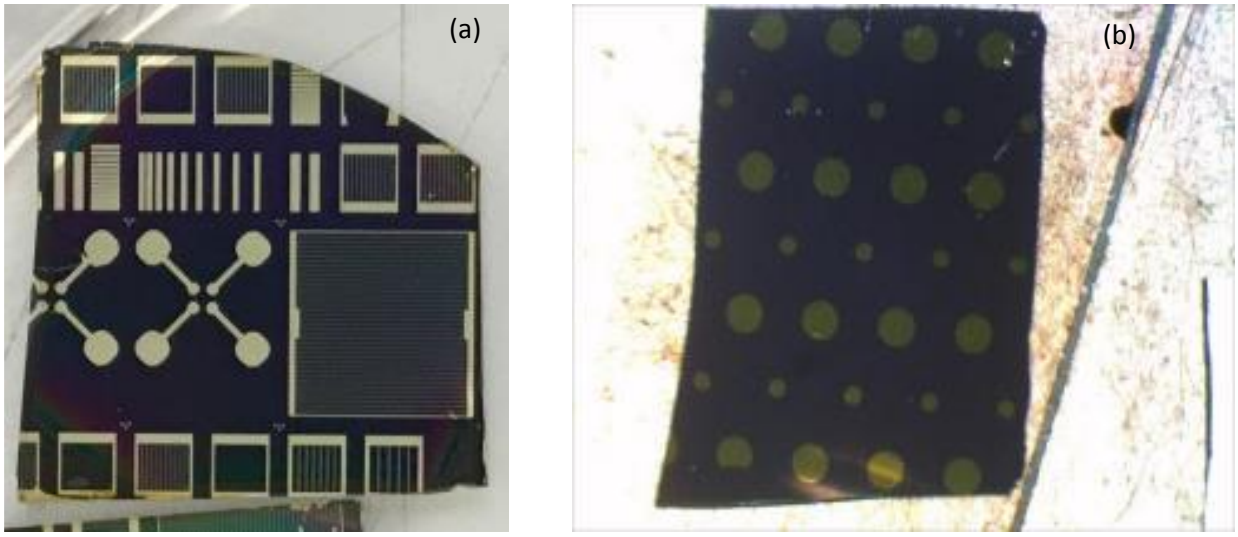

Figure V.8 Photograph of mesa-structures based on GaP/*p*-Si used for electric measurements (a) and mesa-structures (b) formed for capacitance measurements.

The third and fourth types of samples are Schottky barriers to n- and p-type silicon wafers after etching of GaP (Figure V.7b and Figure V.7d, respectively). In the first step, the GaP layers were selectively removed by wet etching. For *n*-type silicon, an ohmic contact was formed by the procedure described above. Then, gold dots with diameters of 0.5 and 1 mm were evaporated on the top of the *n*-type silicon wafer to form Schottky diodes to *n*-Si (Au/*n*-Si). For *p*-type silicon, indium was used as an ohmic back contact instead of silver/(*n*)a-Si:H in the case of *n*-Si. Also, Schottky barriers to *p*-Si were fabricated by evaporation of a titanium layer that was covered by a gold layer to protect the contact (Au/Ti/*p*-Si) during dry etching. Finally, mesa-structures were formed by dry etching of 2 μm of silicon. The view of these samples is identical to that of the first types of samples and it is presented in Figure V.8b.

Samples fabricated by the described technology are used for different measurement techniques. The squares with contact grid in Figure V.8a are solar cells and their photoelectrical properties are measured. The mesa-structures for the Hall method were also fabricated and they are shown in Figure V.8a (cross-like contacts with large extremities). Mesa-structures in Figure V.8b were fabricated for capacitance investigations. Structural properties of GaP layers were explored in raw as-grown samples.

Mesa-structures with Schottky diodes on GaP/*n*-Si (sample #1 and sample #3) were fabricated by the method shown in Figure V.7a. Capacitance-voltage characteristics were measured for both samples at a frequency of 100 kHz at 80 K (Figure V.9). Again, there is a clear

difference between continuous and PE-ALD samples. Capacitance of sample #1 is almost independent of the applied reverse bias voltage down to -2.5 V. It is a strange behavior because it suggests that the space charge region does not extend into the structure with the applied voltage. The width of SCR at 0 V is approximately 350 nm as estimated from the capacitance value, however the thickness of GaP is only 100 nm according to SEM-images (Figure V.3a): it means that the edge of SCR must be in the silicon wafer at 0 V. In this case, the SCR should extend in the wafer and the capacitance should decrease with increasing reverse voltage. This suggests that the GaP grown by the continuous method may form a highly defective interfacial layer. On the contrary, the *C-V* curve of sample #3 shows the conventional junction behavior: the capacitance decreases versus reverse voltage. It means that the SCR is controlled by the applied voltage so the considered sample can be analyzed by capacitance methods. The N_{CV}-*W* profiling yields a doping level value in reasonable agreement with the doping value in the silicon wafer at voltages below -1 V; more detailed quantitative and qualitative analysis will be presented below for the structure obtained by PE-ALD.

Consequently, sample #3 with GaP grown by PE-ALD shows better structural and electric properties than sample #1 obtained by the continuous process. As a consequence, following studies are focused only on structures grown by the PE-ALD method.

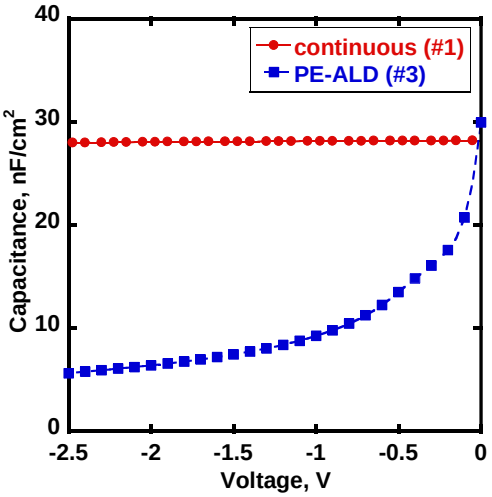

Figure V.9 Capacitance-voltage characteristics of samples grown by continuous (#1) and PE-ALD (#3) methods.

V.3.1 Current-voltage characteristics of n-GaP/p-Si structures grown by PE-ALD

In this section, we used samples described in Figure V.7c with top contacts onto both a-GaP and µc-GaP grown on *p*-Si. Electric properties are explored by current-voltage characteristics

of the solar cell structure and by Hall measurements using coplanar top contacts. The current-voltage characteristics of the solar cells under AM1.5 light are shown in Figure V.10a. These characteristics reflect the existence of a *p*-*n* junction, thus revealing the existence of an *n*-type layer, which will be discussed below. Obviously, the a-GaP sample (J_{SC}=21.82 mA/cm^2 and V_{OC}=0.44 V) shows much better performance than the µc-GaP one (J_{SC}=3.75 mA/cm^2 and V_{OC}=0.32 V). It can be explained by previous structural characterization, in particular by TEM-images where µc-GaP was shown to be defective and inhomogeneous. Thus, a-GaP leads to better passivation of the silicon surface with less interface defects, which leads to higher V_{OC}.

Hall measurements performed at 300 K on both samples confirm the presence of an *n*-type layer. In order to get an order of magnitude of the electron concentration, assuming a homogenous 50 nm thick *n*-type layer yields a value of 1.2×10^{19}cm^{-3} and an electron mobility of 23.45 cm^2/Vs while the conductivity of the µc-GaP sample was three times lower. The *n*-type layer may have three origins:

- the GaP layer itself is highly doped and *n*-type.
- there is an electron rich strong inversion layer at the *p*-Si surface.
- an *n*-Si layer is formed during the growth process due to phosphorous diffusion into the wafer.

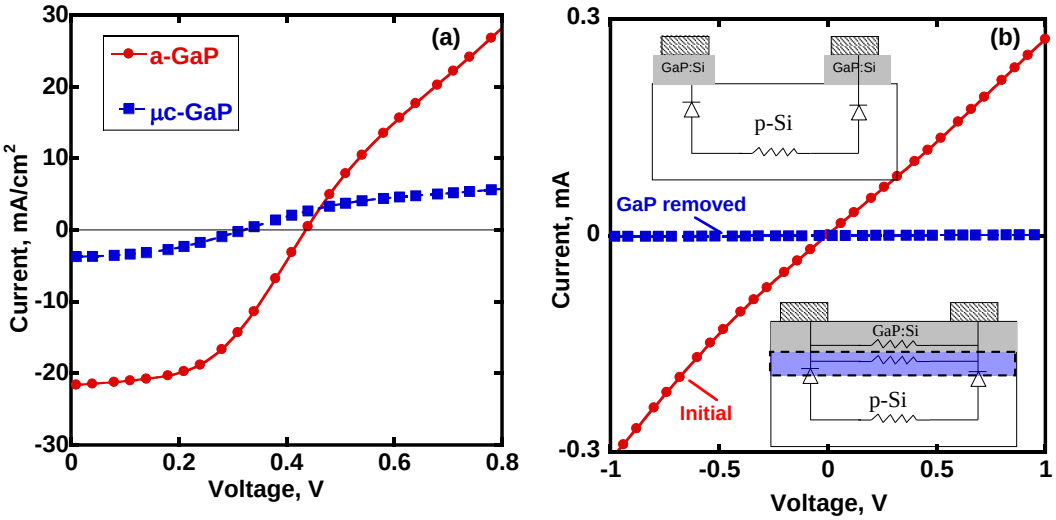

Figure V.10 Light current- voltage characteristics for a-GaP/*p*-Si and µc-GaP/*p*-Si (a) and between two planar electrodes before and after selective GaP etching.

The third one was excluded after following experiments. First, lateral conductivity was measured between two top contacts in the initial sample (Figure V.10b). Then, the GaP layer was selectively etched from the as-grown structure down to the wafer, then the contacts were formed onto silicon and the I-V curve between two contacts was measured again (Figure V.10b). As a

result, the conductivity drastically drops in the structure without GaP so the reason of *n*-type conductivity is related to the existence of GaP on *p*-Si.

Comparing the two first possible origins, it is worth emphasizing that both imply that the GaP layer is *n*-type and highly doped. Indeed, a strong inversion layer in c-Si can only occur if there is sufficient band bending, which in turn implies that the GaP layer is *n*-type in order to have sufficient low work function to provide such a strong and bending. An example of band diagram with strong inversion at the c-Si surface is shown in Figure V.11. In conclusion, we have demonstrated that GaP was grown with *n*-type doping by the PE-ALD method at low temperature under silane flow.

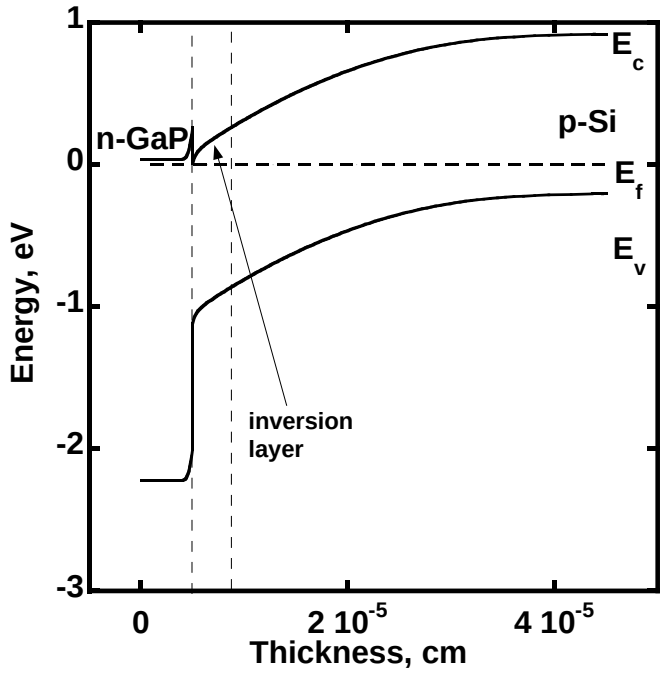

Figure V.11 Example of band diagram of *n*-GaP/*p*-Si at 300 K.

V.3.2 Capacitance characterization of GaP/n-Si structures grown by PE-ALD

In this section, we used Schottky diodes fabricated onto GaP/*n*-Si heterojunctions in samples #2 and #3 by the method shown in Figure V.7a. We also used one sample with gold Schottky barrier to n-Si prepared by the method shown in Figure V.7b. Capacitance-voltage characteristics of the GaP/*n*-Si samples at 80 K and Au/*n*-Si at 300 K are shown in Figure V.12a. The capacitance decreases with increasing amplitude of reverse bias voltage for all samples. Consequently, the extension of the space charge region inside the structures is observed: this is the conventional behaviour of *C*-*V* curves. N_{CV} -*V* and N_{CV} -*W* profiles were plotted for the three samples in Figure V.12b and Figure V.12c, respectively.

The concentration profile for Au/n-Si is almost constant with a value of 1×10^{15} cm^{-3}. It corresponds to the doping concentration of the silicon wafer (2-7 Ω·cm). The experimental profile for a-GaP/*n*-Si shows the constant value of 7×10^{14} cm^{-3}, which also corresponds to the doping concentration of the silicon wafer. However, for the μc-GaP/*n*-Si structure a clear peak of concentration is observed at low bias voltage, which corresponds to the lowest depth of SCR. With the increase of reverse bias voltage (increase of SCR depth) the concentration becomes constant with the same value as in the Si wafer. Also, the capacitance is much higher for bias voltage close to zero in μc-GaP/*n*-Si so the SCR width is lower than in a-GaP/*n*-Si and Au/*n*-Si structures.

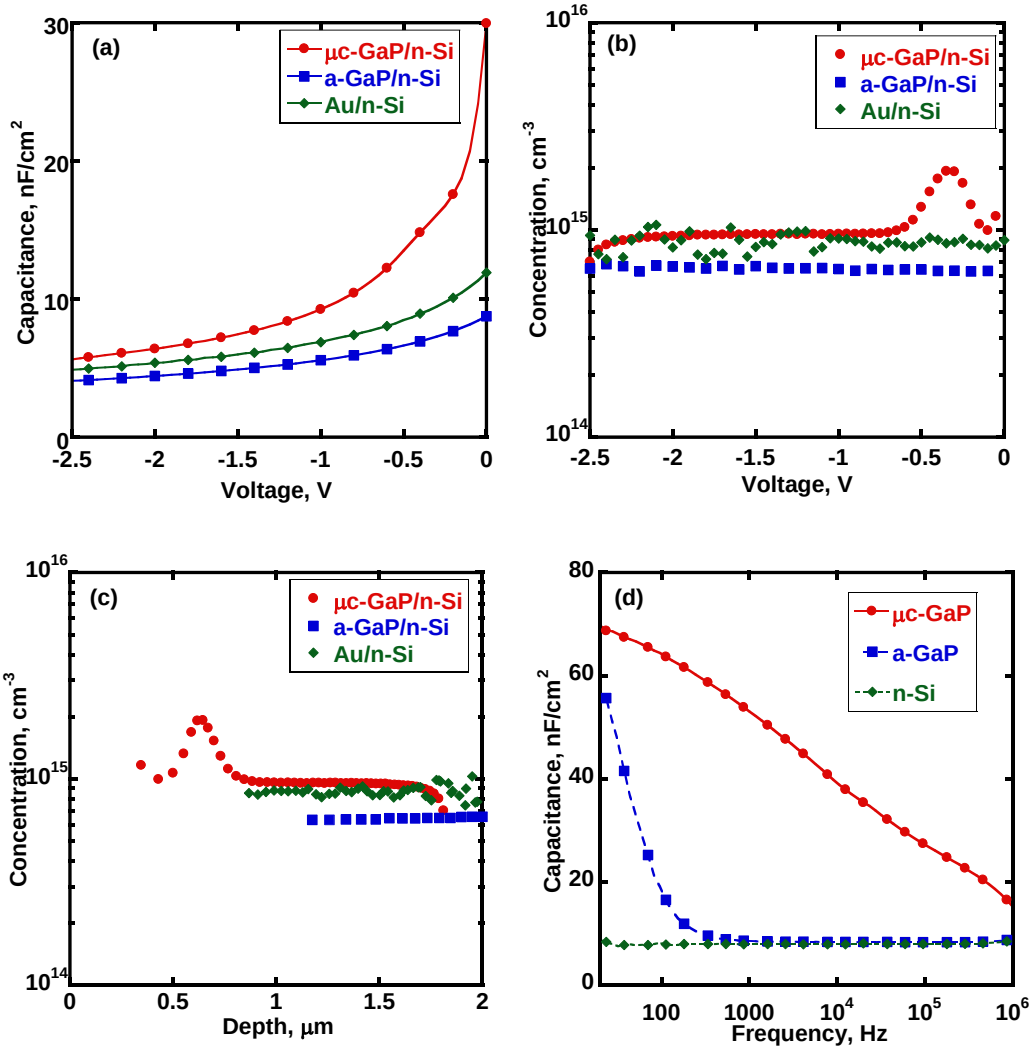

Figure V.12 (a, b, c, d). Analysis of the bias dependence of the measured capacitance of the three types of structures: *C*-*V* (a), N_{CV}-*V* (b) and N_{CV}-*W* (c). Capacitance-frequency dependence of samples (d).

Two differences are observed from the comparison of profiles for a-GaP/*n*-Si and μc-GaP/*n*-Si: smaller width of SCR for μc-GaP/*n*-Si and existence of a peak on its profile at low reverse bias voltage. One of the possible explanations is the different *n*-type doping level in GaP.

We suggest that µc-GaP is more doped compared to a-GaP so the concentration peak appears when SCR extends from GaP to Si through the *n*-GaP/n-Si interface[166]. Figure V.13 shows the simulated band diagram for GaP (n= 1×10^{17} cm^{-3})/Si (n= 1×10^{15} cm^{-3}) heterojunction at zero bias voltage and the concentration profile of electrons at 80 K. The position of the peak in the concentration profile corresponds to the GaP/Si interface: for the experimental µc-GaP/*n*-Si sample a similar phenomenon is observed (Figure V.12c). However, values of SCR width are higher in the experiment than in the simulation. Disparity in the values can come from an imperfect bottom contact to the silicon wafer. Consequently, estimation of the absolute value of interface position from the experiment can be incorrect and should be considered more critically. On the opposite, the described peak does not appear on the profile for a-GaP. It means that the SCR extends inside the silicon wafer even at zero bias voltage. Consequently, a-GaP should be fully depleted at any reverse bias voltage. It explains why the capacitance of µc-GaP/*n*-Si is much higher compared to that of a-GaP/*n*-Si. It is a very important issue because it means that the border of SCR for the a-GaP/*n*-Si sample is further from the heterojunction compared to the µc-GaP/*n*-Si one. Therefore, in case of the a-GaP/*n*-Si sample the DLTS experiment is expected to rather detect the response of defects far from the a-GaP/*n*-Si interface in the bulk silicon. According to the *C-f* dependence in Figure V.12d, µc-GaP/*n*-Si should be more defective than a-GaP/*n*-Si due to higher capacitance step associated with responses from defect levels.

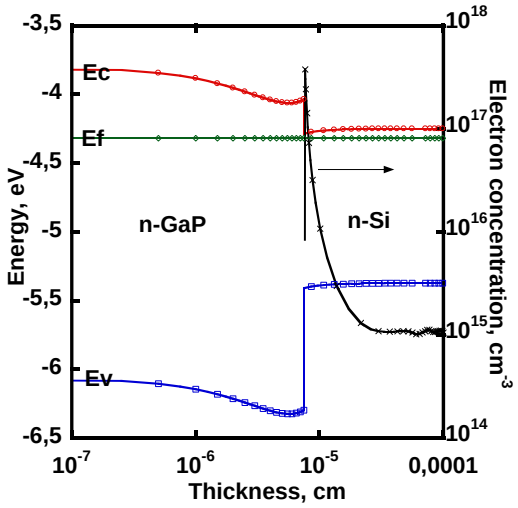

Figure V.13 Band diagram of *n*-GaP/*n*-Si and profile of electron concentration at 80 K.

Results of DLTS measurements are shown in Figure V.14.

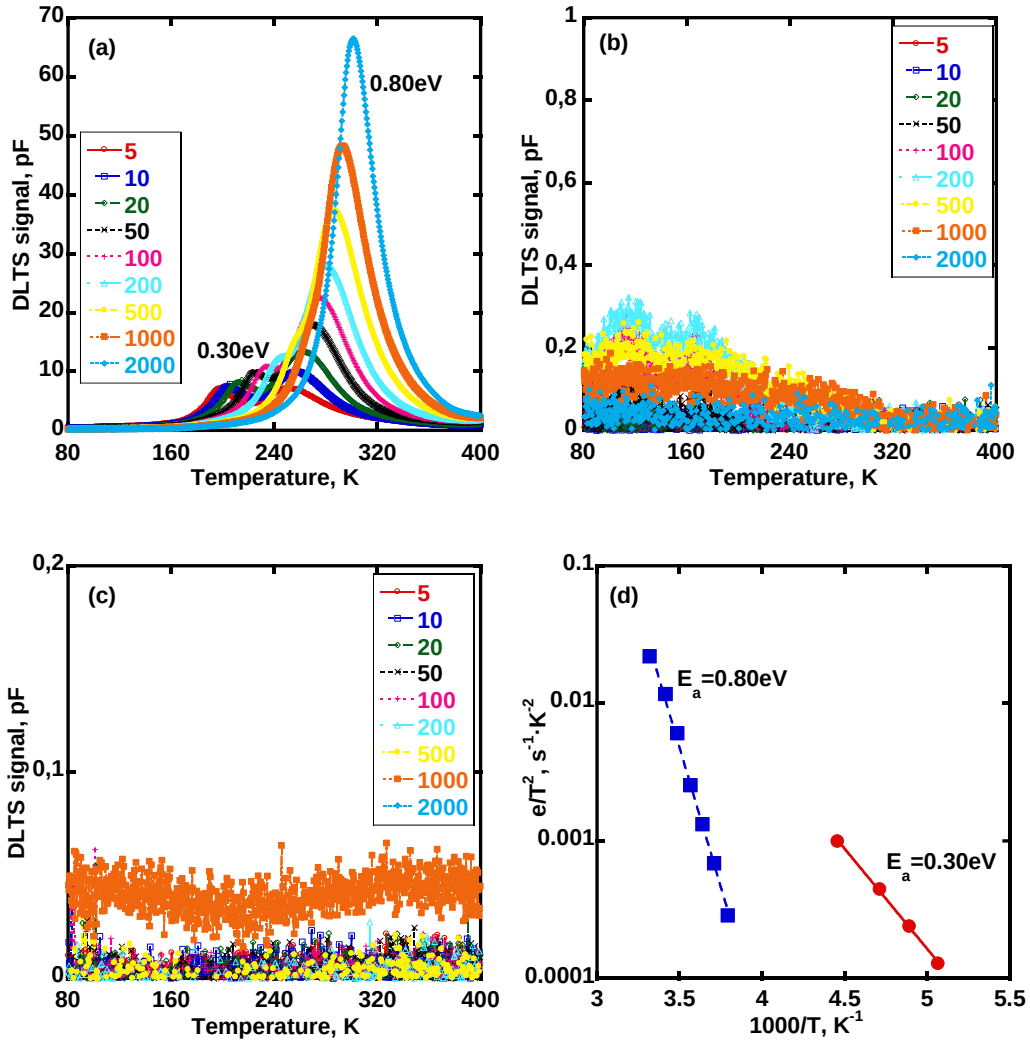

Figure V.14 (a, b, c, d). DLTS spectra $S(T)$ of µc-GaP/*n*-Si (a), a-GaP/*n*-Si (b), and Au/*n*-Si (c) for different rate windows (in s^{-1}). (d)- Arrhenius plots of e/T^2 for the two DLTS peaks detected in the µc-GaP/*n*-Si structure.

DLTS spectra of µc-GaP/*n*-Si (Figure V.14a) have two series of peaks, which are characteristic for the response from two defect levels. According to the Arrhenius plot (Figure V.14d) activation energies for low- and high-temperature levels are equal to 0.30 eV and 0.80 eV, respectively. Both peaks are broadened so non-exponential behavior of the capacitance relaxation due to extended defects can be suggested in this structure[148]. Unfortunately, low thicknesses of the GaP layer and low SCR width estimated from *C-V* measurements do not allow us to define exactly the region in the µc-GaP/*n*-Si structure where the response takes place. The response can be from the GaP/Si interface, from the GaP layer or from the bulk Si. $S(T)$ spectra for a-GaP/*n*-Si do not allow one to extract any defect response within our measurement accuracy (Figure V.14b), because the signal is much lower compared to that of the µc-GaP/*n*-Si sample. Nevertheless, defects described above were not detected in a-GaP/*n*-Si. However, according to the above explanation

the a-GaP layer is fully depleted and the SCR extends deeper in the silicon bulk as opposed to the μc-GaP/*n*-Si structure so a possibility of defect detection is lower in a-GaP. Also, we did not find any peak on the *S*(*T*) spectra of the Au/n-Si structures in the used temperature range (Figure V.14c). It means that the silicon bulk was not degraded by the deposition of the GaP layer in our low-temperature deposition method. Consequently, the detected defects in the μc-GaP/*n*-Si structure are attributed to the μc-GaP layer. Since the detected peaks are broad, the defects can tentatively be attributed to crystalline defects in μc-GaP generated during the growth process. It is confirmed by TEM measurements described above where the layer of μc-GaP has a very defective structure unlike the amorphous GaP (Figure V.5). Thereby, amorphous GaP provides better passivation of the silicon surface by PE-ALD than μc-GaP that leads to defects. Analysis of their nature and value of pre-exponential factors is a complicated issue and it should be explored in future experiments in more details.

In conclusion, according to previous sections a-GaP samples show better photoelectrical, structural and defect-related properties than μc-GaP ones. It can be associated with better passivation of silicon by amorphous GaP, while defects were observed in μc-GaP by DLTS and TEM methods.

V.4 Influence of PE-ALD of GaP on the silicon wafers quality

According to previous discussions, the epitaxial technology requires high temperatures of 500-900 °C leading to degradation of bulk properties of silicon wafers due to activation of non-radiative recombination centres[116,167]. This is why the influence of the PE-ALD growth method on the properties of silicon wafers must be also explored, because the wafer quality is a very crucial issue for the performance of SCs based on the GaP/Si heterojunction. In this section, we used Schottky diodes fabricated to *p*-Si in samples #3 (μc-GaP) and #2 (a-GaP) by the method shown in Figure V.7d. Furthermore, reference samples were fabricated with the same top Schottky diode and back ohmic contact to the initial *p*-type silicon wafer (i.e. without the GaP deposition and etching sequence). All the samples are investigated by capacitance-voltage and DLTS methods.

It was theoretically simulated and experimentally confirmed that the *n*-GaP/*p*-Si heterojunction has advantages over the *p*-GaP/*n*-Si one for photoelectrical structures grown by MBE[154]. Thus, the influence of the PE-ALD growth process of GaP on the electronic quality and properties of *p*-type silicon is a crucial issue for future performance of high efficiency multi-junction solar cells. Here we present measurements of three samples which were fabricated using p-type silicon wafer as described above: Au\Ti*p*-Si is the reference (ref) sample (*i.e* no PE-ALD of GaP), a-PE-ALD is a Schottky barrier formed on p-Si after etching of amorphous GaP, μc-PE-

ALD is a Schottky barrier to *p*-Si after etching of microcrystalline GaP. For these samples $1/C^2(V)$ curves and N_{CV}-W profiles (Figure V.15) were plotted from capacitance-voltage measurements (not shown here) at 80 K.

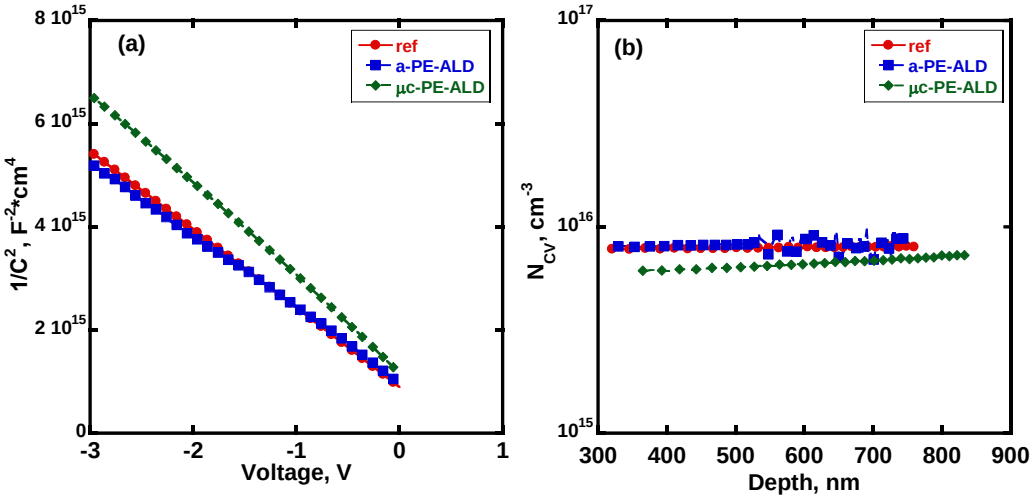

Figure V.15 Analysis of the bias dependence of the measured capacitance of the three structures (Schottky diodes on a reference sample, after etching of a-GaP, after etching of µc-GaP): $1/C^2$-V (a) and N_{CV}-W (b).

For all the samples $1/C^2(V)$ curves have a linear behavior so the charge carrier concentration is uniform in *p*-type silicon. N_{CV}-W profiles show a constant concentration value of about 1×10^{16} cm^{-3} that corresponds to the boron concentration in silicon. This means that passivation of boron doping is not observed after the PE-ALD growth process, which is an encouraging result. Indeed this is for instance a typical problem for solar cells based on a-Si:H/*p*-Si heterostructures due to interaction between hydrogen atoms from the plasma and boron atoms in the silicon wafer during the growth process. It leads to non-linear behaviour of $1/C^2(V)$ as a sharp drop when the space charge region approaches the heterointerface[168–170]. In our case, hydrogen plasma is also used during low-temperature PE-ALD growth of GaP, but it does not lead to boron passivation in *p*-Si. The estimated intercept voltage for $1/C^2(V)$ curves are close for the three samples: 0.60 V for reference, 0.73 V for a-PE-ALD and 0.70 V for µc-PE-ALD. It means that the Schottky barrier height has similar values of 0.65-0.75 eV for Ti/*p*-Si at 80 K, but it is slightly higher than 0.61 eV obtained at room temperature[171]. However, the value of Schottky barrier height should increase with decreasing temperature, so the characteristics of our explored samples are in good correlation with literature data.

DLTS spectra $S(T)$ of the reference *p*-type silicon wafer were measured under the following experimental conditions: V_{rev}= -0.2 V, V_{pulse}= 0.2 V and t_{pulse}=50 ms, respectively. Results are shown in Figure V.16.

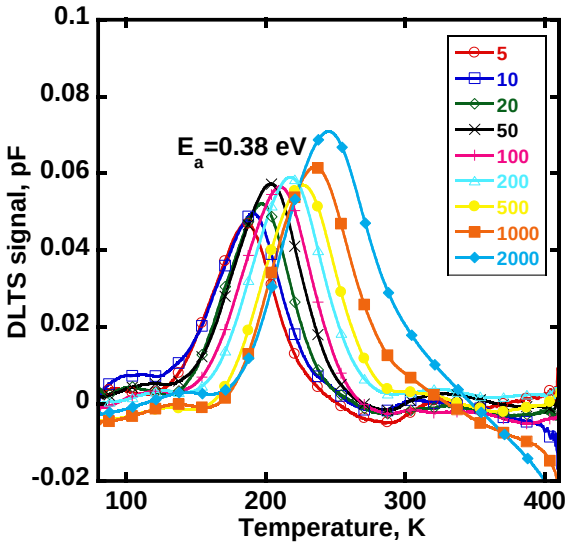

Figure V.16 DLTS spectra *S(T)* of reference Au/Ti/*p*-Si for different rate windows (in s^{-1}).

DLTS spectra exhibit peaks, which are characteristic of the response from defect levels. Experimental peaks are narrow and have almost the same amplitude for different rate windows. It means that the response comes from point defects in silicon. The activation energy and the capture cross section were estimated directly from a linear fit of e/T^2 in an Arrhenius plot. Activation energy and capture-cross section for detected defects in reference *p*-Si are 0.38 eV and 1.8×10^{15} cm^{-2}, respectively. Defect concentration was estimated from the peak amplitude at 3×10^{13} cm^{-3}. DLTS peaks have a positive value so the detected responses correspond to traps for majority charge carriers in *p*-Si. Therefore, the energy position of the defect level is E_v+0.38eV and the capture cross section is for holes. This defect is common for boron-doped p-type silicon and can be attributed to interstitial iron in Si (Fe_i)[172,173].

The existence of Fe_i in our initial silicon wafer is a drawback if we want to properly study the effect of the PE-ALD process on the silicon wafer, so silicon wafers with better quality must be used in the future to exclude the influence of initial defects on the detection of potential defects after the PE-ALD process.

DLTS spectra *S(T)* were obtained for Schottky diodes on silicon wafers, where a-GaP and µc-GaP were wet etched (Figure V.17a and Figure V.17b, respectively). Measurements were done for a reverse bias of 0.2 V, amplitude and duration of filling pulse were equal to 0.2 V and 50 ms, respectively. Both DLTS spectra show a similar shape of DLTS peaks that is different from that in the reference sample. All peaks in the reference sample are narrow and symmetric: it means that the response comes from point defects. However, peaks in both samples in Figure V.17 have broadened asymmetric shape with blurred low-temperature side. There are dominant peaks in the temperature range 150..220K, but estimated values of activation energy are different for a-PE-

ALD (0.17 eV) and µc-PE-ALD (0.09 eV) samples. Nevertheless, peak positions suggest that the defects may have the same nature as those detected in the reference sample above. Discrepancy of activation energies comes from overlapping of responses from several defect levels in these structures. Responses from another defect in the low temperature range are the main differences between the reference sample and that after PE-ALD process. Detailed observation of *S*(*T*) spectra allows us to propose the existence of a second defect in the temperature range 80..150 K. However, the estimation of its parameters is complicated, because the peak is wide and its amplitude is lower than that of the high-temperature peak. The latter became wider after growth process and its amplitude decreased for the µc-GaP sample. This suggests that the initial Fe_i configuration could be modified after the PE-ALD process. Temperature of growth of the GaP layers is 380 °C which could lead to migration of irons and change of its surroundings due to high diffusion coefficients. Additionally, the plasma treatment of the Si surface takes place, which could lead to local heating. Indeed for µc-GaP grown with significantly higher RF power DLTS spectra are strongly modified. Therefore, future experiments should be focused on studies of the influence of plasma power on defect modification in silicon wafers.

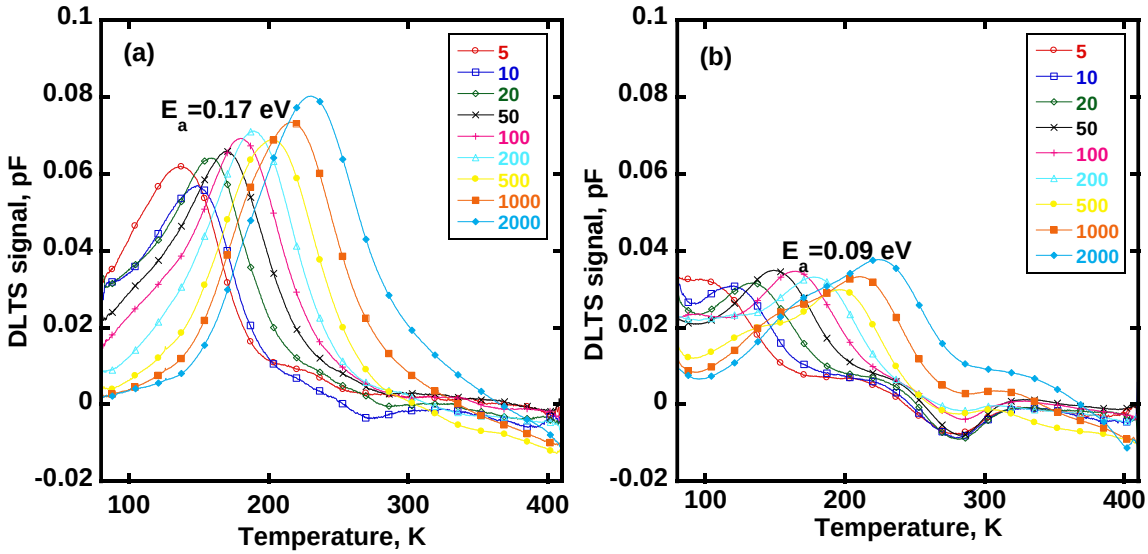

Figure V.17 DLTS spectra *S(T)* of Au/Ti/*p*-Si after etching of a-GaP (a), and µc-GaP (b) for different emission rates (in s^{-1}) obtained by changing the DLTS gate window.

Nevertheless, responses associated with defect levels were not detected at temperatures above 250 K. Therefore, it can be concluded that the PE-ALD growth process does not lead to the formation of deep-levels with high activation energy, suggesting that the quality of boron-doped *p*-type silicon would not be hardly deteriorated during growth of GaP by PE-ALD. This assumption is valid for studied samples grown at RF power of 20 W and 100 W and at low temperature, 380 °C, not leading to deep level formation. Future experiments should be focused

on the improvement of crystal quality of GaP by increasing plasma power rather than the temperature. However, it can lead to degradation of wafer properties so it will be controlled by DLTS measurements for each sample to define optimal growth parameters for future application in photovoltaic.

Summary

In Chapter V, GaP layers were grown on silicon wafers by the standard continuous method and by an innovative method of atomic-layer deposition at low temperature (below 400 °C) in a PECVD-chamber for photovoltaic applications. They were explored by different techniques. According to experimental data the following conclusions can be drawn:

- PE-ALD process has to be favored over continuous PECVD since it leads to better structural and electric properties of the grown GaP layer.
- Increase of RF plasma power from 20 W to 100 W leads to a change of crystalline structure of GaP from amorphous to microcrystalline.
- Silane flow in the GaP growth process induces *n*-type doping of the GaP layer.
- Growth of amorphous GaP leads to passivation of the silicon surface and absence of responses in DLTS spectra and TEM-images.
- Growth of microcrystalline GaP leads to appearance of defects in the structures.
- PE-ALD process does not lead to passivation of boron-doping in *p*-Si.
- Defect level associated with interstitial iron was detected in initial *p*-Si. PE-ALD process leads to modification of this defect level.
- PE-ALD process does not deteriorate the underlying silicon wafers.

Conclusion and perspectives

Photovoltaic nowadays requires new approaches for the fabrication of low-cost high-efficiency multi-junction solar cells. Three different ways were considered to this purpose in the current study that is devoted to perspective III-V semiconductor materials in multi-junction solar cells grown on wafers of IV group elements.

The first method is the introduction of an additional subcell based on 1eV-InGaAsN in the classical GaInP/GaAs/Ge MJSC. It will allow to increase its efficiency for terrestrial and space applications. Single-junction solar cells with different thickness of active layer of *i*-InGaAsN were explored. Dilute nitrides of InGaAsN were grown by the new method of sub-monolayer digital alloys in an MBE chamber. It consists in using original nanoheterostructures based on the InAs/GaAsN superlattice where 7-12 nm thick layers of GaAsN are separated by few monolayers of InAs 0.5 nm thick. As a result, low *p*-type background doping (less 1×10^{15} cm^{-3}) was demonstrated at room temperature in samples with 900 nm and 1200 nm thick InGaAsN layers. According to admittance spectroscopy and deep-level transient spectroscopy measurements the SDA approach leads to defect-free growth up to a thickness of 900 nm. An increase of thickness to 1200 nm leads to the formation of non-radiative recombination centers with an activation energy of 0.5 eV and concentration of $(1\text{-}2)\times10^{15}$ cm^{-3} and of a shallow defect level at 0.20 eV. The latter leads to the appearance of additional doping at room temperature but its concentration is low (5×10^{14} cm^{-3}) so it does not have strong effect on the energy band diagram and on the value of external quantum efficiency. However, further increase in thickness to 1600 nm leads to significant increase of its concentration to a value of $(3\text{-}5)\times10^{15}$ cm^{-3}, while the concentration of deep levels almost remains constant. Therefore, additional free charge carriers appearing due to the ionization of the shallow level change the band diagram from *p*-*i*-*n* to *p*-*n* junction at room temperature. It leads to a drop of external quantum efficiency due to the collapsing of electric field in part of the absorber layer, and to detected non-radiative recombination centers that negatively impact the free carrier lifetimes in InGaAsN.

In a second approach, dilute nitrides of InGaPAsN were studied as perspective alloys for top subcells in MJSC grown on silicon. Single-junction SCs on GaP wafers and MJSC on Si wafers were grown with various composition of the active layers of these alloys. It was established that undoped *i*-layers of GaPAsN are more suitable for photovoltaic application in SC based on *p*-*i*-*n* junctions than *n*-type layers in *p*-*n* junctions due to a more effective built-in electric field acting as a driving force for the photogenerated carriers. This leads to much higher short-circuit current in SCs with *i*-InGaPAsN. Then, a specific feature in the spectral quantum efficiency curves of the

structures was observed: the presence of two peaks, which is explained by the peculiar band diagram of dilute nitrides with two conduction subbands leading to two light absorption mechanisms in these alloys. Additional incorporation of In and As leads to the improvement of photoelectric properties of GaPN according to measurements of EQE and I-V characteristics, and the defect concentration was found to decrease according to admittance spectroscopy measurements. This is related to the compensation of elastic stress arising in GaPN due to incorporation of nitrogen in the phosphorus sublattice and its clusterization. Furthermore, addition of As is preferable to that of In in SCs since this leads to lower defect formation in active *i*-layers of dilute nitrides according to AS and DLTS measurements, and to the improvement of photovoltaic performance according to EQE and I-V experiments. Different defects were detected by capacitance methods in InGaPAsN layers. Some of them can be considered as centers of non-radiative recombination responsible for the low lifetime of charge carriers in these alloys; they are located at E_c-0.44 eV in InP/GaPN layers, and E_c-(0.50-0.55) eV in GaPAsN. Also, the post-growth treatment improves photoelectric properties (EQE increases by 25%) and electronic quality (defect concentration drastically drops) of single- and double- junction SCs based on GaPAsN layers. Finally, the first triple-junction SC with subcells of dilute nitrides was grown on a silicon wafer: its parameters are V_{OC}=2.23 eV and J_{SC}=1.02 mA/cm^2.

The third part of the study was devoted to the investigation of GaP layers grown on silicon wafers in a PECVD chamber for photovoltaic applications. It will allow us to decrease the final cost of perspective MJSCs for industrial production and to exclude the negative influence of high temperatures required in the MBE process. The proposed novel technology is based on plasma-enhanced atomic-layer deposition with alternation of P and Ga sources at low temperature (below 400 °C). Layers of GaP were grown on *n*- and *p*-type silicon wafers at different conditions. Samples with GaP grown by PE-ALD show better structural (SEM) and electric (C-V) properties than samples obtained by a continuous process where flows of P and Ga were used simultaneously. Thus, the PE-ALD method is better adapted to the growth of GaP. According to Raman spectroscopy and TEM measurements, the increase of RF plasma power in the growth process from 20 W to 100 W leads to a change in the structure of GaP from amorphous (a-GaP) to microcrystalline (μc-GaP). The sample with GaP grown with additional silane flow on *p*-Si wafers showed photovoltaic effect explained by the existence of a strong inversion layer in silicon near to the GaP/*p*-Si interface, demonstrating that the grown GaP should be doped and *n*-type. The a-GaP/*p*-Si sample (J_{SC}=21.82 mA/cm^2 and V_{OC}=0.44 V) shows much better performance than the μc-GaP/*p*-Si one (J_{SC}=3.75 mA/cm^2 and V_{OC}=0.32 V). This is explained by a better passivation of the silicon surface during the growth process by a-GaP. Firstly, it is confirmed by TEM images since the interface of μc-GaP/*p*-Si is more inhomogeneous and defective. Secondly, two defect

levels with an activation energy of 0.30 eV and 0.80 eV were detected by DLTS in μc-GaP/*n*-Si unlike in a-GaP/*n*-Si where no defect response was found. Both defects could be attributed to the μc-GaP layer. For boron doped *p*-Si there is no deactivation of boron doping after the PE-ALD process as could be expected from the presence of hydrogen in the plasma. In the reference *p*-Si, defects were detected at a concentration of 3×10^{13} cm^{-3} and at an energy position of E_v+0.38eV, suggesting the presence of interstitial iron in the wafers. PE-ALD growth of GaP leads to some modification of this defect and to the appearance of another response in the low temperature range. However, deeper levels with larger activation energies were not detected in *p*-Si after PE-ALD, suggesting that the quality of *p*-Si does not strongly deteriorate.

In conclusion, all three approaches showed promising result for future investigation. The SDA approach allowed to grow 1 eV-InGaAsN and to define defects that impact the photoelectric properties. In the future, the growth process will be optimized to exclude defect formation in layers thicker than 1 μm, and triple-junction GaInP/GaAs/InGaAsN solar cells will be grown on GaAs wafers. Secondly, we have shown that *i*-GaPAsN layers have better performance than SDA *i*-InP/GaPN in solar cells grown on GaP and Si wafers. Also, we detected deep levels responsible for low lifetimes in these layers. Future experiments will be focused on the growth and the improvement of *i*-GaPAsN layers thicker than 1 μm. Double-junction solar cells will be fabricated on Si wafers with the top subcell based on *p*-*i*-*n* junction with such quaternary alloy where high arsenic content of 20-30% is used to reach the bandgap energy of 1.7 eV. Finally, the PE-ALD method showed the possibility to grow GaP layers on Si wafers, and the solar cells based on *n*-GaP/*p*-Si was fabricated. In the future we will study ways to obtain *p*-type GaP layers and to better monitor the n-type doping concentration. Also, nitrogen will be introduced in the growth process to obtain *i*-GaPN layer, and *p*-*i*-*n* single-junction solar cells will be grown on Si wafers. Consequently, all methods will be developed in future experiments for the fabrication of low-cost high efficiency solar cells.

References

[1] A.F. Ioffe and A. V. Ioffe, Phys. Z. Sowjetunion **7**, 343 (1935).

[2] D.M. Chapin, C.S. Fuller, and G.L. Pearson, J. Appl. Phys. **25**, 676 (1954).

[3] Z.I. Alferov, V.M. Andreev, M.B. Kagan, I. Protasov, I, and V.. Trofim, Sov. Phys. Semicond. **4**, 2047 (1971).

[4] Z.I. Alferov, V.M. Andreev, and V.D. Rumyantsev, Semiconductors **38**, 899 (2004).

[5] B.M. Kayes, H. Nie, R. Twist, S.G. Spruytte, F. Reinhardt, I.C. Kizilyalli, and G.S. Higashi, in *Proc. 37th IEEE Photovolt. Spec. Conf.* (2011), pp. 000004–000008.

[6] K. Yoshikawa, H. Kawasaki, W. Yoshida, T. Irie, K. Konishi, K. Nakano, T. Uto, D. Adachi, M. Kanematsu, H. Uzu, and K. Yamamoto, Nat. Energy **2**, 17032 (2017).

[7] I. Newton, Philos. Trans. R. Soc. London **6**, 3075 (1671).

[8] W. Shockley and H.J. Queisser, J. Appl. Phys. **32**, 510 (1961).

[9] L.C. Hirst and N.J. Ekins-Daukes, Prog. Photovoltaics Res. Appl. **19**, 286 (2011).

[10] S.W. Glunz, R. Preu, and D. Biro, in *Compr. Renew. Energy* (Elsevier, 2012), pp. 353–387.

[11] R.R. King, D.C. Law, K.M. Edmondson, C.M. Fetzer, G.S. Kinsey, H. Yoon, R.A. Sherif, and N.H. Karam, Appl. Phys. Lett. **90**, 98 (2007).

[12] Z.I. Alferov, V.M. Andreev, K.K. Aripov, V.R. Larionov, and V.D. Rumyantsev, Geliotekhnica **6**, 3 (1981).

[13] M.A. Green, Y. Hishikawa, W. Warta, E.D. Dunlop, D.H. Levi, J. Hohl-Ebinger, and A.W.H. Ho-Baillie, Prog. Photovoltaics Res. Appl. **25**, 668 (2017).

[14] F. Dimroth, M. Grave, P. Beutel, U. Fiedeler, C. Karcher, T.N.D. Tibbits, E. Oliva, G. Siefer, M. Schachtner, A. Wekkeli, A.W. Bett, R. Krause, M. Piccin, N. Blanc, C. Drazek, E. Guiot, B. Ghyselen, T. Salvetat, A. Tauzin, T. Signamarcheix, A. Dobrich, T. Hannappel, and K. Schwarzburg, Prog. Photovoltaics Res. Appl. **22**, 277 (2014).

[15] K. Sasaki, T. Agui, K. Nakaido, N. Takahashi, R. Onitsuka, and T. Takamoto, in *9th Int. Conf. Conc. Photovolt. Syst. AIP Conf. Proc.* (2013), pp. 22–25.

[16]NREL Press Release NR-4514, 16 December 2014 (n.d.).

[17] S. Adachi, *Properties of Group-IV, III-V and II-VI Semiconductors* (John Wiley & Sons, Ltd, Chichester, UK, 2005).

[18] J.F. Geisz and D.J. Friedman, Semicond. Sci. Technol. **17**, 769 (2002).

[19] S.R. Kurtz, D. Myers, and J.M. Olson, in *Conf. Rec. Twenty Sixth IEEE Photovolt. Spec. Conf. - 1997* (IEEE, Anaheim, California, 1997), pp. 875–878.

[20] M. Yamaguchi, K.I. Nishimura, T. Sasaki, H. Suzuki, K. Arafune, N. Kojima, Y. Ohsita, Y.

Okada, A. Yamamoto, T. Takamoto, and K. Araki, Sol. Energy **82**, 173 (2008).

[21] M. Weyers, M. Sato, and H. Ando, Jpn. J. Appl. Phys. **31**, L853 (1992).

[22] M. Henini, *Dilute Nitride Semiconductors*, 1st ed. (Elsevier, Amsterdam, 2004).

[23] J. Allen, V. Sabnis, M. Wiemer, and H. Yuen, in *9th Int. Conf. Conc. Photovolt. Syst.* (Miyazaki, Japan, 2013).

[24] A. Aho, R. Isoaho, A. Tukiainen, V. Polojärvi, T. Aho, M. Raappana, and M. Guina, in *AIP Conf. Proc.* (2015), p. 50001.

[25] R. Campesato, A. Tukiainen, A. Aho, G. Gori, R. Isoaho, E. Greco, and M. Guina, E3S Web Conf. **16**, 3003 (2017).

[26] A. Tukiainen, A. Aho, G. Gori, V. Polojärvi, M. Casale, E. Greco, R. Isoaho, T. Aho, M. Raappana, R. Campesato, and M. Guina, Prog. Photovoltaics Res. Appl. **24**, 914 (2016).

[27] S. Kurtz, S.W. Johnston, J.F. Geisz, D.J. Friedman, and a J. Ptak, 31st IEEE Photovoltaics Spec. Conf. Exhib. Lake Buena Vista, Florida (2005).

[28] B. Bouzazi, H. Suzuki, N. Kojima, Y. Ohshita, and M. Yamaguchi, Jpn. J. Appl. Phys. **49**, 121001 (2010).

[29] V. Polojärvi, A. Aho, A. Tukiainen, M. Raappana, T. Aho, A. Schramm, and M. Guina, Sol. Energy Mater. Sol. Cells **149**, 213 (2016).

[30] S.R. Kurtz, A.A. Allerman, E.D. Jones, J.M. Gee, J.J. Banas, and B.E. Hammons, Appl. Phys. Lett. **74**, 729 (1999).

[31] N. Miyashita, N. Ahsan, and Y. Okada, Phys. Status Solidi **214**, 1600586 (2017).

[32] K. Volz, D. Lackner, I. Németh, B. Kunert, W. Stolz, C. Baur, F. Dimroth, and A.W. Bett, J. Cryst. Growth **310**, 2222 (2008).

[33] M.M. Islam, N. Miyashita, N. Ahsan, T. Sakurai, K. Akimoto, and Y. Okada, Appl. Phys. Lett. **105**, 112103 (2014).

[34] N. Miyashita, N. Ahsan, and Y. Okada, Prog. Photovoltaics Res. Appl. **24**, 28 (2016).

[35] D.B. Jackrel, S.R. Bank, H.B. Yuen, M.A. Wistey, J.S. Harris, A.J. Ptak, S.W. Johnston, D.J. Friedman, and S.R. Kurtz, J. Appl. Phys. **101**, 114916 (2007).

[36] V. Polojärvi, A. Aho, A. Tukiainen, A. Schramm, and M. Guina, Appl. Phys. Lett. **108**, 122104 (2016).

[37] E. V. Nikitina, A.S. Gudovskikh, A.A. Lazarenko, E. V. Pirogov, M.S. Sobolev, K.S. Zelentsov, I.A. Morozov, and A.Y. Egorov, Semiconductors **50**, 652 (2016).

[38] M. Sato and Y. Horikoshi, J. Appl. Phys. **66**, 851 (1989).

[39] R. Cingolani, O. Brandt, L. Tapfer, G. Scamarcio, G.C. La Rocca, and K. Ploog, Phys. Rev. B **42**, 3209 (1990).

[40] A.Y. Egorov, A.E. Zhukov, P.S. Kop'ev, N.N. Ledentsov, M. V. Maksimov, and V.M.

Ustinov, Semiconductors **28**, 363 (1994).

[41] S.V. Ivanov, A.A. Toropov, T.V. Shubina, A.V. Lebedev, S.V. Sorokin, A.A. Sitnikova, P.S. Kop'ev, G. Reuscher, M. Keim, F. Bensing, A. Waag, G. Landwehr, G. Pozina, J.P. Bergman, and B. Monemar, J. Cryst. Growth **214**–**215**, 109 (2000).

[42] S. V. Ivanov, O. V. Nekrutkina, S. V. Sorokin, V.A. Kaygorodov, T. V. Shubina, A.A. Toropov, P.S. Kop'ev, G. Reuscher, V. Wagner, J. Geurts, A. Waag, and G. Landwehr, Appl. Phys. Lett. **78**, 404 (2001).

[43] Y. V Bolkhovityanov and O.P. Pchelyakov, Uspekhi Fiz. Nauk **51**, 437 (2008).

[44] R. Fischer, N. Chand, W. Kopp, H. Morkoç, L.P. Erickson, and R. Youngman, Appl. Phys. Lett. **47**, 397 (1985).

[45] M. Yamaguchi, J. Mater. Res. **6**, 376 (1991).

[46] S. Kim, M.-S. Park, D.-M. Geum, H. Kim, G. Ryu, H.-D. Yang, J.D. Song, C.Z. Kim, and W.J. Choi, Curr. Appl. Phys. **15**, S40 (2015).

[47] C.-Y. Tseng, C.-T. Lee, O.P. Pchelyakov, and V. V. Preobrazhenskii, Sol. Energy **118**, 1 (2015).

[48] T. Ogawa, G. Wang, K. Murase, K. Hori, J. Arokiaraj, T. Soga, T. Jimbo, and M. Umeno, in *Twenty-Eighth IEEE Photovolt. Spec. Conf.* (IEEE, 2000), pp. 1308–1311.

[49] T. Tsuji, H. Yonezu, and N. Ohshima, J. Vac. Sci. Technol. B Microelectron. Nanom. Struct. **22**, 1428 (2004).

[50] M.L. Lee, E.A. Fitzgerald, M.T. Bulsara, M.T. Currie, and A. Lochtefeld, J. Appl. Phys. **97**, 11101 (2005).

[51] Y. Alaskar, S. Arafin, D. Wickramaratne, M.A. Zurbuchen, L. He, J. McKay, Q. Lin, M.S. Goorsky, R.K. Lake, and K.L. Wang, Adv. Funct. Mater. **24**, 6629 (2014).

[52] T. Soga, M. Yang, and T.J. and M. Umeno, Jpn. J. Appl. Phys. **35**, 1401 (1996).

[53] C. Renard, N. Cherkasin, A. Jaffre, L. Vincent, A. Michel, T. Molière, R. Hamouche, V. Yam, J. Alvarez, F. Fossard, D. Mencaraglia, and D. Bouchier, Appl. Phys. Lett. **102**, 191915 (2013).

[54] C. Renard, N. Cherkashin, A. Jaffre, T. Molière, G. Hallais, L. Vincent, J. Alvarez, D. Mencaraglia, A. Michel, and D. Bouchier, J. Cryst. Growth **401**, 554 (2014).

[55] C.-P. Chu, S. Ara, T. Nie, K. Yao, X. Kou, L. He, C.-Y. Wang, S.-Y. Chen, L.-J. Chen, S.M. Qasim, M.S. BenSaleh, and K.L. Wang, Cryst. Growth Des. **14**, 593 (2014).

[56] H. Taguchi, T. Soga, and T. Jimbo, Jpn. J. Appl. Phys. **42**, L1419 (2003).

[57] S. Kim, D.-M. Geum, M.-S. Park, C.Z. Kim, and W.J. Choi, Sol. Energy Mater. Sol. Cells **141**, 372 (2015).

[58] S. Essig, S. Ward, M.A. Steiner, D.J. Friedman, J.F. Geisz, P. Stradins, and D.L. Young, Energy Procedia **77**, 464 (2015).

[59] N. Shigekawa, J. Liang, R. Onitsuka, T. Agui, H. Juso, and T. Takamoto, Jpn. J. Appl. Phys. **54**, 08KE03 (2015).

[60] H. Döscher, B. Borkenhagen, G. Lilienkamp, W. Daum, and T. Hannappel, Surf. Sci. **605**, L38 (2011).

[61] K. Yamane, T. Kawai, Y. Furukawa, H. Okada, and A. Wakahara, J. Cryst. Growth **312**, 2179 (2010).

[62] K. Volz, A. Beyer, W. Witte, J. Ohlmann, I. Nmeth, B. Kunert, and W. Stolz, J. Cryst. Growth **315**, 37 (2011).

[63] A.C. Lin, M.M. Fejer, and J.S. Harris, J. Cryst. Growth **363**, 258 (2013).

[64] M.S. Sobolev, A.A. Lazarenko, E. V. Nikitina, E. V. Pirogov, A.S. Gudovskikh, and A.Y. Egorov, Semiconductors **49**, 559 (2015).

[65] E.H. Hussein, S. Dadgostar, F. Hatami, and W.T. Masselink, J. Cryst. Growth **419**, 42 (2015).

[66] E.L. Warren, A.E. Kibbler, R.M. France, A.G. Norman, P. Stradins, and W.E. McMahon, Appl. Phys. Lett. **107**, 82109 (2015).

[67] H. Wagner, T. Ohrdes, A. Dastgheib-Shirazi, B. Puthen-Veettil, D. König, and P.P. Altermatt, J. Appl. Phys. **115**, 44508 (2014).

[68] T. Katoda and M. Kishi, J. Electron. Mater. **9**, 783 (1980).

[69] M. Feifel, T. Rachow, J. Benick, J. Ohlmann, S. Janz, M. Hermle, F. Dimroth, and D. Lackner, IEEE J. Photovoltaics **6**, 384 (2016).

[70] C. Skierbiszewski, P. Perlin, P. Wisniewski, W. Knap, T. Suski, W. Walukiewicz, W. Shan, K.M. Yu, J.W. Ager, E.E. Haller, J.F. Geisz, and J.M. Olson, Appl. Phys. Lett. **76**, 2409 (2000).

[71] I.A. Buyanova, G.Y. Rudko, W.M. Chen, H.P. Xin, and C.W. Tu, Appl. Phys. Lett. **80**, 1740 (2002).

[72] S.R. Kurtz, P. Faine, and J.M. Olson, J. Appl. Phys. **68**, 1890 (1990).

[73] B.M. Kayes, L. Zhang, R. Twist, I.K. Ding, and G.S. Higashi, IEEE J. Photovoltaics **4**, 729 (2014).

[74] D.A. Kudryashov, A.S. Gudovskikh, E. V Nikitina, and A.Y. Egorov, Semiconductors **48**, 381 (2014).

[75] J.N. Baillargeon, K.Y. Cheng, G.E. Hofler, P.J. Pearah, and K.C. Hsieh, Appl. Phys. Lett. **60**, 2540 (1992).

[76] a. Y. Egorov, E.S. Semenova, V.M. Ustinov, Y.G. Hong, and C. Tu, Semiconductors **36**, 981 (2002).

[77] S. Miyoshi, H. Yaguchi, K. Onabe, R. Ito, and Y. Shiraki, Appl. Phys. Lett. **63**, 3506 (1993).

[78] G. Biwa, H. Yaguchi, K. Onabe, and Y. Shiraki, J. Cryst. Growth **189190**, 485 (1998).

[79] G. Biwa, H. Yaguchi, K. Onabe, and Y. Shiraki, J. Cryst. Growth **195**, 574 (1998).

[80] A.A. Lazarenko, E. V. Nikitina, E. V. Pirogov, M.S. Sobolev, and A.Y. Egorov, Semiconductors **48**, 392 (2014).

[81] A.A. Lazarenko, E. V. Nikitina, M.S. Sobolev, E. V. Pirogov, D. V. Denisov, and A.Y. Egorov, Semiconductors **49**, 479 (2015).

[82] S. Almosni, C. Robert, T. Nguyen Thanh, C. Cornet, A. Létoublon, T. Quinci, C. Levallois, M. Perrin, J. Kuyyalil, L. Pedesseau, A. Balocchi, P. Barate, J. Even, J.M. Jancu, N. Bertru, X. Marie, O. Durand, and A. Le Corre, J. Appl. Phys. **113**, 123509 (2013).

[83] N.Q. Thinh, I.P. Vorona, I.A. Buyanova, W.M. Chen, S. Limpijumnong, S.B. Zhang, Y.G. Hong, H.P. Xin, C.W. Tu, A. Utsumi, Y. Furukawa, S. Moon, A. Wakahara, and H. Yonezu, Phys. Rev. B **71**, 125209 (2005).

[84] D. Dagnelund, I.A. Buyanova, X.J. Wang, W.M. Chen, A. Utsumi, Y. Furukawa, A. Wakahara, and H. Yonezu, J. Appl. Phys. **103**, 63519 (2008).

[85] D. Dagnelund, J. Stehr, A. Yu. Egorov, W.M. Chen, and I.A. Buyanova, Appl. Phys. Lett. **102**, 21910 (2013).

[86] B. Tell and F.P.J. Kuijpers, J. Appl. Phys. **49**, 5938 (1978).

[87] G. Ferenczi, P. Krispin, and M. Somogyi, J. Appl. Phys. **54**, 3902 (1983).

[88] P. Kamiński, W. Strupiński, and K. Roszkiewicz, J. Cryst. Growth **108**, 699 (1991).

[89] A. V Skazochkin, Y.K. Krutogolov, and Y.I. Kunakin, Semicond. Sci. Technol. **10**, 634 (1995).

[90] A. V Skazochkin, Y.K. Krutogolov, and G.G. Bondarenko, Semicond. Sci. Technol. **11**, 495 (1996).

[91] K. Ždánský, J. Zavadil, D. Nohavica, and S. Kugler, J. Appl. Phys. **83**, 7678 (1998).

[92] A.F. Basile, S. Hatakenaka, H. Okada, and A. Wakahara, J. Vac. Sci. Technol. A Vacuum, Surfaces, Film. **27**, 531 (2009).

[93] D. Dagnelund, C.W. Tu, A. Polimeni, M. Capizzi, W.M. Chen, and I.A. Buyanova, Phys. Status Solidi **10**, 561 (2013).

[94] O.I. Rumyantsev, P.N. Brunkov, E. V. Pirogov, and A.Y. Egorov, Semiconductors **44**, 893 (2010).

[95] J.F. Geisz, D.J. Friedman, and S. Kurtz, in *Conf. Rec. Twenty-Ninth IEEE Photovolt. Spec. Conf. 2002.* (IEEE, 2002), pp. 864–867.

[96] J.F. Geisz, J.M. Olson, D.J. Friedman, K.M. Jones, R.C. Reedy, and M.J. Romero, in *Proc. 31st IEEE PVSC* (2005), pp. 695–698.

[97] S. Sukrittanon, R. Liu, Y.G. Ro, J.L. Pan, K.L. Jungjohann, C.W. Tu, and S.A. Dayeh, Appl. Phys. Lett. **107**, 153901 (2015).

[98] S. Almosni, P. Rale, C. Cornet, M. Perrin, L. Lombez, A. Létoublon, K. Tavernier, C.

Levallois, T. Rohel, N. Bertru, J.F. Guillemoles, and O. Durand, Sol. Energy Mater. Sol. Cells **147**, 53 (2016).

[99] K. Yamane, M. Goto, K. Takahashi, K. Sato, H. Sekiguchi, H. Okada, and A. Wakahara, Appl. Phys. Express **10**, 75504 (2017).

[100] W. Shan, W. Walukiewicz, J. Ager, E. Haller, J. Geisz, D. Friedman, J. Olson, and S. Kurtz, Phys. Rev. Lett. **82**, 1221 (1999).

[101] W. Shan, W. Walukiewicz, K.M. Yu, J.W. Ager III, E.E. Haller, J.F. Geisz, D.J. Friedman, J.M. Olson, S.R. Kurtz, H.P. Xin, and C.W. Tu, Phys. Status Solidi **223**, 75 (2001).

[102] N. V. Kryzhanovskaya, a. Y. Egorov, E. V. Pirogov, and M.S. Sobolev, J. Surf. Investig. X-Ray, Synchrotron Neutron Tech. **6**, 479 (2012).

[103] B. Kunert, K. Volz, and W. Stolz, Phys. Status Solidi Basic Res. **244**, 2730 (2007).

[104] R. Kudrawiec, J. Appl. Phys. **101**, 23522 (2007).

[105] R. Kudrawiec, J. Appl. Phys. **101**, 116101 (2007).

[106] J. Chamings, S. Ahmed, A.R. Adams, S.J. Sweeney, V.A. Odnoblyudov, C.W. Tu, B. Kunert, and W. Stolz, Phys. Status Solidi **246**, 527 (2009).

[107] C. Karcher, H. Grüning, M. Güngerich, P.J. Klar, B. Kunert, K. Volz, W. Stolz, and W. Heimbrodt, Phys. Status Solidi Curr. Top. Solid State Phys. **6**, 2638 (2009).

[108] E. V. Nikitina, M.S. Sobolev, E. V. Pirogov, and A.Y. Egorov, Tech. Phys. Lett. **39**, 1114 (2013).

[109] C.W. Tu, W.M. Chen, I.A. Buyanova, and J.S. Hwang, J. Cryst. Growth **288**, 7 (2006).

[110] L. Bellaiche, S.-H. Wei, and A. Zunger, Appl. Phys. Lett. **70**, 3558 (1997).

[111] T. Kitatani, M. Kondow, T. Kikawa, Y. Yazawa, M. Okai, and K. Uomi, Jpn. J. Appl. Phys. **38**, 5003 (1999).

[112] H.-P. Komsa, E. Arola, and T.T. Rantala, Appl. Phys. Lett. **92**, 262101 (2008).

[113] R. Kudrawiec, H.B. Yuen, S.R. Bank, H.P. Bae, M.A. Wistey, J.S. Harris, M. Motyka, and J. Misiewicz, J. Appl. Phys. **102**, 113501 (2007).

[114] A.S. Chang, E.S. Zech, T.W. Kim, Y.H. Lin, L.J. Mawst, and R.S. Goldman, Appl. Phys. Lett. **105**, 142105 (2014).

[115] W. Li, M. Pessa, J. Toivonen, and H. Lipsanen, Phys. Rev. B **64**, 113308 (2001).

[116] R. Varache, M. Darnon, M. Descazeaux, M. Martin, T. Baron, and D. Muñoz, Energy Procedia **77**, 493 (2015).

[117] J.R. Gong, S. Nakamura, M. Leonard, S.M. Bedair, and N.A. El-Masry, J. Electron. Mater. **21**, 965 (1992).

[118] F. Rinaldi, Annu. Rep. 31 (2002).

[119] A.S. Gudovskikh, A. V. Uvarov, I.A. Morozov, A.I. Baranov, D.A. Kudryashov, E. V.

Nikitina, and J.-P. Kleider, Phys. Status Solidi Curr. Top. Solid State Phys. **14**, 1700150 (2017).

[120] S.M. Sze and K.K. Ng, in *Phys. Semicond. Devices* (John Wiley & Sons, Inc., Hoboken, NJ, USA, 2006).

[121] J.-P. Kleider, J. Alvarez, A. Brézard-Oudot, M.-E. Gueunier-Farret, and O. Maslova, Sol. Energy Mater. Sol. Cells **135**, 8 (2015).

[122] S.R. Forrest, *Heterojunction Band Discontinuities – Physics and Device Applications* (Elsevier Science Pub. Co., Amsterdam, 1987).

[123] J.P. Kleider and A.S. Gudovskikh, in *MRS Spring Meet. San Fr. 24-28 March, 2008* (San-Francisco, 2008), pp. 75–86.

[124] D.K. Schroder, *Semiconductor Material and Device Characterization* (John Wiley & Sons, Inc., Hoboken, NJ, USA, 2005).

[125] D.L. Losee, J. Appl. Phys. **46**, 2204 (1975).

[126] G. Vincent, D. Bois, and P. Pinard, J. Appl. Phys. **46**, 5173 (1975).

[127] T. Walter, R. Herberholz, C. Müller, and H.W. Schock, J. Appl. Phys. **80**, 4411 (1996).

[128] D. V. Lang, J. Appl. Phys. **45**, 3023 (1974).

[129] W. Shockley and W.T. Read, Phys. Rev. **87**, 835 (1952).

[130] R.N. Hall, Phys. Rev. **87**, 387 (1952).

[131] Y. Zohta and M.O. Watanabe, J. Appl. Phys. **53**, 1809 (1982).

[132] G.L. Miller, D. V Lang, and L.C. Kimerling, Annu. Rev. Mater. Sci. **7**, 377 (1977).

[133] L. Dobaczewski, P. Kaczor, I.D. Hawkins, and A.R. Peaker, J. Appl. Phys. **76**, 194 (1994).

[134] R. Varache, C. Leendertz, M.E. Gueunier-Farret, J. Haschke, D. Muñoz, and L. Korte, Sol. Energy Mater. Sol. Cells **141**, 14 (2015).

[135] T. V. Blank and Y.A. Gol'dberg, Semiconductors **41**, 1263 (2007).

[136] A.I. Baranov, A.S. Gudovskikh, E. V Nikitina, and A.Y. Egorov, Tech. Phys. Lett. **39**, 1117 (2013).

[137] F.C. Frank and J.H. van der Merwe, Proc. R. Soc. A Math. Phys. Eng. Sci. **198**, 216 (1949).

[138] J.H. Van Der Merwe, J. Appl. Phys. **34**, 117 (1963).

[139] M. Dąbrowska-Szata, G. Jóźwiak, and Ł. Gelczuk, Mater. Sci. **23**, 625 (2005).

[140] S.W. Johnston, R. Ahenkiel, A. Ptak, D. Friedman, and S. Kurtz, Nrel/Cp-520-33557 1 (2003).

[141] A. Kosa, L. Stuchlikova, L. Harmatha, J. Kovac, B. Sciana, W. Dawidowski, and M. Tlaczala, Adv. Electr. Electron. Eng. **15**, 114 (2017).

[142] B. Bouzazi, N. Kojima, Y. Ohshita, and M. Yamaguchi, J. Alloys Compd. **552**, 469 (2013).

[143] D.J. Friedman, A.J. Ptak, S.R. Kurtz, and J.F. Geisz, in *Conf. Rec. Thirty-First IEEE Photovolt. Spec. Conf. 2005.* (IEEE, 2005), pp. 691–694.

[144] P. Omling, L. Samuelson, and H.G. Grimmeiss, J. Appl. Phys. **54**, 5117 (1983).

[145] J.W. Matthews and A.E. Blakeslee, J. Cryst. Growth **27**, 118 (1974).

[146] A.E. Zhukov, A.Y. Egorov, V.M. Ustinov, A.F. Tsatsulnikov, M. V Maksimov, N.N. Faleev, and P.S. Kopev, Semiconductors **31**, 15 (1997).

[147] P. Blood and J.W. Orton, *The Electrical Characterization of Semiconductors : Majority Carriers and Electron States* (Academic Press, 1992).

[148] W. Schröter, J. Kronewitz, U. Gnauert, F. Riedel, and M. Seibt, Phys. Rev. B **52**, 13726 (1995).

[149] D. Pons, J. Appl. Phys. **55**, 3644 (1984).

[150] E. PŁaczek-Popko, J. Trzmiel, E. Zielony, S. Grzanka, R. Czernecki, and T. Suski, Phys. B Condens. Matter **404**, 4889 (2009).

[151] T. Wosiński, J. Appl. Phys. **65**, 1566 (1989).

[152] M. Matyas Jr., Phys. Status Solidi **97**, 297 (1986).

[153] J. Dabrowski and M. Schemer, Phys. Rev. B **40**, 391 (1989).

[154] A.S. Gudovskikh, K.S. Zelentsov, A.I. Baranov, D.A. Kudryashov, I.A. Morozov, E.V. Nikitina, and J.-P. Kleider, Energy Procedia **102**, 56 (2016).

[155] I. Sakata and H. Kawanami, Appl. Phys. Express **1**, 91201 (2008).

[156] A. Utsumi, H. Yonezu, Y. Furukawa, K. Momose, and K. Kuroki, Phys. Status Solidi C Conf. **2744**, 2741 (2003).

[157] I.A. Morozov, A.S. Gudovskikh, D.A. Kudryashov, E. V Nikitina, J.-P. Kleider, A. V Myasoedov, and V. Levitskiy, J. Phys. Conf. Ser. **741**, 12088 (2016).

[158] M. Wihl, M. Cardona, and J. Tauc, J. Non. Cryst. Solids **8**–**10**, 172 (1972).

[159] S. Hayashi, Solid State Commun. **56**, 375 (1985).

[160] M. Onuki and H. Kubota, Jpn. J. Appl. Phys. **26**, 1404 (1987).

[161] H. Kubota and M. Onuki, J. Non. Cryst. Solids **115**, 39 (1989).

[162] H. Kubota, T. Matsumoto, T. Hirayu, T. Fujiyoshi, R. Miyagawa, K. Miyahara, and M. Onuki, Sol. Energy Mater. Sol. Cells **35**, 353 (1994).

[163] H. Kubota, T. Tashiro, T. Fujiyoshi, T. Hirayu, and M. Onuki, J. Non. Cryst. Solids **198**–**200**, 383 (1996).

[164] T.F. Lei, C.L. Lee, and C.Y. Chang, Solid. State. Electron. **22**, 1035 (1979).

[165] R. Mientus, R. Wolf, B. Kloth, M. Protsch, and A.N. Pikhtin, Surf. Coatings Technol. **119**, 711 (1999).

[166] H. Kroemer, W. Chien, J.S. Harris, and D.D. Edwall, Appl. Phys. Lett. **36**, 295 (1980).

[167] L. Ding, C. Zhang, T.U. Nærland, N. Faleev, C. Honsberg, and M.I. Bertoni, Energy Procedia **92**, 617 (2016).

[168] J. Damon-Lacoste, P.R.I. Cabarrocas, A.S. Gudovskikh, J.-P. Kleider, P.J. Ribeyron, V. Svrcek, and Y. Veschetti, in *Proc. 19th Eur. Photovolt. Sol. Energy Conf. Exhib. (EU PVSEC), Paris, Fr. 2014, Vol. 2 Cells*, edited by K.W. Hoffmann, J.L. Bal, H. Ossenbrink, W. Palz, and P. Helm (Paris, 2004), pp. 1453–1456.

[169] G.G. DeLeo, Phys. B Phys. Condens. Matter **170**, 295 (1991).

[170] C.T. Sah, J.Y.C. Sun, and J.J.T. Tzou, Appl. Phys. Lett. **43**, 204 (1983).

[171] A.M. Cowley, Solid. State. Electron. **12**, 403 (1970).

[172] O.O. Awadelkarim and B. Monemar, J. Appl. Phys. **64**, 6306 (1988).

[173] A.A. Istratov, H. Hieslmair, and E.R. Weber, Appl. Phys. A Mater. Sci. Process. **69**, 13 (1999).

Appendix A. Contact formation for single-junction SC on GaP

The deposition of metal electrode, used as ohmic contact, is required to study electrical properties of materials of *p*-*n* junctions. Here, we focus on the contact formation for single-junction SCs grown on *n*-GaP wafers. Two methods are studied: indium contacts and gold-based contacts for mesa-structures.

A.1 Indium contacts

As described in Chapter II, *n*-GaP wafer must be covered by titanium from bottom side for its heating during the growth process by IR irradiation in used MBE-equipment. However, the Ti/*n*-GaP is well-known to be a Schottky contact. So titanium could not be used as a bottom electrode, and it was removed after the growth. For our photoelectrical measurements on GaP wafers, indium contacts were chosen due to its simple and quick fabrication procedure.

Firstly, indium dots were deposited on the bottom side. It has been experimentally shown that simultaneous evaporation of indium contacts to front and bottom layers of GaP and subsequent RTA at a temperature higher than 330 °C leads to shunting of the samples due to indium diffusion in active layers. Therefore, initially the indium dots were deposited on the wafer and annealed at 420 °C for 30 seconds in a nitrogen ambient. The I-V characteristics in lateral geometry between adjacent indium dots before and after annealing are shown in Figure A.1.1a. We observe that (i) the In/*n*-GaP contact is ohmic, (ii) and that the resistance value decreases after annealing. In next step, indium dots were deposited on the front side to *p*-GaP layer but it was annealed at 300 °C. The Figure A.1.1b shows the I-V characteristic in lateral geometry for In/*p*-GaP contact. As for In/*n*-GaP, the annealing effect significantly reduces contact resistance. The I-V is almost symmetric but, unfortunately, it is not perfect linear so In/p-GaP is a non-ideal ohmic contact even after temperature treatment.

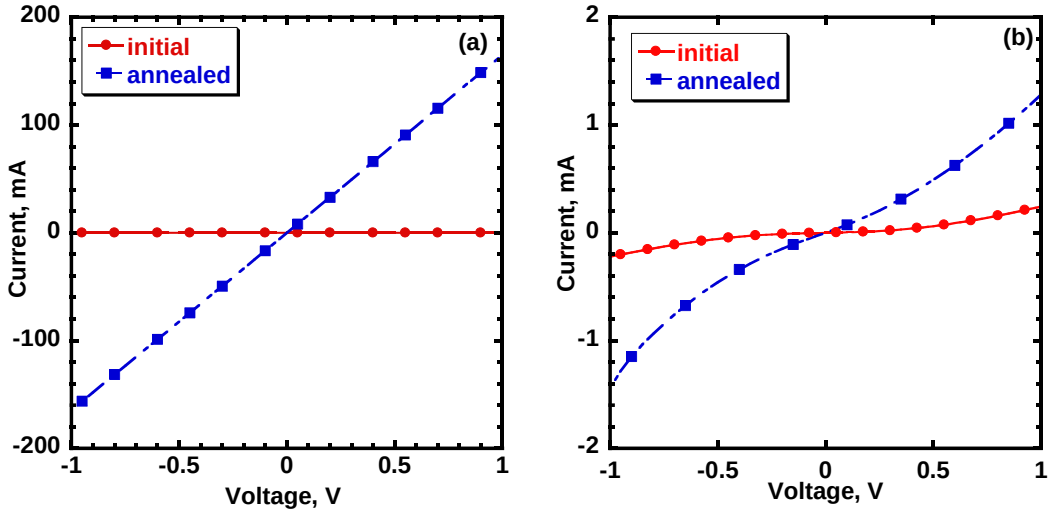

Figure A.1.1 Current-voltage characteristics in lateral geometry between adjacent indium dots on *n*-GaP (a) and *p*-GaP (b) in single-junction SC.

Then, I-V curves under illumination of AM1.5G were measured in SC with *p*-*i*-*n* junction with initial and annealed indium contacts to *p*-GaP front layer (Figure A.1.2). As a result, the I-V curve behavior strongly improved since the bend is not observed after annealing. Finally, RTA leads to significant enhancement of fill factor and consequently efficiency of SCs.

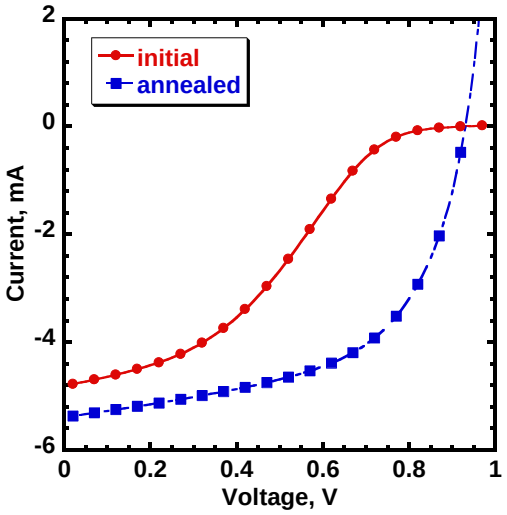

Figure A.1.2 Current-voltage characteristics of SC with the *p*-*i*-*n* junction under illumination AM1.5 with initial and annealed indium contact to *p*-GaP in single-junction SC.

A.2 Mesa-structures

Indium dots are useful contact for express measurements and research of qualitative behavior of structures but titanium polishing and their non-ideal ohmic behavior limits an accurate

quantitative analysis. Thus, the post-growth technology described in Chapter II was applied to fabricate mesa-structures and SCs with desirable geometry.

In the method, metal sandwiches based on classical alloys of Au/Ge and Au/Zn were evaporated for formation of ohmic contacts to bottom *n*-GaP and top *p*-GaP layers, respectively. Further, samples were annealed at 330 °C in a nitrogen ambient during 1 minute. The initial Au/Zn contact showed ohmic behavior due to the high doping level of the top *p*-GaP layer, and it did not almost change after RTA (see I-V curves in Figure A.2.1a). On the other hand, the initial Au/Ge contact resistance on *n*-GaP was high but it significantly decreased by two orders after annealing, and the behavior became ohmic (Figure A.2.1b). As a result, the fabricated contacts are ohmic to both sides of structures so we did not used RTA at higher temperatures.

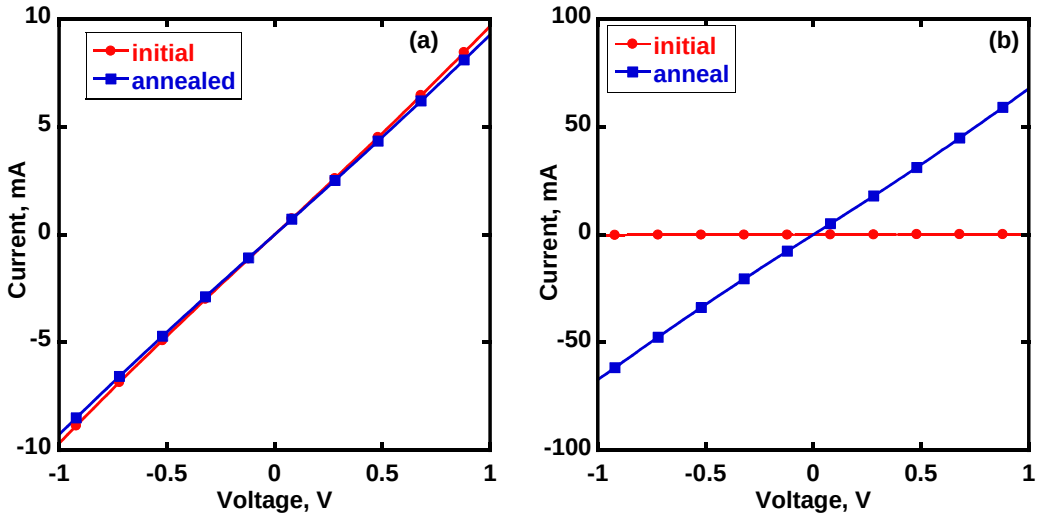

Figure A.2.1 Current-voltage characteristic in lateral geometry between two adjacent contacts to *p*-GaP (a) and *n*-GaP (b) in mesa-structure.

Dark current-voltage characteristics are presented for several mesa-structures with diameter of 0.5 mm for two samples in Figure A.2.2. They have classical rectifying behavior (low current at reverse applied voltage and its exponential growth at forward one) as expected for *p*-*n* junction with a good reproducibility. Only one mesa is shunted in each sample. The reverse current looks very noisy due to extremely low value close to the measuring limit of 10 pA in the used device. It means an absence of shunting and good quality of etching. Therefore, SCs and mesa-structures were fabricated with optimized contacts for accurate measurements.

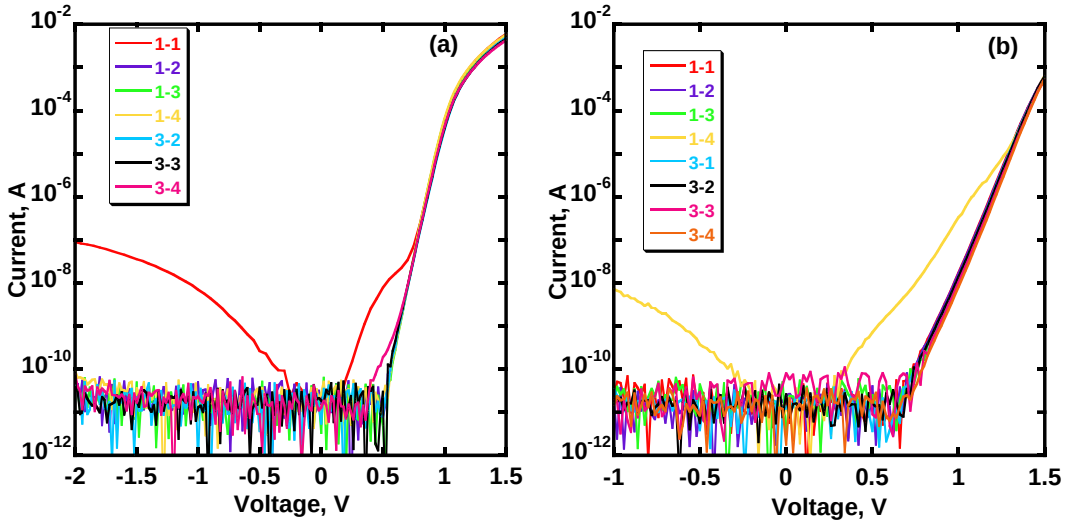

Figure A.2.2 Dark current-voltage characteristic of SC with an active layer of GaPAsN (a) and InP/GaPN (b) for different mesa-structures with diameter 0.5 mm.

Appendix B. Analysis of the spectral response in InGaPAsN based solar cell

As shown in Chapter IV, SCs based on dilute nitrides have two peaks in the spectral response of quantum efficiency that is not due to interference effects. A similar behavior of the spectral characteristics of GaPAsN/GaP heterostructures was also observed in another work[95], where the presence of a short-wavelength maximum is explained by the absorption in the GaP layers (E_g=2.26 eV). For subsequent experiments, the sample #1 is chosen for the investigation of EQE behavior due to its homogeneous composition of GaPAsN and the largest thickness allowing to carry out optical measurements more precisely and to obtain more clear and understandable results. In this work, it was performed a control experiment with wet etching of the *p*-GaP layer and simultaneous EQE measurements. Figure B.1 shows the dependence of EQE on the etched thickness. The shape of the quantum efficiency spectrum remains unchanged during removal of the top *p*- GaP layer. EQE catastrophically falls when 135 nm of *p*-GaP is etched due to disappearance of effective *p*-*n* junction. Therefore, the existence of two peaks in the quantum efficiency spectrum is related to intrinsic properties of the quaternary alloy of GaPAsN.

The observed behavior of spectral characteristics can be related to specific features of the energy-band structure of diluted nitrides such as GaAsN and GaPN[100,101]. According to the band-anticrossing (BAC) model, these solid solutions have two conduction subbands (E_- and E_+) formed as a result of the interaction of a nitrogen level with the conduction band of the initial semiconductors (GaAs and GaP). It is possible to calculate the positions of conduction subbands for the GaPAsN layer in sample #1 for the following hybridization parameters: V_N(GaNAs) = 2.7 eV and V_N(GaNP) = 3.05 eV[105]. As a result, the energies of conduction subbands were found to be E_- = 1.88 eV and E_+ = 2.86 eV.

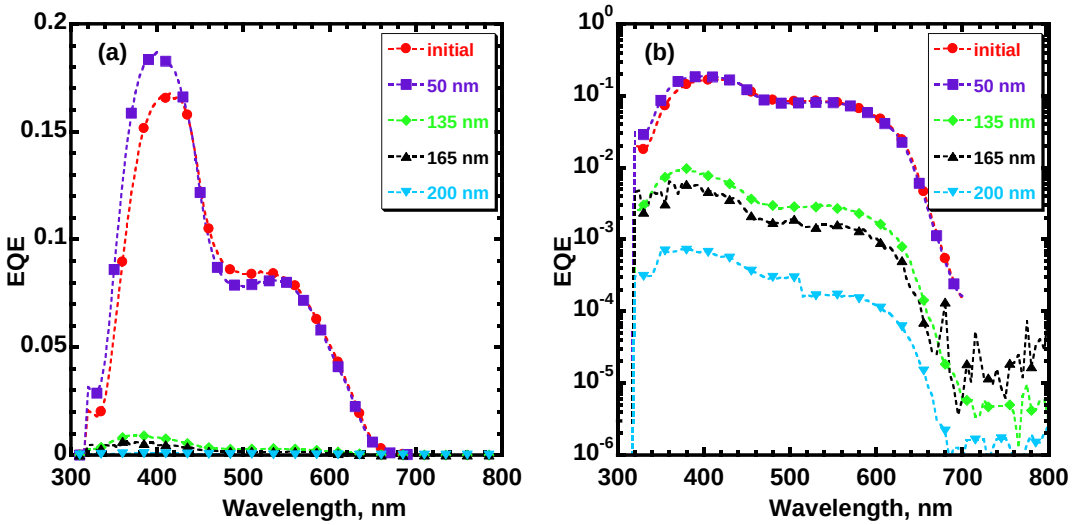

Figure B.1 Dependence of quantum efficiency on etched *p*-GaP thickness in linear (a) and logarithmic (b) scale.

Then, the value of bandgap energy of $GaP_{0.832}As_{0.15}N_{0.018}$ was estimated from different experimental methods applied to sample #1. Firstly, according to the EQE curve, the long-wavelength photosensitivity threshold is located at 650 nm (Figure B.1a). Secondly, the photoluminescence spectrum for this structure has the maximum at the wavelength of 650 nm (Figure B.2).

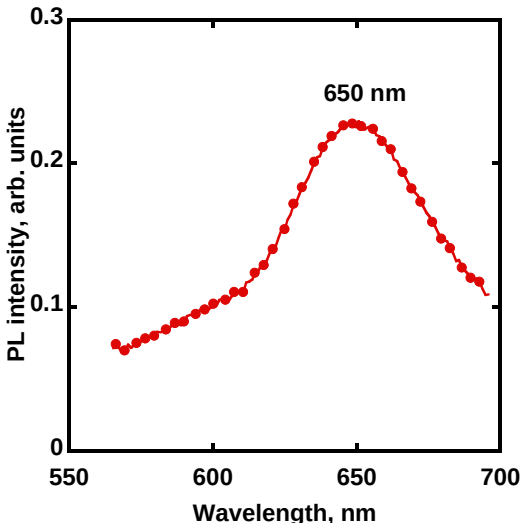

Figure B.2 Photoluminescence spectra of $GaP_{0.832}As_{0.15}N_{0.018}$ layer.

Furthermore, spectra of transmittance and reflection are measured for sample #1 by "Spectrum-SC" setup (Figure B.3a). It allowed to estimate the spectrum of absorption coefficient α for $GaP_{0.832}As_{0.15}N_{0.018}$ material. In case of semiconductor with direct bandgap, subsequent well-known equation is applied:

$$(\alpha h\upsilon)^2 = A^2\left(h\upsilon - E_g\right), \tag{B.1}$$

where A is a constant, $h\upsilon$ is the light quantum of absorbed energy. Therefore, the value of absorption edge E_g corresponded to bandgap energy can be estimated from dependence of $(\alpha h\upsilon)^2$ on $h\upsilon$ (Figure B.3b). In result, it has value 1.95 eV for investigated $GaP_{0.832}As_{0.15}N_{0.018}$ semiconductor material.

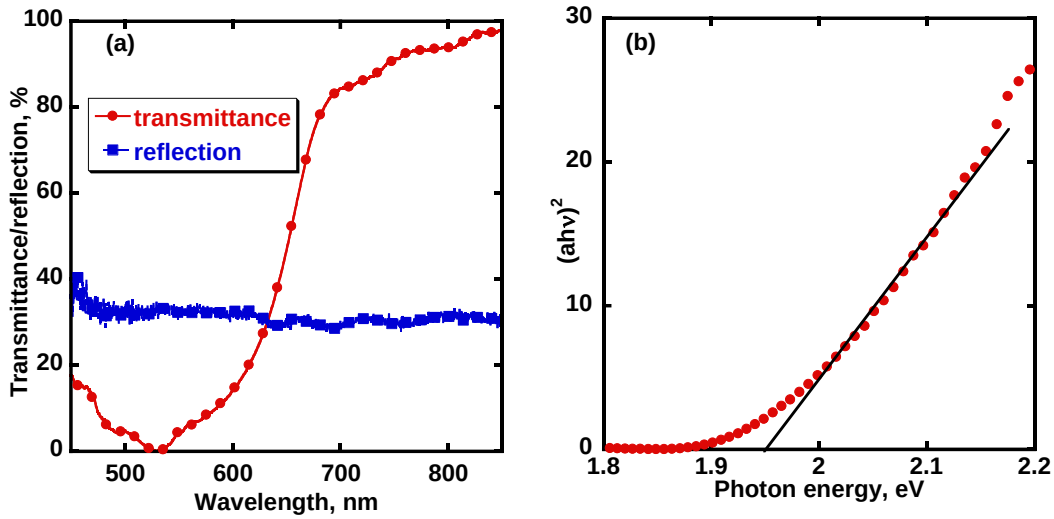

Figure B.3 (a)- Spectra of transmittance and reflection of sample #1, (b)- dependence of $(\alpha h\upsilon)^2$ on $h\upsilon$.

Finally, all obtained above data are summarized for simple understanding in Figure B.4. It shows a dependence of the external quantum efficiency on the incident photon energy for the *p*–*n* structure with layer of $GaP_{0.832}As_{0.15}N_{0.018}$. The long-wavelength photosensitivity threshold and PL peak position (1.9 eV) corresponds to the absorption edge (1.95 eV) estimated from Figure B.3b. Dashed lines of E_- and E_+ correspond to values estimated from BAC-model for dilute nitrides.

A comparison of the calculated energies (dashed lines in Figure B.4) of conduction subbands to experimental spectra leads to a conclusion that the value of 1.9 eV corresponds to an electron transition from the valence band to E_- subband of $GaP_{0.832}As_{0.15}N_{0.018}$. The presence of this conduction subband accounts for the appearance of a long-wavelength maximum on the spectrum of quantum efficiency (Figure I.6). As the photon energy increases above this value, the EQE decreases as a result of the small probability of photon absorption in the E_- subband. However, when the photon energy reaches a value corresponding to the E_+ subband, the absorption increases again to provide the short-wavelength maximum (Figure B.4). Little quantitate disparity

between experiments and estimated energies can be explained by “suggested” arsenic content of 15% in quaternary alloy of GaPAsN. However, in real grown sample it can be less so E_g raises. Nevertheless, a good agreement between theoretical estimates and experimental data confirms the above assumption that the peculiarities of the spectral characteristics of GaPAsN/GaP heterostructures are related to specific features of the energy-band structure of GaPAsN structures.

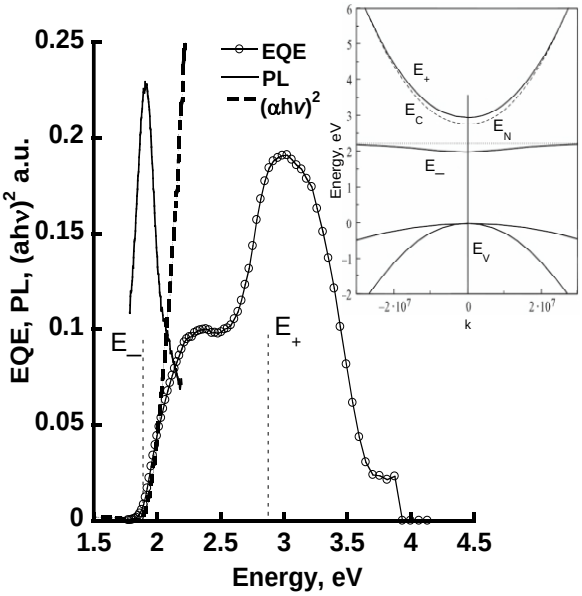

Figure B.4 Plot of external quantum efficiency vs. photon energy for the sample #1 with *p–n* junction (see text for explanations).

It is interesting to note that shape of quantum efficiency for single-junction SC based on InGaAsN/GaAs heterostructures also has the same feature of two overlapping peaks in spectral response due to absorption in both subbands. However, transition energy to E_- and E_+ subbands in InGaAsN lie closer to each other thus it is not easy to discover and distinguish each mechanisms separately.

Appendix C. Contact formation for multi-junction SC on Si

Here, we focus on the contact formation for double-junction SCs grown on *p*-Si wafers with front layer of *n*-GaP. Two methods are studied: indium contacts and gold-based contacts for mesa-structures.

C.1 Indium contacts

As for single-junction SCs, metal contacts must be fabricated with an ohmic behavior for reliable experimental study of MJSCs. Here, *n*-GaP is the front contact layer and wafer *p*-Si is the bottom layer. Both contacts are formed as indium dots deposited by soldering iron. Contact to *p*-Si has perfect ohmic behavior and low resistance without any additional treatment (I-V curve in in Figure C.1.1a). However, initial contact to *n*-GaP did not show the good performance so it was annealed at temperature 330 °C in a nitrogen ambient (Figure C.1.1b). It slightly improved and had linear dependence so it is possible to carry out experimental research of these samples.

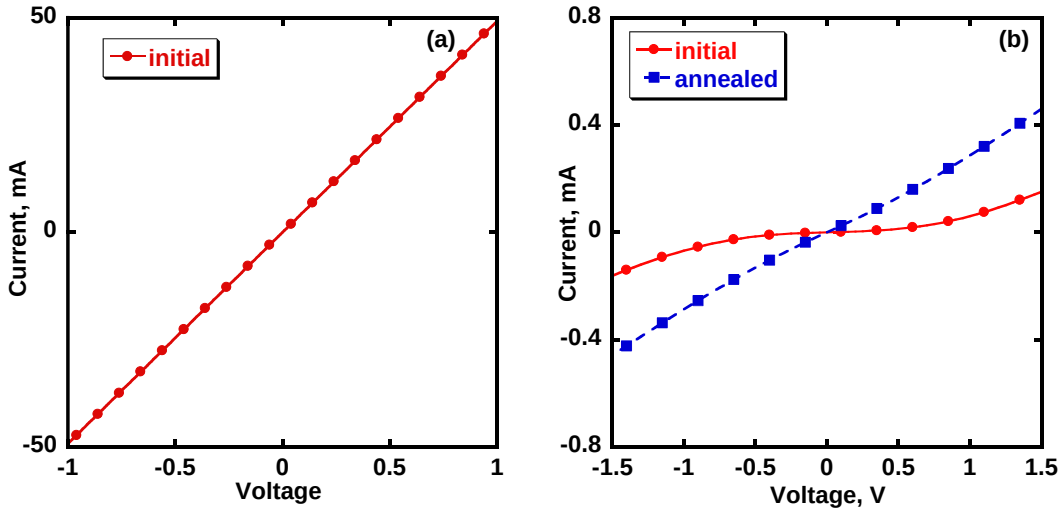

Figure C.1.1 Current-voltage characteristics in lateral geometry between adjacent indium dots on *p*-Si (a) and *n*-GaP (b) in double-junction SC.

Subsequent increase in annealing temperature leads to degradation of I-V characteristics: open-circuit voltage catastrophically dropped. We suppose that it is due to deterioration of the tunnel junction and shunting of the top subcell. The small thickness of cover *n*-GaP layer is the main disadvantage of grown structures due to ohmic contact of Au/Ge formed by germanium

diffusion into *n*-GaP, and it can diffuse in the active *i*-layer and shunt it. Therefore, in the future samples cover layer of *n*-GaP must be thicker. These contacts were used for measurements of photoelectric properties of MJSCs.

C.2 Mesa-structures

Further, mesa-structures were fabricated for capacitance study. The used indium contact to *p*-Si is not useful for future application in industry. Thereby, planar contacts to *p*-Si were done in three steps. First step is chemical vapor deposition of amorphous *p*-Si on the wafer. The second one is vacuum evaporation of silver on the amorphous silicon. The third one is the thermal annealing at 170 °C in an air ambient during the 20 min. The I-V characteristics in lateral geometry are presented in Figure C.2.1a. Then, contacts to front *n*-GaP were fabricated by the evaporation of indium through the mask with holes with diameter of 0.5 mm and 1.0 mm without annealing. As noted above the utilization of classical Au/Ge annealed alloys is dangerous due to a possible degradation of SCs. Finally, the selectively dry etching was applied to form mesa-structures.

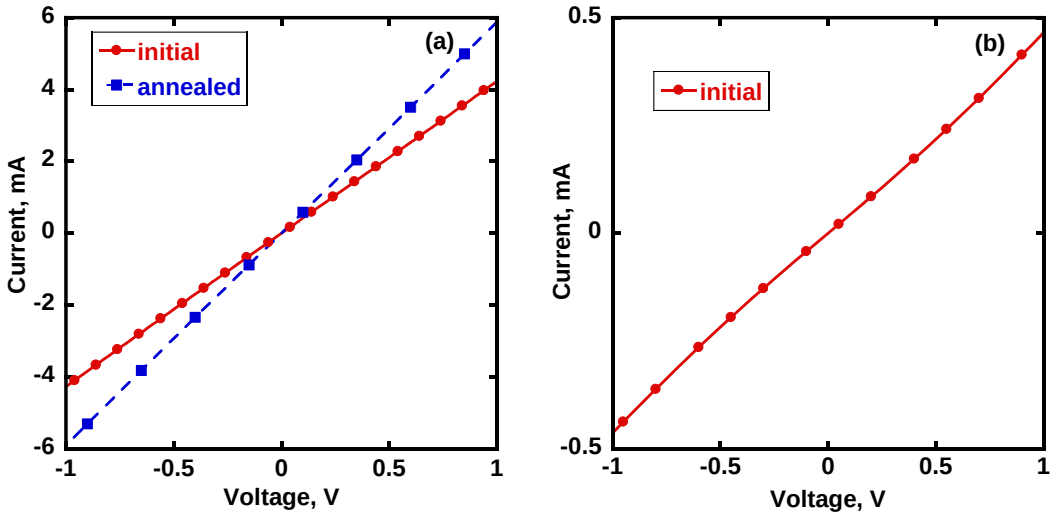

Figure C.2.1 Current-voltage characteristics in lateral geometry between two adjacent contacts to *p*-Si (a) and *n*-GaP (b) in mesa-structure.

Therefore, all fabricated contacts have good quality for carrying out electrical and capacitance measurements of SCs in Chapter IV.

Appendix D. List of abbreviations and symbols

Abbreviations:

AS	admittance spectroscopy
BAC	band-anticrossing
C-V	capacitance-voltage
DLTS	deep-level transient spectroscopy
DOS	density of states
EQE	external quantum efficiency
HEMT	high-electron-mobility transistor
HRTEM	high-resolution transmission electron microscopy
I-V	current-voltage
ICP	inductively coupled plasma
IR	infra-red
IQE	internal quantum efficiency
LED	light-emitting diode
MBE	molecular beam epitaxy
MEE	migration-enhanced epitaxy
MJSC	multi-junction solar cell
ML	monolayer
MOCVD	metalorganic chemical vapor deposition
MOVPE	metalorganic vapor phase epitaxy
PE-ALD	plasma-enhanced atomic layer deposition
PECVD	plasma-enhanced chemical vapor deposition
PL	photoluminescence
PV	photovoltaics
RF	radio-frequency
RIE	reactive ion etching
RTA	rapid thermal annealing
SC	solar cell

SCR	space charge region
SDA	sub-monolayer digital alloy
SEM	scanning electron microscopy
SL	superlattice
TEM	transmission electron microscopy
TJ	tunnel junction
TLM	transfer line measurements
UV	ultra-violet
VPE	vapor phase epitaxy
XPS	X-ray photoelectron spectroscopy

Symbols:

C	capacitance
c_n	capture coefficient of electrons
e_n	electron emission rate
e_p	hole emission rate
E_c	energy position of conduction band
E_N	energy position of nitrogen level
E_T	energy position of defect level
E_v	energy position of valence band
E_g	bandgap energy
f	frequency
f_0	characteristic frequency
FF	fill factor
h	Planck constant
G	conductance
I	current
J_{PM}	current at maximum power point
J_{SC}	short-circuit current
k_B	Boltzman's constant
l_{diff}	diffusion length
m_0	electron mass
m_e	effective mass of electron

m_h	effective mass of hole
N_A	acceptor concentration
N_C	effective density of states in the conduction band
N_{CV}	concentration from C-V curve
N_D	donor concentration
N_T	defect concentration
N_V	effective density of states in the valence band
P_{PM}	maximum power of solar cell
R_s	series resistance of solar cell
R_{sh}	shunt resistance of solar cell
S	surface area
$S(T)$	DLTS spectra
T	temperature
T_0	characteristic temperature
t_{pulse}	time of filling pulse
V	voltage
V_a	applied bias voltage
V_{bi}	build-in potential
V_N	parameter of hybridization in BAC-model
V_{OC}	open-circuit voltage
V_{PM}	voltage at maximum power point
V_{pulse}	amplitude of filling pulse
W	width of space charge region
q	electron charge
α	absorption coefficient
ε	absolute dielectric permittivity
ε_0	dielectric permittivity of vacuum
ε_s	relative dielectric permittivity of semiconductor
η	efficiency of solar cell
λ	wavelength
σ	capture-cross section
υ_{th}	thermal velocity
ω	angular frequency
ω_0	characteristic angular frequency

Appendix E. List of publications and conferences

Peer-review publications:

1. **A. I. Baranov**, A. S. Gudovskikh, D. A. Kudryashov, A. A. Lazarenko, I. A. Morozov, A. M. Mozharov, E. V. Nikitina, E. V. Pirogov, M. S. Sobolev, K. S. Zelentsov, A. Yu. Egorov, A. Darga, S. Le Gall and Jean-Paul Kleider. Defect properties of InGaAsN layers grown as sub-monolayer digital alloys by molecular beam epitaxy // Journal of Applied Physics 123, 161418 (2018); **doi**: 10.1063/1.5011371
2. A. S. Gudovskikh, A.V. Uvarov, I. A. Morozov, **A. I. Baranov**, D. A. Kudryashov, E. V. Nikitina, A. A. Bukatin, K. S. Zelentsov, I. S. Mukhin, A. Levtchenko, S. Le Gall, and J.-P. Kleider. Si doped GaP layers grown on Si wafers by low temperature PE-ALD // Journal of Renewable and Sustainable Energy 10, 021001 (2018); **doi**: 10.1063/1.5000256
3. A. S. Gudovskikh, A. V. Uvarov, I. A. Morozov, **A. I. Baranov**, D. A. Kudryashov, K. S. Zelentsov, A. S. Bukatin and K. P. Kotlyar. Low temperature plasma enhanced deposition approach for fabrication of microcrystalline GaP/Si superlattice // Journal of Vacuum Science & Technology A: Vacuum, Surfaces, and Films 36, 02D408 (2018): **doi**: 10.1116/1.5018259
4. **A. I. Baranov**, A. S. Gudovskikh, D. A. Kudryashov, I. A. Morozov, A. M. Mozharov, E. V. Nikitina, Zelentsov K. S., Darga A., S. Le Gall and J.-P. Kleider. Influence of PE-ALD of GaP on the Silicon Wafers Quality. // Physica Status Solidi A, 1700685, 2017. **doi**:10.1002/pssa.201700685
5. A. S. Gudovskikh, A. V. Uvarov, I. A. Morozov, **A. I. Baranov**, D. A. Kudryashov, E. V. Nikitina, and J.-P. Kleider. n-GaP/p-Si Heterojunction Solar Cells Fabricated by PE-ALD. // Physica Status Solidi C, 1700150, 2017. **doi**: 10.1002/pssc.201700150
6. A.S. Gudovskikh, K.S. Zelentsov, **A.I. Baranov**, D.A. Kudryashov, I.A. Morozov, E.V. Nikitina, J.-P. Kleider. Study of GaP/Si heterojunction solar cells // Energy Procedia. 2016. Vol. 102. pp. 56-63. **doi**: 10.1016/j.egypro.2016.11.318
7. **A. I. Baranov**, A. S. Gudovskikh, K. S. Zelentsov, E. V. Nikitina, A.Yu. Egorov. «Admittance spectroscopy of solar cells based on GaPNAs layers» // Semiconductors, 2015, Volume 49, issue 4, pp. 524-528 **doi**: 10.1134/S1063782615040053

8. **A. I. Baranov**, A. S. Gudovskikh, E. V. Nikitina, A.Yu. Egorov. «Photoelectric properties of solar cells based on GaPNAs/GaP heterostructures». // Technical Physics Letters December 2013, Volume 39, Issue 12, pp 1117-1120. **doi**: 10.1134/S1063785013120171

Conference publications:

1. **A. I. Baranov**, A. S. Gudovskikh, A. Darga, S. Le Gall and J-P Kleider. Capacitance characterization of GaP/n-Si structures grown by PE-ALD // Journal of Physics: Conference Series V.917 (2017) 052027 **doi** :10.1088/1742-6596/917/5/052027
2. **A. I. Baranov**, A. S. Gudovskikh, D. A. Kudryashov, A. M. Mozharov, K. S. Zelentsov and J-P Kleider. Admittance spectroscopy of InGaAsN based solar cells // Journal of Physics: Conference Series V.917 (2017) 052033 **doi** :10.1088/1742-6596/917/5/052033
3. **A. I. Baranov**, J P Kleider, A S Gudovskikh, A Darga, E V Nikitina, A Yu Egorov. Deep-level study of Ga(In)P(NAs) alloys grown on Si substrates // Journal of Physics: Conference Series 741 (2016) 012077 **doi**:10.1088/1742-6596/741/1/012077

Conferences:

1. **A. I. Baranov**, A. S. Gudovskikh, D.A. Kudryashov, I. A. Morozov, A. M. Mozharov, K. S. Zelentsov. Quantum efficiency measurements of subcells in multi-junction solar cells based on III-V/Si. // 5th International School and Conference "Saint-Petersburg OPEN 2018" St Petersburg, Russia, April 2–5, 2018. P. 3-36 (**poster, international**)
2. **A. I. Baranov**, I. A. Morozov, A.V. Uvarov, G. E Yakovlev, J.-P. Kleider. Silicon doping of GaP layers grown by time-modulated PECVD. // 5th International School and Conference "Saint-Petersburg OPEN 2018" St Petersburg, Russia, April 2–5, 2018. P. 3-38 (**poster, international**)
3. **A. I. Baranov**, A. S. Gudovskikh, I. A. Morozov, A. M. Mozharov, E. V. Nikitina, K. S. Zelentsov, A. Darga, S. Le Gall, J.- P. Kleider. Characterization of GaP/Si heterojunctions by space charge capacitance measurements // E-MRS Spring Meeting 2017, Strasburg, France, 22-26 May 2017, EX.3 (**oral, international**)
4. **A. I. Baranov**, A Gudovskikh, J-P Kleider. Capacitance characterization of GaP/n-Si structure grown by PE-ALD // 4th International School and Conference "Saint-Petersburg OPEN 2017" St Petersburg, Russia, April 3–6, 2017. P. 312 (**poster, international**)
5. **A. I. Baranov**, A Gudovskikh, D Kudryashov, K Zelentsov, A Mozharov. Admittance spectroscopy of InGaNAs layers in solar cells // 4th International School and Conference "Saint-Petersburg OPEN 2017" St Petersburg, Russia, April 3–6, 2017. P.324 (**poster, international**)

6. **A.I. Baranov**, AS Gudovskikh, IA Morozov, AM Mozharov, Arouna Darga, Jean-Paul Kleider. Electronic properties of thin GaP layers grown on silicon wafers // Les Journées Nationales du Photovoltaïque, Dourdan, France, 29 November- 02 December 2016 (**oral, French national**)
7. **A.I. Baranov**, A.S. Gudovskikh, K.S. Zelentsov, A.M. Mozharov, E.V. Nikitina, Kleider J.-P. Influence of thickness of InGaNAs- active layer to formation of defect levels and photoelectrical properties of solar cells // PhysicaSPb/2016, St. Petersburg, Russia, 1-3 November (**oral, international**)
8. **A.I. Baranov**, A.S. Gudovskikh, E.V. Nikitina, J.P. Kleider, A.Darga. Defect study of Ga(In)P(NAs) based solar cells grown on silicon // E-MRS Spring Meeting 2016, Lille, France, 2-6 May 2016, T.P1.86 (**poster, international**)
9. **A.I. Baranov**, J P Kleider, A S Gudovskikh, A Darga, E V Nikitina, A Yu Egorov. Deep-level study of Ga(In)P(NAs) alloys grown on Si substrates // International School and Conference "Saint-Petersburg OPEN 2016" St. Petersburg, Russia, March 28 – 30, 2016 (**poster, international**)
10. **A.I. Baranov**, A.S. Gudovskikh, E.V. Nikitina, J.P. Kleider, A.Darga. Admittance spectroscopy of Ga(In)P(NAs) based solar cells grown on silicon // Les Journées Nationales du PhotoVoltaïque, Dourdan, France, 1-4 décembre 2015 (**poster, French national**)
11. **A.I. Baranov**, A.S. Gudovskikh, K.S. Zelentsov, E.V. Nikitina, A.Yu. Egorov «Defect characterization in GaPNAs solar cells»// E-MRS Spring Meeting 2014, Lille, France, 26-30 May 2014, YP1 44 (**poster, international**)
12. **A.I. Baranov**, A.S. Gudovskikh «Computer simulation of the characteristics of photovoltaic cells based on heterojunction GaP / GaNAsP» (2012), XV National Russian Youth Conference on the Physics of Semiconductors and semiconductor opto- and nanoelectronics. (**poster, Russian national**)

Résumé de thèse

Les sources actuelles d'énergie électrique ont divers types d'inconvénients : sécurité (énergie nucléaire), réserves limitées de combustibles fossiles et émission de gaz à effet de serre (pétrole, gaz, charbon), influence négative sur l'environnement (hydroélectricité), etc. Le photovoltaïque (PV) ne présente pas ces inconvénients et constitue un moyen durable de fournir de l'électricité nécessaire au développement et au bien-être de l'humanité sur notre terre. Il permet d'utiliser une source d'énergie infinie à notre échelle - le Soleil - et convertit son rayonnement en énergie électrique.

Par conséquent, le PV est considéré comme une source d'énergie renouvelable prometteuse pour l'avenir. Le dispositif à semi-conducteurs utilisé dans le mécanisme de conversion d'énergie et de production d'électricité est appelé une cellule solaire. Les cellules solaires à jonctions multiples (MJSC pour Multiple Junction Solar Cells) basées sur les composés III-V ont les rendements de conversion les plus élevés et ont presque atteint la barrière psychologique de 50% pour les cellules photovoltaïques à concentrateur[1]. Les valeurs record sont obtenues pour des MJSC réalisées par collage[2] (46%) ou en structure inversée[3] (44,4%) à partir des composés GaInP et GaAs. Cependant, ces méthodes de réalisation posent problème pour un déploiement industriel à grande échelle du fait des étapes mécaniques nécessaires et de leur coût. Par conséquent, la réalisation de MJSC par intégration et croissance monolithique directe sur un substrat présente un grand intérêt. Le record de rendement de conversion est de 45,7% pour une cellule monolithique à quatre jonctions basée sur le système GaInP / GaAs / GaInAs / GaInAs à une concentration de 294 soleils[4].

Cette thèse est donc consacrée à l'étude de méthodes prospectives pour augmenter l'efficacité de cellules à multijonctions par croissance monolithique. Le travail est basé sur l'étude des cellules et sur celle des propriétés des matériaux par des techniques photoélectriques et capacitives, et il peut être divisé en trois parties.

La première partie du travail est l'étude de cellules à simple jonction avec des couches absorbantes non intentionnellement dopées (qui seront appelées "intrinsèques" par la suite) d'InGaAsN (E_g = 1,03 eV) avec différentes épaisseurs (900 nm, 1200 nm et 1600 nm) obtenues par épitaxie par jets moléculaires (MBE) sur substrats de *n*-GaAs, et recouvertes par une couche de *p*-GaAs. Selon des estimations théoriques, la substitution du germanium (bande interdite de 0,66 eV) par un autre semi-conducteur avec une bande interdite de 1 eV pour former la sous-cellule inférieure pourrait augmenter de quelques pourcents l'efficacité de cellules (GaInP / GaAs / Ge) et l'insertion d'une telle sous-cellule comme cellule intermédiaire dans une cellule à 3 jonctions réalisée sur un substrat de Ge permettra d'atteindre une valeur d'efficacité de 52% sous concentration[5,6]. Les couches intrinsèques d'InGaAsN ont été produites sous la forme d'un superréseau InAs / GaAsN obtenu par la séquence de croissance du ternaire GaAsN, de 7 à 12 nm d'épaisseur, suivie de la croissance du binaire InAs, de 0,2 à 0,5 nm d'épaisseur (une monocouche), la séquence étant ensuite répétée pour atteindre l'épaisseur visée. Cette technologie permet la croissance d'alliages InGaAsN avec des flux séparés d'indium et d'azote. Ainsi, des couches minces d'InAs de quelques monocouches compensent les contraintes élastiques apparaissant lors de la croissance de GaAsN sur le substrat de GaAs en raison du désaccord de maille. Le composé semi-conducteur développé par la méthode décrite est désigné par "SDA" (Sub-monolayer digital alloy) et il a été appliqué avec succès pour la croissance des composés III-V[7-9] et II-VI[10,11] par MBE.

La figure 1 présente les courbes courant-tension sous éclairement AM1.5G et l'efficacité quantique externe (EQE) à température ambiante. L'échantillon avec InGaAsN de 900 nm d'épaisseur présente les meilleures performances avec des valeurs de tension de circuit ouvert et de courant de court-circuit de V_{OC} = 0.40 V et J_{SC} = 15.5 mA / cm^2, et la valeur EQE dépasse 50% pour un échantillon sans revêtement antireflet (AR), de sorte qu'il pourrait atteindre 75% dans le cas de l'absence de pertes par réflexion. Lorsque l'épaisseur est augmentée à 1200 nm, la valeur d'EQE diminue légèrement dans la plage des courtes longueurs d'onde en raison des pertes possibles par recombinaison tandis qu'elle augmente légèrement dans la plage des grandes longueurs d'onde en raison de l'absorption améliorée. Ceci conduit à une légère augmentation de J_{SC} (16,0 mA / cm^2) et à une diminution de V_{OC}. Une augmentation supplémentaire de l'épaisseur à 1600 nm conduit à une chute catastrophique de J_{SC} (6,8 mA / cm^2) liée à la diminution de la valeur d'EQE dans la région des courtes longueurs d'onde en raison des pertes par recombinaison élevées.

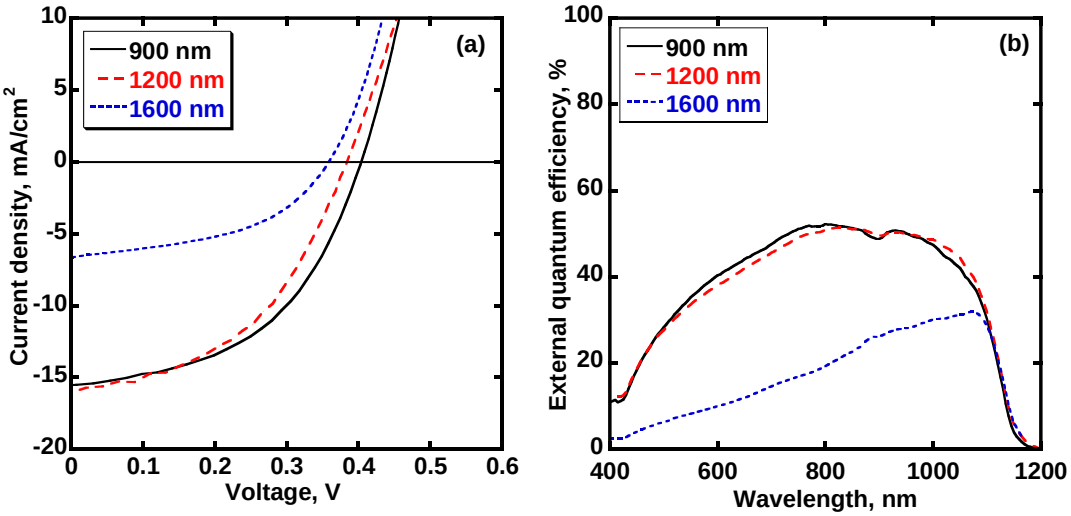

Figure 1. Caractéristiques courant-tension sous éclairement AM1.5G (a) et rendement quantique externe (EQE) (b) de cellules à simple jonction constituées d'un absorbeur d'InGaAsN intrinsèque obtenu par croissance de type SDA de InAs/GaAsN sur substrat GaP.

Les différences observées ont été expliquées par des mesures de capacité de jonction des cellules solaires. Premièrement, à partir des caractéristiques de capacité-tension (C-V), des courbes EQE et à l'aide de simulations, nous avons montré que les échantillons avec InGaAsN (de type SDA) de 900 nm et 1200 nm d'épaisseur présentaient un dopage résiduel de type *p* avec des concentrations de porteurs libres (trous) estimées à moins de 1,0 × 10^{15} cm^{-3} et à 5,0 × 10^{15} cm^{-3} lorsque l'épaisseur de InGaAsN est de 1600 nm. Par conséquent, dans nos couches InAs / GaAsN, les valeurs de dopage résiduel non intentionnel de type *p* sont nettement inférieures à celles trouvées pour les couches de InGaAsN obtenues traditionnellement par MBE[12] (plus de 1,0 × 10^{16} cm^{-3}). La spectroscopie d'admittance (AS pour Admittance Spectroscopy) et la spectroscopie transitoire de niveaux profonds (DLTS pour Deep Level Transient Spectroscopy) ont ensuite été appliquées aux échantillons. Ces méthodes ont permis de détecter des défauts dans la couche intrinsèque d'InGaAsN: leurs paramètres obtenus à partir des tracés d'Arrhenius (figure 2) sont présentés dans le tableau I.

Thickness, nm	E_a, eV	σ, cm^2	N_T, cm^{-3}	Method
1200	0.20	3.0×10^{-17}	5.0×10^{14}	AS
	0.46	1.4×10^{-15}	8.4×10^{14}	AS
	0.82	4.5×10^{-13}	n/e	DLTS
1600	0.18	1.4×10^{-16}	3.5×10^{15}	AS
	0.54	3.4×10^{-14}	1.3×10^{15}	AS
	0.78	1.9×10^{-11}	1.0×10^{15}	DLTS

Table I. Paramètres des défauts détectés dans nos couches non intentionnellement dopées d'InAs/GaAsN.

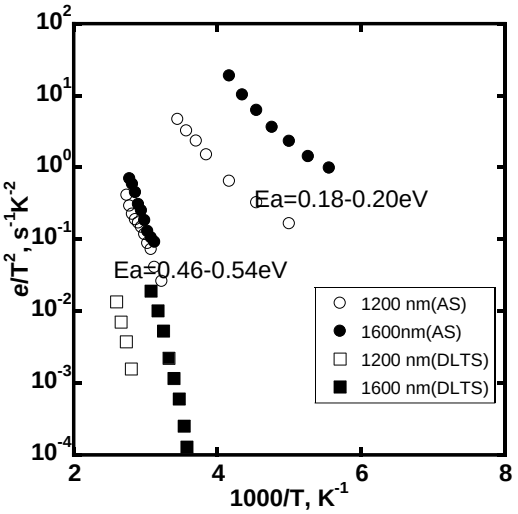

Figure 2. Tracés d'Arrhénius des signatures de défauts obtenus à partir des techniques AS (cercles) et DLTS (carrés) pour les couches de type SDA d'InAs/GaAsN pour des épaisseurs de couches de 1200 nm (symboles ouverts) et 1600 nm (symboles pleins).

Selon les mesures de type AS et DLTS, l'approche SDA conduit à une croissance sans défaut jusqu'à une épaisseur de 900 nm. Une augmentation de l'épaisseur à 1200 nm entraîne la formation de centres de recombinaison non radiatifs avec une énergie d'activation de 0,50 eV (et une concentration estimée à $8,4 \times 10^{14}$ cm^{-3}) et d'un défaut de faible profondeur à 0,20 eV, qui contribue à l'apparition d'un dopage supplémentaire. Cependant, la concentration de ce dernier est faible ($N_T = 5 \times 10^{14}$ cm^{-3}), donc elle n'affecte pas fortement les propriétés photoélectriques. Une augmentation supplémentaire de l'épaisseur de la couche d'absorbeur d'InGaAsN jusqu'à 1600 nm conduit à une augmentation significative de sa concentration à $(3\text{-}5) \times 10^{15}$ cm^{-3}, tandis que la concentration des niveaux profonds augmente également à $1,3 \times 10^{15}$ cm^{-3}. Selon les mesures de diffraction de rayons X, un tel comportement des défauts peut s'expliquer par une relaxation partielle des couches plus épaisses lorsqu'on dépasse l'épaisseur critique dans la croissance hétéroépitaxiale[13,14]. Dans ce cas, il est énergétiquement favorable à ce que les inadaptations de paramètres de maille soient partagées entre les contraintes dans la couche et l'apparition de dislocations. Ainsi, nous pouvons proposer que la couche de 900 nm d'épaisseur est sous contrainte de tension et a une faible concentration de défauts tandis qu'une augmentation de l'épaisseur de couche à 1200 nm conduit à la formation de dislocations et donc des réponses de défauts sont détectées par les techniques capacitives. En outre, des porteurs de charge libres supplémentaires

apparaissant du fait de l'ionisation du niveau peu profond font que les couches a priori non dopées d'InAs / GaAsN deviennent de type *p*, ce qui tend à remplacer les structures de type p^+-*i*-n^+ par des structures de type p^+-*p*-*n* à température ambiante. Ceci conduit à une chute d'EQE due à l'effondrement du champ électrique dans la couche InGaAsN de l'absorbeur et à l'augmentation du nombre de centres de recombinaison non radiatifs qui ont un impact négatif sur la durée de vie des porteurs libres.

La deuxième partie du travail est consacrée à l'étude de cellules solaires à une et plusieurs jonctions avec des couches actives d'InGaPAsN obtenues par croissance MBE sur des substrats de GaP et de Si. Selon les simulations, les valeurs optimales de l'énergie de la bande interdite sont respectivement de 1,1 eV et de 1,7 eV pour les sous-cellules inférieure et supérieure dans les cellules solaires à double jonction[15]. Le silicium constitue le semi-conducteur optimal et le moins cher pour la cellule inférieure, et les nitrures dilués d'InGaPAsN riches en P peuvent voir leur énergie de bande interdite varier dans la plage de 1,5 à 2,1 eV et rester en accord de maille avec GaP et Si. Quatre cellules solaires à simple jonction ont été fabriquées sur des substrats n-GaP avec des couches de contact avant de p-GaP, et avec des couches actives de 1000 nm d'épaisseur de n-GaPAsN pour un échantillon, 300 nm d'épaisseur de *i*-GaPAsN dans deux autres échantillons (avec des différences de traitement de post-croissance (PGT) dans la chambre MBE) et d' InP / GaPN de 350 nm d'épaisseur pour le quatrième. La figure 3 montre les caractéristiques courant-tension sous éclairement AM1.5G et les courbes d'EQE à température ambiante.

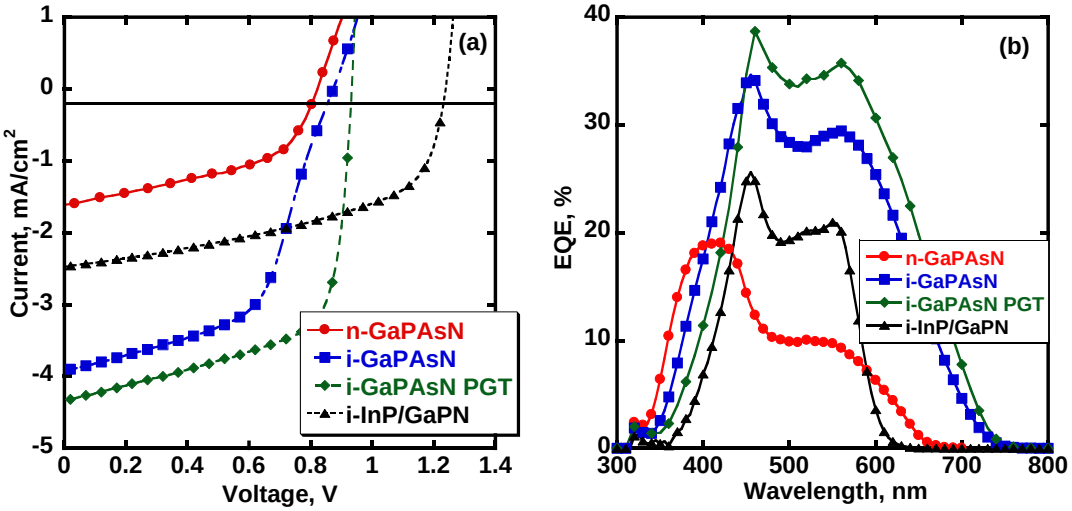

Figure 3. Caractéristiques courant-tension sous éclairement AM1.5G (a) et rendement quantique externe (EQE) (b) de cellules solaires à simple jonction d'InGaPAsN sur GaP.

Ces résultats montrent que les jonctions *p*-*i*-*n* présentent de meilleures performances que les jonctions *p*-*n* en raison de valeurs plus élevées de J_{SC} et d'EQE. Ceci indique une collection plus efficace des porteurs de charge générés en régime de court-circuit de la structure *p*-*i*-*n*, qui peut être liée à la présence d'un champ électrique plus fort dans la couche InGaPAsN non dopée. Par conséquent, en cas de mauvaises durées de vie dans ces nitrures dilués, les jonctions *p*-*i*-*n* sont plus adaptées aux applications photovoltaïques et nous avons concentré nos recherches sur les couches non dopées. Le matériau obtenu InP / GaPN a une énergie de bande interdite plus élevée (2,03 eV) que *i*-GaPAsN (1,7 eV), donc il a une tension de circuit ouvert (V_{OC}) plus élevée, mais une valeur plus faible de J_{SC} et d'EQE en raison des durées de vie plus faibles, qui sont suggérées par le facteur d'idéalité de 1,94 de la caractéristique courant-tension dans les diodes InP / GaPN, plus proche de 2 que celui des diodes en GaPAsN (1,50). Ceci confirme la conclusion d'études antérieures[16] sur la meilleure compensation des contraintes élastiques par l'arsenic par rapport à l'indium. L'azote est un élément du groupe V donc il essaie de se placer dans le sous-réseau des atomes du groupe V dans le réseau de GaP (sites phosphore). L'arsenic est également un élément

du groupe V donc cet atome se trouve également dans les sites de phosphore et il conduit à une compensation de contrainte plus efficace que l'incorporation de l'indium puisque ce dernier est un élément du groupe III. Un traitement de post-recuit supplémentaire améliore la qualité de la cellule avec *i*-GaPAsN (J_{SC} = 4.34 mA / cm^2 et V_{OC} = 0.93 V) donc ce procédé technologique est mieux adapté, mais ses performances sont encore très médiocres. Notons que les courbes d'EQE ont des caractéristiques spécifiques présentant deux pics. Nous l'avons expliqué en détail par deux mécanismes d'absorption dus à l'existence de deux sous-bandes de conduction dans des nitrures dilués de GaPAsN selon le modèle appelé band anticrossing[17,18].

La spectroscopie d'admittance a détecté des défauts avec une énergie d'activation et une section efficace de capture respectives de E_a = 0,20 eV et σ = 1-2 × 10^{-15} cm^2, dans des couches de GaPAsN, et leur concentration est beaucoup plus grande dans n-GaPAsN (un facteur 2) par rapport à celle dans les couches non dopées. Ceci a permis de l'associer au défaut T1 étudié auparavant dans GaP: N dopé par Si[19], décrit comme un complexe Si_{Ga} + V_P. Un seul défaut avec E_a = 0,09 eV et une concentration extrêmement faible a été détecté dans InP / GaPN. Il peut s'agir d'un défaut ponctuel de type donneur formé par des atomes de silicium en site gallium dans le réseau GaP (Si_{Ga})[20]. Ainsi, la spectroscopie d'admittance nous a permis de ne trouver que des impuretés peu profondes pouvant être responsables du dopage de fond dans les couches. Les mesures C-V ont montré un dopage de fond de type *n* plus faible dans les couches InP / GaPN (moins de 1 × 10^{16} cm^{-3}) que dans les échantillons avec GaPAsN (3 × 10^{16} cm^{-3} et 1 × 10^{16} cm^{-3} avec traitement de post-croissance) à 80 K. Les mesures de DLTS nous ont permis de détecter deux pièges à porteurs majoritaires (0,20 eV et 0,56 eV en dessous de la bande de conduction) et un piège à porteurs minoritaires (0,44 eV au-dessus de la bande de valence) dans le GaPAsN non dopé. Après le traitement de post-croissance, la concentration du piège le plus profond a légèrement diminué, mais les réponses de celui à 0,44 eV ont considérablement diminué (voire presque disparu). Un autre recuit des deux échantillons n'a montré aucune réponse d'un autre défaut possible dans la couche de GaPAsN non dopé, donc le défaut observé à E_c-0.56 eV peut être considéré comme le principal centre de recombinaison non radiatif responsable des limitations de durée de vie dans GaPAsN non dopé. Les mesures sur des échantillons InP / GaPN ont révélé des réponses de pièges à porteurs majoritaires avec une énergie d'activation de 0,44 eV. Ces défauts ont déjà été détectés dans GaP (N) [21-24] et ont la structure possible de complexes basés sur une paire d'atomes d'azote sur les sites de phosphore (N_P-N_P) et la lacune de gallium V_{Ga}, résultant du déplacement de gallium en raison de l'incorporation d'azote dans le réseau de GaP. En outre, des défauts à E_c-0,55 eV dans GaPAsN non dopé ont été détectés dans la même plage de température et avec des paramètres similaires, ce qui suggère une relation étroite entre les deux défauts. Peut-être celui-ci se transforme –t-il en celui-là en raison de la teneur supplémentaire en arsenic dans l'alliage ? Cependant, un recuit supplémentaire a montré l'existence d'une forte concentration de niveaux profonds dans InP / GaPN, qui agissent comme des centres efficaces de recombinaison non radiative pour les trous et les électrons: elle peut être responsable des durées de vie plus faibles observées dans cet alliage comparées à celles dans GaPAsN. L'échantillon avec GaPAsN non dopé a montré une meilleure performance photoélectrique et une faible concentration de défauts après traitement post-croissance, il devrait donc être utilisé et développé pour les futures cellules solaires.

Plusieurs cellules à multi-jonctions ont également été étudiées (cellules tandem et triple). Pour les cellules tandem, la sous-cellule inférieure a été fabriquée sous la forme d'une homojonction *p*-*n* de silicium dans un substrat de *p*-Si par traitement de pré-croissance dans un flux de phosphore. Ensuite, une jonction tunnel a été développée. Enfin, la sous-cellule supérieure a été déposée. Trois sous-cellules *p*-*i*-*n* supérieures ont été étudiées, l'une à base d'une couche de GaPAs non dopé de 400 nm d'épaisseur, l'autre à partir d'une couche de InP / GaPN non dopé de 200 nm d'épaisseur, la dernière à partir d'une couche de GaPAsN non dopé de 200 nm d'épaisseur. Nous avons également fabriqué une cellule à triple jonction SC, où les sous-cellules du milieu et

du haut étaient respectivement basées sur du GaPAsN non dopé de 200 nm d'épaisseur et du GaPN non dopé de 150 nm d'épaisseur. La couche de contact avant a été fabriquée à partir de *n*-GaP pour toutes les cellules. La figure 4 présente les courbes courant-tension sous illumination AM1.5G et l'EQE pour les sous-cellules supérieures dans les cellules à double jonction. Tout d'abord, il convient de noter que les cellules à double et triple jonction sont fonctionnelles car les valeurs élevées des tensions obtenues en circuit ouvert ne peuvent être expliquées que par la somme des contributions de toutes les sous-cellules. L'échantillon avec GaPAs dans la sous-cellule supérieure a des performances inférieures à celles des échantillons avec des nitrures dilués. En ce qui concerne les cellules à simple jonction, la couche de *i*-GaPAsN est préférable à *i*-InP / GaPN pour les applications photovoltaïques puisque les valeurs d'EQE sont meilleures et celle de J_{SC} est plus élevée. Cependant, leurs valeurs sont encore très faibles pour deux raisons: une faible épaisseur de couches non dopées (200 nm) et une relative mauvaise qualité de ces couches. La faible épaisseur conduit à une absorption de lumière insuffisante, et la faible qualité conduit à une recombinaison non radiative élevée dans les sous-cellules supérieures. Par conséquent, la faible qualité des alliages III-V dans les sous-cellules supérieures est le facteur limitant de la performance des cellules à multi-jonctions, de sorte que ces alliages doivent être améliorés à l'avenir. En outre, les contacts avant non optimisés entraînent un faible facteur de forme et de faibles valeurs d'efficacité des cellules.

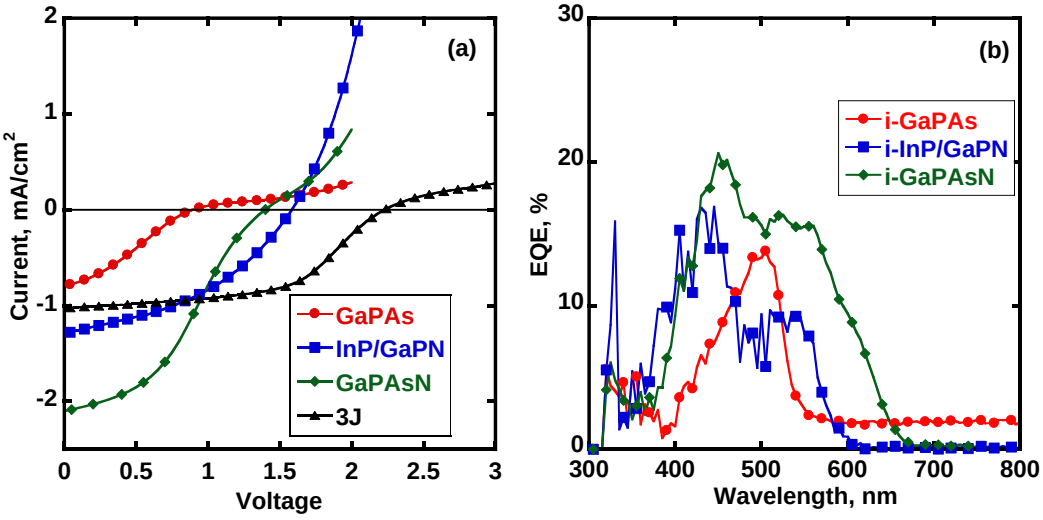

Figure 4. Caractéristiques courant-tension sous éclairement AM1.5G (a) de cellules à multijonctions (3 cellules tandem et une triple) et courbe de rendement quantique externe (b) des sous-cellules supérieurs dans les cellules tandem.

Les techniques de spectroscopie d'admittance, de DLTS et de Laplace-DLTS ont été appliquées à l'étude des défauts de la couche intrinsèque des composés III-V dans les cellules à double jonction. Toutes les méthodes ont montré des résultats similaires et nous ont permis d'obtenir des informations qualitatives sur les propriétés des défauts. L'échantillon avec la couche de GaPAs a la plus forte concentration de défauts avec une énergie d'activation de 0,22 eV. Deux réponses ont été étudiées dans InP / GaPN non dopé: le défaut avec E_a = 0,23 eV est similaire à celui de GaPAs, et un autre défaut avec E_a = 0,44 eV (similaire au défaut détecté dans les cellules à simple jonction à base de InP / GaPN non dopé). GaPAsN a un seul niveau de défauts à E_c-0,50 eV (similaire au défaut détecté dans les cellules à simple jonction à base de ce matériau GaPAsN) avec une concentration plus faible car As compense mieux les contraintes élastiques dans les alliages GaPN que In. Les défauts à E_c-0.44 eV et E_c-0.50 eV peuvent être considérés comme les

principaux centres de recombinaison non-radiative dans ces couches puisqu'il n'y a pas de réponses détectées à des températures plus élevées (jusqu'à la limite de notre équipement).

La troisième partie du travail est consacrée à l'étude des couches de GaP que l'on a fait croître sur des substrats de Si dans un équipement de dépôt chimique en phase vapeur assisté par plasma. Les méthodes d'épitaxie habituelles nécessitent des températures élevées de 500 à 800 °C pour la croissance des composés III-V, ce qui conduit à une dégradation des interfaces et des propriétés de volume du substrat de silicium[25]. De plus, ces technologies sont coûteuses en raison des fortes exigences de vide poussé dans la chambre, de source d'atomes ultra-purs, de maintenance plus compliquée des équipements, etc. Nous avons donc proposé une nouvelle méthode de dépôt de type ALD assistée par plasma. (PE-ALD) pour la croissance de GaP sur Si à des températures inférieures à 400 °C. Elle consiste à faire interagir alternativement de la phosphine (fournissant des atomes de P) et du thriméthylgallium (fournissant des atomes de Ga) sur la surface, conduisant alors à une croissance 2D couche par couche de GaP atomiquement lisse.

Des couches minces de GaP de 50-75 nm ont été déposées sur des plaquettes de silicium de type *n* et de type *p* par trois variantes de la méthode: (i) par des flux continus et simultanés de P et Ga à une puissance de plasma RF de 100 W, (ii) par PE-ALD à une puissance de plasma RF de 20 et 100 W pendant les étapes de dépôt, et (iii) avec un flux supplémentaire de silane visant à utiliser des atomes de Si pour fournir un dopage de GaP de type *n*. La couche de GaP obtenue par le processus continu présente des propriétés structurelles (à partir de mesures de microscopie électronique à balayage) et électriques (à partir de mesures de capacité-tension) inférieures à celles de GaP obtenu par PE-ALD. En outre, la structure du GaP obtenu par PE-ALD passe de amorphe à microcristallin avec l'augmentation de la puissance du plasma RF de 20 W jusqu'à 100 W, tout en maintenant constantes les autres paramètres de croissance. D'après des mesures de spectroscopie Raman (figure 5a), on distingue deux pics à 365 et 402 cm^{-1} dans l'échantillon préparé à 100 W contrairement à celui préparé à 20 W: ils correspondent aux positions des phonons TO et LO dans le GaP microcristallin[26]. Cependant, les structures a-GaP / *p*-Si présentent de meilleures propriétés photoélectriques que celles de µc-GaP / *p*-Si (Figure 5b) en raison d'une meilleure passivation de l'interface GaP / Si confirmée par des mesures en microscopie électronique à transmission. En outre, nous avons révélé l'existence d'une couche d'inversion forte dans le substrat de *p*-Si à l'hétérojonction GaP / *p*-Si due au dopage de type *n* du GaP, démontrant que l'utilisation de flux de silane est une méthode efficace pour obtenir du GaP de type *n* par PE-ALD.

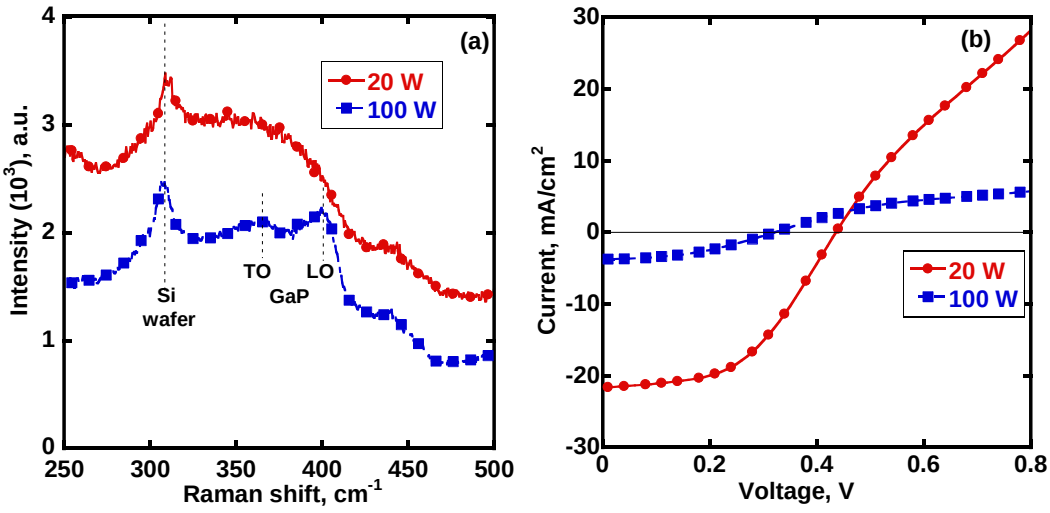

Figure 5. Spectres Raman (a) et caractéristiques courant-tension sous éclairement AM1.5G (b) de films de GaP déposés sur p-Si par la méthode PE-ALD pour deux valeurs de puissance RF du plasma.

Selon les mesures C-V effectuées sur les diodes Schottky formées sur les hétérojonctions GaP / *n*-Si, le GaP microcristallin devrait avoir un niveau de dopage plus élevé que le GaP amorphe puisque ce dernier est presque entièrement dépeuplé à tension nulle (la zone de charge d'espace de la jonction s'étend sur toute son épaisseur). De plus, deux défauts avec des énergies d'activation de 0,30 eV et de 0,80 eV ont été détectés par DLTS dans la structure μc-GaP / *n*-Si, alors qu'aucune réponse n'a été observée dans la structure a-GaP / *n*-Si. Par conséquent, les couches de a-GaP présentent de meilleures propriétés photoélectriques, structurelles et moins de défauts que les couches de μc-GaP grâce à une meilleure passivation de la surface du silicium.

Enfin, l'influence du processus de croissance sur la qualité des substrats de silicium a été explorée. Du GaP a été déposé par PE-ALD sur des substrats de type *n* puis retiré (par gravure) pour étudier la détérioration potentielle des propriétés électroniques dans la tranche de silicium durant le processus de croissance de GaP. Aucun pic DLTS n'a été observé, ce qui signifie que la concentration de défauts est très faible (moins de 1×10^{12} cm^{-3}) et que le processus de croissance n'affecte pas les propriétés du substrat de *n*-Si. Pour le silicium de type *p* dopé au bore, le profil C-V montre qu'il n'y a pas de désactivation du dopage au bore après le procédé PE-ALD, comme on aurait pu s'y attendre de par la présence d'hydrogène dans le plasma. Des mesures sur des diodes Schottky de référence formées sur le substrat de Si de type *p* révèlent la présence de défauts interstitiels de Fe bien connus à une position $E_v + 0{,}38$ eV avec une concentration de 3×10^{13} cm^{-3}. Le GaP obtenu par PE-ALD conduit à une modification de la réponse de ce défaut et à l'apparition d'une autre réponse dans la gamme des basses températures éventuellement liée à des changements de l'environnement ou de la configuration du défaut interstitiel lié au fer. Cependant, des niveaux profonds n'ont pas été détectés dans *p*-Si après PE-ALD, ce qui signifie que la qualité de p-Si ne se dégrade pas fortement.

En conclusion, les trois approches explorées au cours de ces travaux de thèse ont donné des résultats prometteurs. L'approche SDA a permis de développer des couches d'InGaAsN avec un gap de 1eV, et de préciser les défauts qui affectent les propriétés photoélectriques. À l'avenir, le processus de croissance sera optimisé pour exclure la formation de défauts dans des couches plus épaisses que 1 μm, et des cellules solaires GaInP / GaAs / InGaAsN à triple jonction seront réalisées sur des substrats de GaAs. Deuxièmement, nous avons montré que les couches *i*-GaPAsN ont de meilleures performances que celles de SDA *i*-InP / GaPN dans les cellules solaires réalisées sur des substrats de GaP et Si. De plus, nous avons détecté des niveaux profonds responsables des faibles durées de vie dans ces couches. Les futures recherches pourront être axées sur la croissance et l'amélioration des couches de *i*-GaPAsN plus épaisses que 1 μm. Des cellules solaires à double jonction seront fabriquées sur des substrats de Si à partir d'une sous-cellule supérieure utilisant une jonction *p*-*i*-*n* reposant sur un tel alliage quaternaire avec une teneur élevée en arsenic de 20-30% afin d'atteindre l'énergie de bande interdite de 1,7 eV. Enfin, la méthode PE-ALD a montré la possibilité de faire croître des couches de GaP sur des substrats de Si, et des cellules solaires à base de *n*-GaP / *p*-Si ont été fabriquées. Dans le futur, nous étudierons des moyens d'obtenir des couches de GaP de type *p* et de mieux contrôler la concentration de dopage de type *n*. De plus, de l'azote sera introduit dans le processus de croissance pour obtenir une couche d'i-GaPN, et des cellules solaires à simple jonction *p*-*i*-*n* seront réalisées sur des substrats de Si. Par conséquent, toutes les méthodes explorées pourront être développées dans le futur pour la fabrication de cellules solaires à haut rendement et à faible coût.

Références :

[1] A.F. Ioffe and A. V. Ioffe, Phys. Z. Sowjetunion **7**, 343 (1935).

[2] D.M. Chapin, C.S. Fuller, and G.L. Pearson, J. Appl. Phys. **25**, 676 (1954).

[3] Z.I. Alferov, V.M. Andreev, M.B. Kagan, I. Protasov, I, and V.. Trofim, Sov. Phys. Semicond. **4**, 2047 (1971).

[4] Z.I. Alferov, V.M. Andreev, and V.D. Rumyantsev, Semiconductors **38**, 899 (2004).

[5] B.M. Kayes, H. Nie, R. Twist, S.G. Spruytte, F. Reinhardt, I.C. Kizilyalli, and G.S. Higashi, in *Proc. 37th IEEE Photovolt. Spec. Conf.* (2011), pp. 000004–000008.

[6] K. Yoshikawa, H. Kawasaki, W. Yoshida, T. Irie, K. Konishi, K. Nakano, T. Uto, D. Adachi, M. Kanematsu, H. Uzu, and K. Yamamoto, Nat. Energy **2**, 17032 (2017).

[7] I. Newton, Philos. Trans. R. Soc. London **6**, 3075 (1671).

[8] W. Shockley and H.J. Queisser, J. Appl. Phys. **32**, 510 (1961).

[9] L.C. Hirst and N.J. Ekins-Daukes, Prog. Photovoltaics Res. Appl. **19**, 286 (2011).

[10] S.W. Glunz, R. Preu, and D. Biro, in *Compr. Renew. Energy* (Elsevier, 2012), pp. 353–387.

[11] R.R. King, D.C. Law, K.M. Edmondson, C.M. Fetzer, G.S. Kinsey, H. Yoon, R.A. Sherif, and N.H. Karam, Appl. Phys. Lett. **90**, 98 (2007).

[12] Z.I. Alferov, V.M. Andreev, K.K. Aripov, V.R. Larionov, and V.D. Rumyantsev, Geliotekhnica **6**, 3 (1981).

[13] M.A. Green, Y. Hishikawa, W. Warta, E.D. Dunlop, D.H. Levi, J. Hohl-Ebinger, and A.W.H. Ho-Baillie, Prog. Photovoltaics Res. Appl. **25**, 668 (2017).

[14] F. Dimroth, M. Grave, P. Beutel, U. Fiedeler, C. Karcher, T.N.D. Tibbits, E. Oliva, G. Siefer, M. Schachtner, A. Wekkeli, A.W. Bett, R. Krause, M. Piccin, N. Blanc, C. Drazek, E. Guiot, B. Ghyselen, T. Salvetat, A. Tauzin, T. Signamarcheix, A. Dobrich, T. Hannappel, and K. Schwarzburg, Prog. Photovoltaics Res. Appl. **22**, 277 (2014).

[15] K. Sasaki, T. Agui, K. Nakaido, N. Takahashi, R. Onitsuka, and T. Takamoto, in *9th Int. Conf. Conc. Photovolt. Syst. AIP Conf. Proc.* (2013), pp. 22–25.

[16]NREL Press Release NR-4514, 16 December 2014 (n.d.).

[17] S. Adachi, *Properties of Group-IV, III-V and II-VI Semiconductors* (John Wiley & Sons, Ltd, Chichester, UK, 2005).

[18] J.F. Geisz and D.J. Friedman, Semicond. Sci. Technol. **17**, 769 (2002).

[19] S.R. Kurtz, D. Myers, and J.M. Olson, in *Conf. Rec. Twenty Sixth IEEE Photovolt. Spec. Conf. - 1997* (IEEE, Anaheim, California, 1997), pp. 875–878.

[20] M. Yamaguchi, K.I. Nishimura, T. Sasaki, H. Suzuki, K. Arafune, N. Kojima, Y. Ohsita, Y. Okada, A. Yamamoto, T. Takamoto, and K. Araki, Sol. Energy **82**, 173 (2008).

[21] M. Weyers, M. Sato, and H. Ando, Jpn. J. Appl. Phys. **31**, L853 (1992).

[22] M. Henini, *Dilute Nitride Semiconductors*, 1st ed. (Elsevier, Amsterdam, 2004).

[23] J. Allen, V. Sabnis, M. Wiemer, and H. Yuen, in *9th Int. Conf. Conc. Photovolt. Syst.* (Miyazaki, Japan, 2013).

[24] A. Aho, R. Isoaho, A. Tukiainen, V. Polojärvi, T. Aho, M. Raappana, and M. Guina, in *AIP*

Conf. Proc. (2015), p. 50001.

[25] R. Campesato, A. Tukiainen, A. Aho, G. Gori, R. Isoaho, E. Greco, and M. Guina, E3S Web Conf. **16**, 3003 (2017).

[26] A. Tukiainen, A. Aho, G. Gori, V. Polojärvi, M. Casale, E. Greco, R. Isoaho, T. Aho, M. Raappana, R. Campesato, and M. Guina, Prog. Photovoltaics Res. Appl. **24**, 914 (2016).

[27] S. Kurtz, S.W. Johnston, J.F. Geisz, D.J. Friedman, and a J. Ptak, 31st IEEE Photovoltaics Spec. Conf. Exhib. Lake Buena Vista, Florida (2005).

[28] B. Bouzazi, H. Suzuki, N. Kojima, Y. Ohshita, and M. Yamaguchi, Jpn. J. Appl. Phys. **49**, 121001 (2010).

[29] V. Polojärvi, A. Aho, A. Tukiainen, M. Raappana, T. Aho, A. Schramm, and M. Guina, Sol. Energy Mater. Sol. Cells **149**, 213 (2016).

[30] S.R. Kurtz, A.A. Allerman, E.D. Jones, J.M. Gee, J.J. Banas, and B.E. Hammons, Appl. Phys. Lett. **74**, 729 (1999).

[31] N. Miyashita, N. Ahsan, and Y. Okada, Phys. Status Solidi **214**, 1600586 (2017).

[32] K. Volz, D. Lackner, I. Németh, B. Kunert, W. Stolz, C. Baur, F. Dimroth, and A.W. Bett, J. Cryst. Growth **310**, 2222 (2008).

[33] M.M. Islam, N. Miyashita, N. Ahsan, T. Sakurai, K. Akimoto, and Y. Okada, Appl. Phys. Lett. **105**, 112103 (2014).

[34] N. Miyashita, N. Ahsan, and Y. Okada, Prog. Photovoltaics Res. Appl. **24**, 28 (2016).

[35] D.B. Jackrel, S.R. Bank, H.B. Yuen, M.A. Wistey, J.S. Harris, A.J. Ptak, S.W. Johnston, D.J. Friedman, and S.R. Kurtz, J. Appl. Phys. **101**, 114916 (2007).

[36] V. Polojärvi, A. Aho, A. Tukiainen, A. Schramm, and M. Guina, Appl. Phys. Lett. **108**, 122104 (2016).

[37] E. V. Nikitina, A.S. Gudovskikh, A.A. Lazarenko, E. V. Pirogov, M.S. Sobolev, K.S. Zelentsov, I.A. Morozov, and A.Y. Egorov, Semiconductors **50**, 652 (2016).

[38] M. Sato and Y. Horikoshi, J. Appl. Phys. **66**, 851 (1989).

[39] R. Cingolani, O. Brandt, L. Tapfer, G. Scamarcio, G.C. La Rocca, and K. Ploog, Phys. Rev. B **42**, 3209 (1990).

[40] A.Y. Egorov, A.E. Zhukov, P.S. Kop'ev, N.N. Ledentsov, M. V. Maksimov, and V.M. Ustinov, Semiconductors **28**, 363 (1994).

[41] S.V. Ivanov, A.A. Toropov, T.V. Shubina, A.V. Lebedev, S.V. Sorokin, A.A. Sitnikova, P.S. Kop'ev, G. Reuscher, M. Keim, F. Bensing, A. Waag, G. Landwehr, G. Pozina, J.P. Bergman, and B. Monemar, J. Cryst. Growth **214–215**, 109 (2000).

[42] S. V. Ivanov, O. V. Nekrutkina, S. V. Sorokin, V.A. Kaygorodov, T. V. Shubina, A.A. Toropov, P.S. Kop'ev, G. Reuscher, V. Wagner, J. Geurts, A. Waag, and G. Landwehr, Appl. Phys. Lett. **78**, 404 (2001).

[43] Y. V Bolkhovityanov and O.P. Pchelyakov, Uspekhi Fiz. Nauk **51**, 437 (2008).

[44] R. Fischer, N. Chand, W. Kopp, H. Morkoç, L.P. Erickson, and R. Youngman, Appl. Phys. Lett. **47**, 397 (1985).

[45] M. Yamaguchi, J. Mater. Res. **6**, 376 (1991).

[46] S. Kim, M.-S. Park, D.-M. Geum, H. Kim, G. Ryu, H.-D. Yang, J.D. Song, C.Z. Kim, and W.J. Choi, Curr. Appl. Phys. **15**, S40 (2015).

[47] C.-Y. Tseng, C.-T. Lee, O.P. Pchelyakov, and V. V. Preobrazhenskii, Sol. Energy **118**, 1 (2015).

[48] T. Ogawa, G. Wang, K. Murase, K. Hori, J. Arokiaraj, T. Soga, T. Jimbo, and M. Umeno, in *Twenty-Eighth IEEE Photovolt. Spec. Conf.* (IEEE, 2000), pp. 1308–1311.

[49] T. Tsuji, H. Yonezu, and N. Ohshima, J. Vac. Sci. Technol. B Microelectron. Nanom. Struct. **22**, 1428 (2004).

[50] M.L. Lee, E.A. Fitzgerald, M.T. Bulsara, M.T. Currie, and A. Lochtefeld, J. Appl. Phys. **97**, 11101 (2005).

[51] Y. Alaskar, S. Arafin, D. Wickramaratne, M.A. Zurbuchen, L. He, J. McKay, Q. Lin, M.S. Goorsky, R.K. Lake, and K.L. Wang, Adv. Funct. Mater. **24**, 6629 (2014).

[52] T. Soga, M. Yang, and T.J. and M. Umeno, Jpn. J. Appl. Phys. **35**, 1401 (1996).

[53] C. Renard, N. Cherkasin, A. Jaffre, L. Vincent, A. Michel, T. Molière, R. Hamouche, V. Yam, J. Alvarez, F. Fossard, D. Mencaraglia, and D. Bouchier, Appl. Phys. Lett. **102**, 191915 (2013).

[54] C. Renard, N. Cherkashin, A. Jaffre, T. Molière, G. Hallais, L. Vincent, J. Alvarez, D. Mencaraglia, A. Michel, and D. Bouchier, J. Cryst. Growth **401**, 554 (2014).

[55] C.-P. Chu, S. Ara, T. Nie, K. Yao, X. Kou, L. He, C.-Y. Wang, S.-Y. Chen, L.-J. Chen, S.M. Qasim, M.S. BenSaleh, and K.L. Wang, Cryst. Growth Des. **14**, 593 (2014).

[56] H. Taguchi, T. Soga, and T. Jimbo, Jpn. J. Appl. Phys. **42**, L1419 (2003).

[57] S. Kim, D.-M. Geum, M.-S. Park, C.Z. Kim, and W.J. Choi, Sol. Energy Mater. Sol. Cells **141**, 372 (2015).

[58] S. Essig, S. Ward, M.A. Steiner, D.J. Friedman, J.F. Geisz, P. Stradins, and D.L. Young, Energy Procedia **77**, 464 (2015).

[59] N. Shigekawa, J. Liang, R. Onitsuka, T. Agui, H. Juso, and T. Takamoto, Jpn. J. Appl. Phys. **54**, 08KE03 (2015).

[60] H. Döscher, B. Borkenhagen, G. Lilienkamp, W. Daum, and T. Hannappel, Surf. Sci. **605**, L38 (2011).

[61] K. Yamane, T. Kawai, Y. Furukawa, H. Okada, and A. Wakahara, J. Cryst. Growth **312**, 2179 (2010).

[62] K. Volz, A. Beyer, W. Witte, J. Ohlmann, I. Nmeth, B. Kunert, and W. Stolz, J. Cryst. Growth **315**, 37 (2011).

[63] A.C. Lin, M.M. Fejer, and J.S. Harris, J. Cryst. Growth **363**, 258 (2013).

[64] M.S. Sobolev, A.A. Lazarenko, E. V. Nikitina, E. V. Pirogov, A.S. Gudovskikh, and A.Y.

Egorov, Semiconductors **49**, 559 (2015).

[65] E.H. Hussein, S. Dadgostar, F. Hatami, and W.T. Masselink, J. Cryst. Growth **419**, 42 (2015).

[66] E.L. Warren, A.E. Kibbler, R.M. France, A.G. Norman, P. Stradins, and W.E. McMahon, Appl. Phys. Lett. **107**, 82109 (2015).

[67] H. Wagner, T. Ohrdes, A. Dastgheib-Shirazi, B. Puthen-Veettil, D. König, and P.P. Altermatt, J. Appl. Phys. **115**, 44508 (2014).

[68] T. Katoda and M. Kishi, J. Electron. Mater. **9**, 783 (1980).

[69] M. Feifel, T. Rachow, J. Benick, J. Ohlmann, S. Janz, M. Hermle, F. Dimroth, and D. Lackner, IEEE J. Photovoltaics **6**, 384 (2016).

[70] C. Skierbiszewski, P. Perlin, P. Wisniewski, W. Knap, T. Suski, W. Walukiewicz, W. Shan, K.M. Yu, J.W. Ager, E.E. Haller, J.F. Geisz, and J.M. Olson, Appl. Phys. Lett. **76**, 2409 (2000).

[71] I.A. Buyanova, G.Y. Rudko, W.M. Chen, H.P. Xin, and C.W. Tu, Appl. Phys. Lett. **80**, 1740 (2002).

[72] S.R. Kurtz, P. Faine, and J.M. Olson, J. Appl. Phys. **68**, 1890 (1990).

[73] B.M. Kayes, L. Zhang, R. Twist, I.K. Ding, and G.S. Higashi, IEEE J. Photovoltaics **4**, 729 (2014).

[74] D.A. Kudryashov, A.S. Gudovskikh, E. V Nikitina, and A.Y. Egorov, Semiconductors **48**, 381 (2014).

[75] J.N. Baillargeon, K.Y. Cheng, G.E. Hofler, P.J. Pearah, and K.C. Hsieh, Appl. Phys. Lett. **60**, 2540 (1992).

[76] a. Y. Egorov, E.S. Semenova, V.M. Ustinov, Y.G. Hong, and C. Tu, Semiconductors **36**, 981 (2002).

[77] S. Miyoshi, H. Yaguchi, K. Onabe, R. Ito, and Y. Shiraki, Appl. Phys. Lett. **63**, 3506 (1993).

[78] G. Biwa, H. Yaguchi, K. Onabe, and Y. Shiraki, J. Cryst. Growth **189190**, 485 (1998).

[79] G. Biwa, H. Yaguchi, K. Onabe, and Y. Shiraki, J. Cryst. Growth **195**, 574 (1998).

[80] A.A. Lazarenko, E. V. Nikitina, E. V. Pirogov, M.S. Sobolev, and A.Y. Egorov, Semiconductors **48**, 392 (2014).

[81] A.A. Lazarenko, E. V. Nikitina, M.S. Sobolev, E. V. Pirogov, D. V. Denisov, and A.Y. Egorov, Semiconductors **49**, 479 (2015).

[82] S. Almosni, C. Robert, T. Nguyen Thanh, C. Cornet, A. Létoublon, T. Quinci, C. Levallois, M. Perrin, J. Kuyyalil, L. Pedesseau, A. Balocchi, P. Barate, J. Even, J.M. Jancu, N. Bertru, X. Marie, O. Durand, and A. Le Corre, J. Appl. Phys. **113**, 123509 (2013).

[83] N.Q. Thinh, I.P. Vorona, I.A. Buyanova, W.M. Chen, S. Limpijumnong, S.B. Zhang, Y.G. Hong, H.P. Xin, C.W. Tu, A. Utsumi, Y. Furukawa, S. Moon, A. Wakahara, and H. Yonezu, Phys. Rev. B **71**, 125209 (2005).

[84] D. Dagnelund, I.A. Buyanova, X.J. Wang, W.M. Chen, A. Utsumi, Y. Furukawa, A. Wakahara,

and H. Yonezu, J. Appl. Phys. **103**, 63519 (2008).

[85] D. Dagnelund, J. Stehr, A. Yu. Egorov, W.M. Chen, and I.A. Buyanova, Appl. Phys. Lett. **102**, 21910 (2013).

[86] B. Tell and F.P.J. Kuijpers, J. Appl. Phys. **49**, 5938 (1978).

[87] G. Ferenczi, P. Krispin, and M. Somogyi, J. Appl. Phys. **54**, 3902 (1983).

[88] P. Kamiński, W. Strupiński, and K. Roszkiewicz, J. Cryst. Growth **108**, 699 (1991).

[89] A. V Skazochkin, Y.K. Krutogolov, and Y.I. Kunakin, Semicond. Sci. Technol. **10**, 634 (1995).

[90] A. V Skazochkin, Y.K. Krutogolov, and G.G. Bondarenko, Semicond. Sci. Technol. **11**, 495 (1996).

[91] K. Ždánský, J. Zavadil, D. Nohavica, and S. Kugler, J. Appl. Phys. **83**, 7678 (1998).

[92] A.F. Basile, S. Hatakenaka, H. Okada, and A. Wakahara, J. Vac. Sci. Technol. A Vacuum, Surfaces, Film. **27**, 531 (2009).

[93] D. Dagnelund, C.W. Tu, A. Polimeni, M. Capizzi, W.M. Chen, and I.A. Buyanova, Phys. Status Solidi **10**, 561 (2013).

[94] O.I. Rumyantsev, P.N. Brunkov, E. V. Pirogov, and A.Y. Egorov, Semiconductors **44**, 893 (2010).

[95] J.F. Geisz, D.J. Friedman, and S. Kurtz, in *Conf. Rec. Twenty-Ninth IEEE Photovolt. Spec. Conf. 2002.* (IEEE, 2002), pp. 864–867.

[96] J.F. Geisz, J.M. Olson, D.J. Friedman, K.M. Jones, R.C. Reedy, and M.J. Romero, in *Proc. 31st IEEE PVSC* (2005), pp. 695–698.

[97] S. Sukrittanon, R. Liu, Y.G. Ro, J.L. Pan, K.L. Jungjohann, C.W. Tu, and S.A. Dayeh, Appl. Phys. Lett. **107**, 153901 (2015).

[98] S. Almosni, P. Rale, C. Cornet, M. Perrin, L. Lombez, A. Létoublon, K. Tavernier, C. Levallois, T. Rohel, N. Bertru, J.F. Guillemoles, and O. Durand, Sol. Energy Mater. Sol. Cells **147**, 53 (2016).

[99] K. Yamane, M. Goto, K. Takahashi, K. Sato, H. Sekiguchi, H. Okada, and A. Wakahara, Appl. Phys. Express **10**, 75504 (2017).

[100] W. Shan, W. Walukiewicz, J. Ager, E. Haller, J. Geisz, D. Friedman, J. Olson, and S. Kurtz, Phys. Rev. Lett. **82**, 1221 (1999).

[101] W. Shan, W. Walukiewicz, K.M. Yu, J.W. Ager III, E.E. Haller, J.F. Geisz, D.J. Friedman, J.M. Olson, S.R. Kurtz, H.P. Xin, and C.W. Tu, Phys. Status Solidi **223**, 75 (2001).

[102] N. V. Kryzhanovskaya, a. Y. Egorov, E. V. Pirogov, and M.S. Sobolev, J. Surf. Investig. X-Ray, Synchrotron Neutron Tech. **6**, 479 (2012).

[103] B. Kunert, K. Volz, and W. Stolz, Phys. Status Solidi Basic Res. **244**, 2730 (2007).

[104] R. Kudrawiec, J. Appl. Phys. **101**, 23522 (2007).

[105] R. Kudrawiec, J. Appl. Phys. **101**, 116101 (2007).

[106] J. Chamings, S. Ahmed, A.R. Adams, S.J. Sweeney, V.A. Odnoblyudov, C.W. Tu, B. Kunert, and W. Stolz, Phys. Status Solidi **246**, 527 (2009).

[107] C. Karcher, H. Grüning, M. Güngerich, P.J. Klar, B. Kunert, K. Volz, W. Stolz, and W. Heimbrodt, Phys. Status Solidi Curr. Top. Solid State Phys. **6**, 2638 (2009).

[108] E. V. Nikitina, M.S. Sobolev, E. V. Pirogov, and A.Y. Egorov, Tech. Phys. Lett. **39**, 1114 (2013).

[109] C.W. Tu, W.M. Chen, I.A. Buyanova, and J.S. Hwang, J. Cryst. Growth **288**, 7 (2006).

[110] L. Bellaiche, S.-H. Wei, and A. Zunger, Appl. Phys. Lett. **70**, 3558 (1997).

[111] T. Kitatani, M. Kondow, T. Kikawa, Y. Yazawa, M. Okai, and K. Uomi, Jpn. J. Appl. Phys. **38**, 5003 (1999).

[112] H.-P. Komsa, E. Arola, and T.T. Rantala, Appl. Phys. Lett. **92**, 262101 (2008).

[113] R. Kudrawiec, H.B. Yuen, S.R. Bank, H.P. Bae, M.A. Wistey, J.S. Harris, M. Motyka, and J. Misiewicz, J. Appl. Phys. **102**, 113501 (2007).

[114] A.S. Chang, E.S. Zech, T.W. Kim, Y.H. Lin, L.J. Mawst, and R.S. Goldman, Appl. Phys. Lett. **105**, 142105 (2014).

[115] W. Li, M. Pessa, J. Toivonen, and H. Lipsanen, Phys. Rev. B **64**, 113308 (2001).

[116] R. Varache, M. Darnon, M. Descazeaux, M. Martin, T. Baron, and D. Muñoz, Energy Procedia **77**, 493 (2015).

[117] J.R. Gong, S. Nakamura, M. Leonard, S.M. Bedair, and N.A. El-Masry, J. Electron. Mater. **21**, 965 (1992).

[118] F. Rinaldi, Annu. Rep. 31 (2002).

[119] A.S. Gudovskikh, A. V. Uvarov, I.A. Morozov, A.I. Baranov, D.A. Kudryashov, E. V. Nikitina, and J.-P. Kleider, Phys. Status Solidi Curr. Top. Solid State Phys. **14**, 1700150 (2017).

[120] S.M. Sze and K.K. Ng, in *Phys. Semicond. Devices* (John Wiley & Sons, Inc., Hoboken, NJ, USA, 2006).

[121] J.-P. Kleider, J. Alvarez, A. Brézard-Oudot, M.-E. Gueunier-Farret, and O. Maslova, Sol. Energy Mater. Sol. Cells **135**, 8 (2015).

[122] S.R. Forrest, *Heterojunction Band Discontinuities – Physics and Device Applications* (Elsevier Science Pub. Co., Amsterdam, 1987).

[123] J.P. Kleider and A.S. Gudovskikh, in *MRS Spring Meet. San Fr. 24-28 March, 2008* (San-Francisco, 2008), pp. 75–86.

[124] D.K. Schroder, *Semiconductor Material and Device Characterization* (John Wiley & Sons, Inc., Hoboken, NJ, USA, 2005).

[125] D.L. Losee, J. Appl. Phys. **46**, 2204 (1975).

[126] G. Vincent, D. Bois, and P. Pinard, J. Appl. Phys. **46**, 5173 (1975).

[127] T. Walter, R. Herberholz, C. Müller, and H.W. Schock, J. Appl. Phys. **80**, 4411 (1996).

[128] D. V. Lang, J. Appl. Phys. **45**, 3023 (1974).

[129] W. Shockley and W.T. Read, Phys. Rev. **87**, 835 (1952).

[130] R.N. Hall, Phys. Rev. **87**, 387 (1952).

[131] Y. Zohta and M.O. Watanabe, J. Appl. Phys. **53**, 1809 (1982).

[132] G.L. Miller, D. V Lang, and L.C. Kimerling, Annu. Rev. Mater. Sci. **7**, 377 (1977).

[133] L. Dobaczewski, P. Kaczor, I.D. Hawkins, and A.R. Peaker, J. Appl. Phys. **76**, 194 (1994).

[134] R. Varache, C. Leendertz, M.E. Gueunier-Farret, J. Haschke, D. Muñoz, and L. Korte, Sol. Energy Mater. Sol. Cells **141**, 14 (2015).

[135] T. V. Blank and Y.A. Gol'dberg, Semiconductors **41**, 1263 (2007).

[136] A.I. Baranov, A.S. Gudovskikh, E. V Nikitina, and A.Y. Egorov, Tech. Phys. Lett. **39**, 1117 (2013).

[137] F.C. Frank and J.H. van der Merwe, Proc. R. Soc. A Math. Phys. Eng. Sci. **198**, 216 (1949).

[138] J.H. Van Der Merwe, J. Appl. Phys. **34**, 117 (1963).

[139] M. Dąbrowska-Szata, G. Jóźwiak, and Ł. Gelczuk, Mater. Sci. **23**, 625 (2005).

[140] S.W. Johnston, R. Ahenkiel, A. Ptak, D. Friedman, and S. Kurtz, Nrel/Cp-520-33557 1 (2003).

[141] A. Kosa, L. Stuchlikova, L. Harmatha, J. Kovac, B. Sciana, W. Dawidowski, and M. Tlaczala, Adv. Electr. Electron. Eng. **15**, 114 (2017).

[142] B. Bouzazi, N. Kojima, Y. Ohshita, and M. Yamaguchi, J. Alloys Compd. **552**, 469 (2013).

[143] D.J. Friedman, A.J. Ptak, S.R. Kurtz, and J.F. Geisz, in *Conf. Rec. Thirty-First IEEE Photovolt. Spec. Conf. 2005.* (IEEE, 2005), pp. 691–694.

[144] P. Omling, L. Samuelson, and H.G. Grimmeiss, J. Appl. Phys. **54**, 5117 (1983).

[145] J.W. Matthews and A.E. Blakeslee, J. Cryst. Growth **27**, 118 (1974).

[146] A.E. Zhukov, A.Y. Egorov, V.M. Ustinov, A.F. Tsatsulnikov, M. V Maksimov, N.N. Faleev, and P.S. Kopev, Semiconductors **31**, 15 (1997).

[147] P. Blood and J.W. Orton, *The Electrical Characterization of Semiconductors : Majority Carriers and Electron States* (Academic Press, 1992).

[148] W. Schröter, J. Kronewitz, U. Gnauert, F. Riedel, and M. Seibt, Phys. Rev. B **52**, 13726 (1995).

[149] D. Pons, J. Appl. Phys. **55**, 3644 (1984).

[150] E. Płaczek-Popko, J. Trzmiel, E. Zielony, S. Grzanka, R. Czernecki, and T. Suski, Phys. B Condens. Matter **404**, 4889 (2009).

[151] T. Wosiński, J. Appl. Phys. **65**, 1566 (1989).

[152] M. Matyas Jr., Phys. Status Solidi **97**, 297 (1986).

[153] J. Dabrowski and M. Schemer, Phys. Rev. B **40**, 391 (1989).

[154] A.S. Gudovskikh, K.S. Zelentsov, A.I. Baranov, D.A. Kudryashov, I.A. Morozov, E.V. Nikitina, and J.-P. Kleider, Energy Procedia **102**, 56 (2016).

[155] I. Sakata and H. Kawanami, Appl. Phys. Express **1**, 91201 (2008).

[156] A. Utsumi, H. Yonezu, Y. Furukawa, K. Momose, and K. Kuroki, Phys. Status Solidi C Conf. **2744**, 2741 (2003).

[157] I.A. Morozov, A.S. Gudovskikh, D.A. Kudryashov, E. V Nikitina, J.-P. Kleider, A. V Myasoedov, and V. Levitskiy, J. Phys. Conf. Ser. **741**, 12088 (2016).

[158] M. Wihl, M. Cardona, and J. Tauc, J. Non. Cryst. Solids **8–10**, 172 (1972).

[159] S. Hayashi, Solid State Commun. **56**, 375 (1985).

[160] M. Onuki and H. Kubota, Jpn. J. Appl. Phys. **26**, 1404 (1987).

[161] H. Kubota and M. Onuki, J. Non. Cryst. Solids **115**, 39 (1989).

[162] H. Kubota, T. Matsumoto, T. Hirayu, T. Fujiyoshi, R. Miyagawa, K. Miyahara, and M. Onuki, Sol. Energy Mater. Sol. Cells **35**, 353 (1994).

[163] H. Kubota, T. Tashiro, T. Fujiyoshi, T. Hirayu, and M. Onuki, J. Non. Cryst. Solids **198–200**, 383 (1996).

[164] T.F. Lei, C.L. Lee, and C.Y. Chang, Solid. State. Electron. **22**, 1035 (1979).

[165] R. Mientus, R. Wolf, B. Kloth, M. Protsch, and A.N. Pikhtin, Surf. Coatings Technol. **119**, 711 (1999).

[166] H. Kroemer, W. Chien, J.S. Harris, and D.D. Edwall, Appl. Phys. Lett. **36**, 295 (1980).

[167] L. Ding, C. Zhang, T.U. Nærland, N. Faleev, C. Honsberg, and M.I. Bertoni, Energy Procedia **92**, 617 (2016).

[168] J. Damon-Lacoste, P.R.I. Cabarrocas, A.S. Gudovskikh, J.-P. Kleider, P.J. Ribeyron, V. Svrcek, and Y. Veschetti, in *Proc. 19th Eur. Photovolt. Sol. Energy Conf. Exhib. (EU PVSEC), Paris, Fr. 2014, Vol. 2 Cells*, edited by K.W. Hoffmann, J.L. Bal, H. Ossenbrink, W. Palz, and P. Helm (Paris, 2004), pp. 1453–1456.

[169] G.G. DeLeo, Phys. B Phys. Condens. Matter **170**, 295 (1991).

[170] C.T. Sah, J.Y.C. Sun, and J.J.T. Tzou, Appl. Phys. Lett. **43**, 204 (1983).

[171] A.M. Cowley, Solid. State. Electron. **12**, 403 (1970).

[172] O.O. Awadelkarim and B. Monemar, J. Appl. Phys. **64**, 6306 (1988).

[173] A.A. Istratov, H. Hieslmair, and E.R. Weber, Appl. Phys. A Mater. Sci. Process. **69**, 13 (1999).